Characterising Solar Wind Fluctuations at Ion-kinetic Scales

Lloyd David Woodham

A dissertation submitted in partial fulfillment
of the requirements for the degree of
Doctor of Philosophy
of
University College London.

Mullard Space Science Laboratory
Department of Space and Climate Physics
University College London

December 20, 2019

I, Lloyd David Woodham, confirm that the work presented in this thesis is my own. Where information has been derived from other sources, I confirm that this has been indicated in the work.

Abstract

The availability of large *in-situ* datasets makes the solar wind an excellent astrophysical laboratory to probe kinetic processes in a collisionless plasma. As the solar wind turbulent cascade reaches ion-kinetic scales close to the proton gyro-radius, ρ_p, and inertial length, d_p, collective effects lead to interactions between electromagnetic fluctuations and particle velocity distributions. At these scales, wave-particle interactions can lead to the dissipation of turbulent fluctuations and instability growth, which in turn, moderates the macroscopic properties of the plasma.

In this thesis, I use over a decade of magnetic field and ion measurements from the *Wind* spacecraft to investigate the physical processes ongoing at these scales. I make the first in-flight determination of the magnetometer noise-floor, enabling the most accurate interpretation of magnetic field fluctuations at these scales with *Wind* to date. I then conduct three detailed statistical analyses of the spectral properties of these fluctuations.

I first show that the steepening of the power spectrum and a coherent signature in magnetic helicity at ion-kinetic scales are associated with the cyclotron resonance wave-number, k_c, providing evidence for ongoing wave-particle interactions at these scales. I then use magnetic helicity to characterise the polarisation properties of the fluctuations, identifying three populations at ion-kinetic scales: quasi-parallel propagating Alfvén-ion cyclotron and fast magnetosonic-whistler waves driven by proton temperature anisotropy instabilities, as well as highly-oblique kinetic Alfvén wave-like fluctuations from the turbulent cascade. Finally, I show that the KAW-like fluctuations are associated with steeper spectra and higher proton temperatures, suggesting damping of the turbulence.

The results presented in this thesis indicate that wave-particle interactions play an important role in the energy transfer between the turbulent fields and ions in the solar wind, in the absence of collisions. I also show that proton heating in the solar wind depends on the polarisation properties of the fluctuations at ion-kinetic scales and the radial direction in the solar wind, in contradiction to the ergodicity hypothesis. Further investigative work is proposed to confirm these findings and identify specific dissipation mechanisms responsible for turbulent heating.

Impact Statement

Almost all visible matter in the Universe is in the plasma state. Due to the large scales associated with different plasma environments, such as stellar winds, supernovae, black hole accretion disks, and the interstellar medium, these plasmas have low collision rates and likely exhibit a turbulent cascade. There are many open questions on the nature of turbulence in low-collisionality plasmas, especially regarding the eventual dissipation of energy from the turbulent fluctuations. The dissipation mechanisms responsible for heating in astrophysical plasmas are still hotly debated. Understanding energy transport in these plasmas is, therefore, fundamental to our understanding of many physical processes occurring throughout the Universe.

In this thesis, I gain deeper insights into turbulent dissipation in the solar wind, an excellent plasma laboratory allowing us to study the physical processes with spacecraft that have been making *in-situ* measurements of the electromagnetic fields and particles for several decades. As part of my research, I make the first in-flight determination of the noise-floor of the magnetometer onboard the *Wind* spacecraft. This noise-floor enabled me to undertake the most accurate analysis of magnetic field fluctuations ion-kinetic scales in the solar wind with *Wind* and can also be used by other researchers utilising data from this instrument. This work has been published in The Astrophysical Journal and has already been cited many times since publication.

I also use a novel analysis technique to filter the magnetic helicity of solar wind fluctuations at high-frequencies, allowing for the determination of the polarisation properties and information on the propagation direction of these fluctuations from single-spacecraft measurements. I recently published this work in The Astrophysical Journal Letters. This technique can be readily applied to data from other spacecraft, including the *Parker Solar Probe* and *Solar Orbiter* missions to investigate coronal heating and solar wind acceleration processes. These new missions will not only address fundamental questions about the formation of the solar wind but will also provide insights that will aid the forecasting and modelling of space weather. By understanding solar wind dynamics, we can better predict geomagnetic activity at Earth, benefiting not only academia but industry and society as a whole. Space weather is a risk to both spacecraft and astronauts in orbit around the Earth and national electricity grids on the surface of the Earth.

Acknowledgements

There are so many people to acknowledge for supporting me on my journey to becoming an astrophysicist; I can't possibly list everyone here. However, I will do my best to put into words my gratitude towards a select few who got me to where I am today. To anyone I may have missed, *diolch yn fawr*.

First and foremost, I'd like to thank my supervisor, Robert Wicks, for all your support and guidance over the past three years. You taught me so much about the solar wind and instilled in me an attention to detail that I will take with me wherever I go. Our conversations about turbulence lasting for hours were a highlight and something that always reminded me of why I took on the challenge of completing a PhD. I hope I'm the first of many successful students!

To my second supervisor, Christopher Owen, thank you for always asking those difficult questions. You taught me to think carefully about the underlying physical principles when discussing my work. I'd also like to thank Daniel Verscharen, while not my official supervisor, you took the time to support me and my work. Your deep insights in theoretical plasma physics have been illuminating and have undoubtedly contributed to the successful completion of this work. To my collaborators, Bennett Maruca and Benjamin Alterman, thank you for your assistance and advice. I hope we can continue to work together successfully in the future.

To my best friend and 'partner in crime', Ioana, no words can express how grateful I am for your support these past few years. We started this journey together, and while we may not be finishing it at the same time, I'll be there

to support you in your final months. It has been a privilege, mulţumesc!

To the rest of the Plasma Group, thank you for putting up with my rambling and incessant tea drinking. Caoimhe, your smile and enthusiasm have always managed to make me feel better no matter what mood I'm in. Thank you to the other staff members in the group, Jonathan, Colin, and Andrew, for your tough questioning at many discussion forums over the years. To my many office colleagues: Allan, Georgie, Nadine, Jasmine, Georgios, Marina, Frankie, Michaela, Hong Hong, Sam, Mayur, Andy, Seong Yeop, Diego, and Jeff, the frogs will live on in my memory for many years to come. To the rest of the MSSL family, I will miss you.

Thanks to all my friends, both inside and outside academia, wherever you are, for your support. To my housemates, Tom, Lucy, and Jack, it's been a blast. To my parents, thank you for putting up with me over the years. Your love and support mean the world to me.

Finally, I'd like to thank Jonathan Rae and Fouad Sahraoui for taking the time to examine this thesis, as well as STFC for funding my studentship and MSSL for travel support to attend conferences.

To my beloved Nana, you make me aim for the stars

Contents

List of Figures

List of Tables

Chapter 1

Introduction

The solar wind is a supersonic and super-Alfvénic outflow of plasma from the solar corona, filling the heliosphere and convecting with it the interplanetary magnetic field [Parker, 1958, 1963]. It is almost completely ionised, made up primarily of protons and electrons, with a small component of He^{2+} (α-particles) and trace amounts of ions in different charge states made from heavier elements such as C, O, Si, and Fe. The solar wind plasma is highly variable; its speed ranges from about 300 km s^{-1} up to 2,500 km s^{-1}, and its density from a few particles cm^{-3} to hundreds of particles cm^{-3} [Hundhausen, 1970].

At scales larger than the proton gyro-radius, ρ_p, and inertial length, d_p, in the solar wind ($\sim 10^2$ km), the magnetic field is 'frozen-in' to the plasma due to its infinite resistivity, and together they act as a magnetohydrodynamic (MHD) fluid. This fluid exhibits turbulent behaviour, where non-linear interactions between the magnetic field and velocity fluctuations drive a continual cascade of energy from large scales ($\sim 10^6$ km) down to smaller scales (of order the electron gyroradius, $\sim 10^1$ km), where the energy is eventually dissipated [Bruno & Carbone, 2013]. Unlike in a neutral fluid, most space plasmas such as the solar wind are collisionless, i.e., the rate of collisions between particles is too low for collisions to play a dominant role in heating the plasma [Marsch, 2006]. Instead, other processes must contribute to the dissipation of turbulent fluctuations at small scales and heating of the solar wind plasma.

When the energy cascade reaches ion-kinetic scales, the plasma no longer behaves as an MHD fluid, and the collective particle dynamics that characterise kinetic motions of plasma must be considered [Alexandrova et al., 2013; Chen, 2016]. The solar wind is highly conducting, and so large-scale electric fields are typically too small to energise particles. However, at ion-kinetic scales, electromagnetic fluctuations can interact with the velocity distribution functions (VDFs) of different plasma species, leading to the generation of waves, instabilities, and heating through non-resonant and resonant processes such as stochastic heating and Landau/cyclotron damping, respectively.

There are many open questions relating to solar wind turbulence. Where does the turbulent cascade form, from within the corona, or from local driving in the solar wind? How does the cascade modify the macroscopic properties plasma? How does the energy in the turbulent fluctuations get dissipated into heat at small scales? What is more important for energy dissipation, non-linear turbulent heating or resonant wave-particle interactions? Why are α-particles hotter than protons in the solar wind? How do kinetic instabilities interact with the turbulent cascade? Of particular interest in recent years is the dissipation of the turbulent fluctuations, heating the solar wind plasma. Some new insights have been provided as to the nature of the turbulence at kinetic scales [see Kiyani et al., 2015, and references therein], but it is still not known what processes are responsible for the dissipation, under what conditions they occur, and how efficient each mechanism is at heating the plasma.

There are now several large and high-quality *in-situ* datasets, as well as upcoming missions that will provide unparalleled observations to develop our understanding of the dynamics of the solar wind. A deeper understanding of the kinetic processes in a turbulent plasma will provide insights into problems such as coronal heating and solar wind acceleration. This knowledge will also improve our understanding of astrophysical plasmas that are not accessible to spacecraft, including accretion disks and supernovae, making the solar wind an excellent plasma laboratory to understand energy transport throughout the

Universe.

In this thesis, I use over a decade of measurements from the *Wind* spacecraft to probe the spectral properties of the magnetic field fluctuations at ion-kinetic scales. By characterising the fluctuations at these scales, I reveal new insights into turbulence dissipations, proton heating and instability growth in the solar wind. I first discuss the relevant background material necessary to interpret my results in Chapters 2 and 3. I then review and critically analyse the relevant literature and current state of solar wind research in Chapter 4. In Chapter 5 I describe how *in-situ* measurements of the solar wind magnetic field and particle VDFs are made, as well as the spectral and statistical analysis techniques I use to investigate solar wind fluctuations. I then present the main body of my research in Chapters 6-8. Finally, I discuss my conclusions and possible future work in Chapter 9.

Chapter 2

Space Plasma Physics

In this chapter, I cover the background information on plasma physics relevant to the solar wind, and my research discussed later in this thesis. I begin with the definition of a plasma and the characteristic time and length scales associated with it. I then discuss the kinetic theory of plasmas, distribution functions, and Coulomb collisions before using kinetic theory to derive the multi-fluid and magnetohydrodynamical models of a plasma. I then describe plasma waves, instabilities, and wave-particle resonances that are important in the solar wind. Finally, I discuss the solar wind, its general properties, and characterisation of different wind streams.

2.1 What is a Plasma?

A plasma is an ionised gas made up of charged particles. It can either be completely or partially ionised, containing both charged and neutral particles. In a neutral gas, the particles move about randomly and collide with each other, whereas in a plasma the long-range electromagnetic forces also act on the particles through the Lorentz force,

$$\mathbf{F}_L \equiv m_j \frac{d\mathbf{v}_j}{dt} = q_j \left(\mathbf{E} + \mathbf{v}_j \times \mathbf{B}\right), \tag{2.1}$$

where m_j is the mass and $\mathbf{v}_j$ is the velocity of a particle of species, j. Here, $\mathbf{E}$ and $\mathbf{B}$ are the macroscopic electric and magnetic fields that arise from the contributions of all other particles. These long-range interactions lead to the collective behaviour of the charged particles making up a plasma, distinguishing it from a neutral gas [Boyd & Sanderson, 2003]. A plasma is quasi-neutral so that at large scales there are the same number of positive and negative electrical charges, i.e., the overall charge is zero. Quasi-neutrality is maintained because, at small scales, particles move to shield electrostatic effects over the Debye length:

$$\lambda_j \equiv \sqrt{\frac{\varepsilon_0 k_\mathrm{B} T_j}{n_j q_j^2}}, \tag{2.2}$$

where ε_0 is the vacuum permittivity, k_B is the Boltzmann constant, T_j is the temperature, n_j is the number density, and q_j is the charge of particle species j. Throughout this thesis, I use $j = e$ to refer to electrons and $j = i$ for ions, either protons ($j = p$) or α-particles ($j = \alpha$). I also include the sign of the charge in q_j, e.g., $q_p = +e$ and $q_e = -e$, where e is the elementary charge constant. Since $m_e \ll m_i$, electrons are much more mobile than ions and so, it is the distance λ_e over which this shielding occurs. Collective processes are important if the number of electrons within a sphere of radius λ_e is large:

$$n_e \lambda_e^3 \gg 1, \tag{2.3}$$

and if λ_e is much smaller than the characteristic size of the system, L. If Equation 2.3 and $\lambda_e \ll L$ hold, then the shielding of external electric fields by electrons means the particles interact only with a smooth macroscopic electromagnetic field and not as individual moving charges [Bellan, 2008].

2.2 Characteristic Scales in a Plasma

In addition to the Debye length, a plasma contains several other characteristic scales due to the interactions between the charged particles and the electromagnetic fields [Gurnett & Bhattacharjee, 2017]. Due to the cross-product $\mathbf{v}_j \times \mathbf{B}$ in Equation 2.1, the Lorentz force leads to a gyration of particles in the plane perpendicular to the magnetic field. The gyro-frequency of this helical motion is:

$$\Omega_j \equiv \frac{q_j B}{m_j}, \tag{2.4}$$

given in units of rad s^{-1} where $B = |\mathbf{B}|$. Here, the sign of Ω_j refers to the direction of gyration, positive for left-handed and negative for right-handed gyration. The thermal speed is:

$$w_j \equiv \sqrt{\frac{2k_\mathrm{B}T_j}{m_j}}, \tag{2.5}$$

which is the typical speed of the thermal motion of the particles in a plasma (see Section 2.5.2). A plasma can have different temperatures parallel ($T_{j,\parallel}$) and perpendicular ($T_{j,\perp}$) to the field direction, $\hat{\mathbf{b}} \equiv \mathbf{B}/B$, so that there are two thermal speeds: $w_{j,\parallel}$ and $w_{j,\perp}$. The radius of the helical motion of charged particles in a magnetic field is given by the gyro-radius:

$$\rho_j \equiv \frac{w_{j,\perp}}{|\Omega_j|}. \tag{2.6}$$

The plasma frequency is defined as:

$$\omega_{\mathrm{p},j} \equiv \sqrt{\frac{n_j q_j^2}{m_j \varepsilon_0}}. \tag{2.7}$$

Since $m_e \ll m_i$, in the absence of thermal motions ions remain fixed while electrons oscillate with frequency $\omega_{\mathrm{p},e}$ in response to an electric field restoring force, maintaining quasi-neutrality. Light waves with $\omega \lesssim \omega_{\mathrm{p},e}$ cannot propagate in a plasma due to the shielding caused by these oscillations, leading to the inertial length (or skin-depth):

$$d_j \equiv \frac{c}{\omega_{\mathrm{p},j}} = \frac{v_{\mathrm{A},j}}{|\Omega_j|}, \tag{2.8}$$

where $c = 1/\sqrt{\epsilon_0 \mu_0}$ is the speed of light, μ_0 is the vacuum permeability, and $v_{\mathrm{A},j}$ is the Alfvén speed of species j:

$$v_{\mathrm{A},j} \equiv \frac{B}{\sqrt{\mu_0 n_j m_j}}. \tag{2.9}$$

The characteristic speed of Alfvén waves in a plasma (see Section 2.6.3) is given by $v_{\mathrm{A},p}$, which I will refer to as v_A throughout the rest of this thesis. At scales larger than both d_p and ρ_p, the gyration motion of the particles can be neglected and the plasma motion is closely tied to the magnetic field, making a fluid treatment applicable (see Sections 2.5 and 2.5.5). The gyro-radius and inertial length are linked through the plasma β:

$$\frac{\rho_j}{d_j} = \sqrt{\beta_j}, \tag{2.10}$$

where

$$\beta_j \equiv \frac{n_j k_\mathrm{B} T_j}{B^2/2\mu_0}, \tag{2.11}$$

is the ratio of the plasma species thermal pressure ($p_j = n_j k_B T_j$) to magnetic pressure ($p_B = B^2/2\mu_0$). At low β, the magnetic field dominates the motion of the plasma, whereas at high β, the plasma motion convects the magnetic field with it due to the 'frozen-in' effect (see Section 2.5.6).

2.3 Coulomb Collisions

Collisions among particles provide the mechanism for a plasma to increase its entropy and reach thermal equilibrium. In a fully ionised plasma, Coulomb collisions are the primary process where particles exchange momentum and energy. These collisions are not the same as ballistic inelastic collisions between neutral particles; instead, they are small deflections between charged particles due to their induced electric fields [Swanson, 2008]. These collisions result in changes in the trajectories and velocities of the particles. In low-density space plasmas such as the solar wind, the rate of particle collisions is relatively low. Despite this, the effects of collisions on the plasma can still impact its evolution (see Section 4.1).

2.4 Plasma Kinetic Theory

In a plasma, charged particles respond to the Lorentz force (Equation 2.1) arising from the electromagnetic fields, while also contributing as sources of these fields. It is very difficult to analytically solve for the motion of every individual particle at any time. Instead kinetic theory is used, which describes the statistical properties of a plasma with the particle velocity distribution function, $f_j(\mathbf{x}, \mathbf{v}, t)$, for species j. This distribution function is normalised such that:

$$N_j = \int f_j(\mathbf{x}, \mathbf{v}, t) \mathrm{d}^3\mathbf{v} \mathrm{d}^3\mathbf{x}, \tag{2.12}$$

is the number of particles of species j in phase space volume, $(\mathbf{x}, \mathbf{v})$, at time t. When the number of particles in a Debye sphere is sufficiently large (Equation 2.3), the evolution of f_j satisfies the Boltzmann equation:

$$\frac{\partial f_j}{\partial t} + \mathbf{v} \cdot \frac{\partial f_j}{\partial \mathbf{x}} + \mathbf{a} \cdot \frac{\partial f_j}{\partial \mathbf{v}} = \left(\frac{\delta f_j}{\delta t}\right)_{\mathrm{c}}, \tag{2.13}$$

where $\mathbf{a}$ is the acceleration on each of the particles due to the Lorentz force and the right-hand side describes the change in f_j due to particle collisions. Deriving an expression for the collision term is difficult [see Verscharen et al., 2019, and references therein] since the microscopic electric fields that lead to Coulomb collisions also contribute to the macroscopic electric field that appears in the acceleration term.

If the collision term is zero, which is a good assumption in space plasmas due to the low collision rate, the Boltzmann equation becomes a continuity equation for the density in phase space:

$$\frac{\partial f_j}{\partial t} + \mathbf{v} \cdot \frac{\partial f_j}{\partial \mathbf{x}} + \frac{q_j}{m_j} (\mathbf{E} + \mathbf{v} \times \mathbf{B}) \cdot \frac{\partial f_j}{\partial \mathbf{v}} = 0, \tag{2.14}$$

where I have substituted for $\mathbf{a}$ using Equation 2.1. This is called the Vlasov equation [Vlasov, 1945], which from Liouville's theorem, describes the conservation of phase space density along a trajectory in the absence of collisions[1]. The evolution of a collisionless plasma can then be described by Equation 2.14 in tandem with Maxwell's equations for the electromagnetic fields:

$$\nabla \cdot \mathbf{E} = \frac{\rho_{\mathrm{c}}}{\varepsilon_0}, \tag{2.15a}$$

$$\nabla \cdot \mathbf{B} = 0, \tag{2.15b}$$

$$\nabla \times \mathbf{E} = -\frac{\partial \mathbf{B}}{\partial t}, \tag{2.15c}$$

$$\nabla \times \mathbf{B} = \mu_0 \mathbf{j} + \varepsilon_0 \mu_0 \frac{\partial \mathbf{E}}{\partial t}. \tag{2.15d}$$

The total charge density, ρ_c, and current density, $\mathbf{j}$, of the plasma are the sources of the electromagnetic fields, defined as:

$$\rho_{\mathrm{c}} = \sum_j q_j \int f_j \mathrm{d}^3\mathbf{v}, \tag{2.16a}$$

$$\mathbf{j} = \sum_j q_j \int \mathbf{v} f_j \mathrm{d}^3\mathbf{v}. \tag{2.16b}$$

This set of equations is called the Maxwell-Vlasov system of equations [see Montgomery & Tidman, 1964; Swanson, 2008, and references therein].

2.5 Fluid Models of a Plasma

2.5.1 Moments of the Distribution Function

By taking velocity moments of the distribution function, the bulk properties of the plasma can be obtained, such as n_j, $\mathbf{v}_j$, and T_j. These macroscopic properties of the plasma do not contain all of the microphysical properties of f_j, making them easier to work with since they are only functions of space and time. A velocity moment is an integral over the velocity space of f_j. For

---

[1] Liouville's theorem states that if a particle exists in phase space at a time t, then it can be traced to another point in phase space at a time $t + dt$. i.e., particles cannot be created or destroyed.

example, the zeroth, first, and second moments give the number density, n_j, bulk velocity, $\mathbf{u}_j$, and pressure tensor, P_j, respectively:

$$\begin{aligned} n_j &= \int f_j \mathrm{d}^3\mathbf{v}, && (2.17) \\ \mathbf{u}_j &= \frac{1}{n_j}\int \mathbf{v} f_j \mathrm{d}^3\mathbf{v}, && (2.18) \\ \mathsf{P}_j &= m_j \int (\mathbf{v}-\mathbf{u}_j)(\mathbf{v}-\mathbf{u}_j) f_j \mathrm{d}^3\mathbf{v}. && (2.19) \end{aligned}$$

The pressure tensor can be split into two components: $\mathsf{P}_j = p_j \mathsf{I}_3 + \pi$, where π_j is the stress tensor, containing the off-diagonal terms. The charge and current density become:

$$\rho_\mathrm{c} = \sum_j q_j n_j, \tag{2.20a}$$

$$\mathbf{j} = \sum_j q_j n_j \mathbf{u}_j. \tag{2.20b}$$

There is an infinite number of velocity moments, called a moment hierarchy [Gurnett & Bhattacharjee, 2017].

2.5.2 Maxwellian Velocity Distributions

There are several analytical expressions for particle velocity distributions (VDFs) relevant to the solar wind. A gas in thermodynamic equilibrium has a Maxwellian velocity distribution,

$$f_\mathrm{Max}(\mathbf{v}) = \frac{n_j}{\pi^{3/2} w_j^3} \exp\left(-\frac{(\mathbf{v}-\mathbf{u}_j)^2}{w_j^2}\right), \tag{2.21}$$

which is a Gaussian curve with peak situated at $\mathbf{v} = \mathbf{u}_j$ and full width at half maximum w_j. The area under the curve is proportional to n_j. For a Maxwellian distribution, the pressure tensor becomes a scalar and $p_j = n_j k_B T_j$, which using $w_j^2 = 2p_j/n_j m_j$, gives Equation 2.5.

A plasma with a background magnetic field often has a bi-Maxwellian distribution [Stix, 1992]:

$$f_{\mathrm{Bimax}}(\mathbf{v}) = \frac{n_j}{\pi^{3/2} w_{j,\perp}^2 w_{j,\parallel}} \exp\left(-\frac{\left(v_\perp - U_{j,\perp}\right)^2}{w_{j,\perp}^2} - \frac{\left(v_\parallel - U_{j,\parallel}\right)^2}{w_{j,\parallel}^2} \right). \tag{2.22}$$

Here, the pressure tensor is:

$$\mathsf{P}_j = \begin{bmatrix} p_{j,\perp} & 0 & 0 \\ 0 & p_{j,\perp} & 0 \\ 0 & 0 & p_{j,\parallel} \end{bmatrix}, \tag{2.23}$$

where $\pi = 0$. A 1D cut through the bi-Maxwellian distribution parallel or perpendicular to **B** recovers the standard Maxwellian. There are also more complicated distributions such as the kappa distribution [see Verscharen et al., 2019, for more details].

2.5.3 Multi-fluid Equations of a Plasma

Moments of the Vlasov equation can be taken to obtain the multi-fluid plasma equations. The zeroth moment gives the continuity equation:

$$\frac{\partial n_j}{\partial t} + \nabla \cdot (n_j \mathbf{u}_j) = 0, \tag{2.24}$$

which by multiplying by q_j and summing over all species gives the charge continuity equation:

$$\frac{\partial \rho_{\mathrm{c}}}{\partial t} + \nabla \cdot \mathbf{j} = 0. \tag{2.25}$$

The first moment is the momentum equation:

$$n_j m_j \left(\frac{\partial}{\partial t} + \mathbf{u}_j \cdot \nabla \right) \mathbf{u}_j = -\nabla \cdot \mathsf{P}_j + n_j q_j \left(\mathbf{E} + \mathbf{u}_j \times \mathbf{B} \right), \tag{2.26}$$

Here, the convective derivative is:

$$\frac{d}{dt} \equiv \left(\frac{\partial}{\partial t} + \mathbf{u} \cdot \nabla\right). \tag{2.27}$$

If the pressure tensor is isotropic then the term $-\nabla \cdot \mathsf{P}_j$ reduces to $-\nabla p$. Again, this hierarchy of moments extends to infinity, leading to a closure problem [Swanson, 2008]. While the nth moment of the Vlasov equation describes the dynamical evolution of the nth moment of f_j, it includes $(n+1)$st moment of f_j. For example, Equation 2.24 describes the evolution of n_j but includes the higher-order $\mathbf{u}_j$, which is described by Equation 2.26. The hierarchy can be truncated by expressing a higher-order moment of f_j in terms of lower moments only. Typically, this is done by assuming an isotropic ($\mathsf{P}_j = p_j \mathsf{I}_3$) or adiabatic pressure ($p_j \propto n_j^\kappa$, where κ is the adiabatic exponent).

2.5.4 Chew-Goldberger-Low Equations of State

By assuming only slow changes in the magnetic field compared to Ω_j and that $\mathsf{pi} = 0$, the second moment of the Vlasov equation can be used to obtain the conservation laws for the double-adiabatic invariants[2] or the Chew-Goldberger-Low (CGL) invariants [Chew et al., 1956],

$$\frac{d}{dt}\left(\frac{p_{j,\perp}}{n_j B}\right) = 0 \quad \text{and} \quad \frac{d}{dt}\left(\frac{p_{j,\parallel} B^2}{n_j^3}\right) = 0, \tag{2.28}$$

which can be used to model the adiabatic expansion of the solar wind where there is no energy input or loss to/from external sources (see Chapter 4).

2.5.5 Magnetohydrodynamics

Magnetohydrodynamics (MHD) is a single-fluid description of a plasma where the multi-fluid equations are summed over all particles species (usually protons and electrons) in the plasma [Galtier, 2016]. The MHD model describes plasma phenomena that are characterised by low frequencies, $\omega \ll \omega_{\mathrm{p},e}$, and long wavelengths, $\lambda \gg \lambda_e$. For slow temporal variations, the displacement current term, $\varepsilon_0 \mu_0 \, \partial \mathbf{E} / \partial t$, in Ampère's law (Equation 2.15d) can be neglected.

---

[2] An adiabatic invariant is a quantity that stays approximately constant for slowly occurring changes.

The charge density, $\rho_\mathrm{c} = n_i q_i + n_e q_e \simeq 0$ due to quasi-neutrality ($n \simeq n_i \simeq n_e$). The quasi-neutrality condition requires that $|\epsilon_0 \nabla \cdot \mathbf{E}/ne| \ll 1$ so that Gauss' law is dropped. The moments of this magnetofluid are the mass density:

$$\rho \equiv \sum_j m_j n_j, \tag{2.29}$$

the bulk flow velocity,

$$\mathbf{u} \equiv \frac{1}{\rho} \sum_j m_j n_j \mathbf{u}_j, \tag{2.30}$$

and the total pressure, which is assumed to be a scalar:

$$p \equiv \frac{1}{3} \sum_j \mathrm{Tr}\left\{\mathsf{P}_j\right\}. \tag{2.31}$$

The continuity equation becomes

$$\frac{\partial \rho}{\partial t} + \nabla \cdot (\rho \mathbf{u}) = 0, \tag{2.32}$$

and the momentum equation,

$$\rho \left(\frac{\partial}{\partial t} + \mathbf{u} \cdot \nabla \right) \mathbf{u} = -\nabla p + \mathbf{j} \times \mathbf{B}. \tag{2.33}$$

Faraday's law (Equation 2.15c) describes the evolution of $\mathbf{B}$ and since Gauss's law is dropped, the electric field is given by the generalised Ohm's law, derived using the momentum equation for electrons:

$$\mathbf{E} = \underbrace{-\mathbf{u} \times \mathbf{B}}_{\text{Convection}} + \underbrace{\frac{1}{en_e} \mathbf{j} \times \mathbf{B}}_{\text{Hall current}} - \underbrace{\frac{1}{en_e} \nabla \cdot \mathsf{P}_\mathrm{e}}_{\substack{\text{Electron} \\ \text{pressure}}} + \underbrace{\frac{m_\mathrm{e}}{n_e e^2} \frac{d\mathbf{j}}{dt}}_{\substack{\text{Electron} \\ \text{inertia}}}, \tag{2.34}$$

The last term on the right-hand side of Equation 2.34 can be neglected due to the small mass of electrons, $m_e/m_i \ll 1$. Finally, this system of equations is closed by assuming an equation of state, usually an adiabatic plasma, i.e.,

$$\frac{d}{dt}\left(\frac{p}{\rho^{\kappa}}\right)=0. \tag{2.35}$$

Both the Hall and electron pressure terms give rise to finite-Larmor radius effects. The electron pressure term in Equation 2.34 can be neglected if β_e is small, giving a coupled set of equations known as Hall MHD [Davidson, 2017]. A further simplification of this model is to neglect the Hall term in Equation 2.34 to give ideal MHD. This can be done for phenomena occurring at scales $L \gg d_i$ and $L \gg \rho_i$, as well as timescales $\tau \gg 2\pi/\Omega_i$ [Galtier, 2016]. Then, Ohm's law becomes:

$$\mathbf{E}=-\mathbf{u}\times\mathbf{B}. \tag{2.36}$$

Due to the cross product in Equation 2.36, an ideal MHD plasma has $\mathbf{E}_{\parallel}=0$. Here, the $\mathbf{j}\times\mathbf{B}$ term in the momentum equation (2.33) can be replaced using Ampère's law:

$$\mathbf{j}\times\mathbf{B}=\frac{1}{\mu_0}(\nabla\times\mathbf{B})\times\mathbf{B}\equiv\frac{1}{\mu_0}(\mathbf{B}\cdot\nabla)\mathbf{B}-\nabla\left(\frac{B^2}{2\mu_0}\right), \tag{2.37}$$

This term can be written as a divergence of a tensor $(\nabla\cdot\mathsf{T})$ in the momentum equation,

$$\rho\left(\frac{\partial}{\partial t}+\mathbf{u}\cdot\nabla\right)\mathbf{u}=-\nabla\cdot(\mathsf{T}+\mathsf{P}), \tag{2.38}$$

where

$$\mathsf{T}=-\frac{\mathbf{BB}}{\mu_0}+\mathsf{I}_3\frac{B^2}{2\mu_0}. \tag{2.39}$$

The first term is a magnetic tension force that acts along the magnetic field, and the second term is the magnetic pressure force that acts in all directions. Throughout this thesis, I use p to refer to the thermal pressure and P to refer to the total plasma pressure, $P=p+B^2/2\mu_0$ [Gurnett & Bhattacharjee, 2017].

2.5.6 Collisional Plasmas and Resistive MHD

For a collisional plasma, velocity moments of the collision term on the right-hand side of the Boltzmann equation (2.13) can be taken, giving additional collisional terms in the multi-fluid and MHD equations. The zeroth moment is zero, stating that density is conserved during Coulomb collisions (see Section 2.3). The first moment is $\mathbf{R}_j$, the collisional drag of a species of charged particles flowing relative to another species. By neglecting small temperature gradient effects,

$$\mathbf{R}_e \simeq -m_e n_e \nu_c (\mathbf{u}_e - \mathbf{u}_i) = n_e e \mathbf{j}/\sigma, \tag{2.40}$$

where $\sigma = n_e e^2/m_e \nu_c$ is the plasma conductivity and ν_c is the average frequency of collisions between electrons and ions [see Boyd & Sanderson, 2003]. Here, it is assumed that the conductivity is a scalar. In reality, the magnetic field results in a different σ parallel and perpendicular to the field, resulting in a tensor (see Section 2.6). For a plasma consisting of electrons and protons, $\mathbf{R}_p = -\mathbf{R}_e$, and $\mathbf{R}_j$ is included on the right-hand side of the momentum equation (2.26) for each species. In the MHD equations, Ohm's law (Equation 2.36) then includes the Joule heating term, $\mathbf{j}/\sigma$ [Baumjohann & Treumann, 1997b]. The same approximations to obtain the ideal MHD equations can be used to obtain the resistive MHD equations, where

$$\mathbf{E} = -\mathbf{u} \times \mathbf{B} + \frac{\mathbf{j}}{\sigma}. \tag{2.41}$$

In the absence of a magnetic field, the simple Ohm's law ($\mathbf{j} = \sigma \mathbf{E}$) is returned. From the resistive MHD equations, an evolution equation for $\mathbf{B}$ can be derived from Ampère's law and Ohm's law, called the induction equation:

$$\frac{\partial \mathbf{B}}{\partial t} = \nabla \times (\mathbf{u} \times \mathbf{B}) + \eta \nabla^2 \mathbf{B}, \tag{2.42}$$

where $\eta = 1/\mu_0 \sigma$ is the plasma resistivity (sometimes called the magnetic diffusivity). The first term is the convection term and the second term is the diffusion term. When the convection term dominates the diffusion term,

$$\frac{\partial \mathbf{B}}{\partial t} = \nabla \times (\mathbf{u} \times \mathbf{B}), \tag{2.43}$$

which gives the ‘frozen-in’ theorem, stating that the bulk motion of a plasma across field lines is not possible and the magnetic flux through a co-moving surface is conserved [Gurnett & Bhattacharjee, 2017]. In the opposite case,

$$\frac{\partial \mathbf{B}}{\partial t} = \eta \nabla^2 \mathbf{B}, \tag{2.44}$$

which describes the diffusion of the magnetic field. The collision rate in space plasmas is typically very low, $\nu_c \ll 1$, and the plasma conductivity becomes very large $\sigma \gg 1$. Therefore, the Joule heating term is usually dropped. This also means that the ratio of the convection to the diffusion term is large for these plasmas and at large scales, the magnetic field is ‘frozen-in’ to the plasma. However, at small scales and in boundary layers, resistivity can lead to diffusion of the magnetic field and as I discuss later, viscous damping of magnetic field fluctuations (see Section 3.2).

2.6 Plasma Fluctuations and Waves

Waves are periodic or quasi-periodic fluctuations in both space and time arising from the action of a restoring force. The electromagnetic forces in a plasma provide restoring forces, supporting many types of waves and fluctuations. Linear theory is usually used to describe plasma waves, which considers a wave consisting of a small perturbation from an equilibrium value, i.e., for example, the magnetic field: $\mathbf{B}(\mathbf{r},t) = \mathbf{B}_0 + \delta\mathbf{B}(\mathbf{r},t)$, where $\mathbf{B}_0$ is the constant background equilibrium value and $\delta\mathbf{B}$ is the fluctuating perturbation of $\mathbf{B}(\mathbf{r},t)$ [Stix, 1992]. Linear theory requires $|\delta\mathbf{B}| \ll |\mathbf{B}_0|$ and assumes plane waves:

$$\delta\mathbf{B}(\mathbf{r},t) \propto \mathrm{Re}\left\{\tilde{\mathbf{B}}(\mathbf{k},\omega)\exp\left[i\left(\mathbf{k}\cdot\mathbf{r} - \omega t\right)\right]\right\}, \tag{2.45}$$

where $\tilde{\mathbf{B}}(\mathbf{k},\omega)$ is the complex Fourier amplitude of $\mathbf{B}(\mathbf{r},t)$, $\mathbf{k}$ is the wave-vector of the wave ($k = 2\pi/\lambda$ is the wave-number, where λ is the wavelength of the wave) and is real, and $\omega = \omega_{\mathrm{r}} + i\gamma$ is the complex frequency. Here, γ is the linear growth or damping rate of the wave, depending on its sign. The phase, $\mathbf{v}_{\mathrm{ph}}$, and group, $\mathbf{v}_{\mathrm{g}}$, velocities of the wave are defined as:

$$\mathbf{v}_{\mathrm{ph}} = \frac{\omega(\mathbf{k})}{k}\hat{\mathbf{k}} \quad \text{and} \quad \mathbf{v}_{\mathrm{g}} = \frac{\partial \omega(\mathbf{k})}{\partial \mathbf{k}}. \tag{2.46}$$

The phase velocity is parallel to $\mathbf{k}$ and gives direction and speed of the propagation of the wavefront or phase, $\phi(\mathbf{r},t) = \mathbf{k}\cdot\mathbf{r} - \omega t$. The group velocity gives the direction of the flow of energy and information contained in the wave, which can be in a different direction to $\mathbf{v}_{ph}$ [Gary, 1993].

2.6.1 The Wave Equation and Dispersion Relation

A linear dispersion relation is a mathematical expression that connects solutions of ω and $\mathbf{k}$, giving a self-consistent description of the electromagnetic field and particle fluctuations. If a dispersion relation has multiple solutions for a given $\mathbf{k}$, then each solution corresponds to a distinct mode. To obtain the dispersion relation of plasma waves, Maxwell's equations (2.15) are linearised by writing in Fourier space [Gurnett & Bhattacharjee, 2017]. The Fourier transform of a function $f(x)$ is given by the integral:

$$\tilde{F}(k) = \int_{-\infty}^{\infty} f(x)\mathrm{e}^{-ikx}\mathrm{d}x. \tag{2.47}$$

A function of space and time $f(\mathbf{r},t)$ is related to its Fourier transform by:

$$f(\mathbf{r},t) = \int_{-\infty}^{\infty} \tilde{F}(\mathbf{k},\omega)\mathrm{e}^{i(\mathbf{k}\cdot\mathbf{r}-\omega t)}\mathrm{d}^3\mathbf{k}\,\mathrm{d}\omega. \tag{2.48}$$

In Fourier space, temporal and spatial derivatives are $\partial/\partial t \to -i\omega$ and $\nabla \to i\mathbf{k}$, respectively. Maxwell's equations can therefore be written as:

$$\mathbf{k}\cdot\tilde{\mathbf{E}} = -\frac{i\tilde{\rho}_{\mathrm{c}}}{\varepsilon_0}, \tag{2.49a}$$

$$\mathbf{k}\cdot\tilde{\mathbf{B}} = 0, \tag{2.49b}$$

$$\mathbf{k}\times\tilde{\mathbf{E}} - \omega\tilde{\mathbf{B}} = 0, \tag{2.49c}$$

$$\mathbf{k}\times\tilde{\mathbf{B}} + \frac{\omega}{c^2}\tilde{\mathbf{E}} = -i\mu_0\tilde{\mathbf{j}}, \tag{2.49d}$$

where $\mathbf{E}(\mathbf{r},t) = \delta\mathbf{E}(\mathbf{r},t) = \mathrm{Re}\{\tilde{\mathbf{E}}(\mathbf{k},\omega)\exp[i(\mathbf{k}\cdot\mathbf{r}-\omega t)]\}$. To quantify the interaction between the waves and particles the plasma susceptibility tensor $\boldsymbol{\chi}_j$ of species j, is defined:

$$\tilde{\mathbf{j}}_j = \boldsymbol{\sigma}_j\cdot\tilde{\mathbf{E}} = -i\omega\varepsilon_0\boldsymbol{\chi}_j\cdot\tilde{\mathbf{E}}, \tag{2.50}$$

where $\boldsymbol{\sigma}_j$ is the conductivity tensor, and $\tilde{\mathbf{j}}_j$ is the Fourier amplitude of the current density of species j. Therefore, $\boldsymbol{\chi}_j$ describes the degree of polarisation of species j and hence, a current in response to any perturbations by the wave electromagnetic fields. By summing over all species, the dielectric tensor $\boldsymbol{\epsilon}$ can be defined as the sum of the contributions from all plasma species:

$$\boldsymbol{\epsilon} = 1 + \sum_j \boldsymbol{\chi}_j. \tag{2.51}$$

Combining Equations 2.49 and 2.50 and summing over all species gives the wave equation in terms of $\boldsymbol{\epsilon}$:

$$\mathbf{n}\times(\mathbf{n}\times\mathbf{E}) + \boldsymbol{\epsilon}\cdot\tilde{\mathbf{E}} = \mathcal{D}\cdot\tilde{\mathbf{E}} = 0, \tag{2.52}$$

where $\mathbf{n} = \mathbf{k}c/\omega$ is the refractive index and $\mathcal{D}(\mathbf{k},\omega)$ is the dispersion tensor:

$$\mathcal{D} \equiv n^2\left(\frac{\mathbf{kk}}{k^2} - \mathbf{1}\right) + \boldsymbol{\epsilon}(\mathbf{k},\omega). \tag{2.53}$$

Solutions for the dispersion relation have the form:

$$\det[\mathcal{D}(\mathbf{k},\omega)] = 0, \tag{2.54}$$

To determine the possible wave modes supported by the plasma, $\boldsymbol{\epsilon}$ is calculated for the relevant plasma conditions and then solved for the roots of Equation 2.54. I provide the solution of the dielectric tensor for a streaming bi-Maxwellian distribution from kinetic theory in Appendix A. Under the assumption of weak wave damping $|\gamma| \ll \omega_r$, γ can also be obtained from Equation 2.54 by splitting the dispersion relation into its real and imaginary parts [see Baumjohann & Treumann, 1997b].

2.6.2 Wave-Particle Resonances

In a plasma, wave-particle resonances such as Landau and cyclotron resonance can lead to a transfer of energy between fluctuations and particles. Quasi-linear diffusion describes the evolution of the plasma distribution function in velocity-space that arises from these wave-particle interactions, provided that f_j evolves slowly compared to the timescale of the fluctuations, $\tau \gg 2\pi/\omega_r$. This process is quasi-linear because the fluctuations are solutions to the linear dispersion relation, but the field amplitudes are quadratic [see Verscharen et al., 2019]. The diffusion or pitch-angle scattering of particles is directed from larger to smaller f_j tangent to circles in the $v_\parallel$-$v_\perp$ plane defined by:

$$\left(v_\parallel - \frac{\omega_\mathrm{r}}{k_\parallel}\right)^2 + v_\perp^2 = \text{constant}. \tag{2.55}$$

During the diffusion, the particles with resonant velocity v_res gain energy from the wave if $\left(v_\perp^2 + v_\parallel^2\right)$ increases, or lose it if $\left(v_\perp^2 + v_\parallel^2\right)$ decreases. If the wave loses energy then it is said to be damped, whereas it is growing (instability) if it gains energy. In Figure 2.1, I show schematics of the different wave-particle resonances that can occur, along with the resulting changes to particle VDFs. The only particles that participate in the resonance have $v_\parallel$:

$$v_\mathrm{res} \equiv \frac{\omega_\mathrm{r} - \ell\Omega_j}{k_\parallel}, \tag{2.56}$$

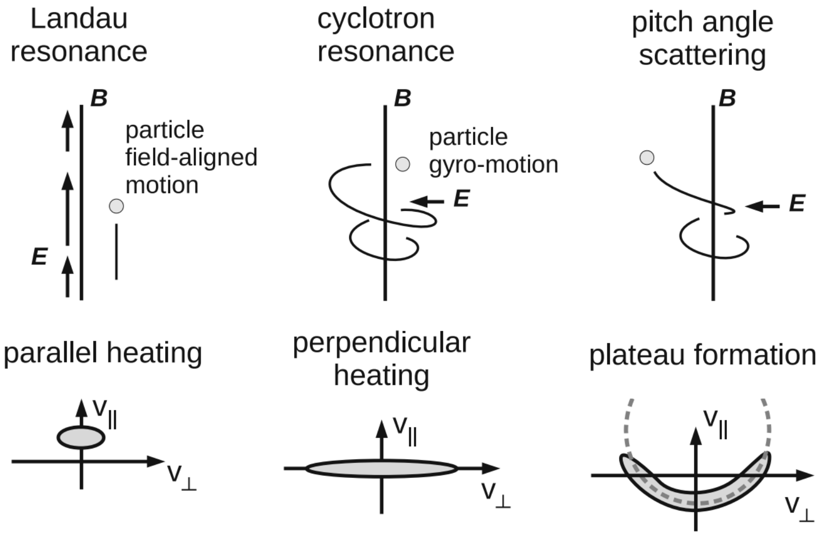

Figure 2.1: Schematic of the different types of wave-particles resonances: Landau, cyclotron and pitch-angle scattering, along with the resulting changes to the particle VDFs. Figure adapted from Narita [2017].

where the right-hand side is the Doppler-shifted frequency of the wave in the plasma frame. In this frame, the damping will be most efficient when $\omega = \ell\Omega_j$ so that $v_{res} = 0$, i.e., at the peak of the VDF. For $\omega < \ell\Omega_j$, damping will be weaker. The $\ell = 0$ term corresponds to Landau and transit-time damping where from Equation 2.56, only particles travelling at the wave phase speed can resonate. Therefore, if the wave has a fluctuating parallel electric field, $\delta\mathbf{E}_{\|} \neq 0$, the particle will experience a constant electric field in the plasma frame, accelerating the particle by the Lorentz force (Equation 2.1):

$$m_j \frac{d\mathbf{v}_{j,\|}}{dt} = q_j \delta\mathbf{E}_{\|} \tag{2.57}$$

This transfer of energy from the wave to the plasma results in a reduction of the wave amplitude and therefore, damping. Transit-time damping [Barnes, 1966] is the magnetic analogue of Landau damping and occurs when the wave has a fluctuating parallel component of the magnetic field, $\delta\mathbf{B}_{\|} \neq 0$:

$$m_j \frac{d\mathbf{v}_{j,\|}}{dt} = -\mu k_{\|} |\delta\mathbf{B}_{\|}|, \tag{2.58}$$

where $\mu = mv_{\perp}^2/2B$ is the magnetic moment, an adiabatic invariant of the gyration motion of charged particles around magnetic field lines [Stix, 1992]. The magnetic mirror force replaces $\mathbf{F} = q\mathbf{E}$ and acts to trap particles in an inhomogeneous magnetic field, leading to pitch-angle scattering.

The $\ell \neq 0$ terms correspond to cyclotron damping, which acts to transfer energy from the wave into the perpendicular velocity of the particles. From Equation 2.56, cyclotron resonance for $\ell = \pm 1$ occurs when the particle gyro-frequency equals the rotation of the fluctuating perpendicular electric field, $\delta\mathbf{E}_{\perp}$, of a circularly polarised wave. Therefore, in the particle rest-frame, it experiences a constant accelerating electric field. The sign of ℓ depends on the direction of gyration of the particles, which is opposite for negative and positive charges. Therefore, left-hand circularly polarised waves can resonate with ions and right-handed waves with electrons. Higher orders of ℓ correspond to different harmonics of the gyro-frequency of the particles [Gary, 1993].

2.6.3 Alfvénic Modes

Alfvén waves are electromagnetic waves with a restoring force of magnetic tension and at large scales ($kd_p \ll 1$ and $k\rho_p \ll 1$) obey the linear dispersion relation:

$$\omega_{\mathrm{r}} = \pm \left| k_{\|} \right| v_{\mathrm{A}}. \tag{2.59}$$

The sign indicates the direction parallel (+) or anti-parallel (-) to the magnetic field, $\mathbf{B}_0$. In a Maxwellian plasma, Alfvén waves are only weakly damped and the fluctuating magnetic field $\delta\mathbf{B}$ is perpendicular to both $\mathbf{k}$ and $\mathbf{B}_0$ [Gurnett & Bhattacharjee, 2017]. They are non-compressive, with negligible fluctuations in both n_j and $|\mathbf{B}|$. However, these waves exhibit a characteristic correlation or anti-correlation between velocity and magnetic field fluctuations, which in the MHD approximation is:

$$\frac{\delta\mathbf{u}}{v_{\mathrm{A}}} = \mp \frac{\delta\mathbf{B}}{B_0}, \tag{2.60}$$

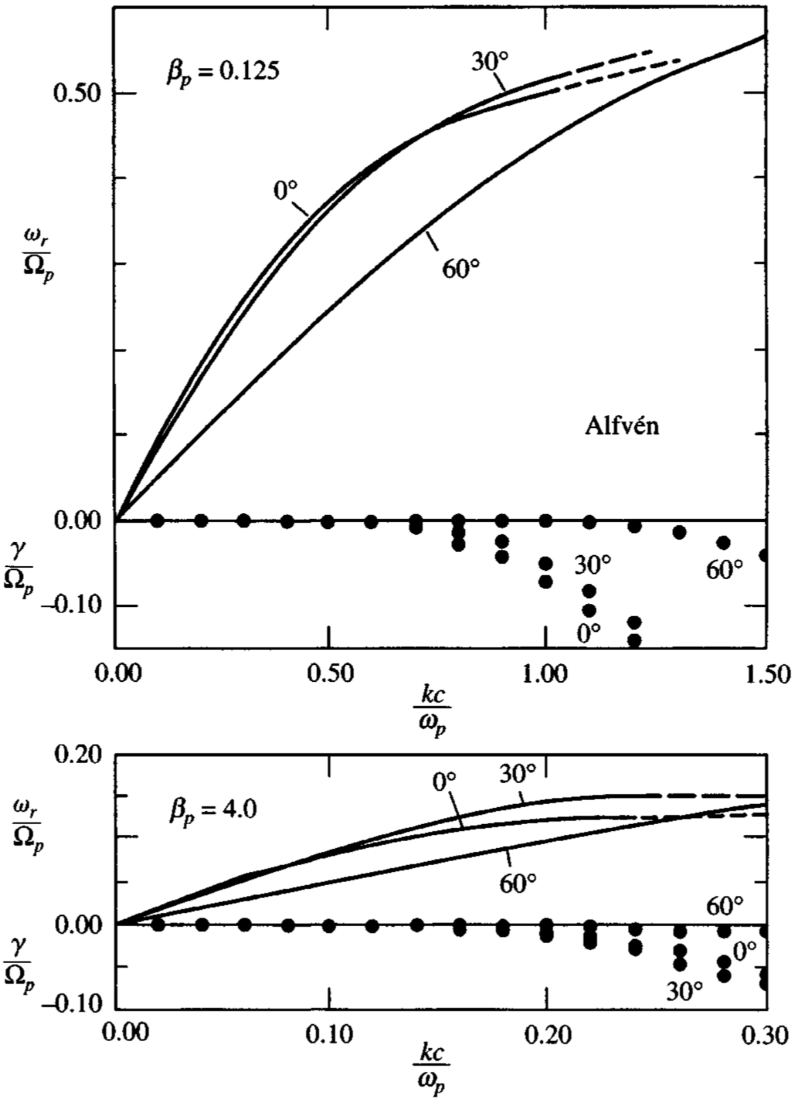

Figure 2.2: The frequency, $\omega_\mathrm{r}/\Omega_p$, and damping rate, γ/Ω_p, of Alfvén waves as a function of $kc/\omega_{p,p} \equiv kd_p$ for different angles, θ_{kB}, of propagation and different values of β_p. A dashed line indicates that the wave is heavily damped with $\gamma < -|\omega_\mathrm{r}|/2\pi$. Here, $v_A/c = 10^{-4}$. Alfvén waves are more strongly damped at higher β_p. Figure from Gary [1993].

where $v_\mathrm{A} = B_0/\sqrt{4\pi\rho}$ is the Alfvén speed. Fluctuations with this same correlation or anti-correlation are said to be Alfvénic.

At small scales, the dispersion relation of Alfvén waves splits into two branches: the kinetic Alfvén wave (KAW) at $k_\perp \rho_p \gtrsim 1$ and $k_\perp \gg k_\parallel$, and the Alfvén ion-cyclotron (AIC) wave at $k_\parallel d_p \gtrsim 1$ and $k_\perp \ll k_\parallel$. I show in Figure 2.2, the dispersion relation of Alfvén waves for different values of β_p and angles of propagation θ_{kB} between $\mathbf{k}$ and $\mathbf{B}_0$ from Gary [1993]. For KAWs at $k_\perp \rho_p \gtrsim 1$, finite Larmor radius effects modify the properties of the Alfvén wave, leading to the dispersion relation in the gyro-kinetic limit [Howes et al., 2006]:

$$\omega_\mathrm{r} = \pm \frac{\left|k_\parallel\right| v_\mathrm{A} k_\perp \rho_p}{\sqrt{\beta_p + 2/(1+T_e/T_p)}}. \tag{2.61}$$

KAWs are obliquely propagating low-frequency ($\omega_\mathrm{r} \ll \Omega_p$) electromagnetic waves and in this limit, have right-handed elliptical polarisation [Howes et al., 2006; Schekochihin et al., 2009]. Unlike large-scale Alfvén waves, KAWs are compressive and exhibit fluctuations in n_j and $|\mathbf{B}|$, leading to a non-zero $\mathbf{E}_\parallel$. KAWs can Landau resonate with both ions (at high β_p) and electrons (at low β_p), heating in the parallel direction.

On the other hand, AIC waves are quasi-parallel propagating and in the cold plasma (two-fluid) limit ($\beta \simeq 0$, i.e., the L-mode) their dispersion relation is [Verscharen, 2012]:

$$\frac{\omega_\mathrm{r}}{\Omega_p} = \pm \frac{k^2 d_p^2}{2} \left(\sqrt{1 + \frac{4}{k^2 d_p^2}} - 1 \right). \tag{2.62}$$

AIC waves are also low frequency, $\omega_\mathrm{r} \ll \Omega_p$, and are left-hand circularly polarised. This sense of rotation is the same as ion gyration in a magnetic field, leading to cyclotron resonance (Equation 2.56 with $\ell = +1$) and proton heating in the perpendicular direction. The θ_{kB} and β_p at which the polarisation of the Alfvén wave changes sign (see Section 8.1) was determined by Gary [1986].

2.6.4 Compressive Modes

The dispersion relation of MHD waves is [Gurnett & Bhattacharjee, 2017]:

$$\mathcal{D}(k,\omega) = \left(v_{ph}^2 - v_A^2 \cos^2\theta_{kB}\right) \left[v_{ph}^4 - v_{ph}^2 \left(v_A^2 + v_s^2\right) + v_A^2 v_s^2 \cos^2\theta_{kB}\right] = 0, \tag{2.63}$$

where $v_s = \kappa k_B T/m$ is the sound speed. The first root, $v_{ph}^2 - v_A^2 \cos^2\theta_{kB} = 0$, is simply the Alfvén wave dispersion relation (Equation 2.59). The second root gives the dispersion relation of compressive MHD modes:

$$\omega_{\mathrm{r}} = \pm k \left[\frac{1}{2}\left(v_A^2 + v_s^2\right) \pm \frac{1}{2}\sqrt{\left(v_A^2 - v_s^2\right)^2 + 4 v_A^2 v_s^2 \sin^2\theta_{kB}} \right]^{1/2}, \tag{2.64}$$

where the second ± sign gives the fast (+) and slow (-) magnetosonic modes. Following the MHD convention, waves that exhibit an anti-correlation between δn and $\delta|\mathbf{B}|$ are characterised as slow waves [Klein et al., 2012]. From kinetic theory, there are many solutions with this characteristic anti-correlation, although two solutions are typically called the kinetic slow mode [Narita & Marsch, 2015]. The first is the ion-acoustic wave, with

$$\omega_{\mathrm{r}} = \pm \left|k_{\parallel}\right| \sqrt{\frac{3k_{\mathrm{B}}T_{p,\parallel} + k_{\mathrm{B}}T_{e,\parallel}}{m_p}}, \tag{2.65}$$

which is quickly damped even at large scales, leading to parallel ion heating. At very large θ_{kB}, the damping rate decreases and this mode no longer propagates, exhibiting pressure balance. For a sufficient $T_{\perp}/T_{\parallel} > 1$, this mode can become unstable, leading to the mirror-mode instability (see Section 2.7).

In the kinetic regime, the fast mode is defined as a solution to the linear dispersion relation that exhibits a characteristic positive correlation between n and $|\mathbf{B}|$ fluctuations [Klein et al., 2012]. At small scales, fast modes include whistler waves, lower-hybrid waves and kinetic magnetosonic waves, collectively referred to as fast-magnetosonic whistler (FMW) modes. For $kd_e \ll 1$, in the cold plasma limit the FMW wave dispersion relation for quasi-parallel propagation is [Verscharen, 2012]:

$$\frac{\omega_{\mathrm{r}}}{\Omega_p} = \pm \frac{k^2 d_p^2}{2}\left(\sqrt{1 + \frac{4}{k^2 d_p^2}} + 1\right). \tag{2.66}$$

This mode is also called the R-mode and connects to the Alfvén branch at large scales. In Figure 2.3, I show the dispersion relation of parallel-propagating FMW waves for different values of β_p and angles of propagation θ_{kB} from Gary

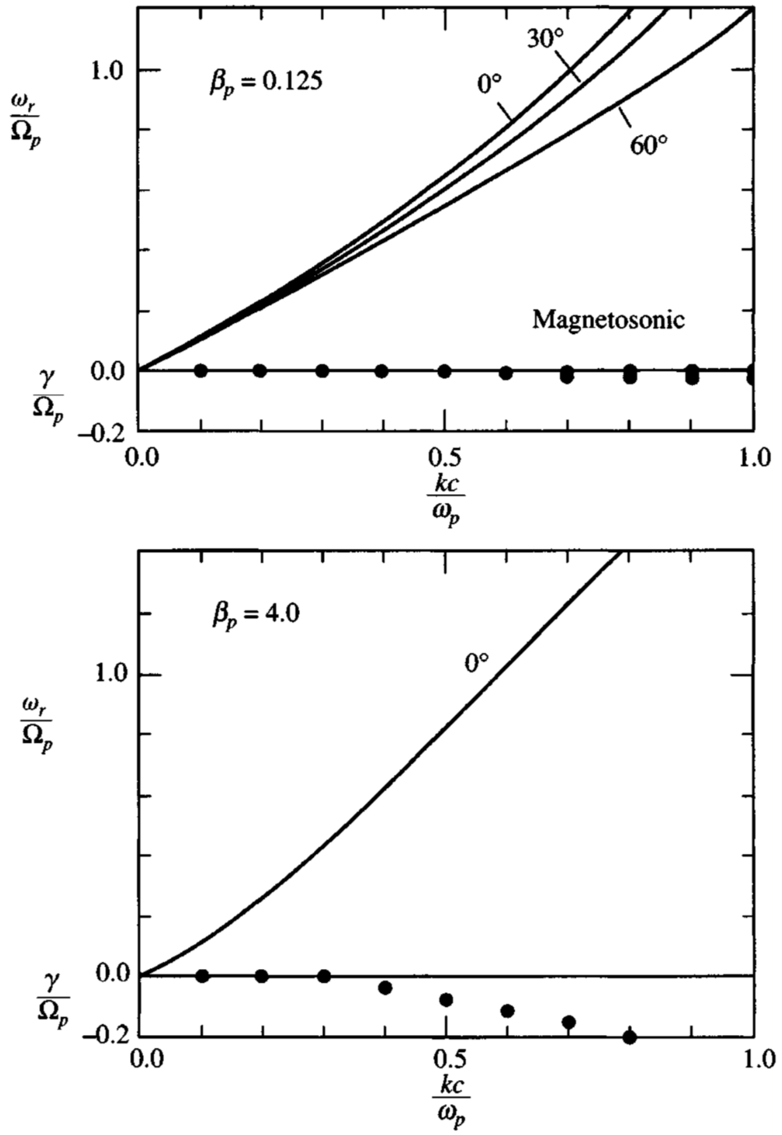

Figure 2.3: The frequency, $\omega_\mathrm{r}/\Omega_p$, and damping rate, γ/Ω_p, of parallel-propagating FMW waves as a function of $kc/\omega_{p,p}$ for different angles, θ_{kB}, of propagation and different values of β_p. A dashed line indicates that the wave is heavily damped with $\gamma < -|\omega_\mathrm{r}|/2\pi$. Here, $v_A/c = 10^{-4}$. Figure from Gary [1993].

[1993]. These quasi-parallel FMW waves are right-hand polarised, meaning they can cyclotron resonate with electrons through the $\ell = -1$ resonance, leading to perpendicular electron heating. At $kd_p \gg 1$ and oblique propagation, the FMW becomes the dispersive whistler wave, and at quasi-perpendicular propagation, the FMW mode becomes the lower-hybrid mode [Verscharen et al., 2019]. Oblique FMW modes can also resonate with ions through other resonances, including Landau resonance with $\ell = 0$.

2.7 Kinetic Instabilities in a Plasma

Instabilities are mechanisms that transfer energy from free-energy sources, such as non-Maxwellian particle distributions, to plasma waves that initially have amplitudes at the thermal-noise level. These modes have a growth rate $\gamma > 0$ and grow exponentially with time, $\mathbf{A}(\mathbf{r}, t) \propto e^{\gamma t}$, extracting energy from the source of free energy. This growth is linear in the sense that $\gamma/\Omega_j \ll 1$ and $\delta\mathbf{B}/\mathbf{B}_0 \ll 1$ (see Equation 2.45). When the amplitude reaches a saturation value, non-linear behaviour can then limit the growth of the instability [Baumjohann & Treumann, 1997a].

Throughout this thesis, I focus on kinetic-scale instabilities driven by wave-particle interactions, that is, instabilities with wavelengths of order d_i and ρ_i that are driven by non-thermal structures (departures from the Maxwellian distribution) in ion velocity distributions. By driving instabilities and transferring energy from the particles to the electromagnetic fields, the velocity space structures are reduced, and the system approaches local thermodynamic equilibrium. Once the system reaches equilibrium, the instability stops growing and is in a state of marginal stability ($\gamma = 0$).

One of the most common sources of free energy for driving these kinetic instabilities is temperature anisotropy with respect to the background magnetic field, $T_{i,\perp}/T_{i,\|}$. This anisotropy in the VDF can lead to quasi-linear diffusion from resonance with wave-modes, leading to growing instabilities. There are four main instabilities driven by temperature anisotropy of ion species

[Gary, 1993]. The ion-cyclotron and mirror-mode instabilities are caused by $T_{i,\perp}/T_{i,\parallel} > 1$, driving unstable parallel propagating AIC and non-propagating oblique kinetic slow modes, respectively. On the other hand, at $T_{i,\perp}/T_{i,\parallel} < 1$, the parallel and oblique (Alfvén) firehose instabilities drive unstable parallel propagating FMW and non-propagating oblique Alfvén modes, respectively.

Two parameters, $\beta_{i,\parallel}$ and $T_{i,\perp}/T_{i,\parallel}$, have a significant impact on the growth rate of these instabilities. For each of the four ion temperature anisotropy instabilities, a contour of constant maximum growth rate, γ_m, as a function of $\mathbf{k}$ can be drawn through the $\beta_{i,\parallel}$-$T_{i,\perp}/T_{i,\parallel}$ parameter space, as shown in Figure 2.4 from Klein & Howes [2015]. An analytical model can be derived for the instability contours in the this parameter space; a common example of such a model describes an inverse relationship between $\beta_{i,\parallel}$ and $T_{i,\perp}/T_{i,\parallel}$ [e.g., Gary & Lee, 1994; Gary et al., 1994a,b]. In particular, Hellinger et al. [2006] proposed:

$$\frac{T_{p,\perp}}{T_{p,\parallel}} = 1 + \frac{a}{\left(\beta_{p,\parallel} - b\right)^{c}}, \tag{2.67}$$

where a, b, and c are constant parameters calculated from fits to solutions of the plasma dispersion relation (Section 2.6). Each unstable mode and the desired growth rate will give different values for these free parameters. The choice of γ_m can be somewhat arbitrary; usually $\gamma_m/\Omega_p = 10^{-2}$ or $\gamma_m/\Omega_p = 10^{-3}$ is used. A faster growth rate is usually avoided since the plasma fluctuations are large enough that the linear regime may not be an accurate description. I calculate the values of these three fit parameters for each of the four instabilities and different maximum growth rates in Chapter 7.

In addition to temperature anisotropy, faster 'beam' components separated from the 'core' of a distribution or drifts between different particle species (see Section 4.1) can contribute to excess parallel pressure or induce non-zero currents, driving kinetic instabilities (see Section 4.2). These distributions can resonate with unstable parallel propagating AIC and FMW waves, decelerating the drifting population. Similar analytical models to Equation 2.67 can also be

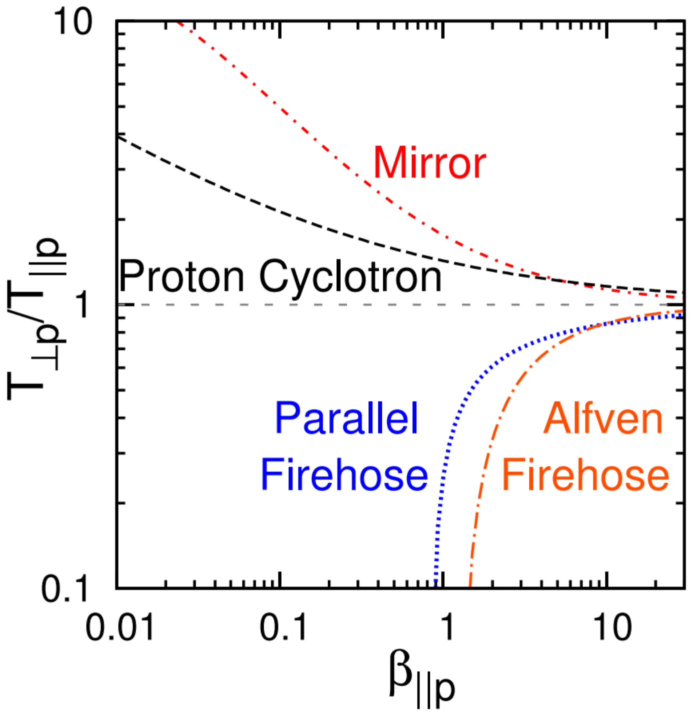

Figure 2.4: Marginal instability contours of constant maximum growth rate $\gamma_m/\Omega_p = 10^{-3}$ for the four proton temperature anisotropy instabilities using Equation 2.67. Figure from Klein & Howes [2015].

used for these instabilities. Ion beams and drifts can either drive instabilities on their own or act as additional sources of free energy, enhancing the growth rate of a temperature anisotropy instability or acting to stabilise the system. In the latter case, these additional components of the VDFs will give different values for a, b, and c, changing the instability contours significantly [Price et al., 1986; Podesta & Gary, 2011a; Maruca, 2012; Matteini et al., 2015].

2.8 The Solar Wind

In this thesis, I focus on the solar wind, a continuous plasma outflow originating from the solar corona that expands out into interplanetary space to form the heliosphere [Parker, 1958, 1963; Hundhausen, 1972]. It is completely ionised, consisting of electrons, protons, α-particles, and small abundances of heavy ions, such as oxygen, in different ionisation stages [Hundhausen, 1970]. The corona is hot, with typical temperatures of both protons and electrons of about

$\sim 1\times 10^{6}$ K, and the plasma expands radially outwards, becoming supersonic ($u \gg v_s$) and super-Alfvénic ($u \gg v_A$) within a few solar radii [Hansteen et al., 1999]. This leads to radial gradients in the plasma parameters with distance, R. At about 10 solar radii, the average radial velocity is constant, $\mathbf{u} \approx U_r\,\hat{\mathbf{e}}_r \approx$ constant (in spherical coordinates) where $\mathbf{u} \simeq \mathbf{u}_p$ and $n \simeq n_p$. Under steady-state conditions the continuity equation (Equation 2.24) becomes:

$$\nabla \cdot (n\mathbf{u}) = 0, \tag{2.68}$$

leading to the radial density profile, $n \propto r^{-2}$. This gradient can be steeper in regions of super-radial expansion and acceleration closer to the Sun [Cranmer & van Ballegooijen, 2005]. In the rest of this thesis, I will use $\mathbf{v}_{sw}$ to refer to the velocity of the solar wind.

In the corona, $\beta \ll 1$ and the solar magnetic field causes the highly electrically conducting plasma to co-rotate with the Sun due to the 'frozen-in' condition (see Section 2.5.5). However, as the plasma outflow expands outwards, it begins to dominate the evolution of the magnetic field and convects the field out into interplanetary space [Weber & Davis, 1967]. Due to the solar rotation, this interplanetary magnetic field is wound into spirals in the ecliptic plane, producing the Parker spiral [Parker, 1958; Levy, 1976; Behannon, 1978; Mariani et al., 1978, 1979]. The Parker spiral angle, ϕ_{rB}, increases with distance from the Sun:

$$\tan\phi_{rB} = \frac{B_\phi}{B_r} = \frac{\Omega_\odot \sin\theta_B}{U_\mathrm{r}}\left(R_\mathrm{eff} - R\right), \tag{2.69}$$

where B_ϕ and B_r are the azimuthal and radial magnetic field components, $\Omega_\odot$ is the angular solar rotation speed, θ_B is the polar angle (see next section), and R_eff is the effective co-rotation radius [Hollweg & Lee, 1989], typically 10-20 solar radii [Bruno & Bavassano, 1997]. At 1 AU, $\phi_{rB} \sim 45^\circ$, and increases further out in the heliosphere [Thomas & Smith, 1980; Forsyth et al., 2002]. The magnitude of the magnetic field also decreases with distance:

$$B_0 \propto \frac{\sqrt{1+\tan^2\phi_{rB}}}{r^2}, \tag{2.70}$$

which is the same as density, $B_0 \propto r^{-2}$ when $\tan^2\phi_{rB} \ll 1$ at small R, and $B_0 \propto r^{-1}$ when $\tan^2\phi_{rB} \gg 1$ at large R. The solar magnetic field varies over the solar cycle, leading the variations in the large-scale structure of the solar wind in response to solar activity. The magnetic field is dipole-like during solar minimum and more complex at solar maximum [see Owens & Forsyth, 2013]. The solar wind emanating from different poles of the Sun leads to sector structure where the radial component of the large-scale magnetic field can be directed either anti-sunward (inward sector) or sunward (outward sector). Fluctuations in the magnetic field at small scales can lead to deviations from the Parker spiral. Sectors of different polarity are separated by the heliospheric current sheet (HCS), which during solar minimum is close to the ecliptic plane of the Sun. At solar minimum, the shape of the HCS is more complicated, and it can be situated at higher latitudes [Russell et al., 2016].

The solar wind is an excellent laboratory to study fundamental physical processes in a plasma. Over the past few decades, many spacecraft have taken *in-situ* measurements of the solar wind, greatly enhancing our understanding of solar wind physics. In Table 2.1 I give typical characteristic plasma scales for the solar wind. The ion-kinetic scales (d_p and ρ_p) are of order $\ell \sim 100$ km in the solar wind at 1 AU, corresponding to timescales: $\tau = 2\pi/\Omega_p \sim 10$ s. Current instrumentation can easily resolve these temporal scales, and the spacecraft itself is much smaller than the gyration orbits of protons, limiting its impact on processes ongoing at ion-kinetic scales. The proton collisional mean free path, $\lambda_{\mathrm{mfp},p}$, is about 1 AU in the solar wind, so few proton collisions typically occur as the plasma flows towards the Earth. Therefore, the solar wind can be considered collisionless; however, the rate of collisions does vary with plasma conditions (see Section 4.1.2).

The solar wind is often separated into three different categories [Phillips et al., 1995; McComas et al., 1998, 2000, 2003; Ebert et al., 2009]:

Table 2.1: Characteristic length scales in the solar wind for typical parameters at 1 AU. Values compiled by Verscharen et al. [2019].

Scale	Length	Definition
L	1 AU	Characteristic size of the system
$\lambda_{\mathrm{mfp},p}$	1 AU	Proton collisional mean free path
d_p	100 km	Proton inertial length
ρ_p	80 km	Proton gyro-radius
d_e	3 km	Electron inertial length
ρ_p	2 km	Electron gyro-radius
λ_e	10 m	Electron Debye length

- **Fast wind** (500-800 km s^{-1}) - low-density, originating from open field-lines in coronal holes;
- **Slow wind** (300-500 km s^{-1}) - more variable and higher density, originating from open streamers, loops, and active regions;
- **Transient structures** - eruptive events such as coronal mass ejections (CMEs) during solar maximum.

The exact origin of slow solar wind is still unclear [see Kepko et al., 2016, and references therein], but it likely involves magnetic reconnection of oppositely directed field lines through diffusion (see Section 2.5.5), leading to openings in the coronal magnetic field and allowing plasma to escape.

In Figure 2.5, I show the variation of solar wind speed and density between solar minimum and maximum as a function of solar latitude, from Verscharen et al. [2019]. This figure shows that the three-dimensional structure of the solar wind is highly variable. At solar minimum, there is a clear boundary between fast and slow wind with latitude. However, this is not the case during solar maximum, where the occurrence of different wind streams shows little dependence on latitude. There are also boundaries in the ecliptic plane between fast and slow streams. The association of different streams with different source regions suggests that the magnetic-field configuration in the corona plays a crucial role in determining the properties of solar wind streams.

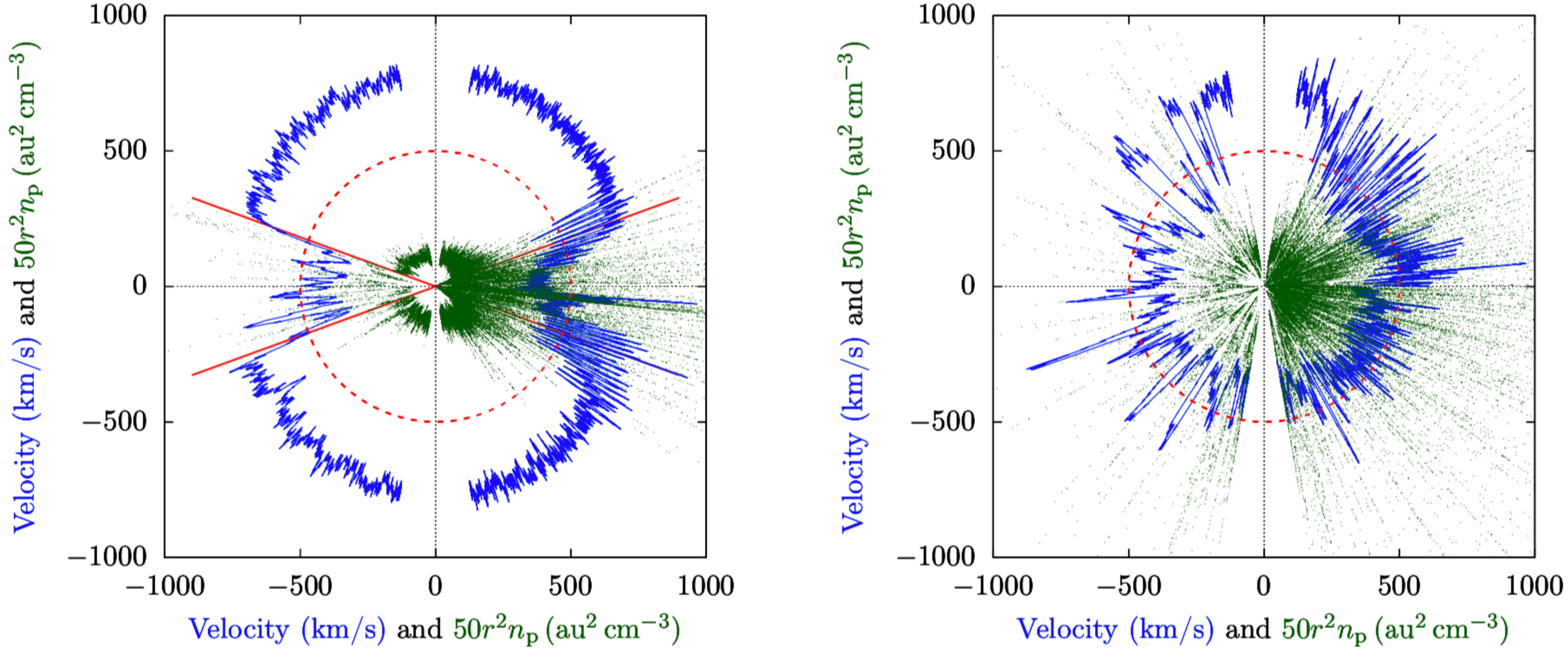

Figure 2.5: Ulysses observations of the solar wind radial velocity (blue) and density (green) at different heliographic latitudes. The radial decrease in velocity with distance is compensated by multiplying by r^2. The red circle represents $v_{sw} = 500$ km/s and $nr^2 = 10$ AU^2 cm^{-3}. Left panel: Ulysses' first polar orbit during solar minimum (1990-1997). Right panel: Ulysses' second polar orbit during solar maximum (1997-2004). Figure from Verscharen et al. [2019], adapted from McComas et al. [2000, 2008].

The fast and slow wind exhibit additional distinguishing properties compared to speed and density. The fast wind is more Alfvénic [Tu & Marsch, 1995] and has a higher proton temperature [Neugebauer, 1976; Wilson III et al., 2018]. It is also less collisional, allowing for more kinetic non-Maxwellian features of the particle VDFs to survive the thermalisation of Coulomb collisions [Marsch et al., 1982b; Marsch & Goldstein, 1983; Livi et al., 1986; Kasper et al., 2008; Bourouaine et al., 2011; Durovcová et al., 2017]. A smooth transition in the distribution of wind speed [Xu & Borovsky, 2015; Camporeale et al., 2017] means that the traditional classification of wind streams by speed is not perfect. Depending on the source region, the solar wind plasma can exhibit properties of both slow and fast wind [e.g., Stansby et al., 2019a].

2.9 Spacecraft Coordinate Systems

Throughout this thesis, I refer to two different orthogonal coordinate systems when discussing spacecraft measurements in the solar wind. The first, geocentric solar ecliptic (GSE) coordinates, are commonly used in space physics and are fixed with respect to the Earth-Sun line. In this coordinate system, $\hat{\mathbf{X}}$ is directed from the Earth toward the Sun, $\hat{\mathbf{Z}}$ is perpendicular to the ecliptic plane of the Earth's orbit (north), and $\hat{\mathbf{Y}}$ completes the right-handed system [Russell et al., 2016]. Alternatively, in the radial-tangential-normal (RTN) coordinate system, $\hat{\mathbf{R}}$ is defined in the direction of a line from the Sun to the spacecraft, $\hat{\mathbf{T}}$ is defined as the cross product of the Sun's spin axis and $\hat{\mathbf{R}}$, and $\hat{\mathbf{N}}$ completes the right-handed system. The angles θ_B and ϕ_B of the magnetic field in the RTN coordinate system in Figure 2.6 are defined as:

$$\phi_B = \arctan\left(\frac{B_T}{B_R}\right) \quad \text{and} \quad \theta_B = \arctan\left(\frac{B_N}{\sqrt{B_R^2 + B_T^2}}\right). \tag{2.71}$$

For the *Wind* spacecraft located at the L1 Lagrange point (Section 5.1), there is a simple transformation between the two coordinate systems: $\hat{\mathbf{R}} \simeq -\hat{\mathbf{X}}$, $\hat{\mathbf{T}} \simeq -\hat{\mathbf{Y}}$, and $\hat{\mathbf{N}} \simeq \hat{\mathbf{Z}}$ (see Figure 2.6). Here, $\mathbf{v}_{sw}$ is directed along the $-\hat{\mathbf{X}}$ and

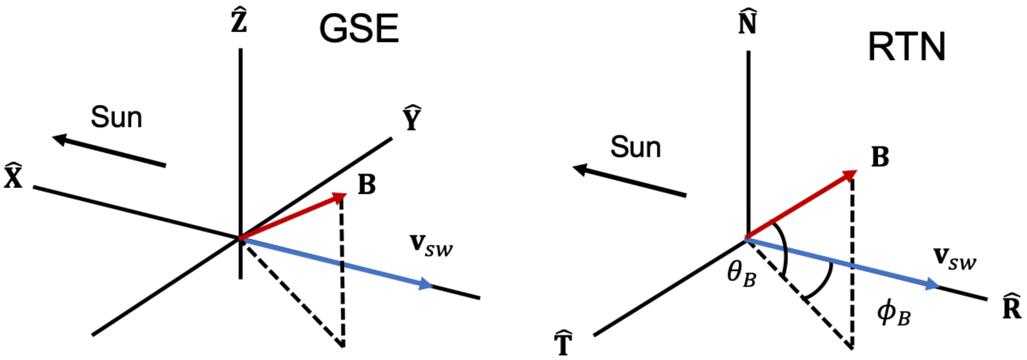

Figure 2.6: The GSE and RTN coordinate systems for the *Wind* spacecraft. The angles θ_B and ϕ_B are defined in the main text.

$\hat{\mathbf{R}}$ directions. This transformation assumes that the spacecraft is stationary with respect to the Earth's orbit around the Sun. Since the spacecraft orbits about the L1 point, this RTN frame is not inertial but rather fixed with respect to the Sun-Earth line.

Chapter 3

Turbulence in Plasmas

In this chapter, I review the relevant background information on plasma turbulence. I begin by discussing laminar and turbulent flows, MHD turbulence, the non-linear energy cascade, and Kolmogorov phenomenology. I then cover the more complicated phenomenological models associated with plasma turbulence, including the effects of characteristic plasma scales on the physics of the cascade. Finally, I discuss the statistical analysis of turbulent fluctuations and the limitations of single-spacecraft observations. I only address incompressible turbulence here since compressive fluctuations make up only about 10% of the total energy in the solar wind [Chen, 2016].

3.1 Laminar and Turbulent Flows

In a fluid, there are two dynamical states. Laminar flow describes a state where all fluid elements flow in the same direction, with no lateral mixing between parallel layers. In contrast, turbulent flow involves irregular changes in both velocity and pressure of the fluid, as well as the mixing of mass between layers. Figure 3.1 shows a photograph of the transition from laminar to turbulent flow for a water jet from Frisch [1995]. Turbulence is fundamentally non-linear and chaotic in both space and time, meaning that a small change in initial conditions can lead to an entirely different final state [Frisch, 1995]. These properties make turbulence difficult to study theoretically since the precise properties of a turbulent flow cannot be predicted accurately. Instead,

Figure 3.1: Photograph of a water jet, showing the transition from laminar to turbulent flow. The non-uniform, irregular structure of the flow is evident and appears as vortices of different sizes Figure from Frisch [1995], adapted from van Dyke [1982].

statistical methods are used since the average properties of a turbulent system are not as sensitive to disturbances [Biskamp, 2003].

The motion of a neutral fluid is governed by the Navier-Stokes equation, which for an incompressible ($\rho = \text{const.}$) fluid is:

$$\frac{\partial \mathbf{u}}{\partial t} + (\mathbf{u} \cdot \nabla)\,\mathbf{u} = -\frac{\nabla p}{\rho} + \nu \nabla^2 \mathbf{u}, \tag{3.1}$$

This equation is analogous to the MHD momentum equation (2.33) for a plasma and includes an additional viscous term here due to particle collisions, where ν is the kinematic viscosity [Frisch, 1995]. The constant density of the fluid also leads to the mass conservation equation reducing to a divergence-less condition for the velocity: $\nabla \cdot \mathbf{u} = 0$. The Navier-Stokes equation describes the motion of a fluid eddy or vortex due to the external forces acting on it. The non-linear $(\mathbf{u} \cdot \nabla)\,\mathbf{u}$ term shows that if an eddy has a large enough gradient in $\mathbf{u}$, it can distort and stretch another eddy as they advect across each other, producing smaller vortices. These dynamics act to mix the fluid by convection rather than diffusion and lead to a transfer of kinetic energy between eddies of different scales [Chiuderi & Velli, 2015].

3.2 MHD Turbulence

Unlike the Navier-Stokes equation, the presence of a magnetic field in a plasma introduces intrinsic anisotropy into the dynamics. There is also the additional presence of flowing currents due to moving charges and the collective behaviour of the particles results in non-local interactions (see Section 2.1). These effects strongly differentiate plasma turbulence from its fluid counterpart. At frequencies $\omega \ll \Omega_p$, the MHD approximation (Section 2.5.5) can be used to describe a plasma. The incompressible MHD equations can be written as:

$$\frac{\partial \mathbf{u}}{\partial t} + (\mathbf{u}\cdot\nabla)\,\mathbf{u} = -\frac{\nabla P}{\rho} + \nu\nabla^2\mathbf{u} + (\mathbf{b}\cdot\nabla)\,\mathbf{b}, \tag{3.2a}$$

$$\frac{\partial \mathbf{b}}{\partial t} + (\mathbf{u}\cdot\nabla)\,\mathbf{b} = (\mathbf{b}\cdot\nabla)\,\mathbf{u} + \eta\nabla^2\mathbf{b}, \tag{3.2b}$$

with $\nabla\cdot\mathbf{u} = 0$ and $\nabla\cdot\mathbf{b} = 0$. Here, $\mathbf{b}$ is the magnetic field in Alfvén units: $\mathbf{b} = \mathbf{B}/\sqrt{\mu_0\rho}$ [Biskamp, 2003; Galtier, 2016]. The first equation is simply the MHD momentum equation (2.33) where the $\mathbf{j}\times\mathbf{B}$ term has been replaced using Equation 2.37. The second equation is the induction equation (2.42), where the convective term has been rewritten using vector identities. There are now four non-linear terms, each contributing to non-linear dynamics. Both the velocity and magnetic field interact with themselves and each other non-linearly.

3.2.1 The Reynolds Number

When the velocity, magnetic field, or their gradients become large enough, the non-linear terms dominate over the dissipative terms, and the motion of the plasma becomes turbulent. To quantify this, the Reynolds number:

$$Re = \frac{UL}{\nu}, \tag{3.3}$$

and its magnetic counterpart, the magnetic Reynolds number:

$$R_{\mathrm{m}} = \frac{v_A L}{\eta}, \tag{3.4}$$

are used. Here, U is the characteristic velocity, and L is the characteristic length scale of the plasma. These two parameters represent a measure of the relative strength between the convective and diffusion terms for the velocity and magnetic field, respectively. Different plasmas with similar Reynolds numbers will exhibit similar states of turbulence. The larger Re or R_{m}, the more the non-linear terms dominate the dissipative terms and the more turbulent the behaviour of the fluid. In astrophysical plasmas, R_{m} is usually very high; however, the ratio of both Reynolds numbers, the Prandtl number $P_{\mathrm{m}} = \eta/\nu$, can vary significantly [Bruno & Carbone, 2013].

3.2.2 The Rugged Invariants

The incompressible MHD equations conserve three quantities in the absence of dissipation, often referred to as rugged invariants,

$$E = \frac{1}{2}\int_V \left(u^2 + b^2\right) d^3\mathbf{r}, \tag{3.5}$$

$$H_c = \int_V \mathbf{u}\cdot\mathbf{b}\, d^3\mathbf{r}, \tag{3.6}$$

$$H_m = \int_V \mathbf{A}\cdot\mathbf{B}\, d^3\mathbf{r}. \tag{3.7}$$

These invariants are the total energy, E, the cross-helicity, H_c, a measure of the correlation between the velocity and magnetic fields, and the magnetic helicity, H_m, a measure of the degree of magnetic flux tube linkage [Davidson, 2017]. Here, the magnetic vector potential $\mathbf{A}$ is defined by $\mathbf{B} = \nabla \times \mathbf{A}$.

3.2.3 Elsässer Notation

The MHD equations can be written in a more symmetrical form using Elsässer variables [Elsässer, 1950], uncovering a fundamental process that differentiates plasma turbulence from fluid turbulence. Elsässer variables are given by $\mathbf{z}^{\pm} = \mathbf{u} \pm \mathbf{b}'$, where $\mathbf{b}' = \mathbf{b} - \mathbf{b}_0$. Here, $\mathbf{b}'$ is the fluctuating magnetic field and $\mathbf{b}_0$ is the background field in Alfvén units, i.e., the Alfvén speed. Equations 3.2a and 3.2b can then be re-written as:

$$\frac{\partial \mathbf{z}^{\pm}}{\partial t} \mp (\mathbf{b}_0 \cdot \nabla)\, \mathbf{z}^{\pm} + \left(\mathbf{z}^{\mp} \cdot \nabla\right) \mathbf{z}^{\pm} = -\frac{\nabla P}{\rho} + \nu^{+} \nabla^2 \mathbf{z}^{\pm} + \nu^{-} \nabla^2 \mathbf{z}^{\mp}, \tag{3.8}$$

where the dissipative coefficients are $2\nu^{\pm} = \nu \pm \eta$ [Bruno & Carbone, 2013]. The divergence-less condition is $\nabla \cdot \mathbf{z}^{\pm} = 0$. This equation describes Alfvénic fluctuations propagating parallel ($\mathbf{z}^{+}$) and anti-parallel ($\mathbf{z}^{-}$) to $\mathbf{B}_0$ with speed $\mathbf{b}_0$. In general, these perturbations are non-linear Alfvénic wave-packets with arbitrary amplitude and shape. They are also decoupled from all other perturbations such as compressive fluctuations. All four non-linear terms are now combined into one, $\left(\mathbf{z}^{\mp} \cdot \nabla\right) \mathbf{z}^{\pm}$, which reveals that the non-linear coupling *only* occurs between oppositely propagating fluctuations. This process is called the Alfvén effect [Schekochihin & Cowley, 2007; Bruno & Carbone, 2013]. If either $\mathbf{z}^{+} = 0$ or $\mathbf{z}^{-} = 0$, the non-linear term vanishes and the turbulent cascade stops.

3.3 The Non-linear Energy Cascade

The incompressible Navier-Stokes and ideal MHD equations are scale-invariant, and therefore, fluctuations in both the velocity and magnetic field are self-similar over many scales. This fundamental property of the equations governing turbulence leads directly to the phenomenological model of a non-linear energy cascade. For fluid turbulence, this model is based on the picture of turbulence as a collection of vortices at all scales. These vortices decay non-uniformly into smaller and smaller eddies before eventual dissipation due to viscosity and resistivity at the smallest scales where the diffusion terms become important. Kolmogorov [1941] further developed this idea into an energy cascade process. Energy is injected at a length scale, L, and transferred by non-linear interactions towards smaller scales where it is ultimately dissipated. A characteristic length scale ℓ_D exists where dissipative effects will begin to be experienced by the flow, which scales with the Reynolds number,

$$\ell_D \sim L Re^{-3/4}. \tag{3.9}$$

Therefore, the larger the Reynolds number, the smaller the dissipative length scale compared to L. At very large Reynolds numbers, the injection and dissipation scales are separated by several orders of magnitude. The energy in this process is conserved and spread over all scales, such that for a stationary situation, the energy injection and dissipation rates must be balanced. At intermediate scales, $\ell_D \ll \ell \ll L$, called the *inertial range*, the energy transfer rate (per unit mass), ε, is constant, and energy is transferred to smaller and smaller scales only by the inertia of the eddies. The energy injection rate is given by $\varepsilon_L \sim U^2/\tau_L$, where $\tau_L \sim L/U$ is the characteristic time of the energy injection process, and the dissipation rate is $\varepsilon_D \sim U^2/\tau_D$, where $\tau_D \sim L^2/\nu$. The ratio between these two rates is:

$$\frac{\varepsilon_L}{\varepsilon_D} \sim \frac{\tau_D}{\tau_L} \sim Re. \tag{3.10}$$

This means that for very large Reynolds numbers, the system cannot dissipate all of the energy injected at the largest scales [Frisch, 1995]. The excess energy cascades towards smaller scales where the dissipation is more efficient than advection and the viscosity term dominates over the non-linear term.

3.4 The Kolmogorov Spectrum of Turbulence

The energy cascade can be visualised with the spectrum (see Section 3.7) of turbulence, which gives the energy in the fluctuations as a function of wave-number. In Figure 3.2, I show a typical energy spectrum for a turbulent fluid from Narita [2012]. The inertial range separates the injection wave-number k_L and the dissipation wave-number k_D. At wave-numbers $k < k_L$, the fluctuations are no longer correlated and therefore, linked to the energy injection process. Since energy is conserved in the inertial range, the spectrum will show a power-law in k. This spectrum can be easily found using dimensional arguments. By taking increments in the fluctuating velocity, $\delta \mathbf{u}(\ell) = \mathbf{u}(\mathbf{r}+\ell) - \mathbf{u}(\mathbf{r})$, between two spatial points in the fluid separated by distance, ℓ, the energy associated with these fluctuations is δu_ℓ^2 and the characteristic time τ_ℓ for the

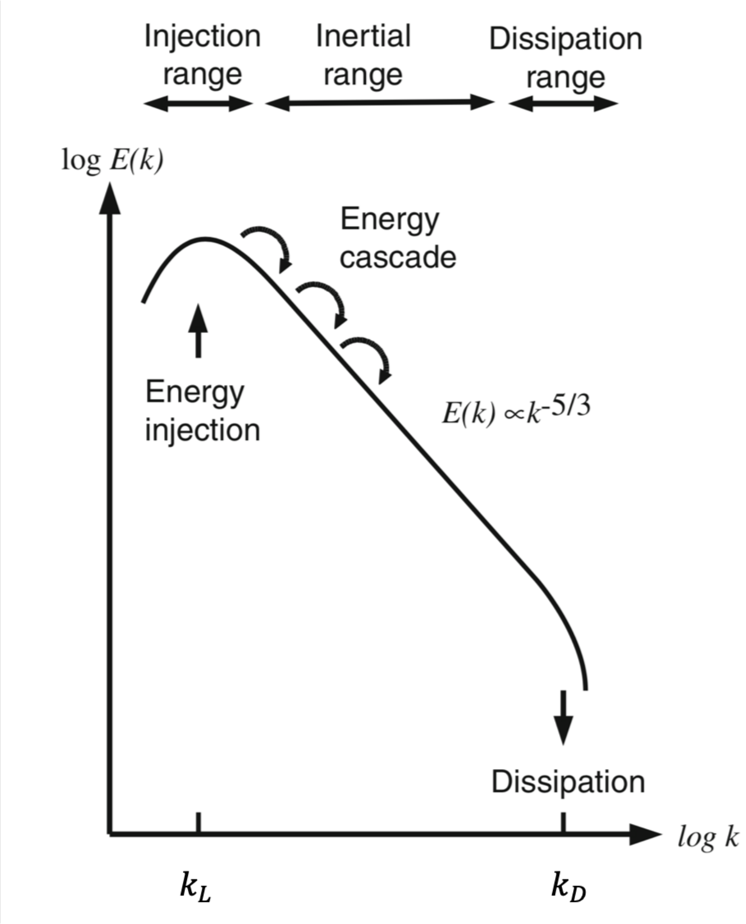

Figure 3.2: A typical energy spectrum of turbulence in a neutral fluid according to Kolmogorov's scaling. The inertial range is characterised by a $k^{-5/3}$ power-law. Figure from Narita [2012].

energy to cascade to smaller scales is $\ell/\delta u_\ell$, by dimensional arguments. The energy transfer rate (per unit mass) is, therefore,

$$\varepsilon \sim \frac{\delta u_\ell^2}{\tau_\ell} \sim \frac{\delta u_\ell^3}{\ell}, \tag{3.11}$$

known as the Kolmogorov-Obukhov law, $\delta u_\ell \sim (\varepsilon\ell)^{1/3}$. By assuming that the inertial range is isotropic, homogeneous, and does not depend on energy-injection or dissipation, the energy spectrum where $k = 2\pi/\ell$ is,

$$E \sim \int E(k)dk \Rightarrow E(k) \sim \varepsilon^{2/3}k^{-5/3}. \tag{3.12}$$

This is the main result of K41 phenomenology of turbulence [Kolmogorov, 1941; Frisch, 1995], which is based on arguments discussed in this section. At $k > k_D$, dissipation causes an exponential decay of the energy spectrum.

3.5 Models of Plasma Turbulence

There are many different phenomenological models of plasma turbulence, which are more complicated than the Kolmogorov picture [see Schekochihin, 2018]. These models provide scaling predictions that can be compared to observations to distinguish the physical processes taking place.

3.5.1 Iroshnikov-Kraichnan Phenomenology

Iroshnikov [1964] and Kraichnan [1965] first derived the spectrum for MHD turbulence, based on the Alfvén effect (see Section 3.2.3). For the non-linear interaction between oppositely propagating Alfvén waves aligned parallel to the magnetic field, there are now two length scales, $\ell_{||}$ parallel to the field, and λ perpendicular to the field. Assuming $\delta z_\ell^+ \sim \delta z_\ell^- \sim \delta u_\ell \sim \delta B_\ell$, then $\varepsilon \sim \delta u_\ell^2/\tau_\ell$ can again be used to define the energy transfer rate through scale ℓ. However, there is now a dimensional ambiguity over which timescale to use when defining τ_ℓ since two timescales are associated with each wave-packet. These are the Alfvén time $\tau_A \sim \ell_{||}/v_A$, the time it takes an Alfvénic wave-packet to propagate a distance $\ell_{||}$ along $\mathbf{B}_0$, and the non-linear eddy time $\tau_{NL} \sim \lambda/\delta u_\lambda$, the time it takes an Alfvénic wave-packet to break up. Iroshnikov and Kraichnan showed that the non-linear interactions are slowed down by a factor τ_{NL}/τ_A compared to the fluid case by the sweeping of the fluctuations across each other, so that $\tau_\ell \sim \tau_{NL}^2/\tau_A$. Therefore from Equation 3.11,

$$\delta u_\lambda \sim (\varepsilon v_A)^{1/4}\lambda^{1/4} \Rightarrow E(k) \sim (\varepsilon v_A)^{1/2} k^{-3/2}, \tag{3.13}$$

assuming isotropy, $\ell_{||}/\lambda \sim 1$. Equation 3.13 is the Iroshnikov-Kraichnan spectrum. This derivation assumes weak interactions where the change in amplitude of the waves is negligible compared to δu_ℓ. In other words, the turbulence is weak, and the non-linear interactions happen very slowly compared to wave motion, $\tau_A \ll \tau_{NL}$.

3.5.2 Goldreich-Sridhar Phenomenology & Critical Balance

Since the degree of non-linearity increases towards smaller scales, Goldreich & Sridhar [1995] argued that there will always be a scale ℓ in the inertial range where $\tau_A \ll \tau_{NL}$ no longer holds, and the assumption of weak turbulence is not justified. They instead proposed that the turbulence in a plasma naturally develops towards a state of strong turbulence where $\tau_A \sim \tau_{\mathrm{NL}}$. This conjecture is called critical balance, since an Alfvénic wave-packet of size λ is broken up by non-linear interactions over the same timescale it takes the wave-packet to propagate a distance $\ell_{||}$ along the field. The cascade time is then the same as fluid turbulence, $\tau_\ell \sim \tau_{NL}$, giving a perpendicular cascade with the Kolmogorov spectrum (Equation 3.12),

$$E(k_\perp) \sim \varepsilon^{2/3} k_\perp^{-5/3}. \tag{3.14}$$

In addition, along the field, $\tau_\ell \sim \tau_A$, giving a parallel cascade with a steeper spectrum, $E(k_{||}) \sim k_{||}^{-2}$. The relation between the two scales is $\ell_{||} \sim v_A \varepsilon^{-1/3} \lambda^{2/3}$. This relation reveals that scale-dependent anisotropy will arise in a strong turbulent cascade [Cho & Vishniac, 2000; Maron & Goldreich, 2001], where parallel correlations are along a local mean-field, rather than the global mean magnetic field. Small-scale fluctuations will propagate along this local field and do not know the difference between a perturbation at larger scales and the true mean-field. This property of the turbulence is important in the solar wind (see Section 4.3)

3.5.3 Boldyrev Phenomenology & Dynamic Alignment

Boldyrev [2006] later proposed that the non-linear time should include an additional factor of the alignment angle, θ_λ, between the velocity and magnetic field fluctuations: $\tau_{NL} \sim \lambda / (\delta z \sin\theta_\lambda)$. They argued that this factor is needed because the fluctuations and their gradients are mostly in the plane perpendicular to the mean-field. Within this plane, the gradients are perpendicular to the fluctuations due to the solenoidal nature of $\mathbf{B}$, leading to a reduction in the non-linear terms if the fluctuations are more aligned. They proposed that $\delta\mathbf{u}$ and $\delta\mathbf{b}$ align to the maximum amount permitted at each scale, leading to $\theta_\lambda \propto k_\perp^{-1/4}$. This phenomenon is called dynamic alignment, and like critical balance, is another manifestation of Alfvénic fluctuations being the basic element of MHD turbulence.

Boldyrev phenomenology leads to three-dimensional anisotropy with eddies at small scales $l_\| \gg \xi \gg \lambda$, where ξ is the characteristic length in the fluctuation direction and λ is the direction perpendicular to both $l_\|$ and ξ. The spectra in each direction are:

$$E\left(k_\lambda\right) \propto k_\lambda^{-3/2}, \quad E\left(k_\xi\right) \propto k_\xi^{-5/3}, \quad E\left(k_\|\right) \propto k_\|^{-2}. \tag{3.15}$$

More recently, further refinements to these models have been proposed [Lithwick et al., 2007; Beresnyak & Lazarian, 2008; Chandran, 2008; Perez & Boldyrev, 2009; Podesta & Bhattacharjee, 2010; Chandran et al., 2015; Mallet & Schekochihin, 2017; Loureiro & Boldyrev, 2017a,b].

3.5.4 Turbulence at Kinetic Scales

As the energy cascade proceeds to ever smaller scales, it eventually reaches characteristic proton scales such as the proton gyro-radius, ρ_p, and inertial length, d_p. At these scales, ion-electron decoupling and wave dispersion effects can lead to changes in the physics of the turbulent cascade, as well as dissipation and plasma heating. In particular, scale invariance is broken, and the energy spectrum can steepen or deviate from a power-law. Several names have been proposed for this range of scales, reflecting the different physical processes that may be ongoing. In this thesis, I use ‘ion-kinetic scales’ to reflect that the scales associated with this range are close to the characteristic proton scales where ideal MHD breaks down and the individual motion of the protons must be considered.

Similarly to Alfvénic turbulence described by incompressible MHD, phenomenological models have been developed for an energy cascade between ion-kinetic and electron-kinetic scales. Early models were based on extensions to ideal MHD such as Hall MHD that describe a turbulent cascade of whistler waves [Cho & Lazarian, 2004]. However, Alfvénic turbulence at large scales has instead, been proposed to transition to kinetic Alfvén turbulence at sub-ion scales, reflecting the fact that the KAW is the continuation of the oblique Alfvén mode in this regime [Leamon et al., 1998b; Howes et al., 2008; Schekochihin et al., 2009; Boldyrev & Perez, 2012]. Both models give a scale-dependent anisotropy of $k_\parallel \propto k_\perp^{1/3}$ [Boldyrev et al., 2013], stronger than for Alfvénic turbulence. The energy spectra obtained from these models are:

$$E\left(k_\perp\right) \propto k_\perp^{-7/3}, \quad E\left(k_\parallel\right) \propto k_\parallel^{-5}. \tag{3.16}$$

A key difference, however, is that kinetic Alfvén turbulence is low frequency ($\omega \ll \Omega_i$), compared to whistler turbulence ($\omega \gtrsim \Omega_i$). Therefore, unlike whistler turbulence, density fluctuations are non-negligible. The scaling of the electric field and density fluctuations in this range are: $E_E\left(k_\perp\right) \propto k_\perp^{-1/3}$ and $E_n\left(k_\perp\right) \propto k_\perp^{-7/3}$. A modification of these predictions was suggested by Boldyrev & Perez [2012], who observed a concentration of energy into two-dimensional current sheets in their kinetic Alfvén turbulence simulations. Assuming that the cascade is only active within these sheets, a weaker anisotropy is obtained, $k_\parallel \propto k_\perp^{2/3}$, and the energy spectra for the magnetic field fluctuations become:

$$E\left(k_\perp\right) \propto k_\perp^{-8/3}, \quad E\left(k_\parallel\right) \propto k_\parallel^{-7/2}. \tag{3.17}$$

3.6 Dissipation of Plasma Turbulence

Most space plasmas are collisionless, so other physical mechanisms must be responsible for the dissipation of turbulent fluctuations and heating of a plasma in the place of collisions. Since the turbulence is made up of fluctuations that have properties consistent with plasma waves, wave-particle resonances such as Landau and cyclotron resonance are a possible route for wave damping via quasi-linear diffusion (Section 2.6.2). These resonances, however, are reversible. To heat a plasma, there must be an irreversible increase in entropy. The change in the entropy of species j is given by Boltzmann's H-theorem:

$$\frac{\mathrm{d}S_j}{\mathrm{d}t} = \frac{\mathrm{d}}{\mathrm{d}t}\left(-\int \frac{\mathrm{d}^3\mathbf{r}}{V}\int \mathrm{d}^3\mathbf{v} f_j \ln f_j\right) = -\int \frac{\mathrm{d}^3\mathbf{r}}{V}\int \mathrm{d}^3\mathbf{v}\ln f_j \left(\frac{\delta f_j}{\delta t}\right)_{\mathrm{c}} \tag{3.18}$$

Therefore, the only way to increase entropy is through collisions [Schekochihin et al., 2008]. In a collisionless plasma, energy in the electromagnetic fluctuations is transferred into entropy fluctuations, $\delta f_j^2/f_{0,j}$, where $f_j(\mathbf{x},\mathbf{v},t) = f_{0,j}(\mathbf{v}) + \delta f_j(\mathbf{x},\mathbf{v},t)$ (see Appendix A). These fluctuations then cascade to small scales in velocity space through a mixture of linear (Landau damping) [Schekochihin et al., 2008] and non-linear phase mixing [Dorland & Hammett, 1993; Tatsuno et al., 2009]. At small enough scales, the velocity space structure can then be smoothed by collisions, increasing entropy and ultimately, heating the plasma.

Stochastic heating is a non-resonant process that arises from magnetic field fluctuations at scales ($k_\perp \rho_j \sim 1$) and low frequencies ($\omega \ll \Omega_j$). These fluctuations cause perturbations to the gyration orbits of the particles, that if large enough, can become stochastic in the plane perpendicular to $\mathbf{B}_0$ [e.g., Chandran et al., 2010, 2013]. Therefore, the particles experience stochastic changes in their energy due to the fluctuating fields. The particles diffuse in $v_\perp^2$, leading to perpendicular heating.

Turbulence naturally develops localised coherent structures that are characterised by sharp gradients in velocity or the magnetic field. These coherent structures, such as current sheets, are associated with higher temperatures and non-Maxwellian features in particle VDFs. These sheets can lead to dissipation through magnetic reconnection, the rearrangement of the magnetic field through resistive diffusion (Equation 2.44), transferring energy from the field into the plasma particles [see Matthaeus & Velli, 2011].

3.7 Statistical Description of Turbulence

3.7.1 Random Processes, Stationarity & Ergodicity

In a turbulent plasma such as the solar wind, it is difficult to determine the detailed behaviour of fluctuations in the plasma analytically. Instead, the statistical properties of the fluctuations are investigated by taking a time-series of spacecraft measurements and modelling them as an ensemble of many realisations of a random process [Matthaeus & Smith, 1981]. An ensemble, $\{x(t)\}$, is a set of outcomes, $x_i(t)$, of a random process, where $i = 1, 2, ..., N$. The properties of a random process can be determined by averaging over the entire ensemble of N possible functions $x_i(t)$ generated by the random process. For a time t_1, the mean value μ_x and the autocorrelation function R_x (the first and joint moments of the probability density function) can be defined:

$$\mu_x(t_1) = \langle x(t_1) \rangle = \lim_{N \to \infty} \frac{1}{N} \sum_{i=1}^{N} x_i(t_1), \tag{3.19}$$

$$R_x(t_1, t_1 + \tau) = \langle x(t_1) x(t_1 + \tau) \rangle = \lim_{N \to \infty} \frac{1}{N} \sum_{i=1}^{N} x_i(t_1) \cdot x_i(t_1 + \tau), \tag{3.20}$$

where $\langle ... \rangle$ designates ensemble average. If both $\mu_x(t_1)$ and $R_x(t_1, t_1 + \tau)$ are independent of time, that is, $\mu_x(t_1) = \mu_x$ and $R_x(t_1, t_1 + \tau) = R_x(\tau)$, the sample function, $x(t)$, is weakly stationary. Strong stationarity requires all higher-order moments and joint moments to also be time-independent [Batchelor, 1970]. If $x(t)$ is Gaussian distributed, higher-order odd moments are zero and even moments are completely described by second-order moments. Therefore, the concept of weak stationarity naturally extends to strong stationarity and the mean and auto-correlation function completely describe a Gaussian stochastic process.

Ergodicity is an important concept that means a time average over just one sample function, $x_i(t)$, can be taken as an ensemble average over all states in phase space for a stationary process, i.e., all statistical information can be obtained from this one function. This property is an advantage for data measured by spacecraft since it means that a stationary random process is adequately sampled by averaging over a single time series. Matthaeus & Goldstein [1982b] show that the solar wind magnetic field fluctuations are often representative of a weakly stationary and ergodic process, as long as coherent structures are excluded. They found that the mean and autocorrelation function computed within a sub-interval converges to the values estimated for the entire interval after a few correlation times, τ_c, i.e., the majority of the phase space has been sampled.

3.7.2 The Power Spectral Tensor

Statistical information about turbulence in a plasma is contained within the n-point correlation functions of the fluctuating fields, $\mathbf{u}$ and $\mathbf{B}$ [Batchelor, 1970]. The two-point magnetic field autocorrelation tensor is:

$$\mathsf{R}^B_{ij}(\mathbf{r}) = \langle B_i(\mathbf{x}) \cdot B_j(\mathbf{x}+\mathbf{r}) \rangle \,, \tag{3.21}$$

where the indices $i, j = 1, 2, 3$ represent the different components of $\mathbf{B}$. Here, $\mathbf{r}$ is the position vector defined with respect to $\mathbf{x}$. For weak homogeneity[1], there is zero mean-field, $\mathbf{B}_0 = \langle \mathbf{B}(\mathbf{x}) \rangle = 0$, and $\mathsf{R}^B_{ij}(\mathbf{r})$ is independent of $\mathbf{x}$. Therefore, $\mathsf{R}^B_{ij}(\mathbf{r})$ describes the structural correlation between different components of $\mathbf{B}$ with distance $\mathbf{r}$, averaged over an ensemble of two points in space. Similarly, the velocity autocorrelation and cross-correlation tensors are:

$$\mathsf{R}^u_{ij}(\mathbf{r}) = \langle u_i(\mathbf{x}) \cdot u_j(\mathbf{x}+\mathbf{r}) \rangle \,, \tag{3.22}$$

$$\mathsf{R}^{uB}_{ij}(\mathbf{r}) = \frac{1}{2} \langle u_i(\mathbf{x}) \cdot b_j(\mathbf{x}+\mathbf{r}) + b_i(\mathbf{x}) \cdot u_j(\mathbf{x}+\mathbf{r}) \rangle \,, \tag{3.23}$$

All three tensors have similar properties, for example, $\mathsf{R}_{ij}(\mathbf{r}) = \mathsf{R}_{ji}(-\mathbf{r})$ and $\partial \mathsf{R}_{ij}(\mathbf{r})/\partial r_i = \partial \mathsf{R}_{ij}(\mathbf{r})/\partial r_j = 0$. From the Wiener-Khinchin theorem [Wiener, 1930; Khintchine, 1934], the power spectral tensor $\tilde{\mathsf{S}}_{ij}(\mathbf{k})$ is the Fourier trans-

---

[1] Homogeneity is the similar to stationarity but in a spatial sense.

form of the autocorrelation tensor $R_{ij}(\mathbf{r})$,

$$\tilde{\mathsf{S}}_{ij}(\mathbf{k}) = \iiint \mathsf{R}_{ij}(\mathbf{r}) \exp(-i\mathbf{k}\cdot\mathbf{r})\, d^3\mathbf{r}. \tag{3.24}$$

For example, the magnetic field power spectral tensor is then:

$$\tilde{\mathsf{S}}^B_{ij}(\mathbf{k}) = \left\langle \tilde{B}^*_i(\mathbf{k})\cdot\tilde{B}_j(\mathbf{k})\right\rangle, \tag{3.25}$$

where the asterisk designates the complex conjugate: $\tilde{B}^*_i(\mathbf{k}) = \tilde{B}_i(-\mathbf{k})$. The diagonal components are by definition real, since the transforms are complex numbers. Likewise, the off-diagonal elements are complex.

The rugged invariants (see Section 3.2.2) are particularly useful when studying turbulence because non-linear effects do not modify them [Woltjer, 1958a,b]. Matthaeus & Goldstein [1982a] define the invariants in terms of the fluctuating fields:

$$E = \frac{1}{2}\left\langle |\delta\mathbf{u}|^2 + |\delta\mathbf{b}|^2\right\rangle, \tag{3.26}$$

$$H_c = \langle \delta\mathbf{u}\cdot\delta\mathbf{b}\rangle, \tag{3.27}$$

$$H_m = \langle \delta\mathbf{A}\cdot\delta\mathbf{B}\rangle. \tag{3.28}$$

The spectra of these invariants can be obtained directly from the trace of the power spectral tensor, $\mathrm{Tr}\left\{\tilde{\mathsf{S}}_{ij}(\mathbf{k})\right\} \equiv \tilde{\mathsf{S}}_{11} + \tilde{\mathsf{S}}_{22} + \tilde{\mathsf{S}}_{33}$; the kinetic power spectrum, $E_u(\mathbf{k}) \equiv \mathrm{Tr}\left\{\tilde{\mathsf{S}}^u_{ij}(\mathbf{k})\right\}$, the magnetic power spectrum, $E_B(\mathbf{k}) \equiv \mathrm{Tr}\left\{\tilde{\mathsf{S}}^B_{ij}(\mathbf{k})\right\}$, and the cross-helicity spectrum, $H_c(\mathbf{k}) \equiv \mathrm{Tr}\left\{\tilde{\mathsf{S}}^{uB}_{ij}(\mathbf{k})\right\}$.

3.7.3 Reduced Spectra and Taylor's Hypothesis

Most measurements in space are taken by a single spacecraft, which means the auto-correlation tensors R^B_{ij}, R^u_{ij} and R^{uB}_{ij} are only determined along a single direction defined by the flow past the spacecraft. In other words, the separations $\mathbf{r}$ are collinear along the flow direction. Therefore, a full Fourier decomposition is not possible and instead, only reduced spectra can be measured [Matthaeus & Goldstein, 1982a]. In other words, if r_1 is the direction of flow past the spacecraft, only $\mathsf{R}_{ij}(r_1,0,0)$ can be calculated. Hence, the reduced power spectral tensor is:

$$\tilde{\mathsf{S}}_{ij}^{(r)}(k_1) = \int \mathsf{R}_{ij}(r_1,0,0)\exp(-ik_1r_1)\,dr_1 = \iint \tilde{\mathsf{S}}_{ij}(k_1,k_2,k_3)\,dk_2\,dk_3. \tag{3.29}$$

The power spectral tensor is therefore integrated over the plane perpendicular to the flow direction. The reduced spectra of the invariants, which depend only on the wave-number k_1, are: $H_m^{(r)}$, $H_c^{(r)}$, and $E^{(r)} = E_v^{(r)} + E_B^{(r)}$. Except for isotropic symmetry, information is lost by computing the reduced version of $\tilde{\mathsf{S}}_{ij}(\mathbf{k})$ and the full wave-vector $\mathbf{k}$ of the fluctuations cannot be determined. Even with axisymmetric symmetry, no manipulation of the reduced spectrum allows the extraction of $\mathbf{k}$ [for example, see Wicks et al., 2012].

Spacecraft observations consist of a time-series of measurements and do not directly sample the spatial structure of the plasma in order to calculate the correlation tensors (e.g., Equation 3.21). Instead, Taylor's 'frozen-in' flow hypothesis [Taylor, 1938] can be applied to solar wind measurements, since the solar wind is super-Alfvénic and the flow of the plasma past the spacecraft is much faster than the the timescales for the evolution of the plasma.[2] Therefore, a time-series can be considered as a one-dimensional spatial cut through the plasma and correlation tensors calculated from two-time single-point measurements, e.g., $\mathsf{R}_{ij}^B(\tau) = \langle B_i(t)\cdot B_j(t+\tau)\rangle$. The Doppler shift of the fluctuations into the spacecraft frame is: $\omega_{sc} = \omega_{pl} + \mathbf{k}\cdot\mathbf{v}_{sw} \simeq \mathbf{k}\cdot\mathbf{v}_{sw}$ where ω_{pl} is the frequency in the plasma frame. Therefore, the reduced power spectrum can be written as:

$$\tilde{\mathsf{S}}_{ij}^{(r)}(f_{sc}) = \iiint \tilde{\mathsf{S}}_{ij}(\mathbf{k})\delta(2\pi f_{sc} - \mathbf{k}\cdot\mathbf{v}_{sw})\,d^3\mathbf{k}, \tag{3.30}$$

where $\omega_{sc} = 2\pi f_{sc}$ [Wicks et al., 2012]. The $\mathbf{k}\cdot\mathbf{v}_{sw}$ term in this equation

---

[2] This is only true at MHD scales. For wave modes with increasing phase speeds with larger k, e.g., whistler waves, Taylor's hypothesis can be violated at smaller scales.

shows that for $\theta_{kv} = 0°$, fluctuations are measured at their actual k. However for oblique angles, the waves are measured at higher k. Since the turbulent amplitude decreases with increasing k, Taylor's hypothesis means that $\tilde{\mathsf{S}}^{(r)}_{ij}(f_{sc})$ is most sensitive to the lowest k measured. Equation 3.25 becomes:

$$\tilde{\mathsf{S}}^{(r)}_{ij}(f_{sc}) = \left\langle \hat{B}^*_i(f_{sc}) \cdot \hat{B}_j(f_{sc}) \right\rangle . \tag{3.31}$$

The ensemble average is calculated by averaging the output of the Fourier transform over a sufficiently long interval, typically several τ_c (see Section 5.4.2 for more details).

3.7.4 Magnetic Helicity

Based on arguments by Matthaeus & Goldstein [1982a], the magnetic helicity spectrum $H_m(\mathbf{k})$ is related to the magnetic field power spectral tensor,

$$\tilde{\mathsf{S}}^{B}_{ij}(\mathbf{k}) - \tilde{\mathsf{S}}^{B}_{ji}(\mathbf{k}) = i\varepsilon_{ij\ell} k_l H_m(\mathbf{k}), \tag{3.32}$$

where,

$$\varepsilon_{ij\ell} = \begin{cases} +1, & \text{if } (i,j,\ell) \text{ is } (1,2,3),(2,3,1), \text{ or } (3,1,2), \\ -1, & \text{if } (i,j,\ell) \text{ is } (3,2,1),(1,3,2), \text{ or } (2,1,3), \\ 0, & \text{if } i = j, \text{ or } j = \ell, \text{ or } \ell = i, \end{cases} \tag{3.33}$$

$\varepsilon_{ij\ell}$ is the Levi-Civita Symbol, which accounts for the sign of the helicity under different permutations. Equation 3.32 shows that the helicity depends only on the imaginary part of the off-diagonal components of $\tilde{\mathsf{S}}^{B}_{ij}(\mathbf{k})$. The presence of $\varepsilon_{ij\ell}$ means the helicity gives the solenoidal structure of the magnetic field fluctuations in the plane perpendicular to the wave-vector component k_l, in the frame of the spacecraft. Reversing the ordering of the indices i and j simply causes a change in sign of $H_m(\mathbf{k})$. Since $\tilde{\mathsf{S}}^{B}_{ij}(\mathbf{k})$ is Hermitian ($\tilde{\mathsf{S}}_{ij} = \tilde{\mathsf{S}}^*_{ji}$),

$$H_m(\mathbf{k}) = \frac{2\,\mathrm{Im}\left\{\tilde{\mathsf{S}}^{B}_{ij}(\mathbf{k})\right\}}{\varepsilon_{ijl} k_l}, \tag{3.34}$$

A reduced form of magnetic helicity can be obtained from $\mathsf{R}^B_{ij}(r_1,0,0)$,

$$\iint \mathrm{Im}\left\{\tilde{\mathsf{S}}^B_{23}(\mathbf{k})\right\} dk_2\, dk_3 = \frac{k_1}{2} \iint H_m(\mathbf{k})\, dk_2\, dk_3, \tag{3.35}$$

where H_m has been integrated over the two transverse components to the radial flow [Matthaeus et al., 1982; Wicks et al., 2012]. Therefore:

$$H^{(r)}_m(k_1) = \frac{2\,\mathrm{Im}\left\{\tilde{\mathsf{S}}^{(r)}_{23}(k_1)\right\}}{k_1}, \tag{3.36}$$

This derivation of magnetic helicity only includes the contributions to helicity from fluctuations in $\mathbf{B}$, making it a measure of the polarisation properties of magnetic field fluctuations at a particular k_1. The reduced magnetic helicity can be normalised by the power in the magnetic field fluctuations,

$$\sigma^{(r)}_m(k_1) = \frac{k_1\, H^{(r)}_m(k_1)}{E_B(k_1)}, \tag{3.37}$$

which varies between [-1,1], assuming positive or negative values, depending on the sense of rotation of the correlation between the two transverse components to k_1. Using this definition, $\sigma_m < 0$ indicates left-handed fluctuations and $\sigma_m > 0$, right-handed fluctuations.

Chapter 4

Literature Review: Ion-kinetic Processes in the Solar Wind

In this chapter, I critically review the literature relevant to the research documented later in this thesis. I focus on kinetic processes at ion-kinetic scales in the solar wind. I begin by discussing the properties of ion VDFs in the solar wind and the role of collisional relaxation. Next, I review kinetic instabilities in the solar wind, with particular emphasis on proton temperature anisotropy instabilities. Then, I cover solar wind turbulence, the nature of the power spectrum of magnetic field fluctuations at ion-kinetic scales, and the properties of the fluctuations at these scales. Finally, I address the unanswered questions in the field and the motivation for my work in subsequent chapters.

4.1 Ion Distributions in the Solar Wind

Spacecraft instruments have been measuring ion VDFs for decades. These distributions often exhibit non-Maxwellian features driven by a combination of large-scale expansion effects, local kinetic processes, and the feedback of small-scale processes on the large-scale evolution. The kinetic physics of the solar wind plasma is well-documented [see reviews by Marsch, 2006; Verscharen et al., 2019]. Here I focus on observations of proton and α-particle (He^{2+}) distributions, the limitations of these measurements, and the role of collisional relaxation.

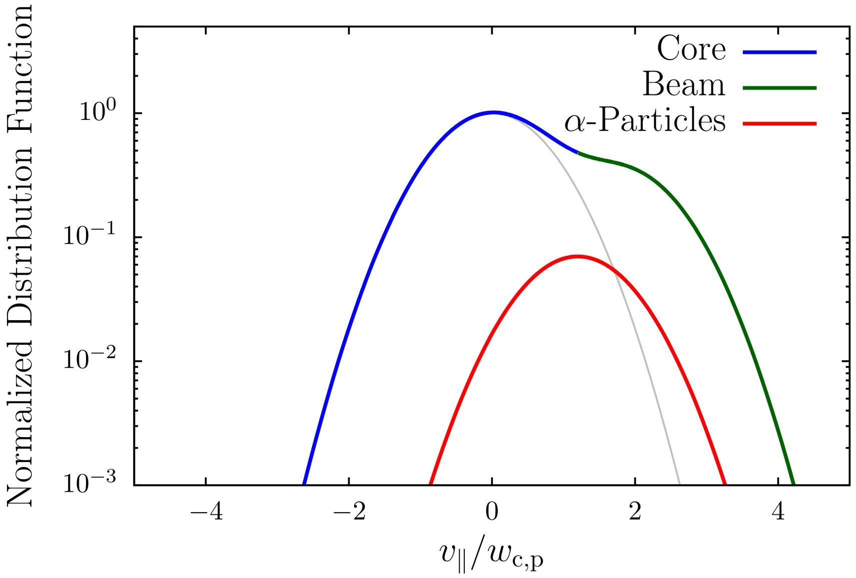

Figure 4.1: Cuts through the VDFs of protons and α-particles along $\mathbf{B}$, normalised by the peak of the proton distribution function. The grey curve shows the underlying core distribution. The distributions are shown in the reference frames in which the proton core distribution is at rest. Figure adapted from Verscharen et al. [2019].

4.1.1 Protons and α-particles

I show in Figure 4.1, typical cuts of ion VDFs along $\mathbf{B}$ in the solar wind from Verscharen et al. [2019]. Proton distributions often show the presence of a beam directed anti-sunward, a second proton component streaming faster than the proton core component along the direction of $\mathbf{B}$ with speed $v_\parallel \gtrsim v_{\mathrm{A}}$ [Asbridge et al., 1974; Feldman et al., 1974; Marsch et al., 1982b; Goldstein et al., 2000; Tu et al., 2004; Alterman et al., 2018]. This beam is more prevalent in fast wind streams and appears as a shoulder to the core component (in the rest frame of the core) toward greater $v_\parallel$ in Figure 4.1. Protons also show temperature anisotropies with respect to the magnetic field, $T_{p,\perp}/T_{p,\parallel}$, which leads to different widths of the distribution in the $v_\parallel$ and $v_\perp$ directions [Hundhausen et al., 1967a,b; Marsch et al., 1981; Kasper et al., 2002a; Marsch et al., 2004; Hellinger et al., 2006; Bale et al., 2009; Maruca et al., 2012a]. This is highlighted in Figure 4.2 from Alterman et al. [2018], showing a proton core distribution with different widths along $v_\parallel$ and $v_\perp$. In this example,

$T_{p,\perp}/T_{p,\parallel} > 1$, which is common in fast wind streams at 1 AU; in slow wind, however, $T_{p,\perp}/T_{p,\parallel} < 1$ is more common. In the inner heliosphere, $T_{p,\perp}/T_{p,\parallel}$ generally increases, showing evidence of processing of proton VDFs as the solar wind evolves with heliocentric distance [Matteini et al., 2007].

A significant minor ion species in the solar wind are α-particles. They are dynamically important due to their larger mass ($m_\alpha = 4m_p$), even though their number density is small compared to protons, $n_\alpha \lesssim 0.05n_p$. Like a proton beam, α-particles can drift with respect to the proton core along the magnetic field direction with speed $v_\parallel \lesssim v_{\mathrm{A}}$ [Ogilvie, 1975; Asbridge et al., 1976; Marsch et al., 1982a; Neugebauer et al., 1994, 1996; Steinberg et al., 1996; Reisenfeld et al., 2001; Berger et al., 2011; Gershman et al., 2012; Bourouaine et al., 2013]. In Figure 4.1, the α-particle population is shown as a separate shifted distribution with respect to the proton core, centred around the α-proton drift speed, $\mathbf{v}_d = \mathbf{v}_\alpha - \mathbf{v}_p$. The α-particle distribution often exhibits $T_{\alpha,\perp}/T_{\alpha,\parallel} < 1$, as seen in Figure 4.2. In fact, the parallel temperature of α-particles in the solar wind is typically several times larger than protons, $T_{\alpha,\parallel} \gtrsim 4T_{p,\parallel}$, suggesting preferential heating of heavier ions [Kasper et al., 2007, 2008, 2012].

Many studies have used measurements from the inner heliosphere with spacecraft such as *Helios* or *Wind* to show evidence of non-Maxwellian features of ion VDFs in the solar wind. These spacecraft take only a snapshot of the plasma as it flows past the spacecraft. Therefore, the evolution of the plasma with time and heliospheric distance is difficult to investigate. In particular, the origin of different non-Maxwellian features is not well understood. Are they formed in the corona and persist out to 1 AU or in the solar wind by local processes? How does the solar wind process the VDFs as it evolves? While the use of larger datasets can be used to give a statistical representation of the average solar wind plasma conditions, they require algorithms to produce moments of the ion VDFs, which may not always be accurate (e.g., see Section 5.3.5). This drawback is amplified by limited instrument resolution and the low densities of particles in the solar wind, making it difficult to resolve peaks

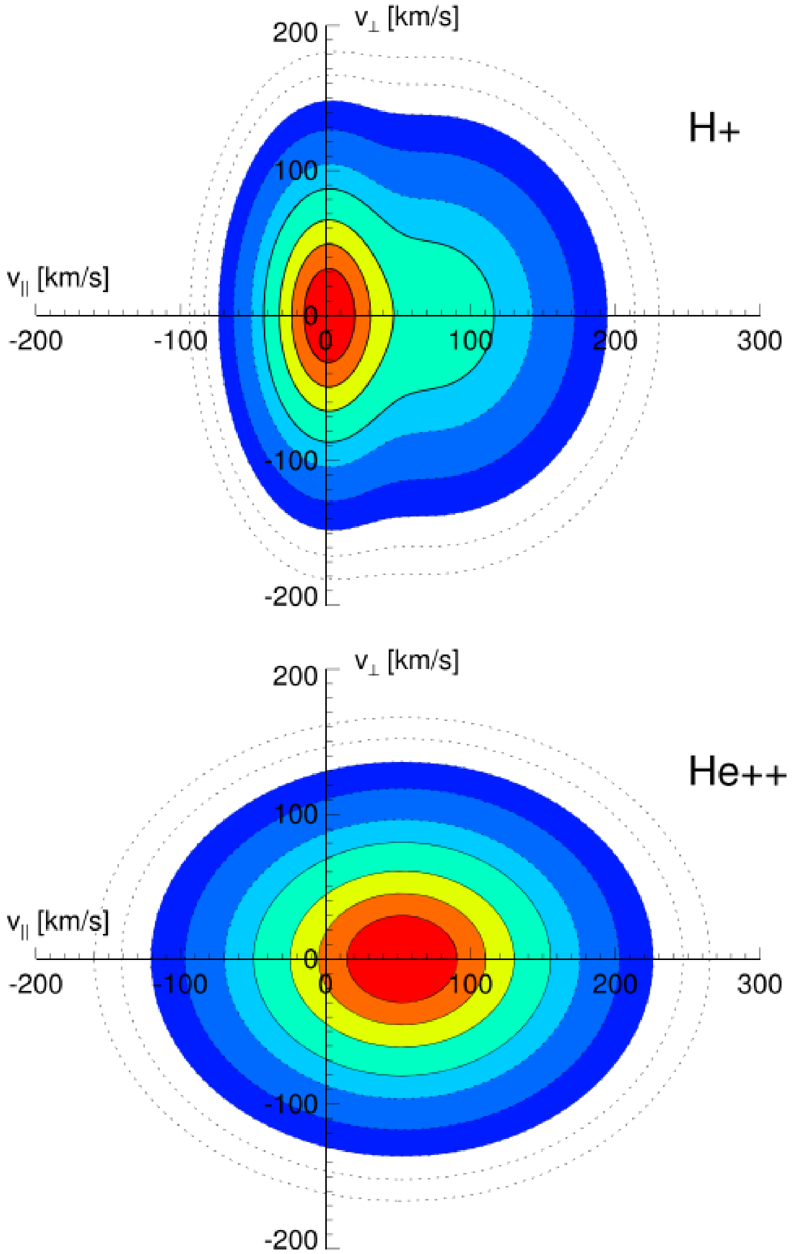

Figure 4.2: Schematics of typical proton (top) and α-particle (bottom) VDFs in fast wind streams. The proton beam can be identified by the secondary shoulder at large $v_\parallel$ in the top panel, whereas the α-particles in the bottom panel drift faster along $v_\parallel$ compared to the proton core. Figure from Alterman et al. [2018].

in the VDFs (see also, Section 5.3). VDFs are rarely measured at a high enough cadence to capture variations at ion-kinetic scales. However, a careful analysis of ion VDFs taking into account these drawbacks and coupled with higher resolution magnetic field measurements (see Section 5.2) can be used to probe the processes at these scales.

4.1.2 Collisional Relaxation

The observed distributions of ions vary in shape and change widely depending on local *in-situ* conditions, measurement location in the heliosphere and phase of the solar cycle [see Verscharen et al., 2019, and references therein]. The non-equilibrium features of these distributions, such as temperature anisotropies, beams, and drifts, are less pronounced in the slow solar wind than in the fast wind. This effect is typically attributed to the greater collisional relaxation rates and the longer expansion times in the slow wind [Maruca et al., 2013; Kasper et al., 2008, 2017], so that the distributions tend toward thermal equilibrium (i.e., a Maxwellian). From Kasper et al. [2017], I show in Figure 4.3, different measures of non-Maxwellian behaviour plotted as a function of Coulomb number,

$$N_{\mathrm{c}} \equiv \frac{\tau}{\tau_{\mathrm{c}}} = \frac{R}{u_r \tau_{\mathrm{c}}}, \tag{4.1}$$

an estimate of the number of collisional timescales that have elapsed in a parcel of plasma as it travels to a radial distance, R. Here, τ is the expansion time with constant radial flow speed, u_r and τ_{c} is the collisional timescale for proton-proton collisions. A collisionally old plasma with $N_{\mathrm{c}} \gg 1$ is closer to thermal equilibrium than a collisionally young plasma with $N_{\mathrm{c}} \ll 1$. It can be seen in Figure 4.3 that typical non-Maxwellian features of the ion VDFs are generally associated with fast wind streams, but that their occurrence is better correlated with N_{c}, which is inversely proportional to wind speed. However, it is important to note that the concept of Coulomb number has significant limitations. The definition for N_c only accounts for a single collision timescale,

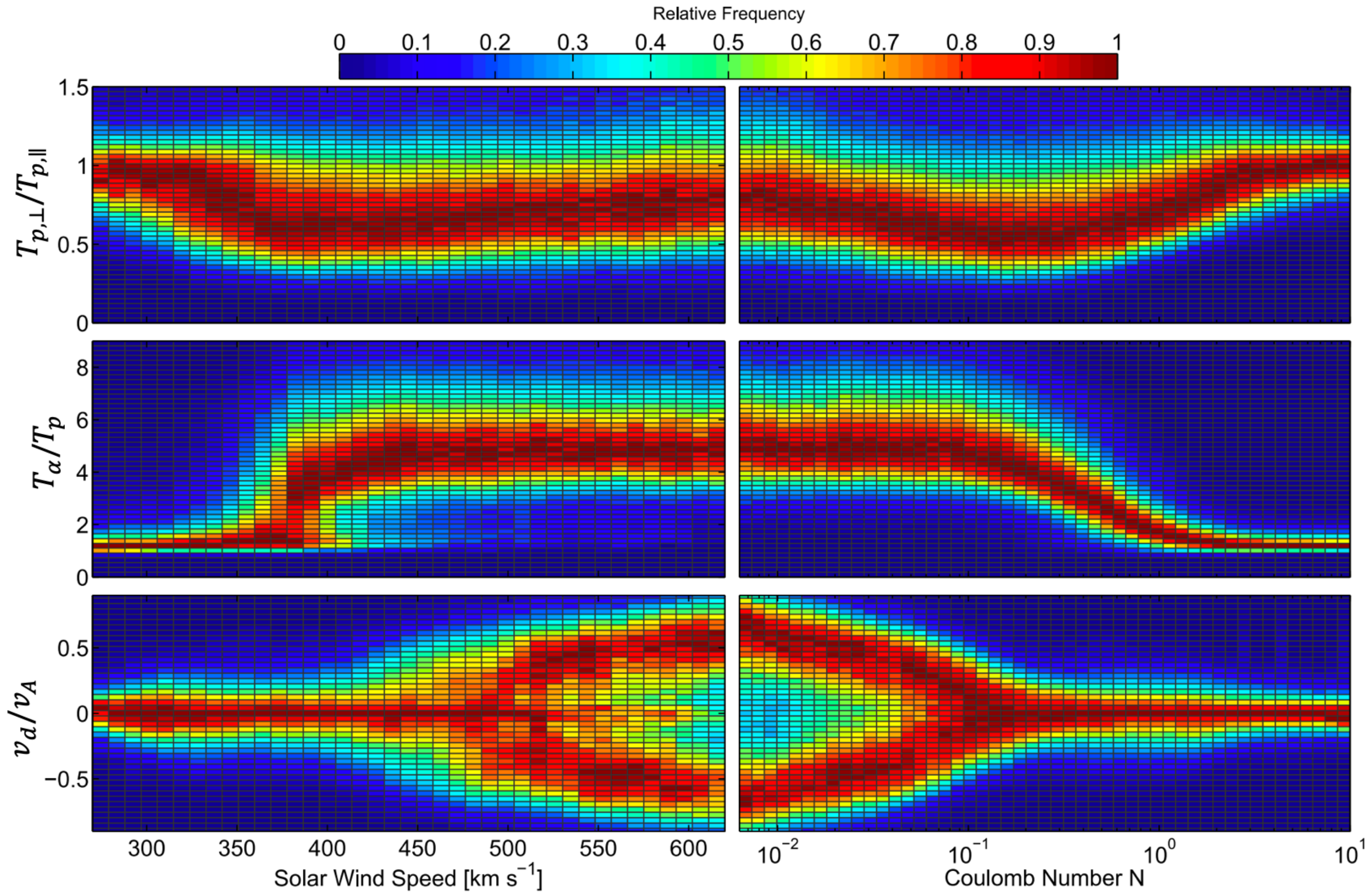

Figure 4.3: Column-normalised histograms of three parameters with solar wind speed (left column) and Coulomb number N_c (right column). Top: proton temperature anisotropy, $T_{p,\perp}/T_{p,\parallel}$; Middle: ratio of α-particle and proton temperatures, T_α/T_p; Bottom: α-proton differential flow normalised by the Alfvén speed, v_d/v_{A}. Figure from Kasper et al. [2017].

$\tau_{\rm c}$, making it difficult to account for the interactions of multiple departures from equilibrium. This can be seen in Figure 4.3, where $T_{p,\perp}/T_{p,\parallel}$ and T_α/T_p tend to their equilibrium values (unity) at different values of $N_{\rm c}$. It is also assumed that $\tau_{\rm c}$ remains constant with distance R. In reality, $\tau_{\rm c}$ depends on both density and temperature, which both have strong radial trends and can change due to local processes in the solar wind. Despite this, $N_{\rm c}$ can give an estimate of the collisional age of solar wind plasma in order to filter for conditions where non-Maxwellian features are most prevalent.

4.2 Kinetic Instabilities in the Solar Wind

Kinetic instabilities (see Section 2.7) in the solar wind can generate small-scale magnetic field fluctuations that exist in tandem with the turbulent cascade, and act as an effective viscosity for the plasma, influencing the thermodynamic evolution of the solar wind. Their small-scale structure can affect large-scale processes such as expansion and vice versa. These topics are reviewed by Matteini et al. [2012], Yoon [2017], and Verscharen et al. [2019]. In this thesis, I focus mainly on proton temperature anisotropy instabilities that can inject energy into the solar wind through wave-particle resonances at ion-kinetic scales, bringing the plasma back towards temperature isotropy.

Initial investigations of proton temperature anisotropy instabilities in the solar wind explored the $T_{p,\perp} > T_{p,\parallel}$ and $T_{p,\perp} < T_{p,\parallel}$ limits separately. Gary et al. [2001] used *ACE* observations to show that the AIC instability contours limit the maximum value of $T_{p,\perp}$ and similarly, Kasper et al. [2002a] used *Wind* data to show that the proton temperature anisotropy is bounded by the parallel firehose instability contours. Later, Hellinger et al. [2006] showed that the distribution of temperature anisotropy in the slow wind is well-constrained by the contours of the mirror-mode and oblique firehose instabilities. The distributions of minor ions [Maruca et al., 2012a; Bourouaine et al., 2013] are similarly constrained by their relevant instability contours.

In Figure 4.4, I plot the probability density distribution of solar wind data

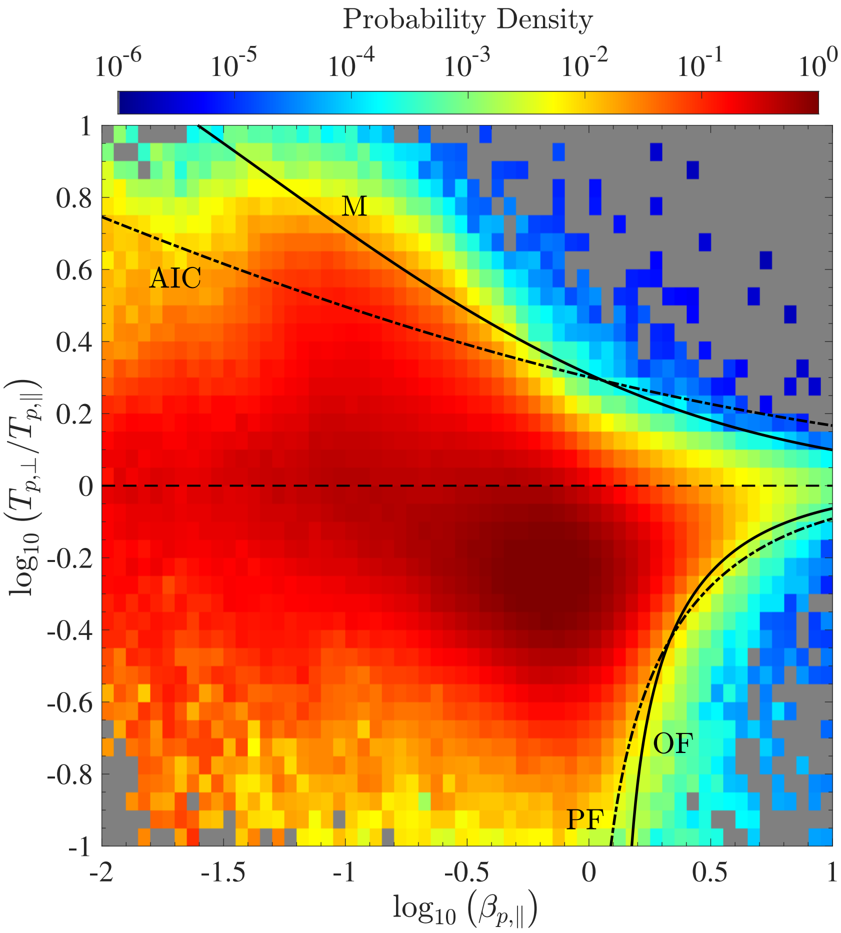

Figure 4.4: Probability density distribution of solar wind data from *Wind* across the $\beta_{p,\parallel}$-$T_{p,\perp}/T_{p,\parallel}$ plane, with contours of constant maximum growth rate, $\gamma/\Omega_p = 10^{-2}$, for the proton temperature anisotropy instabilities: AIC, mirror-mode (M), parallel (PF), and oblique firehose (OF). Further information on this figure is provided in Chapter 7.

in the $\beta_{p,\parallel}$-$T_{p,\perp}/T_{p,\parallel}$ plane using measurements from the *Wind* spacecraft. The solar wind is not completely constrained by all the instability contours (see Section 2.7), and a significant proportion of the distribution extends beyond the AIC contour. Several explanations have been proposed for this, including insufficient efficient energy extraction [Shoji et al., 2009], the stabilising effects of minor ions and drifts [Maruca et al., 2012b], or quasi-linear flattening of the resonant region [Isenberg et al., 2013], although there is currently no consensus. Matteini et al. [2007] show from *Helios* and *Ulysses* data at different heliocentric distances that the radial trend of the solar wind plasma in the $\beta_{p,\parallel}$-$T_{p,\perp}/T_{p,\parallel}$ plane shows a shallower gradient than CGL predictions (Equation

2.28), until it is constrained by the instability contours at $T_{p,\perp} < T_{p,\|}$. Hence, CGL theory [Chew et al., 1956] for double adiabatic expansion is insufficient to explain the radial evolution of the plasma and suggests ongoing heating mechanisms.

More recently, studies have investigated the properties of magnetic field fluctuations to infer the presence of modes driven by these temperature anisotropy instabilities. For example, several studies [He et al., 2011; Podesta & Gary, 2011b; Klein et al., 2014] find the presence of a peak in the magnetic helicity spectrum near Ω_p in the spacecraft frame that could be due to instability-driven waves. Bale et al. [2009] used *Wind* observations to show enhanced magnetic fluctuations near the contours for the temperature anisotropy instabilities (see Figure 4.5), also suggesting that unstable modes are generated in plasma located near to these contours in phase space. Other quantities are also enhanced in unstable parameter regions, for example, ion temperature [Maruca et al., 2011; Bourouaine et al., 2013].

Multiple sources of free energy from beams, drifts and temperature anisotropies are all simultaneously present under typical solar wind conditions [Kasper et al., 2008, 2017]. Beam components and drifts between particle species can also drive instabilities in the solar wind and growth rate contours can also be associated with these features of the particle VDFs. For example, Bourouaine et al. [2013] show that the α-proton drift is constrained by growing unstable parallel-propagating AIC and FMW modes, resulting in a deceleration of the α-particles [Verscharen et al., 2015]. Several studies have investigated the role of beams and drifts in stabilising or enhancing the growth of proton temperature anisotropy instabilities. For example, both the mirror-mode and oblique firehose instability contours depend on the total energy in the system. Chen et al. [2016] show that the combined effect of ion and electron temperature anisotropies and relative drifts between species gives an oblique firehose contour that better constrains the solar wind data. Podesta & Gary [2011a] show that the presence of an α-proton drift leads to an enhancement

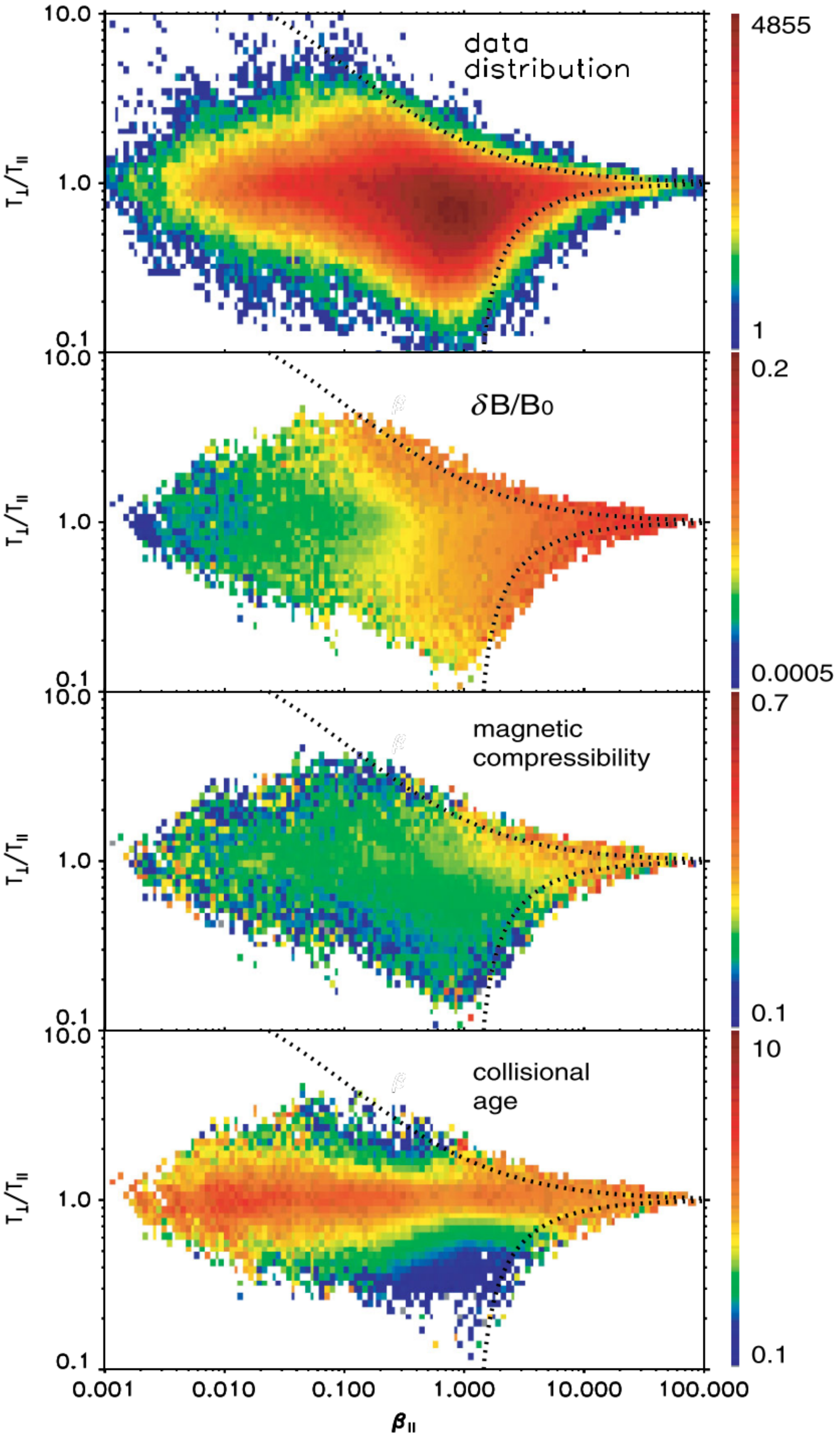

Figure 4.5: From top to bottom: The distribution of solar wind data, amplitude of magnetic fluctuations, $\delta B/B_0$, magnetic compressibility, $\delta B_\parallel^2/\delta B^2$, and Coulomb number, N_c, in the $\beta_\parallel$-$T_{p,\perp}/T_{p,\parallel}$ plane. Also plotted are contours for the oblique firehose (lower dotted line) and mirror (upper dotted line) instabilities. Figure from Bale et al. [2009].

in the growth of the AIC and parallel firehose instabilities, and preferential driving in the anti-sunward and sunward directions, respectively.

Vafin et al. [2018] show that contours of the temperature anisotropy instabilities incorporating the presence of beams better constrain solar wind data for $\beta_{p,\parallel} < 1$ observations than for no beams. Verscharen et al. [2013a]; Bourouaine et al. [2013] use linear Vlasov theory to provide limits on temperature anisotropy and α-particle drift speeds that are also consistent with solar wind observations. Numerical simulations [e.g., Maneva & Poedts, 2018] have also studied the simultaneous impact of drifts and temperature anisotropies. These studies show that instabilities generated by the presence of multiple non-Maxwellian features in ion VDFs can enhance instability growth rates. Therefore, their coupling is important in the solar wind and should be considered in studies investing kinetic instabilities. An analytical model developed by Ibscher & Schlickeiser [2014] for the coupling effects of temperature anisotropy and drifts can explain the lack of observations at $\beta_{p,\parallel} < 1$ and $T_{p,\perp} < T_{p,\parallel}$ (the bottom left region of Figure 4.4). However, Bale et al. [2009] do not find enhanced fluctuations in this region that would arise from unstable modes. Instead, Vafin et al. [2019] explained that the lack of data in this is due to collisional effects. The explanation for the lack of data in this region of the figure is still under debate.

The studies discussed here have primarily investigated instabilities in the reduced $\beta_{p,\parallel}$-$T_{p,\perp}/T_{p,\parallel}$ parameter space. However, as mentioned, $\beta_{p,\parallel}$ and $T_{p,\perp}/T_{p,\parallel}$ alone are not the only parameters that can affect the growth of the proton temperature anisotropy instabilities. For example, a significant ion drift can enhance the growth or stabilise these instabilities. Hellinger & Trávníček [2014] show that enhanced quantities near the instability contours may result from underlying correlations between solar wind temperatures and speeds. Therefore, care must be taken when interpreting results for any systematic correlation between variables plotted in this plane and $\beta_{p,\parallel}$ and $T_{p,\perp}/T_{p,\parallel}$. Most studies report on the agreement between growth rate contours and the constrained data in this plane, but do not quantify this agreement. For example, the contours for the parallel and oblique firehose instabilities are very similar, and from Figure 4.4, it is difficult to conclude which contour best constrains the data. Data distributions in the $\beta_{p,\parallel}$-$T_{p,\perp}/T_{p,\parallel}$ plane are often not normalised to account for logarithmic binning, making inspection by eye difficult. This comparison is further complicated by the fact that these contours change depending on the presence of other particle species. Moreover, it is important to account for the blurring of temperature anisotropy observations due to the finite time required to construct an ion VDF [Verscharen & Marsch, 2011; Maruca & Kasper, 2013], that can lead to contours not constraining the data. Many studies conclude that data constrained by these contours is evidence for the presence of instabilities in the solar wind, but do not show evidence of ongoing driving of these modes or under which solar wind conditions they occur. Can evidence of these modes be found directly from magnetic field fluctuations and under which conditions are they most common?

Recently, Klein et al. [2017] used the Nyquist instability criterion to account for multiple free energy sources for instabilities. This method avoids the drawbacks of analytical models and instead determines if a system supports any growing modes at a particular **k** by performing a complex contour integration. Klein et al. [2018] apply this criterion to a statistically random set of solar wind observations modelled as a collection of proton core, proton beam, and α-particle components (each with distinct anisotropies, densities, and drifts) to find that a majority of intervals are unstable. Most of these unstable modes are resonant instabilities at ion-kinetic scales, and around 10% of the intervals have instabilities with growth rates of order the non-linear turbulent cascade rate at these scales, which indicates that they may grow quickly enough to compete with the background turbulence. However, Klein & Howes [2015] use linear Vlasov theory to argue that instabilities are unlikely to have any significant effect on the evolution of the turbulent cascade in the solar wind, suggesting that instability fluctuations can be considered separate from the turbulent cascade when investigating turbulent dissipation.

4.3 Turbulence in the Solar Wind

The solar wind contains fluctuations over many scales and several orders of magnitude in frequency, suggesting the presence of a turbulent cascade (See Chapter 3). This cascade is believed to develop in the corona, and persist as the slow wind expands out into the heliosphere [Goldstein et al., 1995; Tu & Marsch, 1995; Bruno & Carbone, 2013]. A typical example of a power spectrum of the magnetic field fluctuations in the solar wind from Verscharen et al. [2019] is shown in Figure 4.6. In this section, I interchange between frequency, scale and wave-number, which can all be related to each other using Taylor's hypothesis (Section 3.7.3): $f_\ell = kv_{sw}/2\pi = v_{sw}/\ell$.

At the lowest frequencies, $f \lesssim 10^{-4}$ Hz, corresponding to temporal scales over many days, there is a power-law of f^{-1}. This range of frequencies is called the energy injection or $1/f$ range and includes the temporal variability of the Sun. It is at these frequencies that the energy is injected into the cascade by processes in the corona, leading to the generation of large-scale Alfvén waves propagating dominantly outwards from the Sun into the solar wind [Coleman, 1966; Belcher & Davis Jr., 1971]. Due to local processes, such as wave reflection [Verdini et al., 2012; Perez & Chandran, 2013; Tenerani & Velli, 2017] or wave coupling [Chandran, 2018], counter-propagating Alfvénic fluctuations can be produced, leading to the non-linear interactions necessary for the turbulent energy cascade (see Section 3.2.3). The $1/f$ range has been observed frequently in fast wind streams [e.g., Matthaeus et al., 2007], and recently in slow wind [Bruno et al., 2019]. The exact origins of this range are still under debate [Matthaeus & Goldstein, 1986; Velli et al., 1989; Mangeney, 1991; Matteini et al., 2018]. However, it is thought that at f_{c}, corresponding to the correlation time, τ_{c}, the fluctuations lose the memory of their origin in the solar atmosphere (i.e., no longer originate in the corona) and instead, are a product of the *in-situ* dynamics of the solar wind. The correlation length,

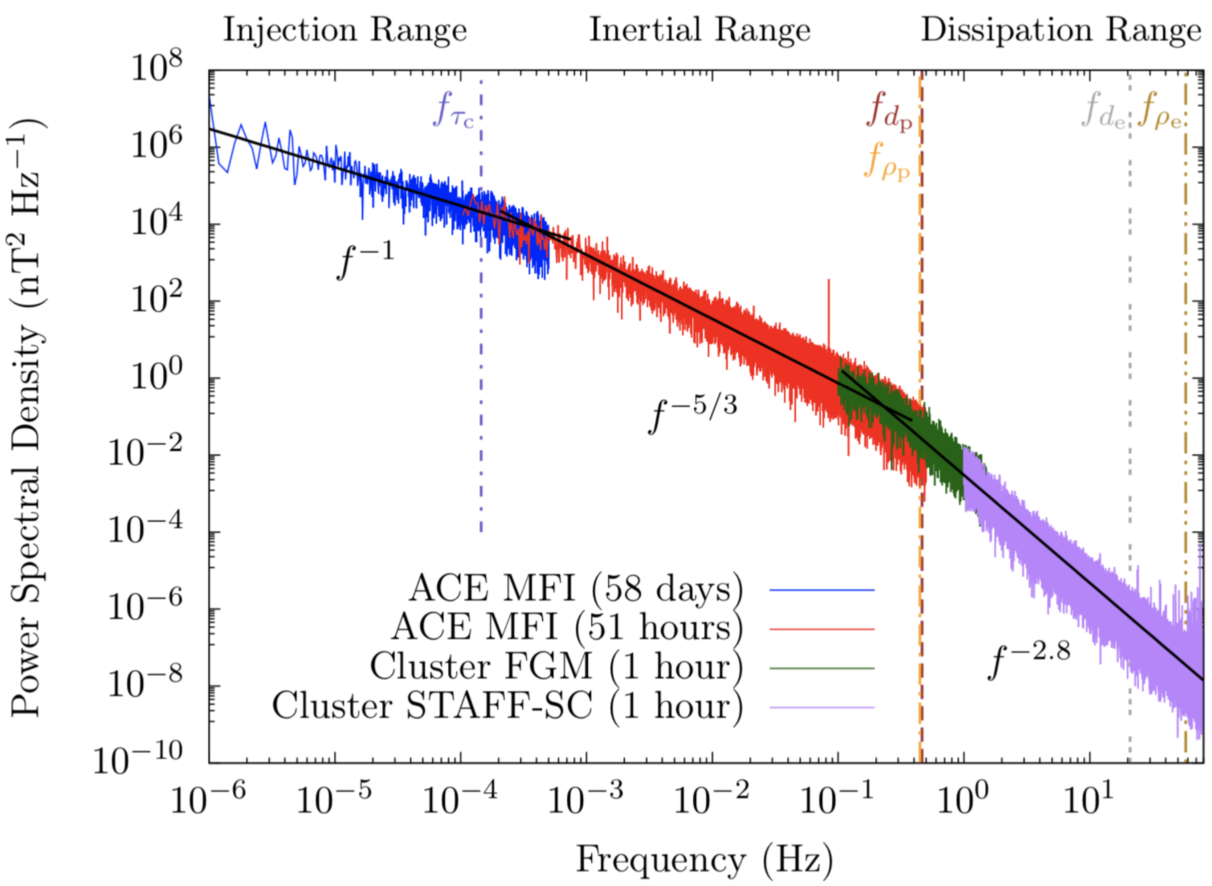

Figure 4.6: Power spectral density of magnetic field fluctuations in the solar wind spanning eight orders of magnitude in frequency, calculated from four nested intervals from *ACE* and *Cluster* observations at 1 AU. The black lines show power-laws of f^{-1}, $f^{-5/3}$, and $f^{-2.8}$, which are characteristic of the injection, inertial, and sub-ion ranges, respectively. The vertical lines show characteristic plasma scales converted to frequencies using Taylor's hypothesis: $f_\ell = kv_{sw}/2\pi = v_{sw}/\ell$, using the average plasma properties from the 1 hour *Cluster* FGM interval. Figure from Verscharen et al. [2019].

λ_c, therefore, is the size of the largest energy-containing 'eddies' or structures in the turbulent flow.

At frequencies $10^{-4}\,\text{Hz} \lesssim f \lesssim 1\,\text{Hz}$, the spectrum of magnetic field fluctuations shows a typical Kolmogorov inertial range scaling of $f^{-5/3}$ extending over several decades, characteristic of a MHD turbulent energy cascade from large to small spatial scales [see Tu & Marsch, 1995; Alexandrova et al., 2013; Bruno & Carbone, 2013; Kiyani et al., 2015; Chen, 2016, and references therein]. The dynamics in this range are thought to evolve independently of the fluctuations at $f < f_c$ and are constrained only by the rate of energy transfer between different scales, ε. Therefore, the physics of the energy cascade in this range are thought to be universal. The extent of the inertial range in frequency can be extremely variable [Sorriso-Valvo et al., 2007; Marino et al., 2012], and in highly Alfvénic solar wind streams, the inertial range is extended towards lower frequencies [Wicks et al., 2013].

Many studies show that in the inertial range, the fluctuations are anisotropic with respect to the mean magnetic field [see reviews by Horbury et al., 2012; Oughton et al., 2015]. The fluctuations have $k_\perp \gg k_\parallel$, i.e., they are elongated along the field compared to across the field. This anisotropy is consistent with strong turbulence models (see Section 3.5). More recently, techniques have been developed to measure the anisotropic scaling with respect to a local mean magnetic field. The need to use a local mean-field to test the critical balance predictions was identified in simulations [Cho & Vishniac, 2000; Maron & Goldreich, 2001; Milano et al., 2001]. This is because the linear term associated with the propagation of Alfvén waves in Equation 3.8 is sensitive to the mean magnetic field at the location and scale of the wave. Horbury et al. [2008] developed a technique to calculate the power spectrum at different angles to a local mean-field in the solar wind. Studies using this method have found that at the largest scales ($k\rho_p \lesssim 10^{-3}$) of the inertial range the turbulence is isotropic and $\delta B/B_0 \sim 1$, but becomes increasingly anisotropic towards smaller scales ($10^{-3} \lesssim k\rho_p \lesssim 1$), with power-law indices of

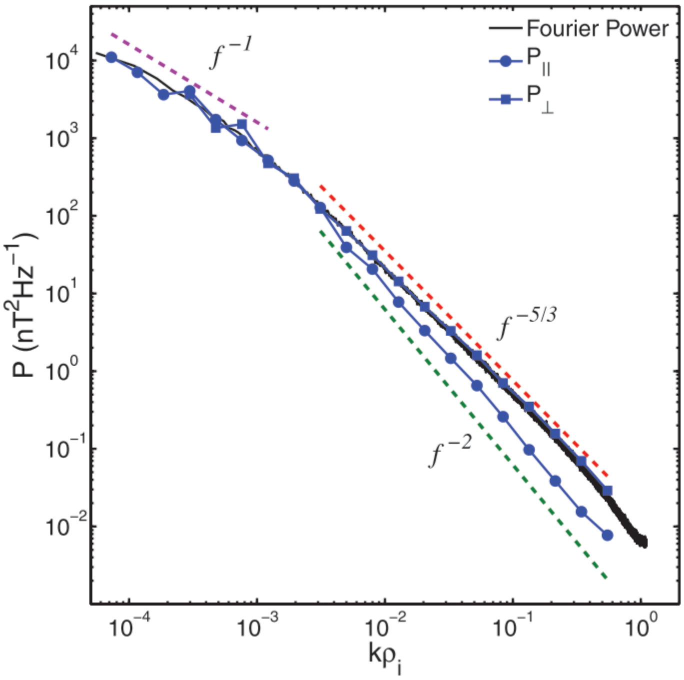

Figure 4.7: Wavelet (blue) and Fourier (black) power spectral density of magnetic field fluctuations in the solar wind from *Ulysses* observations showing the anisotropy of the inertial range using the method developed by Horbury et al. [2008]. Figure from Wicks et al. [2010].

power spectrum are −5/3 across and −2 along the local mean-field [Podesta, 2009; Luo & Wu, 2010; Wicks et al., 2010; Chen et al., 2011b]. This result is shown in Figure 4.7 from Wicks et al. [2010]. The latter power-law of −2 is only observed when using a scale-dependent local mean-field, and not a global mean-field.

While power is dominantly contained in Alfvénic fluctuations in the solar wind, there is also a compressive component due to non-Alfvénic modes (Section 2.6.4), involving variations of the density, δn, and magnetic field magnitude, $\delta|\mathbf{B}|$. The average fraction of magnetic energy in the compressive component in the inertial range is about 10% [Chen, 2016]. These fluctuations also have scaling properties suggestive of a turbulent cascade [e.g., Celnikier et al., 1983; Marsch & Tu, 1990; Manoharan et al., 1994; Kellogg & Horbury, 2005; Hnat et al., 2005; Issautier et al., 2010; Chen et al., 2011a]. Spectra of compressive fluctuations have long been measured in the solar wind [see Alexandrova et al., 2013; Bruno & Carbone, 2013]. For example, Chen et al. [2011a] show that the spectral indices of both δn and $\delta|\mathbf{B}|$ are close to -5/3. They also have lower power than the magnetic field fluctuations, consistent with less energy in compressive fluctuations. Howes et al. [2012] compare solar wind measurements of the (anti-)correlation between δn and $\delta|\mathbf{B}|$ to that produced from a critically-balanced spectrum of kinetic slow waves plus an isotropic spectrum of kinetic fast waves. They find that only slow modes, and not fast modes, contribute to the compressive power, consistent with Yao et al. [2011]. While slow modes are expected to be strongly Landau damped in a $\beta \sim 1$ plasma, their existence can be explained by their anisotropy [Lithwick & Goldreich, 2001; Schekochihin et al., 2009; Chen et al., 2012a].

At frequencies $f \sim \Omega_i/2\pi$ in the plasma frame, typically between 0.1 and 1 Hz in the spacecraft frame at 1 AU, the spectrum of magnetic field fluctuations steepens, as first reported by Coleman [1968] and Russell [1972]. Many other studies have since followed due to the availability of higher cadence measurements from *WIND*, *Cluster*, and other spacecraft missions [see Alexandrova et al., 2013; Chen, 2016]. The shape of the spectrum at these ion-kinetic scales is somewhat variable over about an order of magnitude in frequency and typically has a spectral exponent between -2 and -4 [Smith et al., 2006; Hamilton et al., 2008; Koval & Szabo, 2013], depending on plasma conditions such as magnetic energy, anisotropy of the fluctuations with respect to the mean magnetic field and bulk plasma velocity. This small range of frequencies is sometimes referred to as a transition range, due to the transition between the MHD regime and the kinetic regime, and therefore, the properties of plasma fluctuations. In Figure 4.8, I show examples of solar wind magnetic field spectra at ion-kinetic scales from Bruno et al. [2014], highlighting the variable nature of the transition range.

Several studies have shown evidence of a turbulent cascade in the solar wind at sub-ion scales ($k\rho_p >> 1$) down to electron-kinetic scales ($k\rho_e \sim 1$),

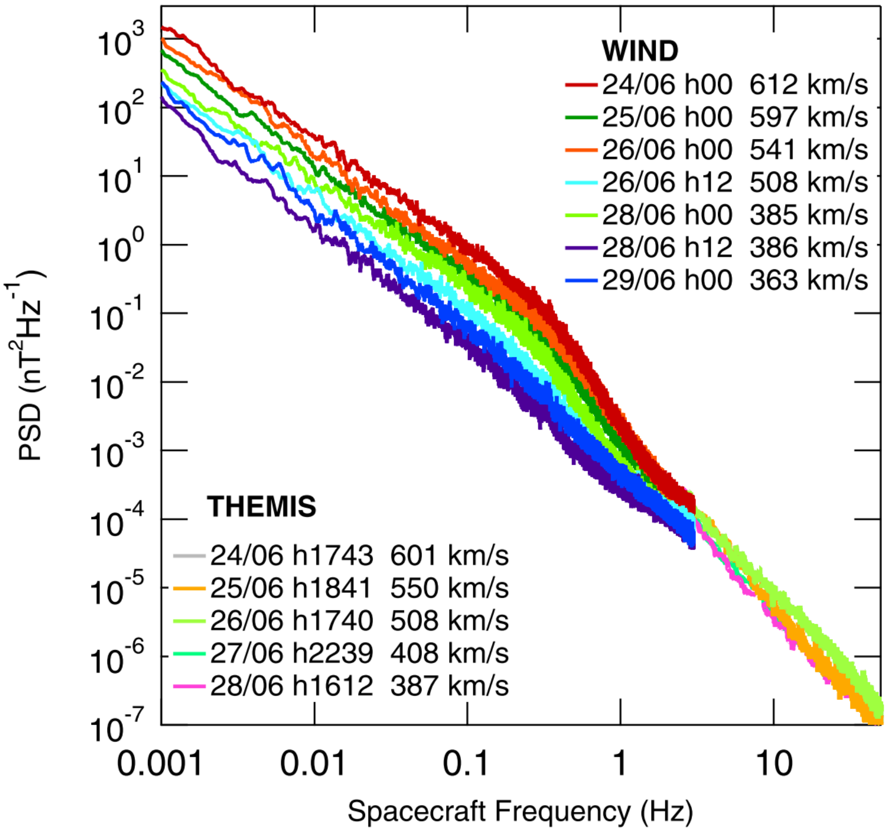

Figure 4.8: Power spectra of magnetic field fluctuations in the solar wind. Data is obtained from *Wind* MFI and *THEMIS-C* search-coil instruments for streams with different speeds, highlighting the variable nature of the spectra at ion-kinetic scales. Figure from Bruno et al. [2014].

where the power spectrum exhibits another transition [Alexandrova et al., 2009, 2012; Sahraoui et al., 2009, 2010]. I show in Figure 4.9, example magnetic field power spectra from the large to electron-kinetic scales from Alexandrova et al. [2009] and Sahraoui et al. [2009]. At sub-ion scales ($3 \lesssim f \lesssim 30$ Hz), the power-law of the magnetic field spectrum is less variable and has a spectral index close to -2.8 [e.g., Leamon et al., 1998b; Alexandrova et al., 2009, 2012; Kiyani et al., 2009; Sahraoui et al., 2009, 2010; Chen et al., 2010a]. This spectral slope seems to be independent of the local plasma parameters at quasi-perpendicular angles between the solar wind flow and the magnetic field, $\theta_{vB} \sim 90^\circ$, sampling oblique fluctuations [Alexandrova et al., 2009, 2012]. The less variable nature of this sub-ion range suggests that there is a small-scale inertial range or an electron-inertial range, in analogy with the inertial range.

The transition range could then be the scales where dissipation at ion-kinetic scales occurs, before the rest of the energy in the cascade continues towards smaller scales. At electron-kinetic scales, Alexandrova et al. [2012] found that magnetic field spectrum deviates from a power-law and instead, closely follows an exponential decrease as a function of the electron gyro-radius:

$$E\left(k_{\perp}\right) = E_0 k_{\perp}^{-8/3} \exp\left(-k_{\perp}\rho_e\right), \tag{4.2}$$

where E_0 is the amplitude of the spectrum, which is dependent on solar wind plasma parameters [Alexandrova et al., 2011]. This result is independent of solar wind properties including wind speed, β_i and β_e, highlighting the universality of the cascade at electron scales. This exponential decrease is compatible with damping at electron scales [Alexandrova et al., 2009; Smith et al., 2012], in analogy with the dissipation of hydrodynamic turbulence. An alternative description by Sahraoui et al. [2010] consists of two power-laws separated by a break. Few studies have investigated physical processes ongoing at such small scales (high frequencies) in the solar wind, due to the limitations of instrument resolution and also the low amplitude of the fluctuations at these scales, which is close to the noise-floor of these instruments. There are still many open questions about what happens to the cascade at these scales, although these are outside the scope of this thesis. Instead, I focus on the processes ongoing at ion-kinetic scales, where more data are available, and these limitations are not as restrictive.

4.3.1 The Spectral Break at Ion-kinetic Scales

The steepening in the magnetic field power spectrum occurs close to the characteristic proton scales, d_p and ρ_p, where the fluid picture given by MHD breaks down, and it is necessary to take into account kinetic effects of the individual particles. At these ion-kinetic scales, dissipative [e.g., Sahraoui et al., 2010] and dispersive[1] [e.g., Kiyani et al., 2013] effects become important (see Section

---

[1] frequency dispersion is caused by waves travelling with different v_{ph} for different $\mathbf{k}$

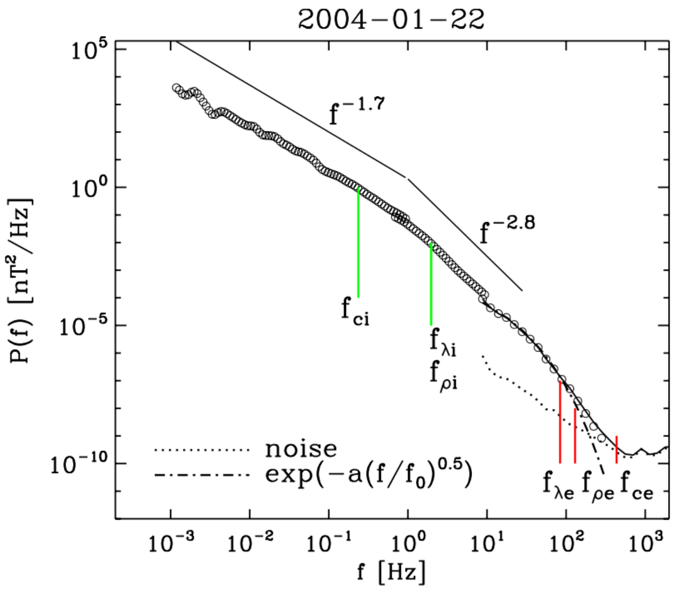

(a) Magnetic field spectrum from a solar wind interval measured by *Cluster* FGM (up to 1 Hz), STAFF-SC (up to 10 Hz), and STAFF-SA ($f \geq 8$ Hz). Solid line: initial spectrum, open circles: spectrum after the noise subtraction. Vertical bars indicate plasma kinetic scales, Doppler-shifted using Taylor's hypothesis. The dash-dotted line indicates exponential fit $\sim \exp[-a(f/f_0)^{0.5}]$, with $f_0 = f_{\rho e}$ and $a \simeq 9$. Figure from Alexandrova et al. [2009].

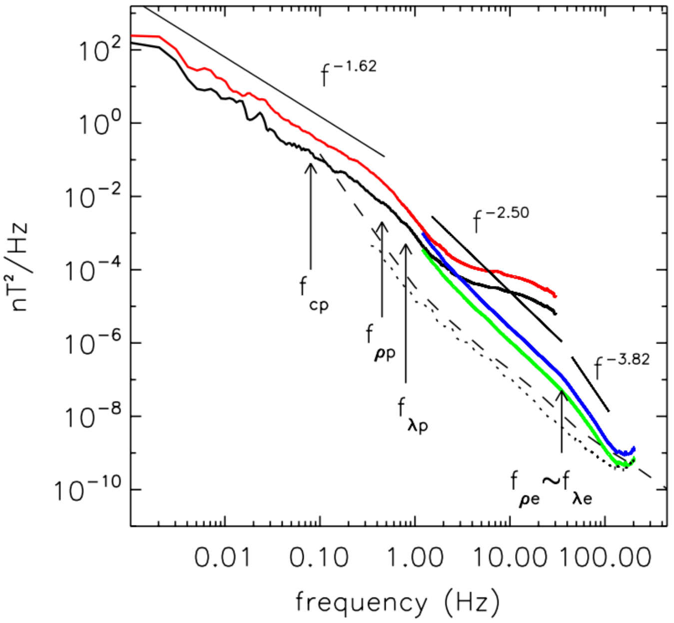

(b) Parallel (black) and perpendicular (red) magnetic spectra from *Cluster* FGM and STAFF-SC (respectively, green and blue). The STAFF-SC noise level as measured in the laboratory and in-flight are plotted as dashed and dotted lines, respectively. The straight black lines are power-law fits to the spectra. The arrows indicate plasma kinetic scales, Doppler-shifted using Taylor's hypothesis. Figure from Sahraoui et al. [2009].

Figure 4.9: Example magnetic field spectra at kinetic scales in the solar wind.

3.6), and energy can be transferred between electromagnetic fluctuations and the plasma particles via wave-particle resonances, and reconnecting magnetic fields. In addition, instabilities can also be driven at these scales [see Section 4.2; Matteini et al., 2012; Klein & Howes, 2015].

The physics of the transition range is still relatively unknown and hotly debated. Therefore, understanding the spectrum at ion-kinetic scales is crucial in order to understand turbulence and heating in collisionless plasmas. There are many important open questions about which processes transport energy through the transition range and how they affect the properties of the plasma. Several different characteristic plasma scales have been suggested to correspond to the spectral break at ion-kinetic scales. Each scale is associated with different plasma processes that can help reveal which mechanisms are relevant for the changing physical processes of the cascade and damping of the fluctuations at these scales.

The transition from incompressible MHD to Hall MHD (see Section 2.5.5) occurs at $kd_p \sim 1$ and can explain the observed spectral steepening without invoking dissipation [Galtier, 2006; Galtier & Buchlin, 2007; Servidio et al., 2007; Matthaeus et al., 2008, 2010]. Hall MHD includes wave dispersion effects, modifying the non-linear interactions between different eddies by speeding up energy transfer to smaller scales and generating a cascade of energy beyond ion-kinetic scales [Alexandrova et al., 2008]. The proton inertial length, d_p, is also relevant for 2D turbulence dissipation, which occurs through reconnection of current sheets generated along the magnetic field direction from strong transverse field fluctuations. These small-scale structures have length $\sim d_p$ and strongly interact with protons across induced electric fields, exchanging energy with the particles [Leamon et al., 2000; Dmitruk et al., 2004]. Alternatively, the proton gyro-radius, ρ_p, has been proposed for the transition between Alfvénic and kinetic Alfvén turbulence at $k_\perp \rho_p \sim 1$ [Schekochihin et al., 2009; Boldyrev & Perez, 2012], where KAW-like fluctuations propagating at large angles oblique to the local mean-field (see Section 2.6.3) can Landau damp

[Leamon et al., 1998b, 1999; Howes et al., 2008].

Another explanation is that the spectral break occurs when the frequency in the spacecraft frame is of the order of the ion-cyclotron frequency, $f_{sc} \sim \Omega_p/2\pi$ [Coleman, 1968; Marsch et al., 1982a; Denskat et al., 1983; Goldstein et al., 1994; Marsch et al., 2003; Gary & Borovsky, 2004; Smith et al., 2012]. At these frequencies, circularly polarised parallel propagating waves can undergo cyclotron resonance with protons. Leamon et al. [1998b] proposed a wave-number, k_c, for the onset of cyclotron damping of Alfvén waves [see also Gary, 1999]. I provide the derivation of k_c in Appendix B. The waves do not necessarily need to be parallel propagating for resonance to occur; as long as there is a large enough $k_\parallel$ component, a wave can resonate with the proton population, even if it has a significant $k_\perp$ component. If there is a significant population of AIC waves in the solar wind, then k_c may coincide with the observed spectral break.

Several past studies have explored the physical processes behind the observed spectral steepening by comparing characteristic ion scales with the spectral break measured from *in-situ* data. Leamon et al. [1998b] first studied 33 intervals using *Wind*, finding the correlation of the break with k_c to be poor. They also found that up to 90% of the energy in the inertial range is carried by waves propagating at highly oblique angles to $\mathbf{B}_0$ than parallel-propagating Alfvénic fluctuations, consistent with the findings of 20% slab ($k_\perp \simeq 0$) and 80% 2D ($k_\parallel \simeq 0$) turbulence by Bieber et al. [1996]. In the dissipation range, they found their energy is roughly equal (about 50%) for both, indicating preferential dissipation of oblique structures. They concluded that cyclotron damping of the slab component alone could not fully account for dissipation at these scales.

In subsequent studies, Leamon et al. [1998a, 1999] proposed that dissipation of the turbulent cascade at ion-kinetic scales is a balance between equally important cyclotron-resonant and non-cyclotron-resonant processes, the latter of which likely operates best at highly oblique angles. They suggested that

KAWs, which would constitute part of the turbulence at highly oblique angles, may be damped by processes such as Landau damping, which would result in a break at ρ_p. An additional study by Leamon et al. [2000] repeated some of the analysis of Leamon et al. [1998b] comparing the break with the gyro-frequency and cyclotron resonant wave-number as before, but this time also including the inertial length, to determine if quasi-2D current sheets are responsible for dissipation at oblique wave-vectors. For oblique propagation, they found the best correlation for d_p, although they again do not rule out cyclotron resonance.

Smith et al. [2001b] studied a two-day period of very tenuous solar wind from 1999 using the *ACE* spacecraft, during which $\beta_p \ll 1$. These conditions allowed for a separation of the gyro-scale and inertial length (from Equation 2.10) and the possibility to determine which may be responsible for the break. They found that the break was at lower frequencies than seen for typical solar wind conditions at 1 AU, consistent with the decreasing inertial length frequency in the spacecraft frame. On the other hand, the Doppler-shifted cyclotron frequency remained roughly constant, and the gyro-radius in the spacecraft frame moved to higher frequencies. It should be noted, however, that as the inertial length was found to be an order of magnitude larger than the gyro-radius, that this result is also consistent with $1/k_c$, which will approximately coincide with d_p in this case (Equation B.3).

A statistical study of 960 spectra conducted by Markovskii et al. [2008] using *ACE* observations at 1 AU compared several theoretical scales to the break. They concluded that the scales alone could not completely account for the observed break, likely due to several processes controlling the behaviour of the turbulence at these scales. Instead, a combination of both scale and fluctuation amplitude at the break scale, $\delta B_b/B$, provided a better correlation, highlighting that the dissipation is intrinsically non-linear. This result, however, is somewhat inconclusive, since all the scales provided a correlation that was only slightly weaker than that of the combination. Markovskii et al. [2008] were only able to conclude on the most likely contribution to the break, and could not rule out the possibility of cyclotron damping or steepening due to the Hall effect. Ion instabilities can also contribute to $\delta B_b/B$ when the ion temperature anisotropy is large enough [Bale et al., 2009].

Perri et al. [2010] took an alternative approach and studied the radial dependence of the break frequency, f_b, using several time intervals of high-speed streams from *Ulysses* in the outer heliosphere and magnetic field data from *Messenger* between 0.3-0.5 AU. However, they could not determine local solar wind conditions for the latter intervals due to the lack of plasma observations from *Messenger*. They found that the break frequency was independent of distance between 0.3-4.9 AU, in contradiction to the radial dependence of ρ_p, d_p, and the Doppler-shifted Ω_p. Typical large variations in solar wind parameters in the inner heliosphere likely meant that only intervals of fast wind were not studied using the *Messenger* data. They concluded that the observed break could be caused by a combination of different physical processes or associated with a remnant signature of coronal turbulence.

Bourouaine et al. [2012] later conducted a similar study, analysing magnetic field spectra from fast steams measured by *Helios* between 0.3-0.9 AU, again finding that f_b remained almost constant (between 0.2-0.4 Hz) while d_p and ρ_p varied with distance. However, they did conclude that by assuming a dominant 2D nature ($k_\perp \gg k_\parallel$) of the turbulent fluctuations, i.e., $2\pi f = k v_{sw} \sin\theta_{vB} \cos\phi_k$, where ϕ_k is the angle between $\mathbf{k}$ and its projection in the $\mathbf{v}_{sw}$-$\mathbf{B}$ plane[2], there was a better agreement between the break frequency and d_p than the ρ_p, relating to the Hall effect or the formation of current sheets, which heat ions through reconnection. This result is consistent with Leamon et al. [2000] at 1 AU. Both results do not rule out the possibility of damping of parallel fluctuations via cyclotron resonance, even if the break is attributed to processes governing the evolution of 2D turbulence.

More recently, Bruno & Trenchi [2014] used higher resolution data from high-speed streams using *Messenger*, *Wind* and *Ulysses* to show that the break

---

[2] This is obtained from $2\pi f = k v_{sw} \cos\theta_{kv}$, for fluctuations with $k_\perp \gg k_\parallel$.

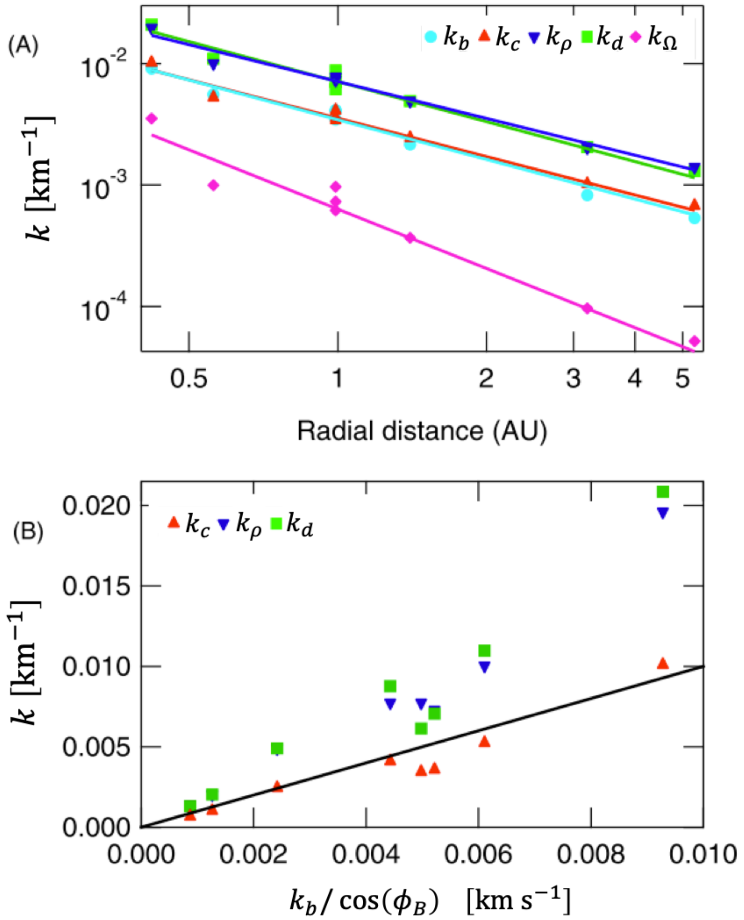

Figure 4.10: (a) The radial behaviour of the wave-numbers associated with the spectral break, k_b, proton inertial length, k_d, proton gyro-radius, k_ρ, cyclotron resonance wave-number, k_c, and proton gyro-frequency, k_Ω, converted using Taylor's hypothesis. Lines of best fit are also shown. (b) The wave-numbers, k_c, k_ρ, and k_d, as a function of $k_b/\cos\phi_B$. Figure from Bruno & Trenchi [2014].

wave-number has a radial dependence, decreasing almost linearly ($k_b \sim R^{-1.09}$) with distance from 0.42-5.3 AU. The difference of this result to previous studies likely arises from the use of radial alignments between pairs of spacecraft to estimate solar wind parameters at *Messenger* and study the same solar wind stream as it moves throughout the heliosphere. They found the best correlation with k_c, as seen in Figure 4.10, as well as smaller correlations with $1/\rho_p$ and $1/d_p$. This correlation remained even when accounting for the angle between wave propagation and sampling directions, $\cos\phi_B$, and so the authors concluded that cyclotron damping occurs at ion-kinetic scales.

Chen et al. [2014] expanded on the study by Smith et al. [2001b], using several intervals of *Wind* data where $\beta_{p,\perp} \ll 1$ and $\beta_{p,\perp} \gg 1$. They found that the break coincided with the larger of the two scales, the inertial length for small $\beta_{p,\perp}$ and gyro-radius for large $\beta_{p,\perp}$. This result was not significantly different when accounting for a factor of $\sin\theta_{vB}$ for the different angles between the magnetic field and solar wind flow, for highly anisotropic turbulence. They conclude that the break at ρ_p for high beta intervals is consistent with the dispersion of Alfvén waves at the transition to KAW turbulence. However, the break at d_p for low $\beta_{p,\perp}$ intervals is not consistent with this explanation, and they concluded that it could be due to cyclotron damping, electron Landau damping or current sheets for highly anisotropic turbulence. They suggest that the break at low $\beta_{p,\perp}$ may be due to some non-linear process such as anomalous resistivity, or that the turbulence may have a significant $k_{\|}$ component in the low beta intervals [see also Boldyrev et al., 2015].

All of these studies have produced different conclusions, and there is currently no consensus on the dominant dissipation mechanism that is responsible for the observed spectral break. One of the difficulties with these studies is that the solar wind at 1 AU typically has $\beta_{p,\perp} \sim 1$, so the measured spacecraft-frame frequencies of d_p and ρ_p are approximately equal due to Equation 2.10. Therefore, these two scales can only be clearly separated when $\beta_{p,\perp} \ll 1$ or $\beta_{p,\perp} \gg 1$. It may be that multiple mechanisms are ongoing under different solar wind conditions, and the break occurs at the larger of the two scales. However, when $\beta_{p,\perp} \ll 1$ or $\beta_{p,\perp} \gg 1$, Equation B.3 results in the resonant scale coinciding with the larger of d_p or ρ_p. Therefore, it can also be argued that k_c is consistent with the results of these studies. On the other hand, it may not be appropriate to simply compare the spectral break to just a characteristic plasma scale due to the non-linear nature of the turbulence. The break scale may also be dependent on the amplitude of power.

It is important to note that the magnetic field power spectrum of shows all fluctuations at a specific scale in the solar wind, including the turbulence and those driven by instabilities. The injection of energy at ion-kinetic scales by instabilities may lead to a ‘bump’ in the power spectrum that may artificially cause a steepening that is not directly related to the turbulent cascade. Therefore, care should be taken when interpreting such power spectra. There are also several technical challenges with measuring the spectral break. At these frequencies, the amplitude of the fluctuations is small so that the power spectrum approaches the noise-floor of the magnetometer. At the same time, is the break a clear transition between two power-laws or is it more of a gradual transition? Averaging over long timescales will lead to a blurring of different plasma conditions, making it more difficult to determine if a gradual transition due to this averaging or a physical effect. In the latter case, it may not be appropriate to associate a single frequency as the spectral break. These limitations make a statistical study of many spectra difficult, limiting the scope for exploring under which conditions different proton scales best correspond to the break scale.

4.3.2 The Nature of Fluctuations at Ion-kinetic Scales

The studies investigating the spectral steepening at ion-kinetic scales show that just comparing characteristic proton scales with the spectral break is insufficient to probe what processes are ongoing at these scales. However, exploring the properties of the fluctuations at these scales can help constrain possible theories for dissipation of the turbulence and the plasma conditions where different mechanisms occur. For example, the anisotropy of fluctuations at these scales, i.e., whether they are parallel ($k_\parallel \gg k_\perp$), isotropic ($k_\parallel \sim k_\perp$) or perpendicular ($k_\perp \gg k_\parallel$) fluctuations, can be a useful diagnostic to narrow down the possibilities.

While the fluctuations in the inertial range are predominantly Alfvénic [e.g., Belcher & Davis Jr., 1971], the plasma modes which exist in the transition range and at sub-ion scales are more complex. Like the inertial range, the transition range is characterised by magnetic fluctuations with quasi-perpendicular wave-vectors, $k_\perp \gg k_\parallel$ [Sahraoui et al., 2010; Narita et al., 2011; Roberts et al., 2013]. The two perpendicular electromagnetic waves that can exist in a $\beta \sim 1$ plasma for $1/\rho_i \ll k_\perp \ll 1/\rho_e$ are the KAW and the oblique whistler wave [Gary & Smith, 2009; TenBarge et al., 2012; Boldyrev et al., 2013, see also, Sections 2.6.3 and 2.6.4]. Therefore, either strong whistler or kinetic Alfvén turbulence should take over at sub-ion scales [Cho & Lazarian, 2004; Schekochihin et al., 2009; Chen et al., 2010b; Boldyrev & Perez, 2012; Salem et al., 2012]. This prediction is consistent with an increase in magnetic compressibility, $\delta B_\|^2/\delta B^2$, in the transition range [Leamon et al., 1998b; Alexandrova et al., 2008; Hamilton et al., 2008; Turner et al., 2011; Salem et al., 2012; Kiyani et al., 2013]. While $\delta B_\|^2/\delta B^2$ in the inertial range is only about 5%, it can reach 30% at ion-kinetic scales and show a dependence on β_p [Alexandrova et al., 2008; Hamilton et al., 2008]. This increase in can also explain the variation of the spectral index in the transition range [Alexandrova et al., 2007, 2008].

The lack of fast mode fluctuations in the inertial range suggests that there can be little transfer of energy to whistler turbulence at sub-ion scales [Howes et al., 2012]. Sahraoui et al. [2010] find that the fluctuations at ion-kinetic scales have a plasma-frame frequency close to zero, consistent with KAW turbulence. However, Narita et al. [2011] found no clear dispersion relation for KAWs (see Equation 2.61). Despite this, the turbulent fluctuations are non-linear, and so, the dispersion relation of these fluctuations is unlikely to reproduce the result from linear Vlasov theory. These fluctuations can also arise from non-propagating coherent structures like current sheets, filaments and shocks [Rezeau et al., 1993; Veltri et al., 2005; Greco et al., 2010; Perri et al., 2012], or Alfvén vortices propagating with a phase speed close to zero in the plasma-frame [Alexandrova et al., 2006; Alexandrova & Saur, 2008; Alexandrova et al., 2008]. Roberts et al. [2013] recently showed using *Cluster* observations in the fast solar wind that the transition range is likely populated with both KAWs and Alfvén vortices, which is consistent with the findings of Chen et al. [2010a] and Turner et al. [2011] that the turbulence remains anisotropic at sub-ion scales (see also, Section 3.5.4).

Several studies [Chen et al., 2012b; Šafránková et al., 2013, 2015] have measured the spectrum of density fluctuations at ion-kinetic and sub-ion scales, finding that the spectral index shallows from $f^{-5/3}$ to about f^{-1} in the same range of frequencies associated with the increase in magnetic compressibility, and then eventually steepens to -2.8. The close agreement between the magnetic field and density spectra at sub-ion scales is consistent with the transition between MHD Alfvénic and small-scale kinetic Alfvén turbulence [Chandran et al., 2009; Chen et al., 2013c; Šafránková et al., 2013], where the two fields are coupled [Schekochihin et al., 2009; Boldyrev et al., 2013]. The flattening of the density spectrum at ion-kinetic scales can then be explained by the kinetic Alfvén component at small scales taking over from the compressive non-Alfvénic component at larger scales [Harmon & Coles, 2005; Chandran et al., 2009; Chen et al., 2013a]. Chen et al. [2013b] develop a method to distinguish between KAW and whistler turbulence, based on the relative level of density and magnetic field fluctuations:

$$\delta\hat{n} = \sqrt{\frac{\beta_i}{2}\left(1+\frac{T_e}{T_i}\right)\left[1+\frac{\beta_i}{2}\left(1+\frac{T_e}{T_i}\right)\right]}\,\frac{\delta n}{n_0}, \quad \delta\hat{\mathbf{B}} = \frac{\delta\mathbf{B}}{B_0}. \tag{4.3}$$

In this normalisation, the ratio, $r_{KAW} = \delta\hat{n}^2/\delta\hat{B}_\perp^2$, is $r_{KAW} = 1$ for a KAW and $r_{KAW} \ll 1$ for an oblique whistler wave. In Figure 4.11, I show an example of $\delta\hat{n}$ and $\delta\hat{\mathbf{B}}$ spectra in the solar wind from Chen et al. [2013b]. The two spectra have the same amplitude and slope, consistent with $r_{KAW} \sim 1$. This suggests that the turbulence is predominantly kinetic Alfvén in nature, with whistler fluctuations making up only a small fraction, consistent with the transition from Alfvénic turbulence at larger scales. The average ratio in the solar wind is $r_{KAW} = 0.75$, similar to simulations of KAW turbulence [Chen et al., 2013b].

Despite the evidence for KAW turbulence, the spectral index of -2.8 is steeper than the cascade prediction of -7/3 for strong KAW turbulence [Schekochihin et al., 2009]. Several explanations have been proposed to explain this steeper scaling. Alexandrova et al. [2007] propose that it is due to a compressibility effect, whereas Howes et al. [2011] observed a -2.8 scaling in the

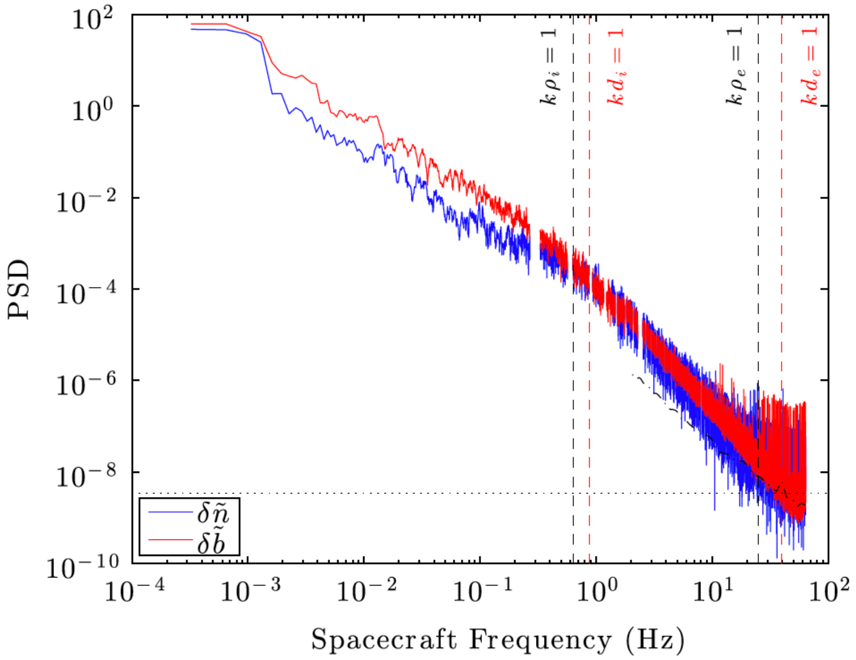

Figure 4.11: Spectra of density $\delta\hat{n}$ and magnetic fluctuations $\delta\hat{\mathbf{B}}$, normalised according to Equation 4.3. The vertical dashed lines correspond to the ion and electron gyro-radii and inertial length scales under the assumption of Taylor's hypothesis. Figure from Chen et al. [2013b].

magnetic spectrum from gyro-kinetic simulations, interpreting the steepening as due to the presence of electron Landau damping. However, the steeper spectrum has also been observed in simulations that do not contain such damping [Boldyrev & Perez, 2012; Franci et al., 2015]. Instead, Boldyrev & Perez [2012] suggest that the concentration of the cascade into 2D structures would lead to a steeper -8/3 spectrum that is closer to the observed value of -2.8. Other explanations have also been proposed [Galtier et al., 2005; Rudakov et al., 2011; Meyrand & Galtier, 2013; Passot & Sulem, 2015; Kobayashi et al., 2017]. It has not yet been determined which combination of these, or other possibilities, are responsible for the steeper than predicted spectra at sub-ion scales.

The polarisation properties of the fluctuations can also reveal more information about which type of modes exist at ion-kinetic scales. Magnetic helicity (see Section 3.7.4) is a useful parameter that gives the polarisation properties of magnetic field fluctuations at different scales. Matthaeus & Goldstein

[1982a] first studied magnetic helicity spectra in the solar wind, using *Voyager* observations between 1-5 AU. They found that in the inertial range, the helicity randomly oscillates between negative and positive values, leading to no overall dominant handedness. Later, Goldstein et al. [1994] studied helicity signatures in the inertial and transition ranges, confirming the findings of Matthaeus & Goldstein [1982a] at low frequencies and concluding that the fluctuations contributing to the helicity at these scales are likely quasi-2D with minimum variance along the local mean-field. In contrast, at ion-kinetic scales they found that a coherent[3] helicity signature appears, suggesting that for anti-sunward propagating fluctuations, they are right-handed. This result can be interpreted as a signature of the damping of left-handed Alfvén waves by cyclotron resonance at frequencies close to Ω_p. However, Howes & Quataert [2010] show that right-handed KAWs alone can also reproduce the observed helicity signature without the need for cyclotron resonance.

Several studies [Leamon et al., 1998b; Hamilton et al., 2008; Brandenburg et al., 2011; Markovskii et al., 2015] also looked at the polarisation of magnetic fluctuations beyond the spectral break, finding a right-handed signature, which they attributed to KAWs. These studies all used Fourier analysis techniques and a global mean magnetic field. More sophisticated methods have recently been employed to investigate the nature of fluctuations at ion kinetic scales and close to the spectral break [He et al., 2011, 2012b,a; Podesta & Gary, 2011b; Klein et al., 2014]. These studies used wavelet transforms and a local mean-field to calculate the normalised magnetic helicity [see Telloni et al., 2012, and references therein], in particular, the technique first developed by Horbury et al. [2008]. This method allows investigation of the polarisation of fluctuations for different angles between the plasma flow and local mean-field orientation, θ_{vB}.

He et al. [2011, 2012a,b] used *STEREO* measurements to find signatures consistent with right-handed KAWs or whistler waves propagating at large

---

[3] A coherent helicity signature has $\sigma_m > 0$ over a range of frequencies.

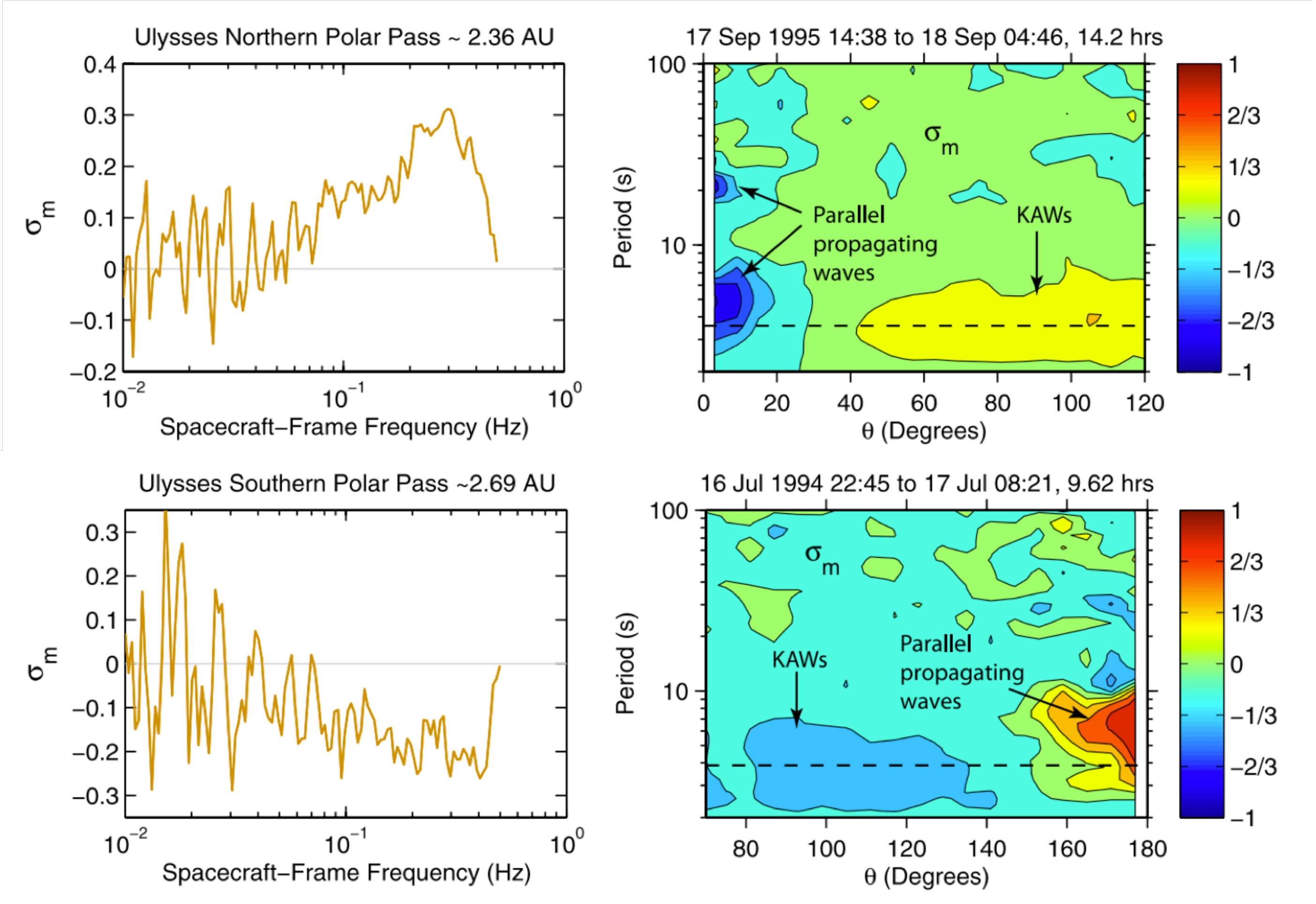

Figure 4.12: Top left: Reduced magnetic helicity spectrum, σ_m, and Top Right: the same helicity spectrum for an outward sector as a function of θ_{vB} using a local mean-field, where the colour bar is σ_m. Bottom Left and Right: same plots for an inward sector showing the reversal in the sign of σ_m. The dashed line in the right plots indicates $k\rho_p = 1$. Figure adapted from Podesta & Gary [2011b].

angles to the local mean-field, as well as left-handed AIC waves propagating quasi-(anti)parallel to the local mean-field, $\mathbf{B}_0$. Several studies have also shown the presence of parallel-propagating AIC waves in the solar wind [Jian et al., 2009, 2010, 2014; Gary et al., 2015]. The helicity signature for each population changes sign for outward and inward fields due to the solar wind sector structure. Outside the range of frequencies, 0.1-1 Hz, the magnetic helicity was generally zero. Podesta & Gary [2011b] confirmed this result using *Ulysses* observations (see Figure 4.12), suggesting that the left-handed signature could also arise from sunward propagating FMW waves since the Doppler shift of these waves makes it difficult to determine the direction of propagation. The proton temperature anisotropy can lead to the driving of these AIC and FMW waves (see Sections 2.7), and Podesta & Gary [2011a] show that the α-particle drift in the solar wind could lead to a preferential driving of these waves that is consistent with this left-handed helicity signature. Klein et al. [2014] later compared observations from *Ulysses* with a model to conclude that the left-handed component is due to a non-turbulent population of AIC or FMW waves.

Telloni et al. [2015] expanded on the work of Bruno & Trenchi [2014], analysing the properties and radial evolution (0.56-0.99 AU) of the high-frequency magnetic fluctuations beyond the spectral break, using radial alignments between *Messenger* and *Wind* of a high-speed stream. They also found the presence of both quasi-parallel left-handed and quasi-perpendicular right-handed fluctuations that they attributed to AIC waves and KAWs, respectively, in agreement with previous studies. In particular, they found that the low-frequency limit of these fluctuations coincides with k_c, indicating the possible role of cyclotron resonance in the steepening of the spectrum. They also found that the inertial length and gyro-radius were situated near the peaks of the two signatures. Bruno & Telloni [2015] showed that within a high-speed stream, the right-hand polarised fluctuations are characterised by larger power and magnetic compressibility than the left-handed fluctuations.

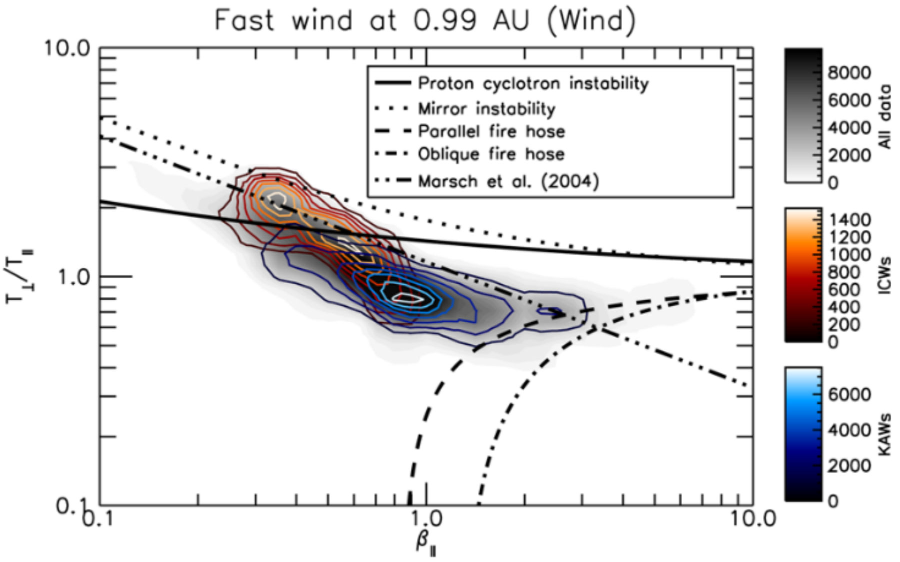

Figure 4.13: Data distribution in $\beta_{p,\|}$-$T_{p,\perp}/T_{p,\|}$ parameter space of KAWs (blue) and AIC waves (red) identified from a single fast stream measured by the *Wind* spacecraft. Included are contours of constant maximum growth rate for the four proton temperature anisotropy instabilities. Figure from Telloni & Bruno [2016].

This result favours the interpretation of AIC waves for the latter component. They also showed that moving from fast to slow wind during the same stream, the spectral slope past the break shallows and the left-handed signature is quickly depleted. They concluded that the right-hand component dominated the left-hand one, producing the net magnetic helicity signature first observed by Goldstein et al. [1994].

Telloni & Bruno [2016] studied the same high-speed stream as Bruno & Telloni [2015] and found that the two polarisation signatures are associated with different plasma stability conditions shown in Figure 4.13, as expected for both AIC waves and KAWs. They find that AIC waves are associated with fluctuations with strong Alfvénic character, while KAWs are associated with fluctuations with a high degree of cross-helicity but dominated by an excess of magnetic over kinetic energy. They suggest that the presence of AIC waves is a direct consequence of the Alfvénic fluctuations present in the inertial range. However, they do not find a correlation between the presence of AIC waves and higher total plasma temperature. While this does not rule out heating by cyclotron resonance, it shows that this mechanism is not the most dominant, at least during the period studied. It may be that the AIC waves arise from instabilities and are not part of the turbulence, which is consistent with k_c. They did find a higher temperature associated with KAWs, which carry more power. They conclude that when the oblique component in the inertial range is dominant, KAWs play a significant role at ion-kinetic scales.

The studies reviewed here have investigated the nature of the fluctuations at ion-kinetic scales in the solar wind using their anisotropy and polarisation properties. The anisotropy of the turbulence cascade supports the transition from Alfvénic fluctuations to KAW-like fluctuations and structures, with only a small amount of power in whistler fluctuations. This work is further supported by studies of the magnetic helicity, which shows a coherent peak at ion-kinetic scales. This peak can be separated into two components with different polarisation properties using local field analysis: a right-handed signature at quasi-perpendicular angles and left-handed signature at quasi-parallel angles. While the right-handed signature is consistent with the KAW component of the turbulence, the left-handed signature is more difficult to diagnose because only a reduced $\mathbf{k}$ can be measured in the solar wind, leading to an ambiguity in the direction of propagation of these fluctuations. Is this signature produced by instabilities or a component of the turbulence, or both? If these fluctuations are really from instabilities, they should be associated with anisotropic proton temperatures, which to date, has only been shown for one fast stream [Telloni & Bruno, 2016]. By filtering for parallel-propagating fluctuations using helicity, and exploring their link with proton temperature, it may be possible to diagnose these fluctuations more clearly.

One fundamental question that arises from the studies of magnetic helicity at ion-kinetic scales is whether the coherent peak at these scales is physical? Howes & Quataert [2010] show that the right-handed helicity peak becomes coherent and then remains relatively constant towards higher frequencies. However, Vasquez & Markovskii [2012] argue that a peak in the helicity arises from the demagnetisation of protons from the magnetic field, leading to a physical decrease towards sub-ion scales. In this case, the peak would be correlated with d_p, but the few studies that have investigated the correlation between the peak at proton scales find a better relationship with ρ_p, where Alfvénic fluctuations transition to KAWs. At the same time, the noise-floor of instruments may lead to an artificial decrease in the helicity, such that the presence of peak is not a physical feature. Therefore, this feature of the helicity spectrum should be interpreted carefully. From Figure 4.12, the two helicity signatures also peak at different frequencies. This result indicates that they are each associated with different processes and therefore, different plasma conditions. Are the different helicity signatures associated with different power spectra? A detailed statistical study to determine under what conditions these different helicity signatures exist has not yet been undertaken.

4.4 Motivation for Research

While significant progress has been made in understanding solar wind turbulence at small scales in recent years, there are still many aspects which remain to be understood. Despite this, there is mounting observational and theoretical evidence that the turbulent fluctuations at small scales exhibit properties of linear wave modes [Denskat et al., 1983; Goldstein et al., 1994; Ghosh et al., 1996; Biskamp et al., 1996, 1999; Leamon et al., 1998b; Cho & Lazarian, 2004; Bale et al., 2005; Galtier, 2006; Sahraoui et al., 2010, 2012; Howes et al., 2006, 2008, 2012; Schekochihin et al., 2009; Gary & Smith, 2009; Chandran et al., 2009; Chen et al., 2010a, 2013b; Salem et al., 2012; Klein et al., 2012; Boldyrev & Perez, 2012]. These studies point to a cascade of KAW-like fluctuations rather whistler-like fluctuations. The transition between the Alfvénic fluctuations in the inertial range and KAW-like fluctuations in at sub-ion scales occurs at ion-kinetic scales, consistent with the polarisation and anisotropy properties of the fluctuations. At these scales, kinetic instabilities can inject energy into the turbulence, and the turbulent fluctuations can dissipate energy into the particle distributions. This coupling of different processes makes it difficult to determine the mechanisms of energy transport across the transition range and towards smaller scales. How much of the power in the fluctuations measured at ion-kinetic scales are generated by instabilities, rather than driven by the turbulent cascade? How much energy is dissipated at these scales and how much is transported to electron-kinetic scales?

One of the major unsolved problems is how the turbulent energy from the electromagnetic fluctuations is dissipated, leading to heating of the plasma. Several possibilities have been proposed (see Section 3.6), including ion cyclotron damping [e.g., Coleman, 1968; Smith et al., 2012], Landau damping [e.g., Howes et al., 2008; Tenbarge & Howes, 2013], stochastic heating [e.g., Chandran et al., 2010], an entropy cascade [Schekochihin et al., 2009] and reconnection associated mechanisms [e.g., Egedal et al., 2012; Drake & Swisdak, 2014]. Identifying which combinations of these operate and under which conditions, is an important area of current research. Initial studies have found indirect evidence for these mechanisms; for example, He et al. [2015a,b] show evidence for Landau and cyclotron resonance in particle distributions. However, the latter is inconsistent with the anisotropy of solar wind fluctuations. More recently, Chen et al. [2019] used a new technique [Klein & Howes, 2016] to provide the first direct observation of Landau damping of turbulent fluctuations at electron scales. The exact mechanisms behind the dissipation of solar wind fluctuations and resultant plasma heating remain hotly debated.

Many studies have investigated the spectral steepening of the power spectrum of magnetic field fluctuations and the coherent peak in magnetic helicity at ion-kinetic scales separately. However, a combined analysis of both to find evidence of the associated ongoing dissipation mechanisms has yet to be undertaken. A statistical study identifying under what solar wind conditions each process dominates will significantly improve our understanding of solar wind turbulence at these scales. In this thesis, I first investigate the correlation between the spectral break and helicity signature at these scales in Chapter 6, finding that they are linked to the same process. In Chapter 7, I then examine the properties of magnetic fluctuations in more detail using magnetic helicity, separating instabilities from the turbulence. Finally, in Chapter 8, I examine the correlation of properties of the turbulent fluctuations with proton temperature, to investigate if there is any link to plasma heating. In these studies, I undertake detailed, careful analysis of the spectral properties of the fluctuations to ensure they are physical and to avoid the drawbacks of statistical studies discussed in this chapter.

Chapter 5

Instrumentation and Analysis Methods

In-situ spacecraft observations of space plasmas such as the solar wind include high-resolution time series of electromagnetic fields and particle VDFs. While these measurements are restricted to plasma in the vicinity of a spacecraft, statistical studies of an ensemble of measurements can provide insights into how kinetic processes affect large-scale evolution of the plasma. In this chapter, I describe how spacecraft instruments measure plasma properties with specific reference to the *Wind* spacecraft, and the spectral analysis tools I use to investigate solar wind fluctuations.

5.1 The *Wind* Spacecraft

The *Wind* spacecraft was launched in November 1994 [Acuña et al., 1995], forming part of the NASA Global Geospace Science (GGS) programme, taking *in-situ* measurements of the near-Earth space environment. The spacecraft spent its first decade of operation exploring the Earth's magnetosphere before moving permanently to the Lagrange (L1) point in June 2004 to measure the solar wind. The spacecraft is cylindrical and spin-stabilised with its spin axis perpendicular to the ecliptic plane, rotating approximately every 3 s.

The spacecraft has numerous instruments on board that have provided over two decades of high-quality *in-situ* measurements of the near-Earth solar

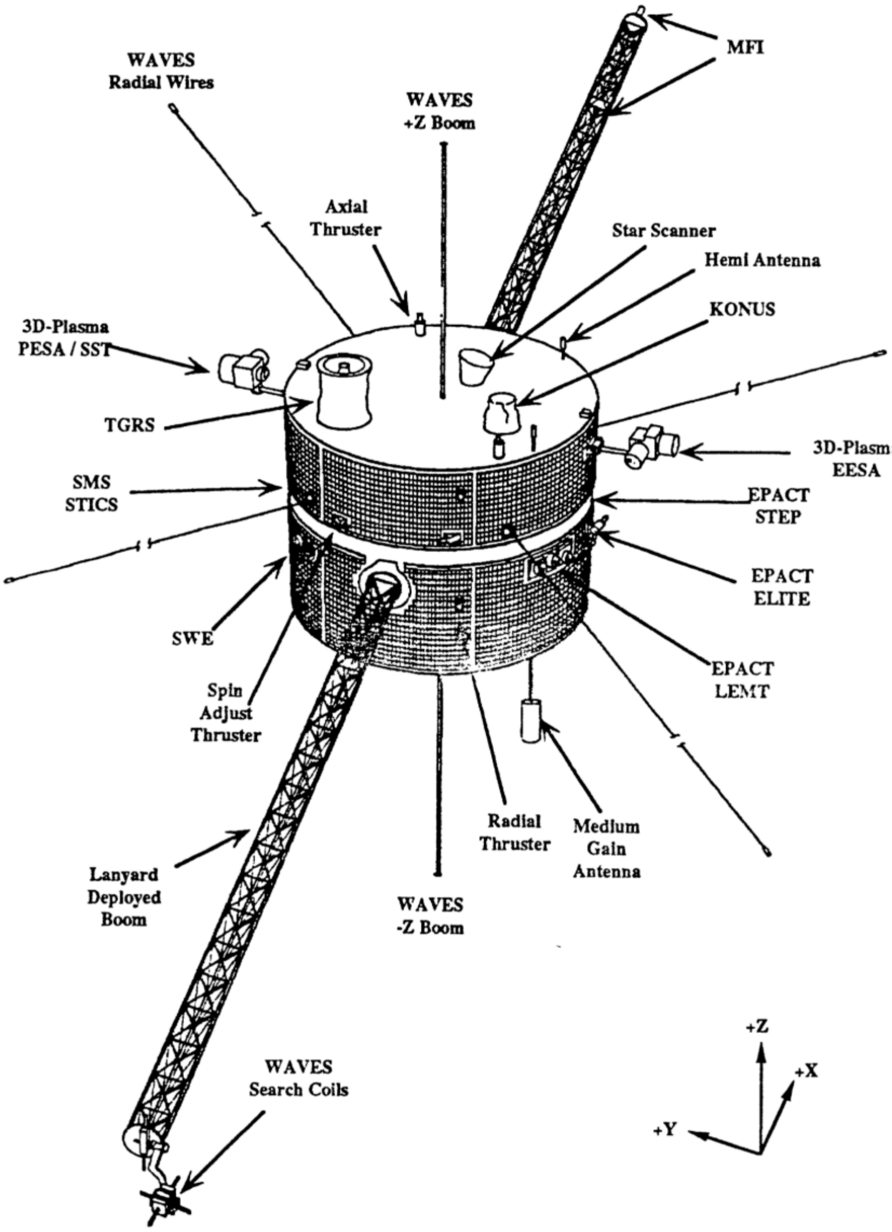

Figure 5.1: Diagram of the *Wind* spacecraft, showing the cylindrical main body, two extended booms and antennae along the spin-axis. Individual instruments onboard are labelled. Image from Harten & Clark [1995].

wind. In Figure 5.1, I show a diagram of the spacecraft with the locations of these instruments from Harten & Clark [1995]. In this thesis, I analyse data from two instruments: the Magnetic Field Investigation (MFI) fluxgate magnetometers [Lepping et al., 1995] providing high-resolution magnetic field measurements, and the Solar Wind Experiment (SWE) Faraday cups [Ogilvie et al., 1995] providing ion moments such as density, velocity and temperatures of protons and α-particles. The following two sections summarise the principles of operation for these instruments and the data produced.

5.2 Magnetic Field Measurements

5.2.1 Fluxgate Magnetometers

A type of magnetometer commonly used onboard spacecraft to measure the magnetic field is the fluxgate magnetometer. A single fluxgate magnetometer can only measure one component of $\mathbf{B}$, and so there are often three sensors configured in an orthogonal formation to measure all three components.

A fluxgate magnetometer takes advantage of the phenomenon of hysteresis in ferromagnetic materials to measure $\mathbf{B}$. Inside a material, $\mathbf{B}$ depends on the auxiliary field, $\mathbf{H}$, that is applied to it and the history of its magnetisation. There exists a critical value $|\mathbf{H}| \geq H_c$ at which the magnetic field saturates at a value, B_s. In a fluxgate magnetometer, a ferromagnetic core is wrapped by two wire coils, a drive coil and a sense coil. The drive coil carries a triangle-wave current, producing an auxiliary field, $H_d(t)$, that has amplitude, H_0, and period, T. The total auxiliary field of the core is then:

$$H(t) = H_d(t) + \Delta H_z, \tag{5.1}$$

where ΔH_z is the contribution from the external magnetic field that the magnetometer is to measure and the z-direction is along the core axis, i.e., the direction along which the component of $\mathbf{B}$ is measured. The auxiliary field generated by the drive coil has an amplitude large enough that the core experiences both negative and positive saturation during one period, i.e., a hysteresis curve. Hence, $B(t)$ in the core will have a truncated triangle wave-form. From Faraday's law, the voltage driven in the sense coil due to the core will, therefore, vary in time:

$$V_s(t) = -\frac{N_s A}{c}\frac{dB}{dt}, \tag{5.2}$$

where N_s is the number of turns in the sense coil, and A is the cross-sectional area of the core. If $\Delta H_z > 0$ then $B(t)$ will be saturated for different lengths of time during negative and positive saturation. Due to this offset, $V_s(t)$ will vary as an irregular square wave with a pulse duration of αT and time between successive positive and negative pulses of βT, where $\alpha = H_c/4H_0$ and $\beta = 1/2\,(1-\Delta H/H_0)$. Since H_0 is large, typically $\alpha \ll 1$ and $\beta \ll 1$. The Fourier series expansion of the sense coil voltage is [Ness, 1970]:

$$V_s(t) = -\frac{2N_s AB_s}{c\alpha T}\sum_{k=1}^{\infty}\left(1-\exp\left[-2\pi i\beta k\right]\right)\frac{\sin\left(\pi\alpha k\right)}{\pi k}\cos\left(\frac{2\pi kt}{T}\right). \tag{5.3}$$

For no external magnetic field, the even harmonics (i.e., $k = 2, 4, 6, ...$) vanish since β and thus ΔH are zero. Therefore, the second harmonic is typically used to determine β, and therefore, B_z from ΔH_z.

5.2.2 Magnetic Field Investigation

The MFI suite [Lepping et al., 1995] on *Wind* consists of a dual triaxial fluxgate magnetometer system to measure the full vector magnetic field, **B**. The outer magnetometer set-up is mounted at the end of a 12 m boom while the inner unit is located approximately halfway along the boom. Each sensor assembly consists of an orthogonal arrangement of three ring-core fluxgate sensors plus additional elements for thermal control. This dual configuration allows the real-time estimation and subtraction of the spacecraft-generated magnetic field in order to obtain a more accurate ambient field.

The magnetometer cores are driven cyclically to saturation by a 15 kHz signal from the MFI data processing unit (DPU). When an external field is present, a signal containing only even harmonics of the drive frequency appears at the output of the sensors. After amplification and filtering, the signal is used to generate a current proportional to the magnitude of the applied field. This current is fed-back to the sensor to negate the effective magnetic field seen by the core. The output of a single-axis magnetometer is then a voltage proportional to the magnitude of the ambient magnetic field along the direction of the sensor axis. The triaxial configuration produces three output voltages proportional to the orthogonal components of the ambient magnetic field.

The two magnetometers feature eight discrete logarithmically-spaced dynamic ranges of ±4 nT to ±65,536 nT, with respective resolutions of ±0.001 to ±16 nT, increasing with each range by a multiple of 4. The default range, which is most applicable to typical solar wind conditions, is ±16 nT, with a respective resolution of ±0.004 nT. The range can be changed automatically if the magnitude of the measured signals exceeds 87.5% of the maximum value of the range, or if it drops below 12.5% of the maximum value. This process avoids the loss of measurements due to the saturation of the magnetic field and ensures proper resolution for low amplitude fields. The magnetometers measure the vector magnetic field with a default resolution of 44 Hz. However, due to telemetry constraints, the data are averaged and compressed onboard before transmission to the ground at a downsampled resolution of 10.87 Hz. I use these high-resolution measurements to determine the spectra of magnetic field fluctuations in this thesis. The onboard downsampling does lead to some aliasing of the signal (see Section 5.4.1) and the noise-floor of the instrument is also important to consider when investigating high-frequency fluctuations in the magnetic field. I discuss these limitations in more detail in Chapter 6.

5.3 Particle Measurements

5.3.1 Faraday Cups

Faraday cup (FC) instruments are commonly used in spacecraft missions to measure particle velocity distributions in different space plasma environments.

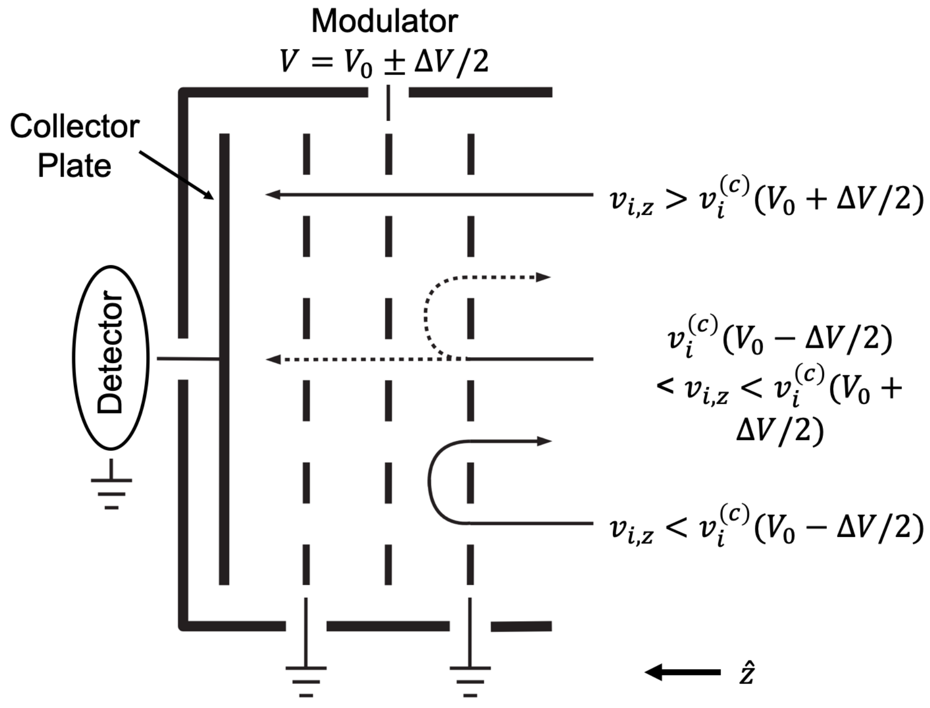

Figure 5.2: Schematic cross-section of a Faraday cup consisting of a metal cup with a collector plate and three mesh grids. An external voltage is applied to the middle modulator grid to differentiate between particle species and energies. The cup is orientated along the $-\hat{\mathbf{z}}$ direction. Image adapted from Maruca & Kasper [2013].

I show a typical FC from Maruca & Kasper [2013] in Figure 5.2, with a look direction orientated along $-\hat{\mathbf{z}}$. It consists of a grounded metal cup with an opening that allows particles to pass through and collide with a collector plate. This aperture is wide enough to allow incoming particles from a broad range of directions or angles of incidence. The particles collide with the metal collector plate to create a current, I, which is measured by an ammeter. This measured current represents the net charge flux from the incoming particles.

Multiple mesh wire grids are placed between the collecting plate and the aperture to differentiate between particle species and energies. Figure 5.2 shows three grids; the outer two are electronically grounded, whereas the middle grid, called the modulator, is connected to an external voltage, V. The difference in voltage between the first outer grid and the modulator creates an electric field that exerts a force ($\mathbf{F} = q\mathbf{E}$) on incoming ions in the $-\hat{\mathbf{z}}$ direction. An ion with mass, m_i, and charge, $q_i > 0$, can only reach the collector if its velocity, $v_{i,z} = \mathbf{v}_i \cdot \hat{\mathbf{z}}$, into the instrument satisfies $1/2 m_i v_{i,z}^2 > q_i V$. In other words, its velocity must exceed a cut-off speed to overcome the electric field acting to reverse its trajectory,

$$v_i^{(c)}(V) \equiv \sqrt{\frac{2q_i V}{m_i}}. \tag{5.4}$$

Therefore, if $V > 0$, then all electrons and only ions with sufficient energy that enter the cup can strike the collector plate. The modulator voltage carries an alternating current (AC) signal in the form of a square wave, $V = V_0 \pm \Delta V/2$, where V_0 is the direct current (DC) offset and ΔV is the amplitude between the two peaks. Therefore, ions with $v_{i,z} > v_i^{(c)}(V_0 + \Delta V/2)$ will always pass through to the collector plate unhindered and ions with $v_{i,z} < v_i^{(c)}(V_0 - \Delta V/2)$ will never pass through the modulator. However, ions with an intermediate velocity, $v_i^{(c)}(V_0 - \Delta V/2) < v_{i,z} < v_i^{(c)}(V_0 + \Delta V/2)$, will only be detected when the amplitude of the voltage is low. This difference in the measured currents between the low and high voltage states suppresses all other contributions that do not vary with the modulator voltage, as well as any other background signals. Since the cut-off speed (Equation 5.4) depends on the mass and charge of an ion species,

$$v_s^{(c)}(V) = \sqrt{\frac{q_s/q_p}{m_s/m_p}} v_p^{(c)}(V), \tag{5.5}$$

a FC can distinguish between different species based on their charge-mass ratio.

5.3.2 The Reduced Distribution Function

By making successive measurements in different voltage windows, FCs can build up an energy distribution of ions. Therefore, a FC can probe the distribution of particles $f_i(v_z)$ as a function of their speed normal to the grids by varying V. Since Equation 5.4 does not depend on speeds perpendicular to the cup axis, the FC measures a reduced distribution function:

$$F_i(v_z) \equiv \iint_{-\infty}^{\infty} f_i(\mathbf{v})\, d^2\mathbf{v}_\perp, \tag{5.6}$$

and can resolve the 3D characteristics of $f_i(\mathbf{v})$ by looking in different directions, e.g., by placing a FC on a rotating spacecraft. Here, $\perp$ refers to the cup axis and not $\mathbf{B}$. To calculate moments of the reduced distribution function, an analytical model for the measured current as a function of a model VDF and instrument geometry is needed. For a non-zero modulating voltage, the contribution to the measured differential current in the collector plate is:

$$\Delta I_i = -\frac{q_i}{2} A(\hat{v}_{i,z}) \int_{v_i^{(c)}(V_0-\Delta V/2)}^{v_i^{(c)}(V_0+\Delta V/2)} v_{i,z} F_i(v_z)\, dv_z, \tag{5.7}$$

where $F_i(v_z)$ is the reduced distribution along the z-axis of the FC and $A(\hat{v}_{i,z})$ is the effective collecting area of the instrument, which is a function of the angle of incidence of the particles flowing into the cup. For a supersonic flow such as the solar wind, $v_i \gg w_i$ so that $f_i(\mathbf{v})$ peaks at $\mathbf{v} = \mathbf{v}_i$ and ions appear as a beam in the sky. Therefore, $A(\theta, \phi)$ is a slowly varying function and can be taken out of the integral [Kasper, 2002]. For a field-aligned bi-Maxwellian VDF in the plasma rest frame ($\mathbf{v}' \equiv \mathbf{v} - \mathbf{v}_i$), the reduced distribution is:

$$F^B_{i,z}(v'_z + v_{i,z}) = \frac{n_i}{\sqrt{8\pi^3} w^2_{i,\perp} w_{i,\parallel}} \int_{-\infty}^{\infty} dv'_y \int_{-\infty}^{\infty} \exp\left[-\frac{{v'_\parallel}^2}{2w^2_{i,\parallel}} - \frac{{v'_\perp}^2}{2w^2_{i,\perp}}\right] dv'_x, \tag{5.8}$$

$$= \frac{n_i}{\sqrt{2\pi} w_{i,z}} \exp\left[-\frac{1}{2}\left(\frac{v'_z}{w_{i,z}}\right)^2\right], \tag{5.9}$$

where ${v'_\parallel}^2 = (\mathbf{v}' \cdot \hat{\mathbf{B}}_0)^2$ and ${v'_\perp}^2 = {v'}^2 - {v'_\parallel}^2$. Here, the unit vector $\hat{\mathbf{B}}_0$ is the average magnetic field over the measurement time in the frame of the FC. Therefore, a reduced bi-Maxwellian distribution is simply an isotropic Maxwellian along a given angle with effective thermal speed, $w_{i,z}$:

$$w_{i,z} = \sqrt{\left(1 - \hat{B}_{z,0}^2\right) w_{i,\perp}^2 + \hat{B}_{z,0}^2 w_{i,\parallel}^2}. \tag{5.10}$$

This projection allows for the determination of temperature anisotropy depending on the orientation of the background magnetic field. Inserting Equation 5.8 into Equation 5.7, the current can be solved analytically [Maruca, 2012], assuming that $\mathbf{B}_0$ does not vary throughout the measurement (see Section 5.3.5) and particles in space with all possible velocities perpendicular to the instrument axis contribute to the current. The total measured current by the FC is a sum over all ion species:

$$\Delta I = \sum_i \Delta I_i + \Delta I^{(n)}. \tag{5.11}$$

where $\Delta I^{(n)}$ represents sources of noise in the measurement.

5.3.3 Solar Wind Experiment

SWE [Ogilvie et al., 1995] consists of a suite of instruments including electrostatic analysers and FCs to measure ion and electron properties in the solar wind. The dual FC system probes ion velocity distributions, $f_i(\mathbf{v})$, by measuring their reduced distribution functions, $F_i(v_z)$, providing moments for protons and α-particles, including density, n_i, bulk velocity, $\mathbf{u}_i$, and temperatures, $T_{i,\perp}$ and $T_{i,\parallel}$. In Figure 5.3, I show a cross-section of the SWE FCs from Ogilvie et al. [1995]. Each cup contains nine mesh grids. Several grounded grids isolate the rest of the spacecraft from electromagnetic interference and prevent the modulator from inducing a current on the collector plate. A suppressor grid also accelerates any secondary electrons back into the collector plate.

The two FCs are located on opposite sides of the spacecraft body and tilted roughly 15° above and below the ecliptic plane, giving a 105° field of view out of this plane. However, due to instrument geometry, at angles of incidence above 45° the collector plate is no longer completely illuminated. Therefore, measurements of particles entering the cup at angles larger than 60° from the ecliptic will have a large uncertainty. The rotation of *Wind* in

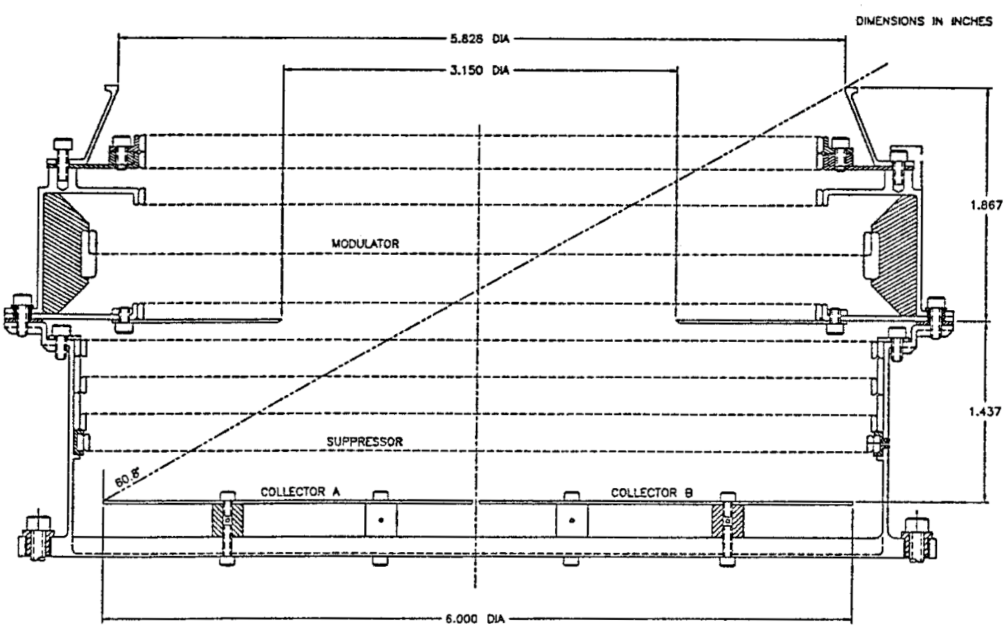

Figure 5.3: Schematic cross-section of the SWE Faraday cup showing the configuration of the nine mesh grids. Figure from Ogilvie et al. [1995].

the ecliptic plane allows the sampling of different angular bins as the FCs look in different directions to obtain a full-sky measurement of the integrated current. There are 20 angular bins covering the entire elliptic plane; 18 spaced at about $\sim 3.5°$ and two directed anti-sunward, each 35° wide.

A single spectrum from the SWE FCs consists of a set of current measurements, ΔI, over a series of angular and voltage (energy) windows integrated over ~ 92 s. After an internal calibration over one rotation of the spacecraft, a 200 Hz square-wave voltage, $V = V_0 \pm \Delta V/2$, is supplied to the modulators for the lowest voltage window, before the instruments scan through successive energy windows, one for each 3 s rotation. These energy windows are logarithmically spaced from 150 eV to 8 keV, and the ends overlap such that: $V_1 + \Delta V_1/2 = V_2 - \Delta V_2/2$ and $\Delta V/V \simeq 10\%$. The instruments can operate in two modes; the first is full-scan, which steps through double-width voltage windows. The second is peak-track, where a subset of single-width energy windows are measured that enclose the window from the previous spectrum where the highest current was observed. In either mode, there are almost always 30 energy windows in each spectrum. Small variations in the spin rate can be caused by variations in the spacecraft temperature so that the length of a single spectrum can vary slightly about 92 s.

5.3.4 Non-linear Fitting of Reduced Distributions

One method to obtain moments of $F_i(v_z)$ from the measured currents for each 92 s spectrum is to fit a model distribution function to the measurements. By substituting a model distribution into Equation 5.7, an expression for ΔI in terms of the fit parameters of the model distributions can be obtained. Non-linear fitting algorithms can then be used to fit this model spectrum to the measured spectrum to derive estimates of the moments of different ion species. Kasper et al. [2006] show that results from non-linear fitting using the SWE FCs are significantly more accurate than other methods. However, if the measurements are not well-represented by the chosen model distribution, then the fitting will not provide accurate results. This technique also requires initial guesses of the fit parameters and the fitting algorithms are usually sensitive to these guesses.

For *Wind*, it is assumed that the FCs only detect protons and α-particles, and both species are fit with a bi-Maxwellian distribution (Equation 5.8). From Equation 5.5, the peak in the current due to the α-particles will be shifted by about a factor of 2 in energy from the proton peak, even though both species have comparable bulk speeds. Therefore, the SWE FCs will measure two distinct peaks that can be fitted separately. However, it should be noted that the presence of a faster proton beam component (see Section 4.1) can make it difficult to distinguish between different peaks. The `apbimax` code [Kasper, 2002] uses the following algorithms to determine n_i, $\mathbf{u}_i$ and $w_{i,\perp/\parallel}$ for both protons and α-particles, i.e., 12 free parameters. The code takes ΔI from SWE, and $\mathbf{B}_0$ from MFI averaged over 92 s and converted into the frame of the FC, assuming the direction does not change during the observation. I show in Figure 5.4, examples of proton and α-particle distributions measured by the SWE FCs from Kasper [2002].

The `apbimax` code uses a multi-step process to derive best-fit values for

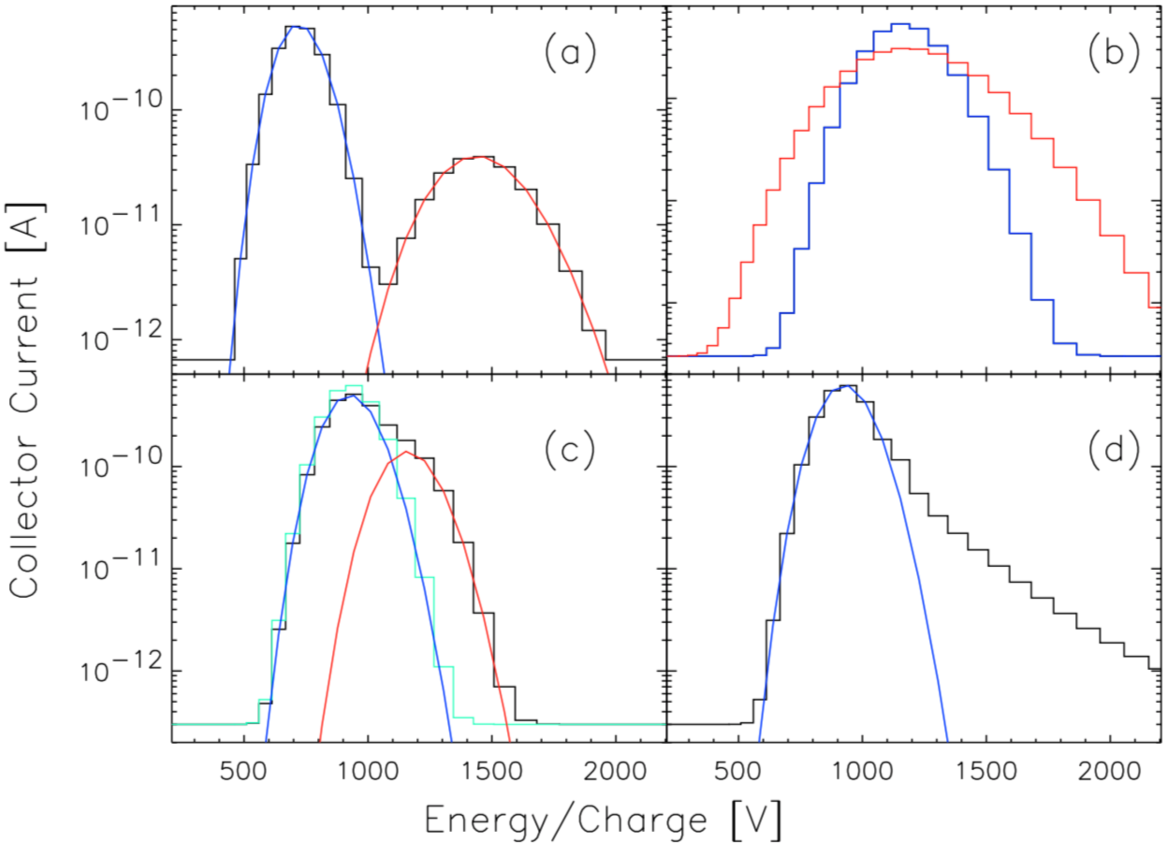

Figure 5.4: Example SWE FC ion distributions (black) measured in the solar wind as a function of the collector current and energy at the centre voltage of each window. Panel (*a*) shows Maxwellian fits to the proton (blue) and α-particle (red) distributions with same bulk speed, where the two peaks are separated due to Equation 5.5. Panel (*b*) shows two proton distributions approximately parallel (red) and perpendicular (blue) to $\mathbf{B}_0$, used to determine temperature anisotropy. Panel (*c*) shows an overlapping proton core (blue) and beam (red) distribution. Panel (*d*) shows a proton distribution with a high-energy tail, which is not well-represented by the model distribution. Figure from Kasper [2002].

these parameters, minimising false or failed convergences by the non-linear algorithm. Firstly, the six free parameters for the protons are estimated to provide initial guesses for the fitting [see Kasper, 2002]. Then, the code selects which values of ΔI to fit the bi-Maxwellian model for protons based on these initial guesses. To avoid contamination from physical sources such as α-particles or instrumental/model issues, the code ensures a minimum current, significant peak height, maximum width of peak and maximum angle of incidence for optimum fitting. A minimum of 40 measurements of the proton distribution are required for analysis to proceed, but typically 200 are chosen. The code then fits the selected currents using the Levenberg-Marquardt non-linear least-squares algorithm for χ^2 minimisation, which also provides one-σ estimates of the uncertainty [Kasper, 2002].

The best-fit values for protons are then used to provide the initial guesses for the α-particles, taking the same velocity and thermal speeds, as well as $n_\alpha \simeq 0.04 n_p$. Then, the point selection is re-run to identify measurements of the protons and α-particles separately. Finally, the code fits for a second time for all 12 free parameters simultaneously. Depending on the derived thermal speed and bulk speed of the α-particles, the code may re-run the fitting another time subtracting the proton distribution. Once the best-fit values of the solar wind parameters have been determined the bulk velocity of the protons in the spacecraft frame is corrected for the 30 km/s aberration produced by the orbital velocity of the spacecraft and Earth around the Sun. It is these 12 parameters for protons and α-particles at a 92 s resolution that I use in my analysis of solar wind fluctuations in this thesis.

5.3.5 Instrumental Issues

There are various caveats to the SWE data due to instrument geometry and the process of obtaining ion moments [Kasper et al., 2006]. In particular, several issues can prevent an accurate determination of $w_{i,\perp}$ and $w_{i,\parallel}$. If there is a large angular fluctuation, ψ_B, in the direction of the magnetic field between 3 s averages over the spacecraft spins that make up each 92 s measurement, any anisotropies in the thermal speed can be blurred out. In other words, the fluctuations in $\mathbf{B}_0$ over the integration time result in a broadening of the distributions. SWE measurements with an angular deviation of $\psi_B > 15°$ are usually neglected to reduce this blurring effect. Small values in $w_{i,\perp}$ and $w_{i,\|}$ are also uncertain due to the finite width of the angular bins of the SWE FCs. Therefore, measurements where the values of $w_{i,\|/\perp} < 15$ km s^{-1} should also be neglected.

Certain orientations of the magnetic field can make it difficult to determine one or both of the thermal speeds due to the geometry of the SWE FCs and orientation on the *Wind* spacecraft. I show in Figure 5.5, the uncertainties in both $w_{p,\|}$ and $w_{p,\perp}$ from Kasper [2002] for different magnetic latitudes, θ_B, and longitudes, ϕ_B (see Section 2.9). The component of the large-scale magnetic field in the ecliptic plane on average lies along the Parker spiral angle of 45°, so the (θ_B, ϕ_B) plane is not evenly covered by the observations. From the Figure, if $\theta_B > 60$, then measurements of $w_{p,\|}$ are more uncertain since the orientation of $\mathbf{B}_0$ is perpendicular to the cup look direction when the signal is strongest (see Equation 5.10). The same is true for $w_{p,\perp}$ when the magnetic field is approximately radial, since $\mathbf{B}_0$ is parallel to the cup look direction. Therefore, to minimise these uncertainties, data where $\theta_B > 60°$ are usually neglected.

Due to their lower densities, α-particles are usually more difficult to resolve, and especially, their temperature anisotropy measurements usually have large uncertainties. Another caveat of the SWE data arises when a proton beam is present, making it difficult to distinguish between the beam and core of protons, or beam and α-particle peak. The proton beam can sometimes be interpreted as an unusually large core proton parallel temperature. Therefore, care should be taken when interpreting measurements of large $T_{p,\|}$. There are additional codes that have been developed to improve on the `apbimax` code analysis, including the `dvapbimax` code [Maruca, 2012; Maruca & Kasper, 2013], which uses an improved model of the α-proton differential flow to reduce the number of fit parameters. It also reduces the effect of deviations in $\mathbf{B}_0$

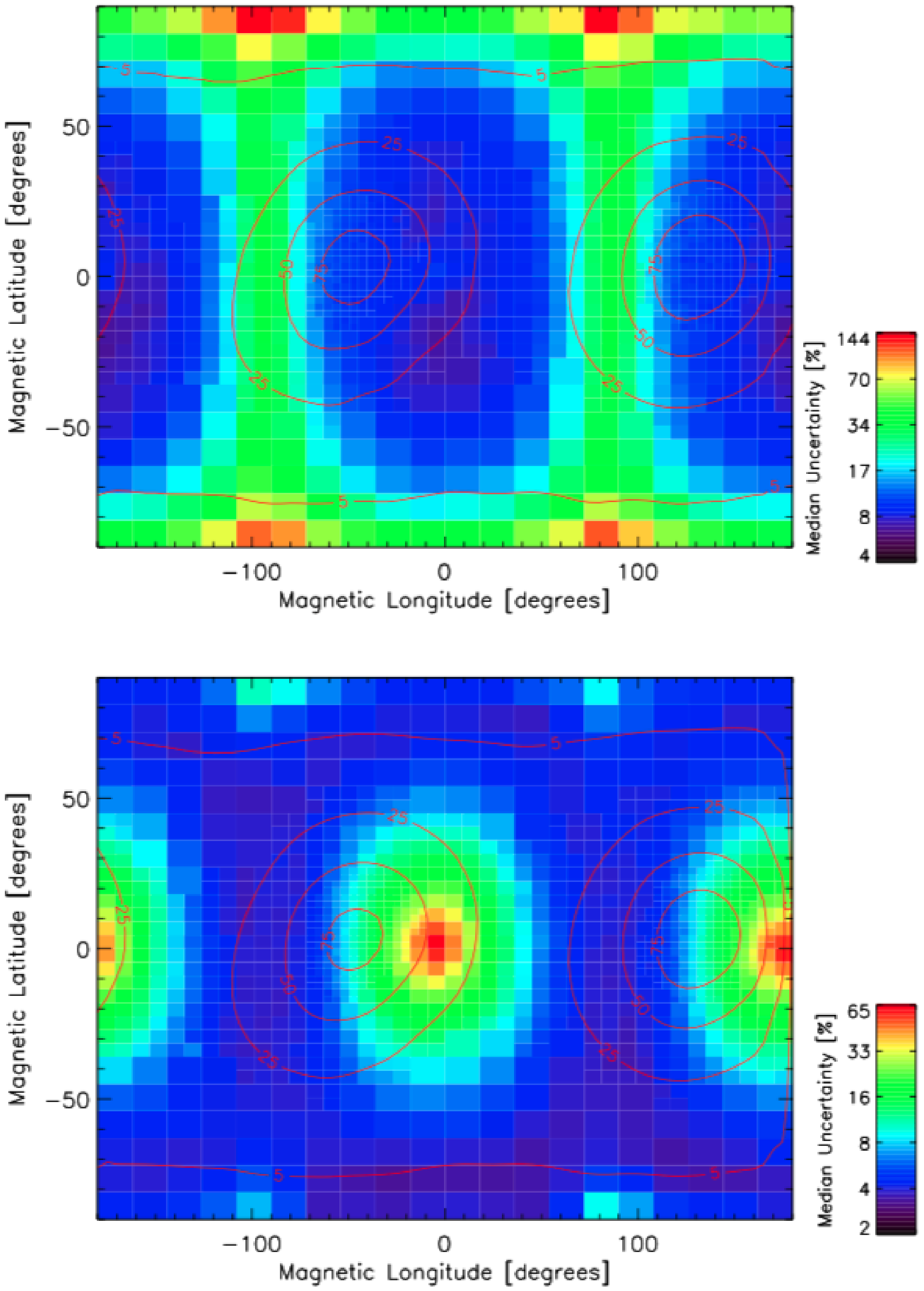

Figure 5.5: The median uncertainty in the proton parallel (upper panel) and perpendicular (lower panel) thermal speeds as a function of magnetic latitude, θ_B, and longitude, ϕ_B (see Section 2.9). The red contours indicate percentages of the SWE data contained within the θ_B-ϕ_B plane, due to the large-scale Parker spiral. Figure from Kasper [2002].

blurring the temperature anisotropy measurement by instead, using $\mathbf{B}_0$ averaged over each spacecraft rotation (3 s). Recently, Alterman et al. [2018] have adapted the `apbimax` code to model the proton core and beam populations separately.

5.4 Spectral Analysis and Signal Processing

Data from spacecraft in the solar wind consist of a time series of measurements that are best analysed using digital signal processing. In this thesis, I am primarily focussed on spectral analysis based on the Fourier and wavelet transforms to investigate the properties of magnetic field fluctuations in the frequency domain. In this section, I first discuss the basics of Fourier analysis, including the discrete Fourier transform (DFT), the Nyquist sampling theorem, and Parseval's theorem. I then introduce wavelet analysis and the continuous wavelet transform (CWT) that I use in my analysis of magnetic field fluctuations in Chapters 6-8.

5.4.1 Fourier Analysis and Digital Signals

The Fourier transform, $\tilde{X}(f)$, for a continuous time variable $x(t)$ or analogue signal (see also Equation 2.47) is:

$$\tilde{X}(f) = \int_{-\infty}^{\infty} x(t)\mathrm{e}^{-i2\pi ft}\mathrm{d}t, \tag{5.12}$$

and the inverse transform is:

$$x(t) = \frac{1}{2\pi}\int_{-\infty}^{\infty} \tilde{X}(f)\mathrm{e}^{i2\pi ft}\mathrm{d}f. \tag{5.13}$$

A Fourier transform decomposes a signal as a function of time into its component frequencies, giving a complex-valued function of frequency whose absolute value represents the amplitude of that frequency present in the original function, and whose complex argument gives phase content [Alessio, 2016]. For real measurements, a time series is a discrete set of values, $x[n]$, sampled from $x(t)$ at a constant sampling period, T_s, where $n = [0, N-1]$ is the discrete time and N is the total number of data points. If the amplitude of $x[n]$ is also discrete, then it is called a digital signal. In this case, the DFT is used:

$$\tilde{X}(k) = \sum_{n=0}^{N-1} x[n] \mathrm{e}^{-i2\pi kn/N}, \tag{5.14}$$

and its inverse:

$$x[n] = \frac{1}{N} \sum_{k=0}^{N-1} \tilde{X}[k] \mathrm{e}^{i2\pi kn/N}, \tag{5.15}$$

where $\tilde{X}(k)$ is the Fourier transform of $x[n]$ and $k = [0, N-1]$ is the discrete frequency, i.e., $f_k = k/NT_s$ or $\omega_k = 2\pi k/NT_s$. The DFT is an approximation of the true Fourier transform since it is performed on a windowed segment of $x(t)$, i.e., outside of the discrete-time interval, the signal is zero. This means that the frequencies are also discretised, leading to a loss of spectral resolution. Another consequence of this process is spectral leakage, where the power at one discrete frequency can leak into neighbouring frequencies [Bracewell, 1999].

The finite length of the time series also leads to sampling constraints. When calculating the DFT of a digital signal, T_s must be small enough so that a correct representation of $x(t)$ is made by sampling. If T_s is too large then information about the signal is lost, and the reconstruction of $x(t)$ from $x[n]$ is not possible. The sampling theorem gives a lower limit for T_s, so that the original signal can be properly represented without aliasing in the frequency domain, i.e., reducing error in the highest frequencies of a DFT due to the lack of a high enough sampling frequency, f_s. The Nyquist frequency,

$$f_N = \frac{1}{2T_s}, \tag{5.16}$$

defines the highest frequency measurable with a DFT for a specific T_s [Nyquist, 1928]. However, if the finite signal contains frequencies higher than f_N, then aliasing cannot be avoided (see Section 6.1). The DFT is computationally intensive, requiring N^2 multiplications. The fast Fourier transform (FFT) algorithm [Cooley & Tukey, 1965] is used to optimise this procedure, exploit-ing the symmetry and periodicity properties of complex exponentials in the definition of the DFT.

5.4.2 Estimating the Power Spectral Density

The total energy of a signal is:

$$E = \int_{-\infty}^{+\infty} |x(t)|^2 \mathrm{d}t, \tag{5.17}$$

which for a pulse-like signal has finite energy, i.e., $E < \infty$. One important property of the Fourier transform is Parseval's theorem:

$$\int_{-\infty}^{\infty} |x(t)|^2 dt = \frac{1}{2\pi} \int_{-\infty}^{\infty} |\tilde{X}(\omega)|^2 d\omega \tag{5.18}$$

which states that the energy of the signal in the time domain is equal to the energy of the signal in the frequency domain [Alessio, 2016]. For a discrete signal, Parseval's theorem becomes:

$$\sum_{n=0}^{N-1} |x[n]|^2 = \frac{1}{N} \sum_{k=0}^{N-1} |\tilde{X}[k]|^2. \tag{5.19}$$

Here, $|\tilde{X}[k]|^2$ is given in units of energy per unit frequency and is called the energy spectral density of $x[n]$. However, a weakly stationary and ergodic process (on which turbulence is modelled, see Chapter 3) that is continuous in time has infinite energy. In this case, the average power over the interval $[0, T]$,

$$P = \lim_{T \to \infty} \frac{1}{T} \int_{0}^{T} |x(t)|^2 dt, \tag{5.20}$$

is used, which can be finite. The power spectral density (PSD) from Parseval's theorem is:

$$\tilde{S}_{xx}(\omega) = \lim_{T \to \infty} \left\langle |\tilde{X}(\omega)|^2 \right\rangle = \int_{-\infty}^{\infty} R_{xx}(\tau) e^{-i\omega\tau} d\tau = \tilde{R}_{xx}(\omega). \tag{5.21}$$

Therefore, the power spectral density, $\tilde{S}_{xx}(\omega)$, is the Fourier transform of the auto-correlation function, $R_{xx}(\tau)$. This is known as the Wiener-Khinchin [Wiener, 1930; Khintchine, 1934] theorem and is used to analyse solar wind data (see Section 3.7.2). An estimate of the true PSD for a finite-length discrete time variable is given by:

$$\tilde{S}_{xx}(\omega) = \frac{T_s}{N}\left|\tilde{X}(\omega)\right|^2, \tag{5.22}$$

where the normalisation factors ensure that the PSD is in physical units. A plot of $\tilde{S}_{xx}(\omega)$ versus ω is called the power spectrum. If $x[n]$ is real, then $\tilde{S}_{xx}(\omega)$ is real, non-negative, and an even function of frequency. The finite length of the time series distorts the estimated spectrum compared to the actual one. This is because the DFT takes the finite length time series as a windowed interval of an infinite signal. As long as $x[n]$ remains stationary and has zero mean, the actual PSD is achieved when $N \to \infty$ and the expected value is formally applied, i.e., Equation 3.31 for magnetic field measurements in the solar wind. This estimate, sometimes called a periodogram, is averaged to obtain a more accurate estimate of the true PSD as the number of estimates and averaging interval approach infinity [Brown & Hwang, 2012]. Algorithms such as the Bartlett or Welch methods can be employed for this averaging [Welch, 1967]. These take the average of the periodograms of multiple segments of the signal that correspond to statistical ensembles of realisations of $x(t)$ evaluated over the specified time window to reduce the variance of the spectral density estimate. Rectangular windows or tapers of varying shape, for example, the Hamming window, can be used, as well as overlapped to minimise spectral leakage [Harris, 1978].

One drawback of these methods is that they do not give any localisation in time. The short-time Fourier transform (STFT) can be used to overcome this, which like the Bartlett or Welch methods, divides the signal into windowed or tapered segments. Each segment is analysed separately so that the spectral variation of the signal with time can be obtained [Alessio, 2016]. This procedure provides a set of spectra as a function of time, i.e., $\tilde{S}_{xx}(\omega, t)$. This set of spectra plotted against both t and ω is called a spectrogram. The segments should be small enough so that the spectral characteristics do not vary significantly between segments, and therefore, stationarity holds. In other words, the typical time-scale of the variations in spectral characteristics of the signal must be longer than the length of the window. However, this does result in lower spectral resolution, particularly at small frequencies. One way to overcome this drawback of the STFT is to use wavelets.

5.4.3 Wavelets and the Continuous Wavelet Transform

Wavelets are an alternative approach to signal processing than using Fourier transforms. A wavelet is a finite-energy (zero-mean) complex wave-form that is localised in both time and frequency. A wavelet transform can be used in a similar way to the Fourier transform in order to analyse the spectral content of a signal, and the output is a function of both time and scale, therefore, including information on the non-stationary features of a signal. Here, scale replaces frequency and is related to the period of the wavelet. A wavelet transform begins with a mother wavelet, ψ_0, which stretched or compressed (retaining the same shape) to produce a daughter wavelet, ψ, at a scale, s. This daughter wavelet is then translated along the length of the signal and cross-correlated with it at every τ, a time delay with respect to the origin of the time axis, t. This process is repeated many times to produce a matrix of correlation values that describes the similarity between the signal and the daughter wavelets, called wavelet coefficients, $W_x^{\psi}(s, \tau)$ [Alessio, 2016]. In Figure 5.6, I show a representation of this process for a time signal, $x(t)$. With an appropriate choice of mother wavelet, the spectral composition of the signal can be obtained.

The wavelet transform has several advantages compared to an STFT. In the latter, the window width is constant, whereas in a wavelet transform the different scale daughter wavelets act as windows that get wider or narrower as s changes. Since the number of oscillations in a wavelet remains constant

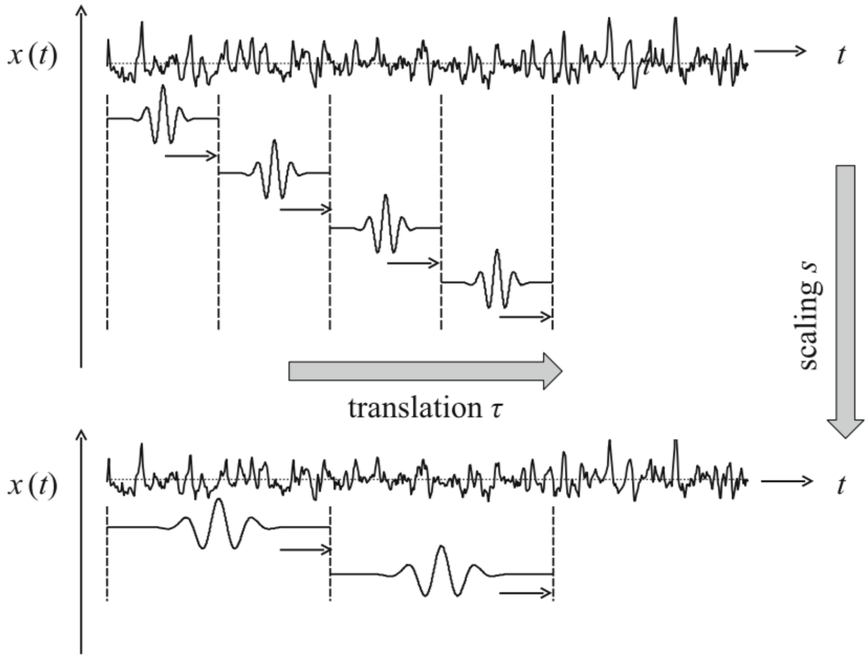

Figure 5.6: A schematic representation of the continuous wavelet transform of a signal, $x(t)$, for two different scaled daughter wavelets. Image from Alessio [2016].

with scale, the wavelet can frame the same number of oscillations in a signal for a range of frequencies by varying s. This property of a wavelet transform allows it to both accurately determine the scale (and frequency) of both large-scale/low-frequency oscillations and localise high-frequency oscillations accurately in time. In this thesis, I am primarily focused on the high-frequency fluctuations in the solar wind magnetic field in short time intervals, making the wavelet transform the most appropriate technique for my analysis.

The continuous wavelet transform (CWT) is defined as:

$$W_x^{\psi}(s,\tau) = \int_{-\infty}^{+\infty} x(t) \frac{1}{\sqrt{s}} \psi_0^* \left(\frac{t-\tau}{s} \right) \mathrm{d}t, \tag{5.23}$$

for a non-stationary continuous signal, $x(t)$, with finite energy and zero mean. The mother wavelet, ψ_0, is related to a daughter wavelet at scale, s, by:

$$\psi(\eta) = \frac{1}{\sqrt{s}} \psi_0(\eta), \tag{5.24}$$

where $\eta = t/s$ is a non-dimensional time. The $1/\sqrt{s}$ factor ensures that the daughter wavelets have the same energy, i.e., the norm of the wavelets are:

$$\|\psi_0(t)\| = \sqrt{E\{\psi_0(t)\}} = \sqrt{\int_{-\infty}^{+\infty} |\psi_0(t)|^2 \, \mathrm{d}t} = 1, \tag{5.25}$$

and $\|\psi(\eta)\| = 1$. Hence,

$$W_x^{\psi}(s,\tau) = \int_{-\infty}^{+\infty} x(t)\psi^*\left(\frac{t-\tau}{s}\right)\mathrm{d}t = \frac{1}{2\pi}\int_{-\infty}^{+\infty} \tilde{X}(\omega)\tilde{\Psi}^*(s\omega)\mathrm{e}^{\mathrm{i}\tau\omega}\mathrm{d}\omega, \tag{5.26}$$

where the convolution becomes a product in Fourier space. Therefore, the CWT can be computed by taking the inverse Fourier transform of the product of the Fourier transforms of $x(t)$ and $\psi^*(\eta)$. For this to hold, a wavelet must satisfy the admissibility condition; that is, it has finite energy and zero mean so that it oscillates about zero. There are also several more complicated requirements, for example, see Alessio [2016]. Complex analytical wavelets satisfy these conditions [Gabor, 1946], for example, the Morlet wavelet:

$$\psi_0(\eta) = \pi^{-1/4}\exp(i\omega_0\eta)\exp(-\eta^2/2), \tag{5.27}$$

where ω_0 is called the frequency parameter. For $\omega_0 = 6$, this wavelet obeys the admissibility condition to computational round-off errors. This wavelet is most similar to a wave-packet, being a complex exponential function modulated by a Gaussian envelope with $\sigma = 1$. In Figure 5.7, I show the real and imaginary parts of several different analytical wavelets [Torrence & Compo, 1998]. Since $\psi_0(\eta)$ is complex, the wavelet coefficients, $W_x^{\psi}(s,\tau)$, are also complex. I use the Morlet wavelet in subsequent chapters instead of other analytical wavelets such as the Paul or Derivative of Gaussian (DOG) wavelets. I compared the spectra of several analytical wavelets, finding no discernible difference between them. The Fourier transform of the Morlet wavelet is:

$$\tilde{\Psi}_0(s\omega) = \pi^{-1/4}\exp\left[-(s\omega-\omega_0)^2/2\right]H(\omega), \tag{5.28}$$

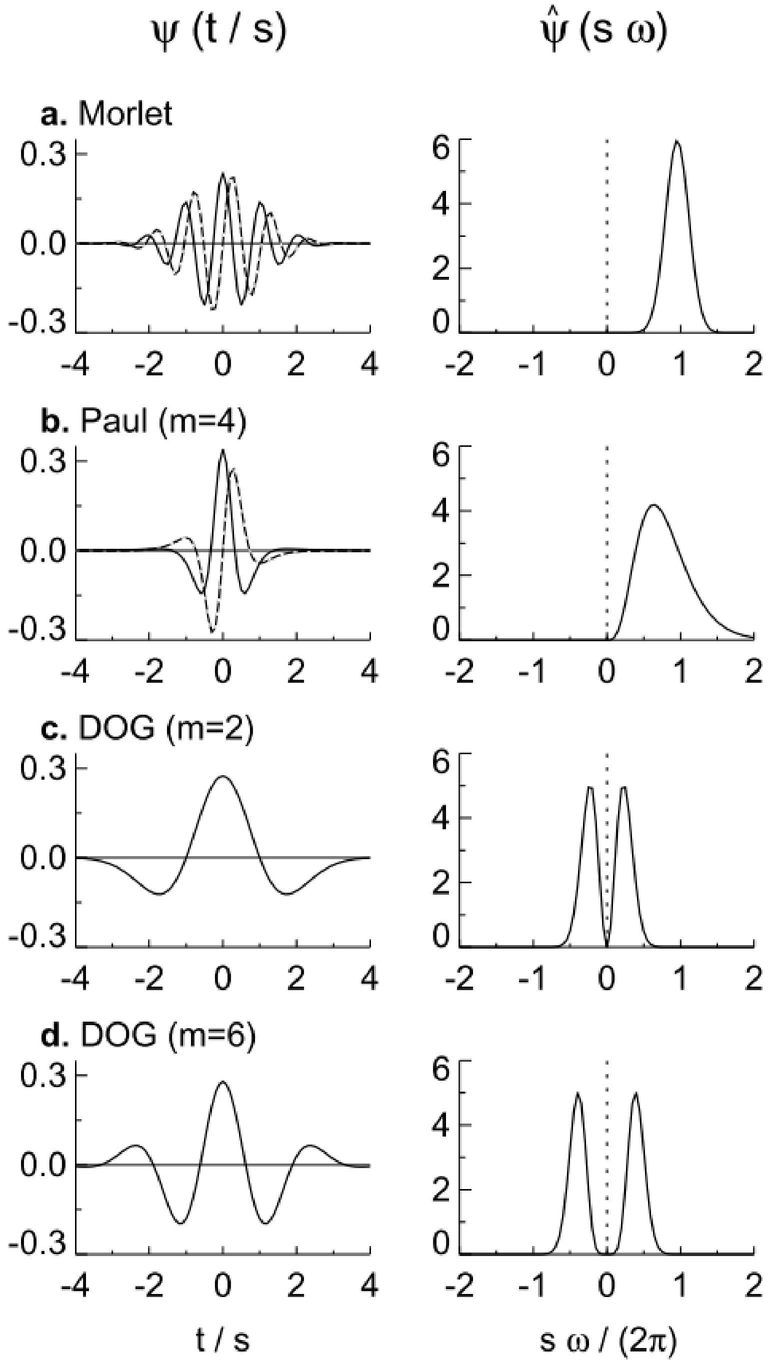

Figure 5.7: Example analytical wavelets and their Fourier transforms: (a) the Morlet wavelet with $\omega_0 = 6$; (b) the Paul wavelet of order $m = 4$; (c) the DOG wavelet of order $m = 2$; and (d) the DOG wavelet of order $m = 6$. In the left column, the solid line is the real part of the wavelet and the dashed line is the imaginary part. Here, $s = 10T_s$. Image from Torrence & Compo [1998].

where $H(\omega)$ is the Heaviside step function, i.e., $H(\omega)=0$ for $\omega<0$, and $H(\omega)=1$ for $\omega\geq 0$. The Fourier transform is real and vanishes at negative frequencies, and is a Gaussian function with a peak $s\omega=\omega_0$ located at $s\omega/2\pi\simeq 1$ [Torrence & Compo, 1998]. Similarly to Fourier transforms, Parseval's theorem for the CWT states that the total energy of a signal, $x(t)$, is:

$$E=\int_{-\infty}^{+\infty}|x(t)|^2dt=\frac{2}{c_\psi}\int_{0}^{+\infty}\int_{-\infty}^{+\infty}\left|W_x^\psi(s,\tau)\right|^2\frac{\mathrm{d}s\mathrm{d}\tau}{s^2}, \tag{5.29}$$

where c_ψ is the admissibility constant:

$$c_\psi=\int_{-\infty}^{+\infty}\frac{|\Psi_0(\omega)|^2}{\omega}\mathrm{d}\omega, \tag{5.30}$$

which for the Morlet wavelet, $c_\psi=0.776$. Hence, $|W_x^\psi(s,\tau)|^2$ is the wavelet energy spectrum, representing the relative contribution to the signal energy for a specific scale, s, and time shift, τ [Alessio, 2016]. The conversion from scale to a Fourier pseudo-frequency for a Morlet wavelet is $f=(\omega_0+\sqrt{2+\omega_0^2})/4\pi s\simeq \omega_0/2\pi s$. Therefore,

$$E(f,\tau)=\frac{2T_s}{c_\psi f_0}\left|W_x^\psi(f,\tau)\right|^2, \tag{5.31}$$

where $f_0=\omega_0/2\pi$. In reality, the signal length is finite and Equation 5.26 must be discretised in both time and scale:

$$W_x^\psi(s,n)=\sum_{n'=0}^{N-1}x\left[n'\right]\psi_0^*\left[\frac{(n'-n)T_s}{s}\right]=\sum_{k=0}^{N-1}\tilde{X}_k\tilde{\Psi}^*(s\omega_k)\exp\left(i\omega_k nT_s\right). \tag{5.32}$$

where, $n'=[0,N-1]$, evaluated at discrete frequencies:

$$\omega_k=\begin{cases}2\pi k/NT_s; & k\leq N/2,\\ -2\pi k/NT_s; & k>N/2.\end{cases} \tag{5.33}$$

Here, the daughter wavelets are scaled and normalised,

$$\psi\left[\frac{(n'-n)\,T_s}{s}\right]=\left(\frac{T_s}{s}\right)^{1/2}\psi_0\left[\frac{(n'-n)\,T_s}{s}\right], \tag{5.34}$$

so that $\psi_0(\eta)$ has unit energy and the wavelet transform is only weighted by the amplitude of the Fourier coefficients, $\tilde{X}_k$, and not by the wavelet function [Torrence & Compo, 1998]. The discrete set of $J+1$ scales are calculated by:

$$s = s_0 2^{j\delta j}, \tag{5.35}$$

where $j = [0, J]$, s_0 is the minimum scale (usually $s_0 = 2T_s$ for the Morlet wavelet from the Nyquist theorem), and δj is the reciprocal ($1/\delta j$ is the number of voices) of the number of scales per octave (jump in factor of 2 in scale). The optimal value for the scale spacing is $\delta j < 0.5$ for the Morlet wavelet. The length of the time series defines the maximum number of scales, usually so that at the largest scale, at least two wavelets have a duration smaller than or equal to the length of the time series: $J = \log_2(NT_s/s_0)/\delta j$ (rounded to the nearest integer). The power spectral density of the signal, $x[n]$, is just the time average of Equation 5.31 over the length of the time series.

One caveat of the CWT is that all scales contribute to a wavelet coefficient for a specific τ. Therefore, due to the finite length of the time-series and size of the wavelet, coefficients at the edges of the time-series become more uncertain since some of the data required to calculate them is missing. The larger the scale, the wider the time intervals adjacent to the edges in which the CWT is disturbed, referred to as the cone of influence (COI). The width of each time interval is the COI at each scale, which for the analytic Morlet wavelet is $\tau_s = \sqrt{2}s$, where τ_s is called the e-folding time [Torrence & Compo, 1998]. These border effects can be minimised by zero-padding or by extending the time-series, calculating the CWT and then cutting the unwanted data. I discuss the use of the CWT with a Morlet wavelet to calculate the power spectrum of magnetic field fluctuations in the next chapter.

Chapter 6

The Spectral Properties of Solar Wind Fluctuations at Ion-kinetic Scales

Many studies [Leamon et al., 1998b, 2000; Smith et al., 2001b; Markovskii et al., 2008; Perri et al., 2010; Bourouaine et al., 2012; Bruno & Trenchi, 2014; Chen et al., 2014] have explored the link between ion characteristic scales and the spectral steepening of the power spectrum of magnetic field fluctuations. However, there is currently no consensus on the dominant dissipation mechanism that is responsible for the observed spectral break. An in-depth study using large amounts of data to identify the break scale and find evidence of the associated ongoing dissipation mechanisms under different solar wind conditions has yet to be undertaken. One major question that arises from these studies is what happens when $\beta_p \sim 1$? Do both d_p and ρ_p affect the break at the same time or does the break instead coincide with the cyclotron resonance scale (see Section 4.3.1), as shown by Bruno & Trenchi [2014]? There are also some tentative links between the coherent magnetic helicity signature and the spectral steepening at these scales [e.g., Bruno & Telloni, 2015; Telloni et al., 2015]. This helicity signature is particularly useful since it can aid the identification of wave modes at ion-kinetic scales in the solar wind, which would, in turn, help narrow down possible dissipation mechanisms.

In this chapter, I quantify the spectral features of magnetic fluctuations at ion-kinetic scales in the solar wind using almost 15 years of data from the *Wind* spacecraft. I conduct a statistical analysis of both the break in the power spectrum and coherent signature in the magnetic helicity at these scales. As part of this study, I make the first in-flight identification of the MFI noise-floor to undertake the most accurate study of magnetic field fluctuations at ion-kinetic scales with *Wind* to date. I find that the spectral steepening and onset of a coherent peak in magnetic helicity are linked to the same physical process, associated with $1/k_c$, suggesting the role of cyclotron resonance at these scales. This work is published in Woodham L. D., Wicks R. T., Verscharen D. and Owen C. J., 2018, The Role of Proton Cyclotron Resonance as a Dissipation Mechanism in Solar Wind Turbulence: A Statistical Study at Ion-kinetic Scales, *The Astrophysical Journal*, **856**:49. The work presented in this chapter uses more data and includes small updates to the algorithms used in the paper, which are described here.

6.1 The MFI Noise-floor

Due to the decreasing amplitude of magnetic field fluctuations with increasing frequency in the solar wind, instrumental and spacecraft-induced noise can lead to magnetic fluctuations of similar or greater amplitude than physical fluctuations. This effect leads to an artificial flattening of the power spectrum of magnetic fluctuations at the highest frequencies. For the MFI instrument, this noise-floor is thought to arise from the analogue-to-digital conversion of the signal, the spacecraft spin, and spin-tone harmonics. The only past measurement for the noise level of the MFI instrument was by Lepping et al. [1995], which was conducted on a prototype sensor before launch. To ensure that the amplitudes of the power spectra that I calculate from MFI data are physical at high frequencies, I first determine the amplitude and frequency dependence of the MFI noise-floor from in-flight measurements.

Measurements of ‘quiet’, smoothly-varying $\mathbf{B}$ are required to measure the

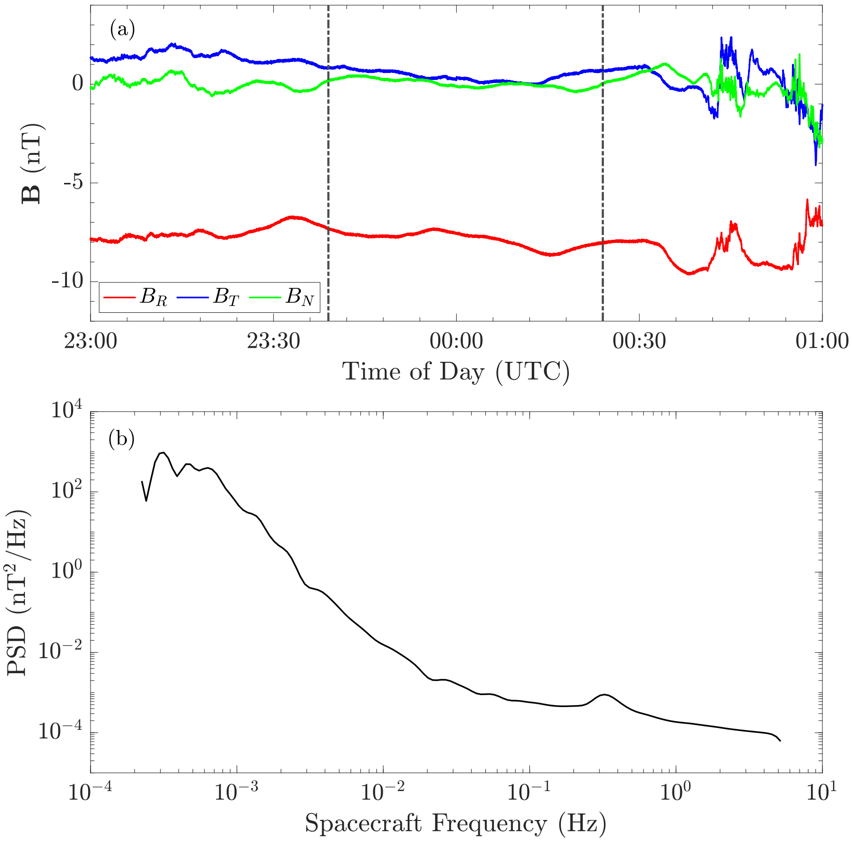

Figure 6.1: An example tail-lobe period (between the dashed lines) of smoothly varying magnetic field measurements from 12-13 February 2004 and the corresponding power spectrum. The noise-floor of the MFI instrument is visible at frequencies $f \geq 0.1$ Hz.

noise level in the magnetic field fluctuations at high frequencies so that there are as few physical fluctuations as possible and noise dominates the measured signal at these frequencies. The solar wind is unsuitable for this due to the presence of broadband turbulent fluctuations. However, the trajectory of the *Wind* spacecraft early in its mission provides the opportunity to calculate the in-flight noise-floor of the MFI instrument. The spacecraft spent considerable time in the Earth's magnetosphere before 2005. In particular, during early 2004, *Wind* made several passes through the tail-lobes of the magnetotail. These high-latitude regions surrounding the central plasma sheet have characteristic low plasma density and stretched-out field lines, providing ideal conditions to identify the noise-floor in a magnetic field power spectrum.

I identify 89 suitable tail-lobe intervals to determine the noise-floor, with smooth variations in **B** lasting at least 30 mins. Several of these intervals are identified using Audification [Wicks et al., 2016] and the rest I select by eye by examining the time series of magnetic field measurements. To find the instrument noise level, I calculate the PSD of each interval using a Morlet CWT (Equation 5.31), padding the time series to remove any border effects and averaging the spectrum over the entire interval. All identified periods are between 30 minutes and several hours, long enough to provide a stable estimate of the PSD. I show in Figure 6.1, an example time series of magnetic field measurements and the corresponding power spectrum for an interval from February 2004. The power spectrum reveals the noise-floor at high frequencies, which is at a similar amplitude in power as found by Lepping et al. [1995]. I further refine the number of selected intervals to 22 by removing those with signals attributed to physical fluctuations at frequencies $f > 0.1$ Hz and list these in Table 6.1. I show the PSD for all 22 periods in Figure 6.2. I average the PSD estimates over all 22 intervals to give one final estimate for the noise-floor, given by the black line in Figure 6.2. The red line shows the original noise-floor estimate published by Lepping et al. [1995].

The major difference in my noise-floor spectrum compared with the original estimate is the peak at 0.33 Hz. I attribute this peak to the spin rate (3 s) of the spacecraft. This peak is notch-filtered as part of the data calibration process described by Koval & Szabo [2013] to remove most of this artefact, but some residual power remains. At frequencies $f > 0.33$ Hz, between the black dashed lines in Figure 6.2, I find a power-law fit of: $\mathrm{PSD} = af^b$, where $a = 1.944 \times 10^{-4}$ and $b = -0.5328$. This high-frequency part of the spectrum is due to the aliasing of the spin-tone harmonics [Koval & Szabo, 2013], which cannot be removed by filtering, and noise from the digitisation process [Bennett, 1948; Russell, 1972]. Another source of noise is the aliasing of power from fluctuations measured at frequencies higher than the Nyquist frequency into the downsampled 11 Hz dataset [Russell, 1972; Klein et al., 2014]. This effect cannot be completely removed by my noise-floor treatment here; however, it

Table 6.1: The 22 intervals of tail lobe data I use to calculate the MFI noise-floor.

Interval	Date/Time
1	29/01/2004 00.36-01.06
2	06/02/2004 09.12-10.06
3	06/02/2004 20.45-21.30
4	07/02/2004 00.30-01.18
5	07/02/2004 03:49-05:13
6	07/02/2004 06.48-07.30
7	07/02/2004 09:08-09:59
8	07.02/2004 10.30-11.00
9	07/02/2004 15.00-15.45
10	07/02/2004 17.00-17.30
11	07/02/2004 20.00-21.45
12	08/02/2004 02.00-03.30
13	12/02/2004 15.24-15.54
14	12/02/2004 23:39-00:24
15	13/02/2004 04.12-05.00
16	13/02/2004 06.12-07.00
17	13/02/2004 13.00-13.30
18	13/02/2004 15.00-15.30
19	13/02/2004 22:39-23:10
20	15/02/2004 00.30-01.30
21	21/04/2004 20.40-21.10
22	22/04/2004 01.30-03.00

likely has only a small effect on the highest frequencies of spectra in the solar wind since turbulent fluctuations have smaller amplitudes at higher frequencies. The amplitude eventually coincides with the original estimate at about 3 Hz and approaching the Nyquist frequency. I take the amplitude of the power spectrum at frequencies $f < 0.1$ Hz as being due to physical fluctuations in the magnetic field and not instrumental or spacecraft-induced noise. This limit is clear from Figure 6.2, where the power spectrum of each interval is highly variable at $f < 0.1$ Hz.

The differences between my noise-floor estimate and the original estimate by Lepping et al. [1995] show that the noise level in the range 0.1-1 Hz is higher than initially thought, highlighting its importance when investigating turbulent phenomena in the solar wind at these frequencies. I use the amplitude of

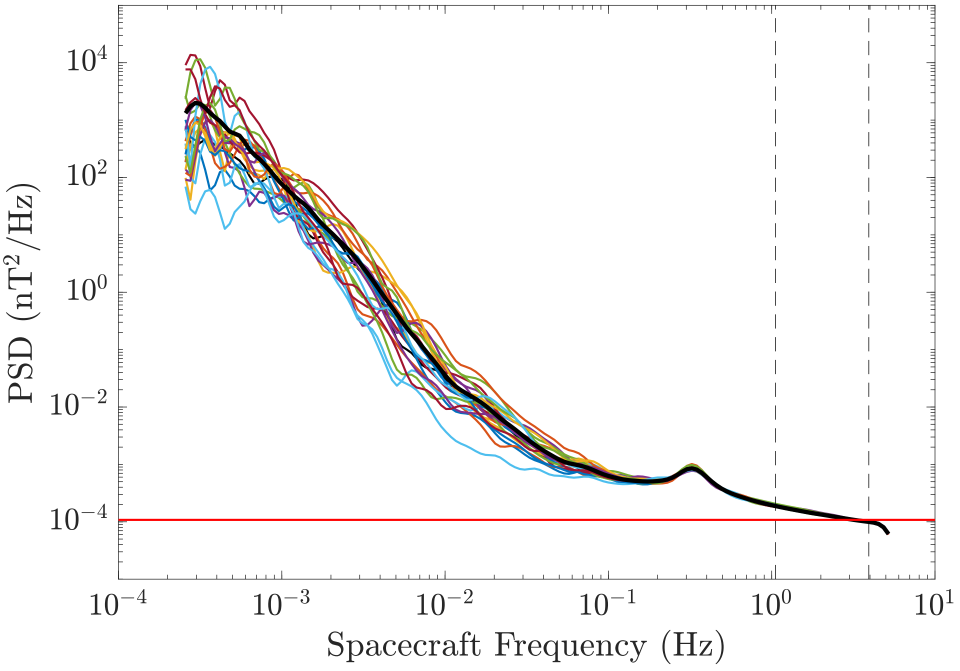

Figure 6.2: The MFI noise-floor in black from averaging of my selected 22 intervals. In red, I show the original estimate from Lepping et al. [1995]. The black dashed lines show the frequency range where I fit a power-law to the noise-floor: PSD $= af^b$, where $a = 1.944 \times 10^{-4}$ and $b = -0.5328$.

the PSD between 0.1-5.4 Hz as the noise-floor in my analysis of the turbulent magnetic field fluctuations later in this chapter and subsequent chapters. I note that the MFI instrument has several dynamic ranges, and it is likely that the noise level at high frequencies has a different amplitude for each range. Despite this, I only consider the noise-floor for the default range, ±16 nT, since the magnetic field components typically do not exceed this threshold during quiet conditions in the solar wind. I also identified intervals from 2000-2003 to determine if the noise-floor has changed with time due to degradation of the instruments, but these intervals show no substantial variation compared to those shown in Figure 6.2.

The fitting of the MFI noise-floor is published in the appendix of Woodham et al. [2018]. This result is the first published in-flight determination of the MFI noise-floor and enables the most accurate interpretation of *in-situ* measurements of high-frequency magnetic field fluctuations with MFI to date.

6.2 Spectral Analysis of Solar Wind Fluctuations

In this section, I describe my method to analyse solar wind magnetic field and ion moment data from the *Wind* spacecraft. I use 11 Hz magnetic field measurements from MFI and 92 s proton moments from SWE. I analyse large intervals (months) of solar wind data at a time and calculate the power and magnetic helicity spectra of magnetic field fluctuations using wavelet analysis. I average the spectra over 92 s so that each spectrum can be associated with a single SWE measurement, enabling the comparison of the spectral features of the fluctuations with the plasma properties.

6.2.1 Data Pre-processing

I first import the SWE Faraday cup data, including the proton moments: velocity $\mathbf{u}_p$, perpendicular thermal speed $w_{p,\perp}$, parallel thermal speed $w_{p,\|}$, proton density n_p, and their respective uncertainties from the non-linear fitting of the reduced particle VDF. I take the proton bulk velocity as the solar wind velocity, $\mathbf{v}_{sw} = \mathbf{u}_p$. In addition to these data, I import the start time of each spectrum measurement, the average magnetic field over the spectrum integration time ($\Delta t \sim$92 s), $\mathbf{B}_{92}$, and the angular deviation of the magnetic field over each measurement,

$$\psi_B = \sum_{i=1}^{N} \arccos(\hat{\mathbf{B}}_i \cdot \hat{\mathbf{B}}_{92})/N, \tag{6.1}$$

where N is the number of spacecraft rotations in a single measurement. I also include the fitting status, an integer between 0 and 11 describing the goodness of fit of the bi-Maxwellian model (see Kasper [2002]). I convert the vectors $\mathbf{v}_{sw}$ and $\mathbf{B}$ into spacecraft RTN coordinates (see Section 2.9) and using $\mathbf{B}_{92}$, I calculate the angle the angles ϕ_B and θ_B. I then pre-process the data to remove data gaps and anomalous or unphysical data. I discard as little data as possible during this pre-processing; instead, when analysing the results, I can filter the processed data to remove measurements which may be unreliable

(Section 5.3.5).

I first discard any measurements where there appears to be an issue with the initialisation of the FC measurement, as well as values for the proton parameters with a fitting status of 0, 1, 2, or 11. These flags indicate no successful convergence during fitting (see Section 5.3.4). I then identify any data gaps present by finding times between successive measurements that are longer than the median gap between measurements. I use the median gap because the length of the spectrum measurement is not constant and can vary by several seconds depending on variations in the spin rate of the spacecraft and the number of scans through energy windows. I do not fill in missing data for the proton moments; however, I do include the time stamps for data gaps to maintain alignment between magnetic field spectra and particle measurements. Finally, I shift all timestamps from the start of each FC measurement by $\Delta t/2$ so that they correspond to the middle of each measurement.

Next, I import the 11 Hz magnetic field data from MFI. I denote the high-resolution magnetic field as $\mathbf{B}$ to differentiate from the spectrum averaged field, $\mathbf{B}_{92}$. I again identify any data gaps present in the data using the same method as before and a constant gap of 0.092 s. If the length of a gap is ≤ 10 measurements, then I fill in the missing values for $\mathbf{B}$ using linear interpolation. If the length of the gap is larger than ten measurements, then I leave the gap present and include the missing time stamps. Finally, I calculate the derived plasma parameters using $\mathbf{B}_{92}$, including $T_{p,\perp/\parallel}$, $\beta_{p,\perp/\parallel}$, v_A, ρ_p, d_p, $1/k_c$, and:

$$\theta_{vB} = \arccos\left(\frac{\mathbf{v}_p \cdot \mathbf{B}_{92}}{|\mathbf{v}_p||\mathbf{B}_{92}|}\right). \tag{6.2}$$

I also calculate the normalised cross helicity,

$$\sigma_c = \frac{2\,(\delta\mathbf{v}\cdot\delta\mathbf{b})}{|\delta\mathbf{v}|^2 + |\delta\mathbf{b}|^2}. \tag{6.3}$$

Here, $\delta\mathbf{b} = \mathbf{b} - \langle\mathbf{b}\rangle_{1h}$ and $\delta\mathbf{v} = \mathbf{v} - \langle\mathbf{v}\rangle_{1h}$, where the mean is over a one hour window centred on the instantaneous values, $\mathbf{b} = \mathbf{B}_{92}/\sqrt{\mu_0\rho}$, and $\mathbf{v} = \mathbf{v}_{sw}$. The cross-helicity, $\sigma_c \in [-1, 1]$, is a measure of Alfvénicity (Equation 2.60), where $|\sigma_c| = 1$ indicates purely unbalanced Alfvénic fluctuations and $\sigma_c = 0$ indicates either balanced Alfvénic fluctuations or a lack of Alfvénic fluctuations. I do not use spectral techniques to calculate σ_c due to the limited cadence of the velocity measurements. An averaging interval of one hour gives the cross helicity in the inertial range, and therefore, an estimate of the Alfvénicity of the fluctuations present in each 92 s spectrum.

6.2.2 Wavelet Analysis

To compute solar wind spectra, I employ a CWT with a Morlet wavelet of frequency, $\omega_0 = 6$, using the method described in Section 5.4.3. I calculate the scales, s, for the Morlet wavelet using Equation 5.35 with $s_0 = 2\delta t$ and $\delta j = 0.1$ to ensure adequate sampling in scale. For the MFI data, $\delta t = 0.092$ s and the total number of scales, $J = 111$. I calculate the equivalent Fourier frequencies for each scale using $f = \omega_0/(2\pi s)$.

I remove border effects associated with the finite width of the wavelets by using a padded time-series. I take the ∼1,000 measurements for **B** associated with each SWE measurement and pad the time series equally at each end with additional MFI data to give 4,096 measurements. Through testing, I found that $N = 4096$ was optimal for speed of the computation[1] and reduction of border effects. I calculate the wavelet coefficients using Equation 5.32 and then the power spectral tensor: $\mathsf{S}_{ij}^{(r)}(f,t) = W_i^*(f,t) \cdot W_j(f,t)$. After discarding the padding measurements, I calculate the PSD using Equation 5.31 and the normalised magnetic helicity spectrum using Equation 3.37, averaged over the original ∼1,000 measurements. I assign each spectrum the time stamp of the particle measurements. If there is a large data gap present (>10 measurements) in the magnetic field data for a spectrum, I neglect the spectrum for that particle measurement. I loop through all FC moments in the dataset, giving one 92 s spectrum of the magnetic field fluctuations for each particle measurement.

---

[1] A power of 2 enables the FFT algorithm to run as efficiently as possible.

By averaging the spectra over the SWE integration time, I improve the accuracy of the amplitude of the power and helicity spectra at each frequency. I note, however, that 92 s is significantly shorter than the correlation time of solar wind turbulence, and so the assumptions of stationarity and ergodicity likely do not hold at low frequencies [Matthaeus & Goldstein, 1982b; Perri & Balogh, 2010]. Therefore, many of the usual results of turbulence are not recovered; for example, the spectra do not always converge to the typical $f^{-5/3}$ power-law expected in the inertial range because I do not average over a large enough ensemble of measurements. Despite this, I am attempting to quantify turbulence at ion-kinetic frequencies and not in the inertial range. An average over 92 s is typically an order of magnitude longer than typical timescales for processes at these frequencies ($\sim$ 1-10 s). Therefore, I should sample enough of the turbulence phase space (see Section 4.3) at these frequencies while still being able to resolve the highly variable nature of the spectra under different plasma conditions.

6.2.3 Estimation of the Break Frequency

To estimate the break frequency, f_b, of each power spectrum at ion-kinetic frequencies, I first fit the spectrum with the following linear function:

$$\log_{10}(\mathrm{PSD}) = m\log_{10}(f) + c, \tag{6.4}$$

where m is the gradient of the line or spectral exponent and c is the intercept. To accommodate for greater uncertainty in the spectra at low frequencies, I fit this function to the power spectra using windows of fixed width in frequency in logarithmic space and obtain m for each window. The frequencies included in each window are $f \in [f_m/3, f_m]$, where f_m is the maximum frequency of the window. Through testing, I found that this window width was optimal to obtain an accurate estimate of m while still being able to localise in frequency the break in the spectrum. For a window j, I set the maximum frequency of the subsequent window as $f_{m,j+1} = f_{m,j}/3^{0.1}$, shifting the windows to lower

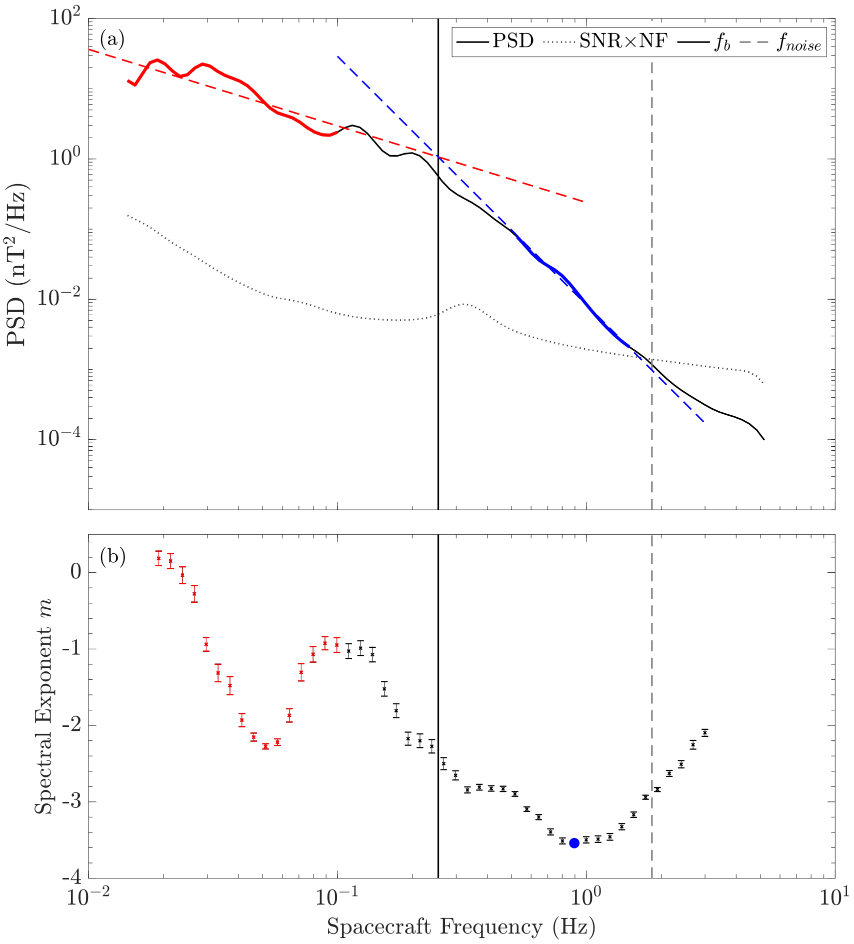

Figure 6.3: (*a*) An example 92 s power spectrum from July 2012 and (*b*) the respective results from my fitting algorithm to estimate f_b, given by the black line. The dotted line in the upper panel is the MFI noise-floor multiplied by a signal-to-noise ratio of 10, and the dashed line is f_{noise}. The red dashed line is a power-law fit to the inertial range (solid red line) giving a spectral exponent of -1.2, and the blue dashed line to the ion-kinetic range (solid blue line), giving an exponent of -3.8.

frequencies as j increases. I take $f_{m,1} = 5.43$ Hz, the Nyquist frequency of the MFI dataset. The power of 0.1 overlaps the windows and provides many fits for m over ion-kinetic frequencies. I continue my windowing process as long as $(f_m/3) > 0.01$ Hz, giving us a total of 47 windows, a sufficient number to give adequate frequency resolution to determine the break in the power spectrum. The central frequency of each window, which I associate with each value of m, is taken as the median of the measured wavelet frequencies in that window.

I show an example 92 s spectrum from July 2012 and the results from my fitting procedure in Figure 6.3. There is a change in m from about -1.2 (red dashed line) to -3.8 (blue dashed line) toward higher frequencies, resulting from the transition between the power-laws for the inertial range and the ion-kinetic range. This transition is not a simple step function because of the finite width of the fitting window at the frequency of the spectral break. To estimate f_b, I determine two power-law fits for the inertial and ion-kinetic ranges and then find the frequency at which these intersect. I estimate the power-law for the inertial range by fitting Equation 6.4 over a fixed window of frequencies, $f \in [0.01, 0.1]$ Hz. I do not use the fits from my windowing procedure here because the windows cover a smaller frequency range towards smaller frequencies and with the increasing uncertainty in the power spectrum at these lower frequencies, the values for m do not converge on a constant value. For the ion-kinetic range, I identify the fit from the windowing procedure with the smallest m, i.e., the steepest gradient. The break frequency is then the intercept between these two power-laws:

$$\log_{10}(f_b) = \frac{c_1 - c_2}{m_2 - m_1}, \tag{6.5}$$

where the subscripts 1 and 2 are the values for the inertial and ion-kinetic range, respectively. The black line in Figure 6.3 is my estimate of f_b for the example spectrum using this method, which agrees well with the break in the spectrum. This method is different from the one used in Woodham et al. [2018], which exclusively used the fits for m, resulting in a discrete range of values for f_b. I have updated my algorithm here to provide a more continuous range of values, and therefore, a better estimate of f_b.

Toward higher frequencies in Figure 6.3, the spectrum flattens and m increases. This flattening is due to the increasing contribution of instrumental noise to the signal at these frequencies. To ensure that my estimate for f_b is physical, I determine a cut-off frequency, f_{noise}, where the amplitude of each 92 s spectrum is equal to a signal-to-noise ratio (S/N) of 10 times my noise-floor estimate from Figure 6.2. For the spectrum in Figure 6.3, f_{noise} is given by the grey dashed line. I neglect an estimate of the break frequency if $f_b \geq f_{noise}$. Close to the Nyquist frequency, there is a second decrease in the spectral exponent, which I attribute to artefacts of the CWT.[2]

6.2.4 Quantification of the Helicity Signature

To quantify the coherent helicity signature (see Section 4.3.2) at ion-kinetic frequencies, I fit a Gaussian function to the coherent peak in the helicity spectra at high frequencies,

$$\sigma_m = \frac{1}{\sqrt{2\pi}\sigma_D} \exp\left\{-\frac{(f - f_p)^2}{2\sigma_D^2}\right\}, \tag{6.6}$$

where the fitting parameters are the standard deviation, σ_D, and the mean, f_p, which corresponds to the frequency of the peak in the helicity signature. For the fitting, I set an initial guesses of $f_p = 0.8$ Hz and $\sigma_D = 0.5$. I show in the top panel of Figure 6.4, the power spectrum from Figure 6.3, along with its corresponding helicity spectrum in the bottom panel, both in black. In the bottom panel, I also plot in red the Gaussian fit to the helicity spectrum using Equation (6.6). The red line gives f_p from the fitting, whereas the black line and grey dashed line are f_b and f_{noise}, respectively. I also calculate a threshold frequency at which there is an enhancement in the helicity at ion-kinetic scales, f_h. To estimate this frequency, I calculate the full-width at half-maximum of the Gaussian peak using $\Delta f = \sigma_D \sqrt{8 \ln(2)}$ and then,

$$f_h = f_p - \Delta f/2. \tag{6.7}$$

I use a minus sign to determine f_h bounded towards lower frequencies. This method is independent of whether the peak in helicity is negative or positive. In Figure 6.4, f_h is given by the blue line. Both f_b and f_h are separated by only about 0.1 Hz. From the results of Section 6.2.3, this result implies that both frequencies may be associated with the same plasma scale and therefore,

---

[2] The finite frequency response of the Morlet wavelet acts to smooth the CWT spectrum compared to a Fourier transform, leading to a decrease in power approaching f_N.

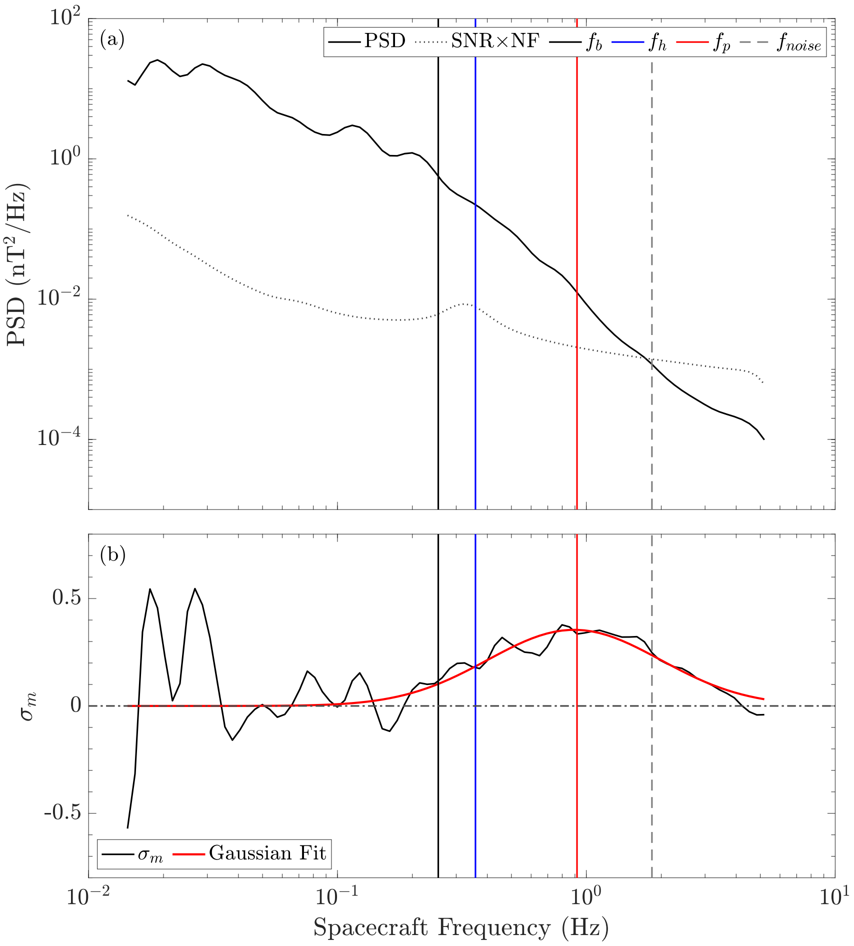

Figure 6.4: (*a*) The example 92 s power spectrum from Figure 6.3 and (*b*) the respective magnetic helicity spectrum and Gaussian fit using Equation 6.6. The frequencies f_b, f_h, f_p, and f_{noise} are given by the black, blue, red, and dashed grey lines, respectively.

due to the same physical process. To investigate this relationship further, I conduct a statistical analysis of f_b and f_h at ion-kinetic scales.

6.3 Statistical Analysis of Solar Wind Fluctuations at Ion-kinetic Scales

6.3.1 Break Frequency

To test the robustness of my fitting algorithm to estimate f_b, I first apply it to consecutive 92 s power spectra for one month, using data from July 2012. Panels (*a*)-(*d*) in Figure 6.5 show time series of the components of **B** in RTN coordinates, the solar wind speed, v_{sw}, proton density, n_p, and β_p, respectively. I smooth **B** using a 51-point median filter here to emphasise the sector structure of the interplanetary magnetic field from the numerous crossings of the heliospheric current sheet, highlighted by the changing sign of the B_R and B_T components. Here, v_{sw} varies between 300 and 700 km/s and n_p from less than 1 cm^{-3} to almost 35 cm^{-3}. There are several periods, often during fast wind intervals, where $\beta_p \sim 1$. At other times β_p typically does not exceed unity and reaches a minimum value of almost 1×10^{-3}. The spacecraft sampled periods of both slow and fast wind, as well as shocks, density enhancements, and transient ejecta, illustrating the variability of the solar wind during this interval, making it ideal for testing my algorithm.

Panel (e) in Figure 6.5 shows a spectrogram of 92 s power spectra from July 2012. In comparison with panels (a)-(d), the spectra and therefore, the turbulent processes in the solar wind, depend on the overall plasma conditions, particularly at high frequencies. Here, white areas indicate data that I have removed, either due to the presence of a large data gap or because the frequencies exceed the defined noise-floor cut-off, f_{noise}. I also plot as solid lines the three characteristic plasma scales, $1/k_c$, d_p, and ρ_p, in magenta, red, and black, respectively. I convert these three scales to frequencies assuming Taylor's hypothesis: $f_L = kv_{sw}/2\pi = v_{sw}/L$, where $L = 2\pi/k$ is the appropriate length scale[3]. According to panel (e), there are several periods during which $f_{noise} < f_L$, emphasising the importance of my noise-floor treatment.

In Figure 6.5(f), I show a contour plot of the spectral exponent, m, versus frequency for the corresponding spectra in panel (e), along with my estimated f_b and f_{kc} in black and red, respectively. Here, I discard values where $f_b \geq f_{noise}$, and also $f_b \leq 0.01$ Hz. This second condition avoids times when the amplitude of fluctuations is so low that a physical break between two power-laws is obscured by noise, and therefore an estimate for f_b by my algorithm is unreliable. I smooth f_b here using a 21-point median filter to improve

---

[3] Here, I use $L = 2\pi d_p$ and $L = 2\pi\rho_p$ so that the units of f_L are s^{-1} since the definitions of these two scales in Section 2.2 gives them in units of m rad^{-1}.

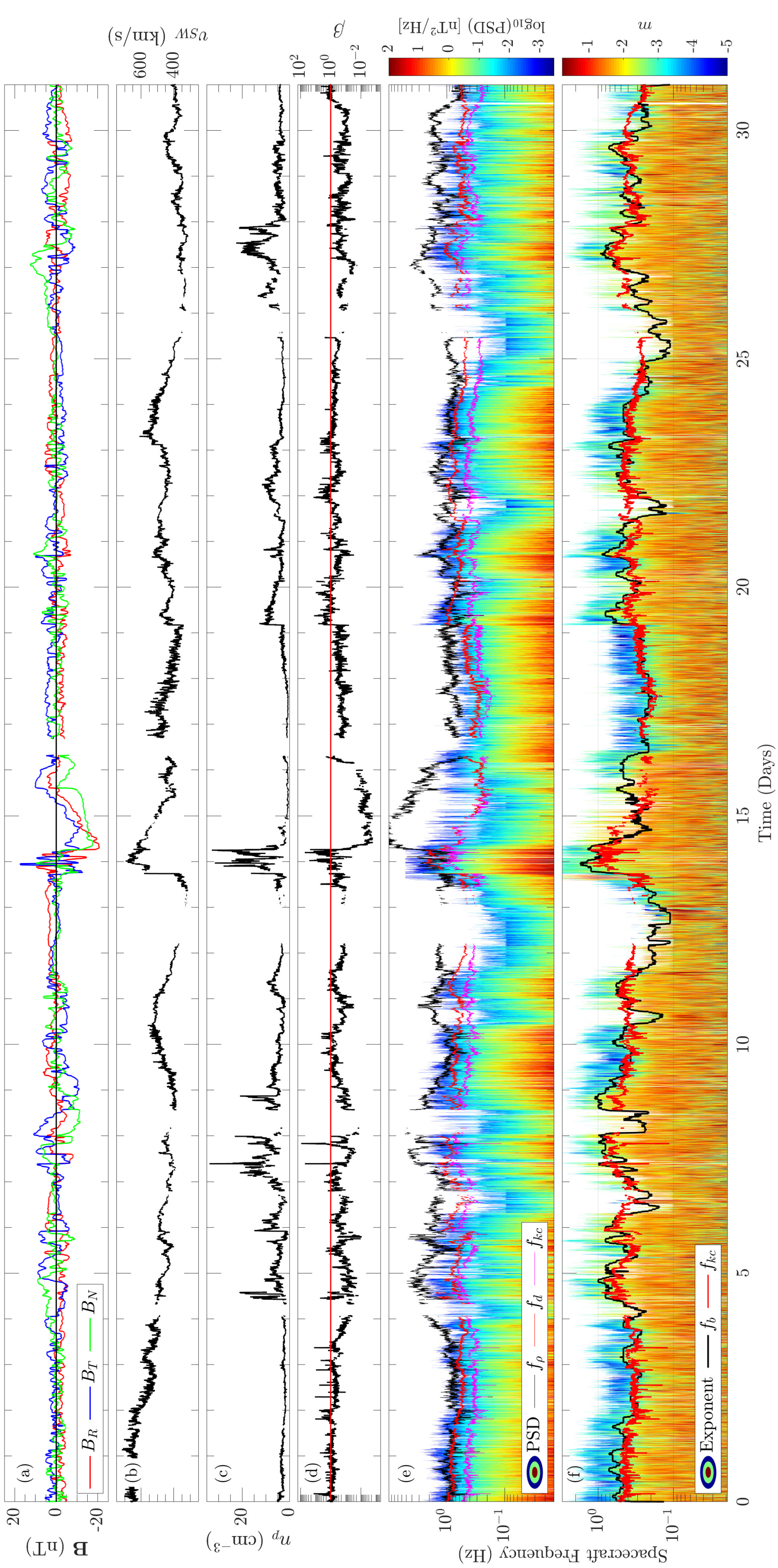

Figure 6.5: July 2012 time series of (*a*) the components of the magnetic field in RTN coordinates, **B**, smoothed using a 51-point median filter; (*b*) the solar wind speed, v_{sw}; (*c*) the solar wind proton density, n_p; and (*d*) β_p. In panel (*d*), the red line indicates $\beta_p = 1$. (*e*) spectrogram of 92 s solar wind magnetic field power spectra. The white areas indicate large data gaps or data with frequencies $f \geq f_{noise}$. I show the characteristic plasma scales, $1/k_c$, d_p, and ρ_p, converted to frequencies using Taylor's hypothesis (see main text) as the solid magenta, red, and black lines, respectively. (*f*) Contour plot of the spectral exponent, m, for the corresponding power spectra in panel (*e*). I also plot f_{kc} in red and the estimated f_b in black for comparison, which I smooth here by a 21-point median filter to improve visualisation of the plot.

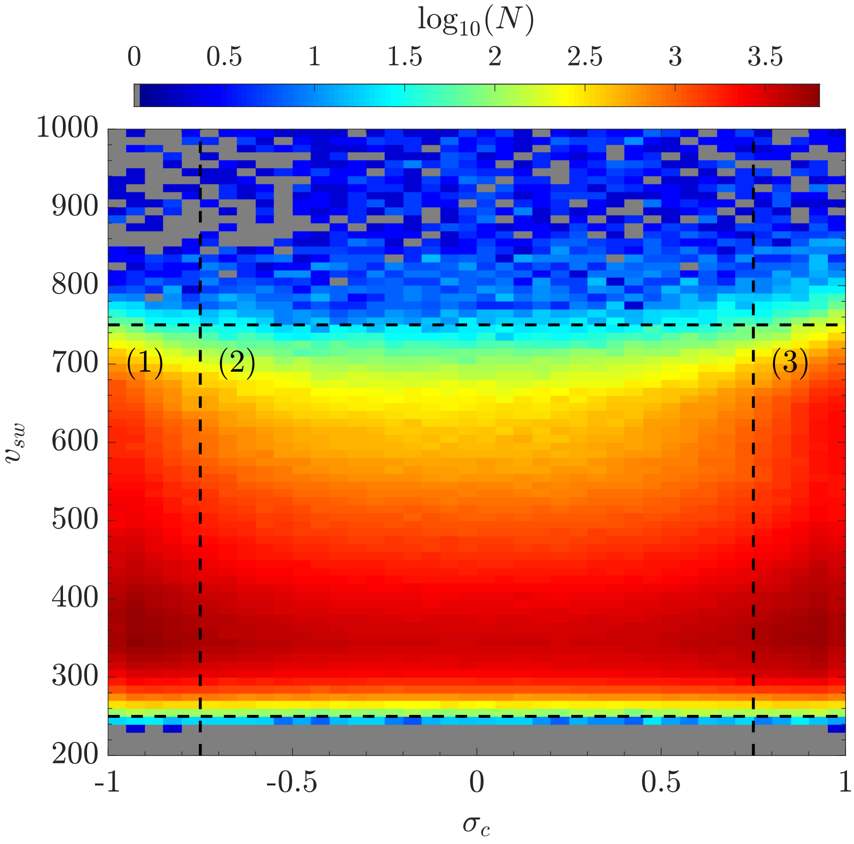

Figure 6.6: Distribution of spectra binned as a function of σ_c and v_{sw}. The regions enclosed by the dashed lines indicate the two regions of this space that I investigate: (1) and (3) Alfvénic wind, and (2) non-Alfvénic wind.

visualisation of the plot. I conclude that my fitting procedure performs an accurate estimate of f_b for the ~29,000 spectra from July 2012, since f_b agrees well with the break in the spectrum from visual inspection of panel (f), where the orange colour (m ~-5/3) transitions to green and blue (m <-2).

I next compare f_b with the three plasma scales as frequencies, f_L, where $L = 1/k_c$, d_p, and ρ_p, extending my analysis to almost 14 years of data, from June 2004-October 2018. I calculate ~4,600,000 power spectra, estimate f_b for each and compare it to the corresponding values for the characteristic plasma scales, f_L. To investigate differences due to the nature of the fluctuations in the solar wind, I determine thresholds using σ_c to categorise solar wind data. In Figure 6.6, I bin the number of spectra as a function of σ_c and v_{sw}. The majority of data splits into three groups: fast Alfvénic wind, slow Alfvénic wind and slow non-Alfvénic wind. I focus here on just Alfvénicity and categorise the wind as Alfvénic with $|\sigma_c| \geq 0.75$ (regions 1 and 3 in Figure 6.6) or non-Alfvénic with $|\sigma_c| < 0.75$ (region 2 in Figure 6.6). I exclude any data with $v_{sw} > 750$ km/s or $v_{sw} < 250$ km/s, in particular to neglect very large wind speeds that often arise from CMEs. There are few spectra (0.22% of the total number of spectra) associated with these values for v_{sw}. I also filter the SWE proton data to remove any unreliable data (see Section 5.3.5), neglecting measurements where $\psi_B > 15°$ (3.44%), $\theta_B > 60°$ (5.83%), and $w_{p,\perp/\parallel} < 15$ km/s (5.91%).

Figure 6.7 shows two-dimensional histograms for f_b as a function of f_{kc}, f_d, and f_ρ in the top, middle, and bottom rows, respectively. I show the results for all data and then separate according to non-Alfvénic and Alfvénic wind in the left, middle, and right columns, respectively. I normalise each column of the binned data in each plot by the maximum number of spectra in a bin for that column, highlighting the most probable f_b as a function of f_L. I neglect values for f_b when $f_b \geq f_{noise}$ (13.72%), as discussed before. Since my algorithm is automated, there is also a proportion of spectra where my estimate of f_b may be unreliable. To try to exclude these spectra, I limit my data to spectra where $-2 \leq m_1 \leq -1$ and $-4 \leq m_2 \leq -2$ from Equation 6.5. I also omit bins with ≤ 10 spectra to avoid under-sampling. In each panel, the black dashed lines give the line $f_b = f_L$, and similarly the black dotted lines are $f_b = f_L\sqrt{2}$ and $f_b = f_L/\sqrt{2}$. These lines indicate the resolution of the wavelet transform about the line $f_b = f_L$ due to the finite width of the Morlet wavelet in frequency space (i.e., the e-folding frequency, see Section 5.4.3).

To quantify the relationship between f_b and f_L, I conduct a statistical analysis of my dataset. I first calculate the Pearson correlation coefficient,

$$R(f_b, f_L) = \frac{1}{N-1}\sum_{i=1}^{N}\left(\frac{f_{b,i}-\mu_b}{\sigma_b}\right)\left(\frac{f_{L,i}-\mu_L}{\sigma_L}\right), \tag{6.8}$$

where μ is the mean and σ is the standard deviation. The coefficient $R \in [-1, +1]$ measures the linear correlation between f_b and f_L. A value of $R = \pm 1$ indicates a positive or negative linear correlation, respectively, whereas zero

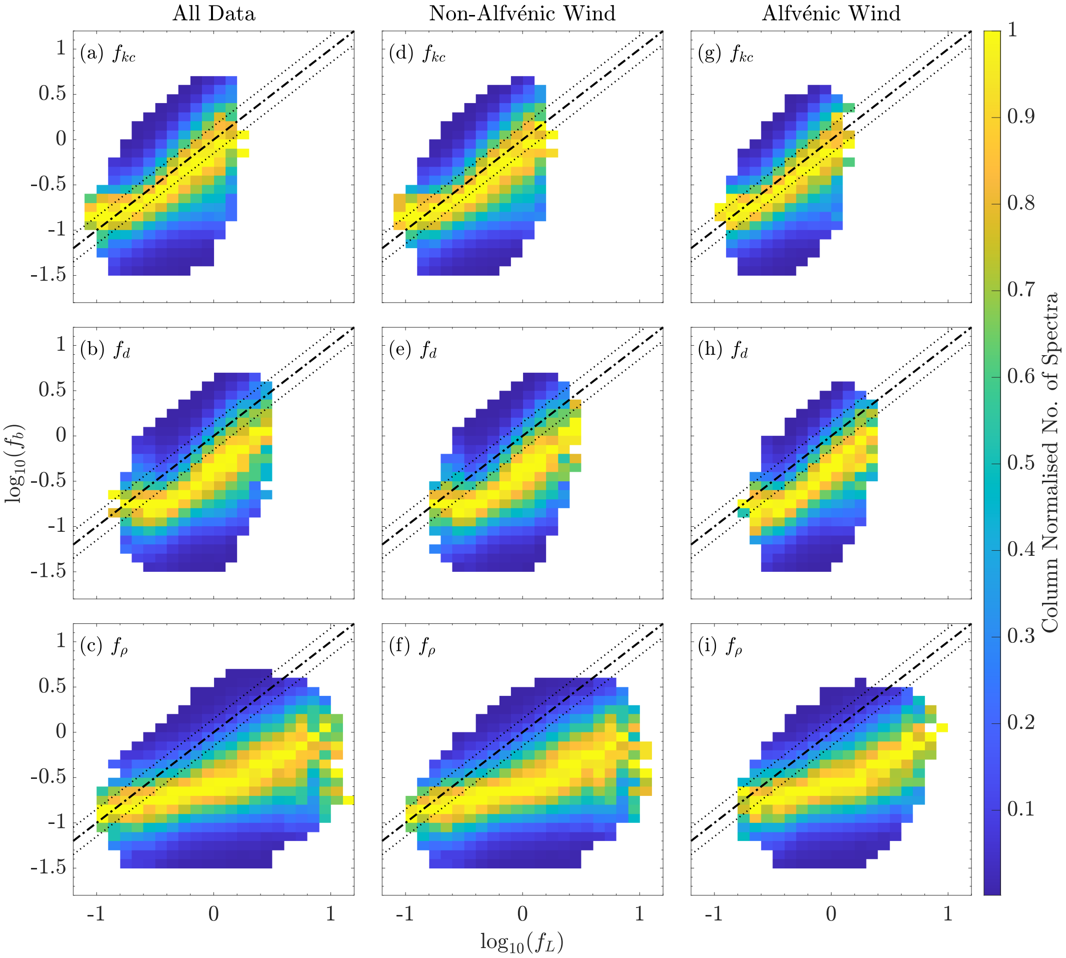

Figure 6.7: (a)-(c) Histograms of the estimated break frequency, f_b, versus the three characteristic plasma scales, converted into frequencies using Taylor's hypothesis - f_L represents f_{kc}, f_d and f_ρ, for each row respectively. (d)-(f) The corresponding results for non-Alfvénic ($|\sigma_c| < 0.75$) intervals. (g)-(i) The corresponding results for Alfvénic ($|\sigma_c| \geq 0.75$) intervals. The colour-bar represents the column-normalised number of spectra. The black dashed lines represent $f_b = f_L$ and similarly, the black dotted lines are $f_b = f_L\sqrt{2}$ and $f_b = f_L/\sqrt{2}$, which give the resolution of the wavelet transform about the line $f_b = f_L$.

indicates no linear correlation. If $|R| = 1$, a linear equation describes the relationship between the variables f_b and f_L. I also define a residual, ξ, which in analogy to the standard deviation is:

$$\xi(f_b, f_L) = \sqrt{\frac{1}{N-1}\sum_{i=1}^{N}\left|f_{b,i} - f_{L,i}\right|^2}, \tag{6.9}$$

where $\xi \geq 0$. The residual gives the difference between my measured f_L and estimated f_b, in other words, a value of ξ closer to zero indicates there is less spread of data about the line $f_b = f_L$. I place more weight here on the statistical significance of ξ over R since a linear relationship does not necessarily imply that $f_b = f_L$. The correlation coefficients are also intrinsically linked because of the similar definitions of the three plasma scales, especially when $\beta_p \sim 1$. As a final test, I count the number of spectra that lie between the two black dotted lines in each panel of Figure 6.7 to determine a percentage of the total number of spectra that satisfy $f_b \simeq f_L$ to within the e-folding frequency. For the total number of spectra, I do not include instances where there are significant data gaps, and where I have discarded values for f_b. For instances where I filter data according to Alfvénicity, the total number of spectra I use is only for that filtered dataset. I give the results of my statistical analysis in Table 6.2.

For all data, both f_{kc} and f_d have moderate correlations with f_b, with values of $R = 0.44$ and $R = 0.41$, respectively, whereas the correlation for f_ρ is weaker at $R = 0.28$. The lowest residual is $\xi = 0.25$ for f_{kc}, while for f_d it is $\xi = 0.43$ and for f_ρ it is even higher at $\xi = 0.96$. These values show that the cyclotron resonance scale, $1/k_c$, is most closely associated with the spectral break (i.e., closest to $f_b \simeq f_L$). This finding is supported by 39.63% of the total number of spectra in my dataset falling within the two red dashed lines for f_{kc} in Figure 6.7(a). In contrast, the percentages are only 16.67% for f_d in panel (b) and 8.63% for f_ρ in panel (c). Therefore, the proton gyro-radius, ρ_p, has a poor relationship with the break frequency, suggesting that it is least likely to be associated with the spectral steepening.

These findings are similar when I separate the data according to

Table 6.2: Correlation coefficients, residuals, and percentages for f_L and f_b from the data shown in Figures 6.7 and 6.8.

	Plasma Scale L	**Correlation** R	**Residual** ξ	**Percentage** %
All Data	k_c	0.44	0.25	39.63
	d_p	0.41	0.43	16.67
	ρ_p	0.28	0.96	8.63
Non-Alfvénic	k_c	0.44	0.26	38.46
	d_p	0.40	0.45	16.24
	ρ_p	0.28	1.00	8.54
Alfvénic	k_c	0.44	0.24	41.59
	d_p	0.43	0.41	16.90
	ρ_p	0.27	0.88	8.63
$\beta_{p,\perp} \sim 1$	k_c	0.46	0.25	44.29
	d_p	0.47	0.45	15.51
	ρ_p	0.45	0.49	13.56

Alfvénicity. For non-Alfvénic wind, f_{kc} has the highest correlation coefficient at $R = 0.44$ and lowest residual at $\xi = 0.26$. During periods of Alfvénic wind, the residual for f_{kc} is slightly smaller ($\xi = 0.24$) than non-Alfvénic wind and is still the smallest for all three scales. From panels (d) and (g) in Figure 6.7, there is only a small difference visually between the two cases. Also, comparing panels (f) and (g), 41.59% of spectra fall within the resolution limit of my wavelet transform for f_{kc} in Alfvénic wind, which is higher than for non-Alfvénic wind (38.46%). The correlation coefficients for both f_{kc} and f_d in Alfvénic wind are almost equal, at $R \simeq 0.44$, which are only slightly larger than their non-Alfvénic wind values. Transitioning from non-Alfvénic to Alfvénic wind in panels (e) and (h), the percentages of spectra where $f_b \simeq f_d$ increase slightly from 16.24% to 16.90%. From these values, the relationship between f_{kc} and f_b is maintained even with changes in Alfvénicity but is strongest in Alfvénic streams.

According to Equations 2.10 and B.3, $1/k_c$ will coincide with the larger of the two scales, d_p or ρ_p, when $\beta_{p,\perp} \ll 1$ or $\beta_{p,\perp} \gg 1$, respectively, assuming an isotropic temperature (i.e., $\rho_p \simeq \sigma_p$). This expectation is consistent with observations by Chen et al. [2014] showing that the spectral break occurs at

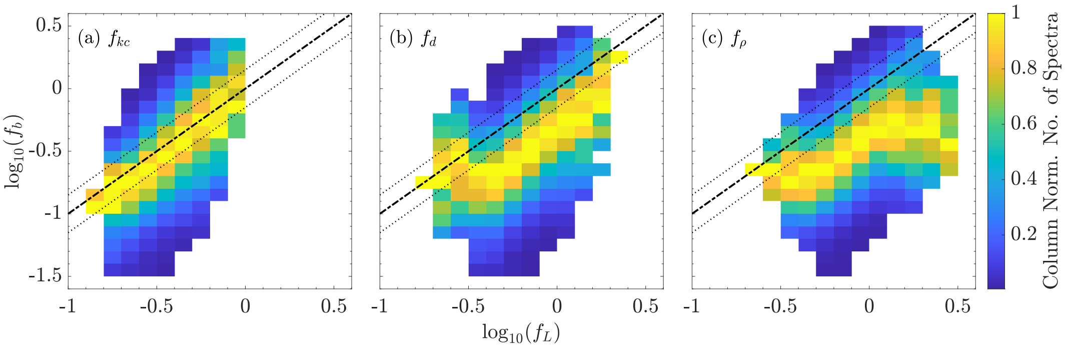

Figure 6.8: Histograms of the estimated break frequency, f_b, versus the three characteristic plasma scales, converted into frequencies using Taylor's hypothesis - f_L represents f_{kc}, f_d and f_ρ, for each panel respectively. The data used are for periods where $0.95 \geq \beta_{p,\perp} \leq 1.05$. The colourbar represents the column-normalized number of spectra. The black dashed lines represent $f_b = f_L$ and similarly, the black dotted lines are $f_b = f_L\sqrt{2}$ and $f_b = f_L/\sqrt{2}$, which give the resolution of the wavelet transform about the line $f_b = f_L$.

d_p for $\beta_{p,\perp} \ll 1$ and at ρ_p for $\beta_{p,\perp} \gg 1$, which they note is consistent with a break at $1/k_c$ in both cases. However, by definition, when $\beta_{p,\perp} \sim 1$, $\rho_p \simeq d_p$ and therefore, $1/k_c \simeq \rho_p + d_p \simeq 2\rho_p \simeq 2d_p$. For periods with $\beta_{p,\perp} \sim 1$ as seen in Figure 6.5(d)-(f), both f_d and f_ρ coincide and f_{kc} is shifted to lower frequencies by about a factor of 2. During these periods, there is a good agreement between f_{kc} and f_b. To address what happens when $\beta_{p,\perp} \sim 1$ quantitatively and clearly show the difference between $1/k_c$ and d_p or ρ_p, I filter the data to include only periods where $0.95 \geq \beta_{p,\perp} \leq 1.05$ and show the corresponding histograms in Figure 6.8. In addition, the results from my statistical analysis are shown in the bottom panel of Table 6.2.

Comparing panels (b) and (c) to (a) in Figure 6.8, my measured f_b is consistently shifted to frequencies lower than f_d and f_ρ, i.e., the yellow enhancement in panels (b) and (c) is below the black dashed-line, but in panel (a) it is closer to the dashed line. These plots show that $1/k_c$ is a more likely candidate for the break scale than d_p or ρ_p, and I quantify this result by calculating R and ξ for this dataset. The correlation coefficients are similar for all three scales ($R \simeq 0.46$), however, f_{kc} has the lowest residual at $\xi = 0.25$, compared to $\xi = 0.45$ for f_d and $\xi = 0.49$ for f_ρ. I note that the statistics for f_ρ

improve considerably when considering only periods of $\beta_{p,\perp} \sim 1$, and are very similar in this case for f_d. Again, there is a high percentage for the number of spectra where $f_b \simeq f_{kc}$ at 44.29%, more than double that of the other two scales.

6.3.2 Helicity Onset and Peak Frequency

I first use my method described in Section 6.2.4 to estimate both f_h and f_p for July 2012 to check that it accurately reproduces the features of the helicity spectra. In Figure 6.9(a)-(d), I show again time series of $\mathbf{B}$, v_{sw}, n_p, and β_p for July 2012. In addition, I plot in panel (e) the proton temperature anisotropy, $T_{p,\perp}/T_{p,\|}$, and in panel (d) a spectrogram of 92 s helicity spectra, σ_m, calculated using Equation 3.37. I also plot f_{kc} in red and my estimated f_h from Equation 6.7 in black, which is smoothed by a 21-point median filter. The persistent enhancement in σ_m at higher frequencies varies between about -0.4 and +0.4. Figure 6.9(a) suggests that the sectoral structure of the solar wind is likely responsible for the changing sign in helicity, which is consistent also with the findings of He et al. [2011]. By comparing panels (b) and (f), I find that the helicity enhancement generally weakens or almost completely disappears during periods of slow solar wind. This result shows that the findings of Bruno & Telloni [2015] appear to apply to large volumes of the solar wind.

By inspecting panel (f) in Figure 6.9, when a coherent helicity signature is present, f_h bounds at lower frequencies this enhancement in σ_m and is well-correlated with f_{kc}. This correlation is consistent with Telloni et al. [2015]. At frequencies $f < f_h$, the helicity fluctuates about zero, as expected for the inertial range of solar wind turbulence [Matthaeus & Goldstein, 1982a], showing either a lack of or no dominant coherent circular polarisation of fluctuations. There is an enhanced signature in the helicity that significantly deviates from the characteristic plasma scales between the 12-14th July, peaking at around 0.2 Hz. I associate this signature with AIC wave ‘storms’ produced by unstable particle distributions [Wicks et al., 2016]. These waves are often Doppler-shifted towards lower frequencies than the spectral break since they

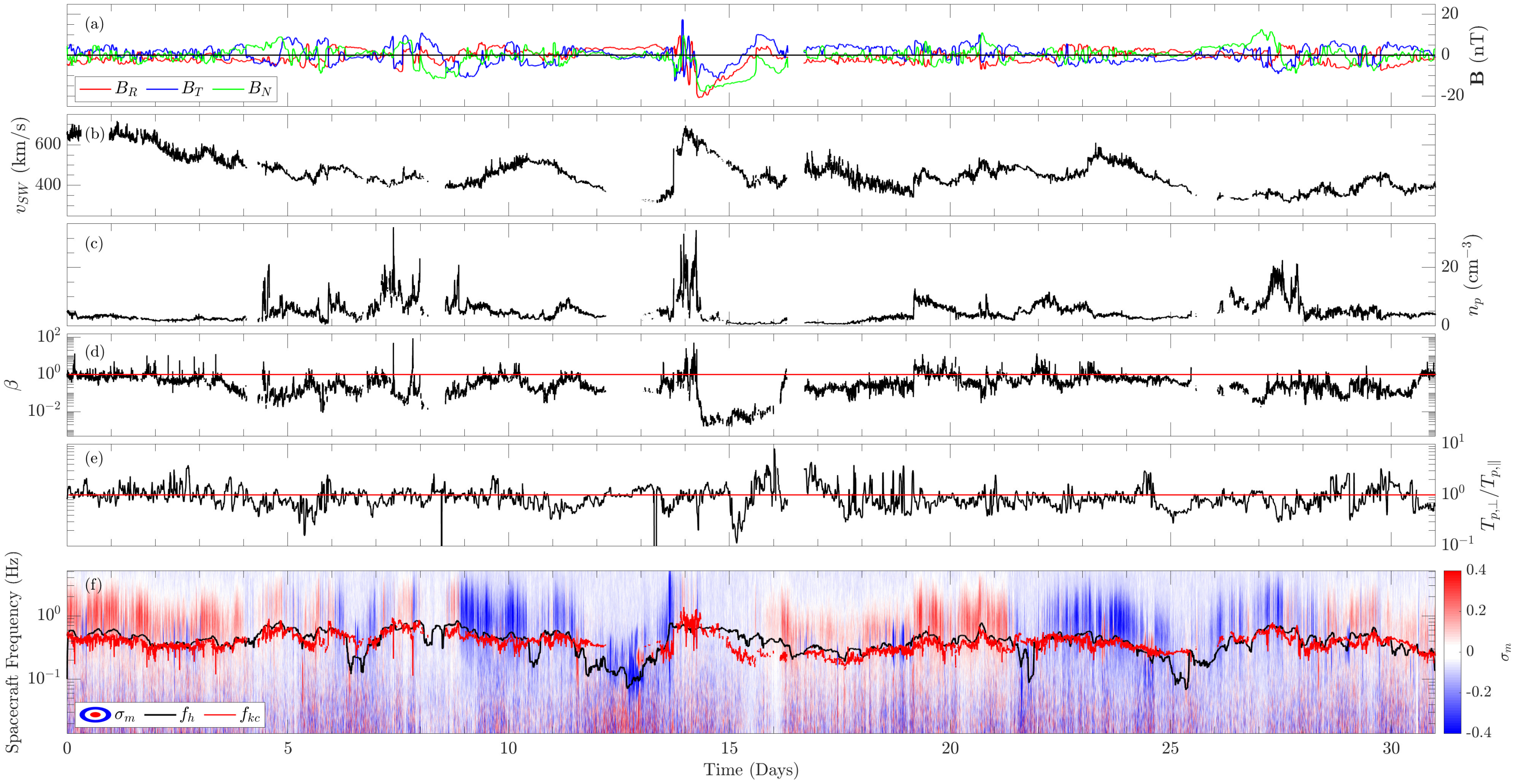

Figure 6.9: July 2012 time series of (*a*) the components of the magnetic field in RTN coordinates, **B**, smoothed using a 51-point median filter to highlight the sector structure of the solar wind, (*b*) the solar wind speed, v_{sw}, (*c*) the solar wind proton density, n_p, and (*d*) β_p, repeated from Figure 6.5, as well as (*e*) proton temperature anisotropy, $T_{p,\perp}/T_{p,\parallel}$. (*f*) Spectrogram of 92 s solar wind magnetic helicity spectra, σ_m, corresponding to the power spectra in Figure 6.5. I also show f_{kc} in red and the estimated helicity onset frequency, f_h, in black, smoothed here by a 21-point median filter to improve visualisation of the plot.

typically propagate towards the Sun, in the opposite direction to the turbulent magnetic fluctuations I consider here [Tsurutani et al., 1994; Jian et al., 2009, 2010, 2014; Roberts & Li, 2015; Roberts et al., 2015; Gary, 2015].

At frequencies $f \gtrsim 1$ Hz, the enhancement disappears, and the helicity returns to a value close to zero. The increasing contribution of instrumental noise at these frequencies, which has random phase, may explain this trend in σ_m. Alternative explanations include aliasing of power at these frequencies [Klein et al., 2014] or the demagnetisation of the protons from the magnetic field [Vasquez & Markovskii, 2012]. The helicity at these frequencies does not change handedness rapidly as a function of frequency like at lower frequencies in Figure 6.9, rather it remains coherent with a value close to zero. While I cannot determine whether this effect is due to the MFI noise-floor or a physical effect, it motivates my fitting of a Gaussian function to the coherent signature. I note that there are times where the helicity signature appears to be cut off at f_N in Figure 6.9. In these rare cases, my Gaussian fit will fail, and my estimates of f_p and f_h will be unreliable. By neglecting spectra where $f_p \geq f_{\mathrm{noise}}$, I try to remove these periods from my dataset. At other times, I find that typically $f_p < f_{noise}$, and therefore, the peak in the helicity signature is physical and that my method to quantify the helicity signature works as required.

I extend my analysis to include data from June 2004-October 2018 in the same way as Section 6.3.1. In Figure 6.10, I show histograms in the same format as Figure 6.7 for f_L against f_h for all data in panels (a)-(c), and then separated into non-Alfvénic and Alfvénic wind in panels (d)-(f) and (g)-(i), respectively. In Figure 6.11, I show in a similar fashion to Figure 6.8, f_L against f_h for periods where $\beta_{p,\perp} \sim 1$. Finally, in Figure 6.12, I plot histograms for f_L against f_p. Here, I discard data with $f_h \geq f_{noise}$ and $f_p \geq f_{noise}$, as well as spectra where $f_h \leq 0.01$ and $f_p \leq 0.01$ Hz. I also exclude values for f_h and f_p where the amplitude of the Gaussian peak $|\sigma_{\mathrm{fit}}| < 0.2$, indicating that my fitting algorithm has likely failed to fit the coherent signature correctly. I provide the results from my statistical analysis for f_L and f_h in Table 6.3 and

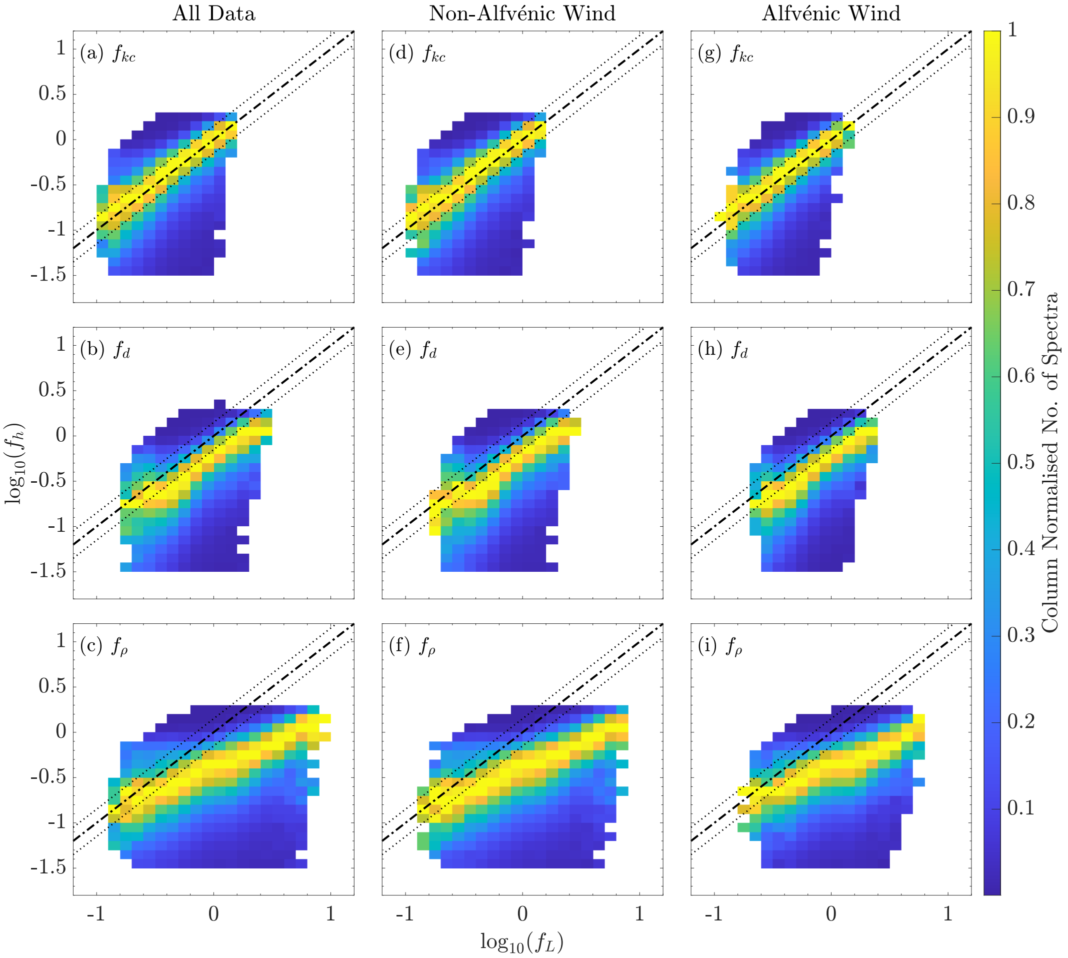

Figure 6.10: (a)-(c) Histograms of the estimated break frequency, f_h, versus the three characteristic plasma scales, converted into frequencies using Taylor's hypothesis - f_L represents f_{kc}, f_d and f_ρ, for each row respectively. (d)-(f) The corresponding results for non-Alfvénic ($|\sigma_c| < 0.75$) intervals. (g)-(i) The corresponding results for Alfvénic ($|\sigma_c| \geq 0.75$) intervals. The colour-bar represents the column-normalised number of spectra. The black dashed lines represent $f_h = f_L$ and similarly, the black dotted lines are $f_h = f_L\sqrt{2}$ and $f_h = f_L/\sqrt{2}$, which give the resolution of the wavelet transform about the line $f_h = f_L$.

Table 6.3: Correlation coefficients, residuals, and percentages for f_L and f_h from the data shown in Figures 6.10 and 6.11.

	Plasma Scale L	**Correlation** R	**Residual** ξ	**Percentage** %
All Data	k_c	0.47	0.20	50.05
	d_p	0.46	0.38	24.81
	ρ_p	0.30	0.86	8.96
Non-Alfvénic	k_c	0.47	0.21	48.21
	d_p	0.45	0.39	24.43
	ρ_p	0.31	0.90	8.95
Alfvénic	k_c	0.47	0.19	52.81
	d_p	0.48	0.37	24.45
	ρ_p	0.28	0.81	8.74
$\beta_{p,\perp} \sim 1$	k_c	0.47	0.20	49.62
	d_p	0.48	0.41	21.15
	ρ_p	0.47	0.45	17.58

for f_L and f_p in Table 6.4.

I find that f_ρ has the worst correlation and largest residuals with f_h regardless of Alfvénicity, which is consistent with Figure 6.10, where the gradient of the peak in data distribution deviates significantly from the black dashed line. I conclude that f_ρ is not directly comparable to f_h. When I consider all data, f_{kc} has the highest correlation coefficient $R = 0.47$ and lowest residual $\xi = 0.20$, compared to $R = 0.46$ and $\xi = 0.38$ for f_d. I find that 50.05% of the total number of spectra fall within the two black dotted lines for f_{kc} in Figure 6.10(a), compared to 24.81% for f_d in panel (b). These percentages are similar for both Alfvénic and non-Alfvénic wind. Besides similar correlation coefficients of about $R \simeq 0.47$ in Alfvénic wind, f_{kc} rather than f_d best satisfies the relationship $f_L \simeq f_h$ from visual comparison of panels (g) and (h). In particular, f_{kc} has the lowest residual of $\xi = 0.19$ for Alfvénic wind, compared to $\xi = 0.21$ in non-Alfvénic wind. Comparing panels (d) and (g), the percentage of spectra within the dotted lines for f_{kc} is higher in Alfvénic wind (52.81%) than in non-Alfvénic wind (48.21%).

As in Section 6.3.1, I also filter the data to include only periods where $0.95 \geq \beta_{p,\perp} \leq 1.05$ and show the corresponding histograms in Figure 6.11, as

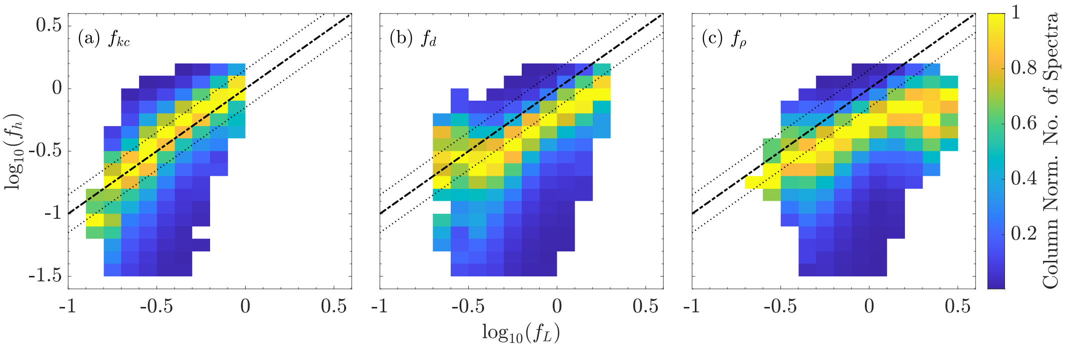

Figure 6.11: Histograms of the estimated break frequency, f_h, versus the three characteristic plasma scales, converted into frequencies using Taylor's hypothesis - f_L represents f_{kc}, f_d and f_ρ, for each column respectively. The data used are for periods where $0.95 \geq \beta_{p,\perp} \leq 1.05$. The colour-bar represents the column-normalized number of spectra. The black dashed lines represent $f_h = f_L$ and similarly, the black dotted lines are $f_h = f_L\sqrt{2}$ and $f_h = f_L/\sqrt{2}$, which give the resolution of the wavelet transform about the line $f_h = f_L$.

well as the results from my statistical analysis in the bottom panel of Table 6.3. My results are similar to those for f_b, showing that f_{kc} best corresponds to f_h. The correlation coefficients are similar ($R \simeq 0.47$) for all three characteristic scales; however, f_{kc} has the smallest residual $\xi = 0.20$, compared to $\xi = 0.41$ for f_d and $\xi = 0.45$ for f_ρ. Again, there is a high percentage of the number of spectra where $f_h \simeq f_{kc}$ at 49.62%, more than double that of the other two scales. I conclude that the onset of the helicity signature is also related to the cyclotron resonant scale and therefore, both the spectral steepening and coherent helicity signature are likely linked to the same physical process: proton cyclotron resonance. This helicity signature is most prevalent when the spacecraft measures Alfvénic wind streams, and therefore, I conclude that there is a stronger relationship between f_{kc} and f_h during these periods, like for f_{kc} and f_b.

From the results for f_p presented in Table 6.4, I find that both f_{kc} and f_d have similar correlation coefficients ($R \simeq 0.58$), regardless of Alfvénicity. There is little difference when comparing visually the three columns in Figure 6.12 for these two scales. However, I find the smallest residuals for f_d, $\xi = 0.43$ for non-Alfvénic and $\xi = 0.40$ for Alfvénic wind streams. In contrast, f_ρ has the

Table 6.4: Correlation coefficients, residuals, and percentages for f_L and f_p from the data shown in Figure 6.12.

	Plasma Scale L	**Correlation** R	**Residual** ξ	**Percentage** %
All Data	k_c	0.58	0.60	14.75
	d_p	0.59	0.42	45.21
	ρ_p	0.34	0.61	47.86
Non-Alfvénic	k_c	0.57	0.59	15.47
	d_p	0.56	0.43	43.35
	ρ_p	0.34	0.66	45.66
Alfvénic	k_c	0.59	0.60	13.66
	d_p	0.62	0.40	48.40
	ρ_p	0.34	0.54	51.08

smallest correlation coefficient $R = 0.34$ but its residuals are comparable to f_{kc} for both non-Alfvénic wind ($\xi = 0.66$) and Alfvénic wind ($\xi = 0.54$). Figure 6.12 shows that f_p correlates with all three scales but there is a significant constant offset in frequency for f_{kc}. When I consider all data, 47.86% of spectra satisfy $f_p \simeq f_\rho$ within the e-folding frequency compared to 45.21% for $f_p \simeq f_d$. These results suggest that f_d best corresponds with the peak in the helicity signature at ion-kinetic frequencies. The additional data used in this Chapter leads to a difference from the conclusions in Woodham et al. [2018], where I instead concluded that f_ρ best corresponds to f_p.

6.4 Discussion and Conclusions

The main result presented in this chapter is the correlation of the cyclotron resonance scale, $1/k_c$, with the spectral steepening of the power spectrum of magnetic field fluctuations and the onset of a coherent magnetic helicity signature at ion-kinetic scales. I find that over almost 15 years of data, the onset of the coherent helicity signature corresponds to $1/k_c$ for 50.05% of the time, within the limits of the e-folding frequency of the Morlet wavelet in my CWT. I also find that 39.63% of the time the spectral break corresponds to $1/k_c$. These correlations hold for most solar wind conditions but are larger for Alfvénic wind streams where the helicity signature is strongest. The helicity

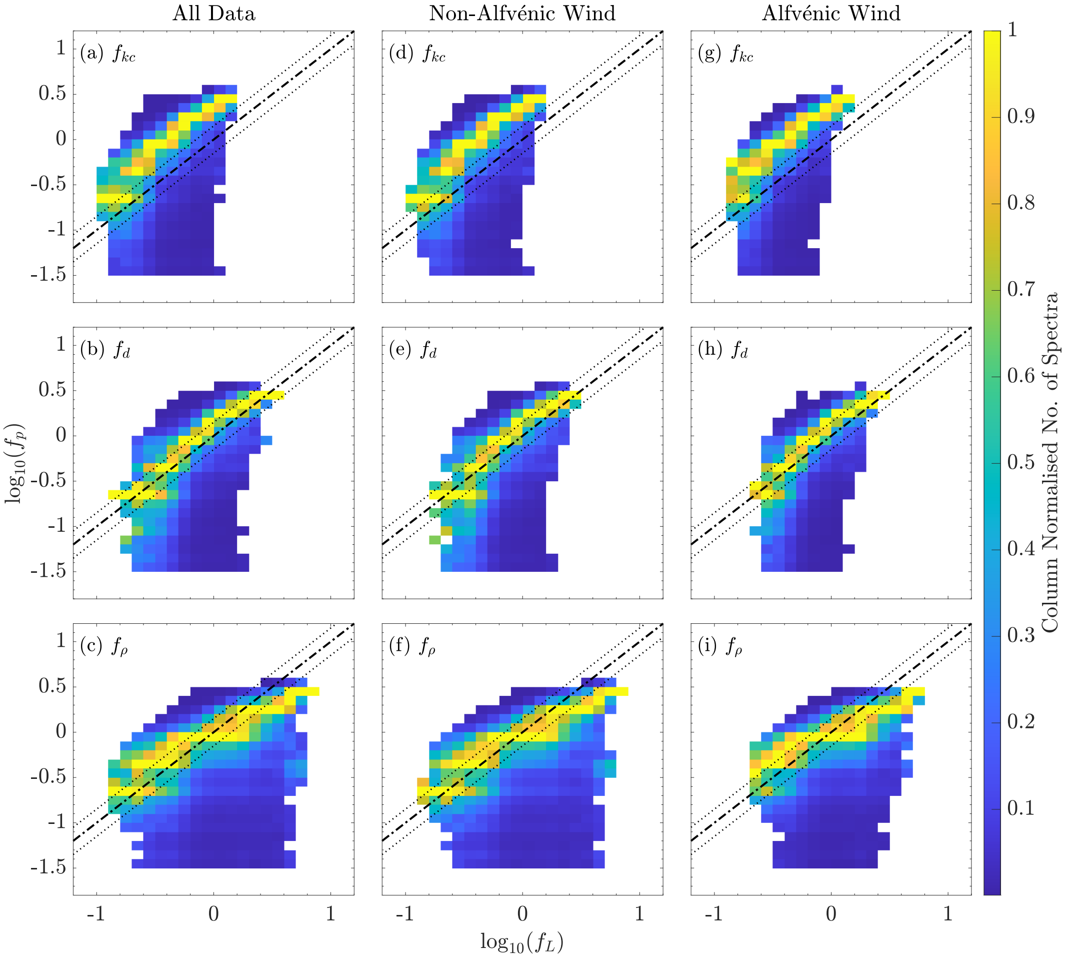

Figure 6.12: (a)-(c) Histograms of the estimated frequency of peak helicity, f_p, versus the three characteristic plasma scales, converted into frequencies using Taylor's hypothesis - f_L represents f_{kc}, f_d and f_ρ, for each row respectively. (d)-(f) The corresponding results for non-Alfvénic ($|\sigma_c| < 0.75$) intervals. (g)-(i) The corresponding results for Alfvénic ($|\sigma_c| \geq 0.75$) intervals. The colour-bar represents the column-normalised number of spectra. The black dashed lines represent $f_p = f_L$ and similarly, the black dotted lines are $f_p = f_L\sqrt{2}$ and $f_p = f_L/\sqrt{2}$, which give the resolution of the wavelet transform about the line $f_p = f_L$.

reaches a maximum at scales comparable to d_p and ρ_p, although it is not as clear which scale, if any, is directly responsible for this spectral feature.

My analysis techniques described in this chapter use power and helicity spectra averaged over 92 s intervals, which does lead to some uncertainty in the spectra. At high frequencies, this uncertainty is smaller since there are a larger number of wavelengths sampled at these smaller scales during the advection of the turbulence past the spacecraft. However, my algorithms to estimate f_b, f_h, and f_p for large intervals of data can still give false determinations due to this uncertainty. For example, uncertainty in the power spectrum may lead to an artificial 'bump' in the power spectrum that my algorithm registers as f_b. The lower percentage of 39.63% for $f_b \simeq f_{kc}$ than 50.05% for f_h may be due to the higher level of uncertainty in measuring the spectral break compared to the onset of the helicity signature. To limit these false determinations, I tested my algorithms on a random sample of 92 s spectra and monthly plots. I do not use averages over longer intervals to limit the blurring of spectral features due to variations in plasma parameters throughout the averaged interval. This ensures that spectral features can be associated with different conditions more accurately.

I ensure that spectral features are physical at high frequencies through my noise-floor treatment, conducting the most accurate investigation of magnetic field fluctuations at ion-kinetic scales with *Wind* to date. I have also accounted for data gaps and data which may be unreliable due to the instrumental effects of the SWE FCs (see Section 5.3.5), as well as data where I identify issues with my estimates for f_b, f_h, and f_p. I use uncertainty in my wavelet transform (i.e., the e-folding frequency) to my advantage to calculate the percentage of data associated with a particular scale. I also remove border effects at low-frequencies due to the wavelet transform (Section 5.4.3). A large amount of data used in this study limits outliers that would skew my statistical analysis. By investigating both the magnetic helicity and spectral break together, I have significantly improved on previous studies that only study the correlation between characteristic scales and one spectral feature.

My results imply that both the spectral steepening and coherent helicity signature are related to the same physical process associated with $1/k_c$, at least a third of the time in the solar wind at ion-kinetic scales. However, the lower percentage of 39.63% for $f_b \simeq f_{kc}$ than 50.05% for f_h indicates that the magnetic helicity may be more closely linked to $1/k_c$ than the spectral steepening, which is likely more sensitive to the processes ongoing at these scales. For example, a peak in the power spectrum may also result from the injection of energy into the magnetic field fluctuations at these scales by kinetic instabilities [e.g., Gary et al., 2015; Wicks et al., 2016]. The spectral steepening does not need to be a simple break between two power-laws at a single frequency, but can also be a range of frequencies where the exponent becomes gradually steeper. This latter case may be more common due to the multiple physical processes occurring at these scales. Therefore, care must be taken when interpreting these results, especially concluding whether dissipation is occurring from the presence of steeper spectral slopes. These drawbacks make interpreting the results of studies measuring the correlation between spectral features and characteristic plasma scales difficult.

One possible interpretation of these results is that proton-cyclotron damping of AIC fluctuations is occurring at these scales, leading to a steeper spectral slope due to dissipation removing energy from the cascade. The resulting helicity signature can then be explained as resulting from the remaining population of KAWs after the AIC waves are damped. The better agreement found in Alfvénic wind between $1/k_c$, the spectral break and the onset of the helicity signature suggests that cyclotron damping primarily occurs in Alfvénic wind streams, which typically have a larger population of AIC waves [Roberts & Li, 2015; Telloni & Bruno, 2016; Lion et al., 2016]. This cyclotron-resonant dissipation is consistent with the shape of proton distributions observed in the fast wind [e.g., Tu & Marsch, 2001; Marsch & Tu, 2001; Tu & Marsch, 2002; Marsch et al., 2004; Heuer & Marsch, 2007; He et al., 2015a,b] and the presence of a transition range [Podesta, 2009; Bourouaine et al., 2010; Bruno et al., 2014; Bruno & Telloni, 2015; Roberts et al., 2017] in Alfvénic wind streams. This interpretation does not rule out the role of other non-linear wave-particle interactions and non-resonant mechanism. Past studies [Leamon et al., 1998a,b, 1999, 2000; Smith et al., 2012] have shown Landau/transit-time damping of ions and electrons likely accounts for the remaining ∼50% of dissipation, which is consistent with my findings that at least 40% of the time cyclotron-resonant damping may be occurring.

The coherent helicity signature disappears or significantly weakens during non-Alfvénic wind periods, in agreement with cyclotron damping [see also Bruno & Telloni, 2015]. However, even with the lack of the coherent helicity signature in non-Alfvénic wind, I still observe a spectral steepening at $1/k_c$. This correlation may persist due to Taylor's hypothesis; fluctuations that give rise to the magnetic helicity at ion-kinetic scales may be present but not measured due to the flow direction of the solar wind past the spacecraft. An alternative explanation for the reduction in the prevalence of a coherent helicity signature in non-Alfvénic wind may be due to different β_p in different wind streams. The dispersion relation for Alfvén waves splits into KAWs or AIC waves at a critical angle to the magnetic field that is dependent on β_p [Gary, 1986, see also Chapter 8], affecting how the helicity signature resulting from Alfvénic fluctuations is observed.

One issue with the interpretation of cyclotron damping of AIC waves is the anisotropic nature of plasma turbulence in the solar wind, which implies a limited role of $k_\parallel$ in the energy cascade in the inertial range due to a higher amount of power in perpendicular wave-numbers [Horbury et al., 2008; Chen et al., 2010a,b; Wicks et al., 2010]. Therefore, it is unlikely that a significant population of AIC waves exists to damp and result in a spectral steepening at these scales. Despite this, I find that the break most often occurs at $k \simeq k_c$ and not $kd_p \simeq 1$ or $k\rho_p \simeq 1$, as clearly shown during periods where $\beta_{p,\perp} \sim 1$. This result is also consistent with studies of turbulence at extreme $\beta_{p,\perp}$ [e.g., Smith et al., 2001a; Chen et al., 2014]. I note that k_c is defined using the dispersion relation of large-scale Alfvén waves (Appendix B). The inclusion of small-scale effects may account for differences between d_p, ρ_p, and $1/k_c$. However, I find that the inclusion an additional $\sin\theta_{vB}$ factor in my definition of the break scale [e.g., Markovskii et al., 2008; Bourouaine et al., 2012; Bruno & Trenchi, 2014; Chen et al., 2014] to account for anisotropic turbulence only slightly improves the correlations for f_d and f_ρ by about 10%. While $k_\perp \gg k_\|$ in the inertial range, the $k_\|$ component has been found to increase around ion-kinetic scales [Bieber et al., 1996; Leamon et al., 1998b; Dasso et al., 2005; Hamilton et al., 2008; Roberts & Li, 2015]. However, this increase may be attributed to instability-driven fluctuations.

Recent studies [Markovskii et al., 2015, 2016; Markovskii & Vasquez, 2016] attribute the coherent helicity signature to the balance of two competing processes. The generation of helicity is due to the increased compressional component of KAW fluctuations at small scales and development of a magnetic field component parallel to the local mean-field [Howes & Quataert, 2010; TenBarge & Howes, 2012; Markovskii & Vasquez, 2013a,b], while the decrease in helicity arises from the demagnetisation of the protons from the magnetic field [Vasquez & Markovskii, 2012]. This interpretation is inconsistent with the interpretation for damping of AIC waves. I also find that the coherent helicity signature disappears towards smaller scales than d_p or ρ_p. This may be due to the demagnetisation of protons [Vasquez & Markovskii, 2012], the increasing balance of sunward and anti-sunward energy fluxes at smaller scales [He et al., 2012a], aliasing of power [Russell, 1972; Klein et al., 2014], or instrumental noise. In the latter case, the helicity signature may form a plateau if the noise-floor is not reached and my Gaussian fit would fail to capture this. While I try to neglect these measurements, this issue makes it difficult to conclude which scales are best associated with the peak. Markovskii et al. [2016] find that the peak is best correlated with the proton gyro-radius modified by the electron beta, β_e: $\rho_p = d_p/\sqrt{\beta_p + \beta_e}$, and is therefore affected by the total plasma pressure. I do not use electron data here, however, if $\beta_p = \beta_e$, then β_e will contribute a maximum factor of $1/\sqrt{2}$, roughly equivalent to the uncertainty in my results from the use of a Morlet wavelet.

Kinetic instabilities may also generate an observed helicity signature at ion-kinetic scales [e.g., Podesta & Gary, 2011a,b], injecting energy into the power spectrum at $1/k_c$. Other studies [e.g., He et al., 2011; Podesta & Gary, 2011b; Klein et al., 2014] have shown that different helicity signatures exist for different wave modes, and this can also be seen in Figure 6.9, where short burst-like intervals of coherent helicity of opposite handedness can be seen embedded within the primary peak and shifted to lower frequencies. These signatures are different to those produced by AIC wave 'storms' at frequencies $f \sim 0.02$ Hz. The correlations of spectral features with $1/k_c$ that I find in this chapter may result from the presence of instabilities as well as the dissipation of turbulence, helping to resolve the issue with cyclotron damping and anisotropy of the turbulent fluctuations. Therefore, it is necessary to split solar wind data according to the magnetic helicity signature of different fluctuations in order to further investigate the physics of the ion-kinetic range. By understanding the origin and nature of the fluctuations at these scales, a better understanding of possible dissipation mechanisms can be gained. In the next chapter, I describe a study in order to investigate these fluctuations in more detail.

Chapter 7

Magnetic Helicity of Solar Wind Fluctuations at Ion-kinetic Scales

In the previous chapter, I showed the need to analyse the nature and origin of turbulent fluctuations to understand more about the physical processes ongoing at ion-kinetic scales in the solar wind. Turbulent fluctuations are not the only source of coherent magnetic helicity at ion-kinetic scales in the solar wind (Section 4.3.2). Several studies [He et al., 2011, 2012a,b; Podesta & Gary, 2011b; Klein et al., 2014; Bruno & Telloni, 2015; Telloni et al., 2015] attribute helicity signatures to instabilities driven by proton temperature anisotropy. These signatures have only recently been directly linked to plasma conditions where these instabilities may be active [Telloni & Bruno, 2016]. However, Telloni & Bruno [2016] only studied a single fast stream and did not investigate the role of beams and ion drifts, which can enhance the growth rates of these instabilities [e.g., Podesta & Gary, 2011a]. By identifying the source of the fluctuations that give rise to the coherent helicity at ion-kinetic scales and the conditions under which they are observed, I can narrow down possible dissipation mechanisms that may be active at these scales.

In this chapter, I use my analysis techniques described in Chapter 6 to measure the wave-vector anisotropy of solar wind fluctuations at ion-kinetic scales. I transform into a local mean-field-aligned coordinate system [Wicks et al., 2012] to separate the different components of magnetic helicity from fluctuations with wave-vector components parallel and perpendicular to the field. This technique is particularly useful because the helicity at ion-kinetic scales shows two distinct signatures, one at quasi-parallel angles and the other at oblique angles [e.g., He et al., 2011; Podesta & Gary, 2011b; Klein et al., 2014]. I identify three distinct populations: quasi-parallel propagating AIC and FMW waves driven by proton temperature anisotropy instabilities and obliquely propagating KAW-like fluctuations from the turbulent cascade. The parallel-propagating fluctuations are preferentially driven in opposite directions due to the presence of an α-particle-proton differential flow. A significant result from this work is the lack of turbulent fluctuations with a significant $k_{\|}$ component at ion-kinetic scales, which restricts the cyclotron damping interpretation from the previous chapter. This work is published in Woodham et al., 2019, Parallel-propagating Fluctuations at Proton-kinetic Scales in the Solar Wind Are Dominated By Kinetic Instabilities, *The Astrophysical Journal Letters*, **884**:L53.

7.1 Measuring Wave-vector Anisotropy with Magnetic Helicity

To separate the components of magnetic helicity arising from different fluctuations at ion-kinetic scales, I use a method described by Wicks et al. [2012]. This method allows me to exploit the anisotropic nature of the magnetic field power spectral tensor of solar wind turbulence and Taylor's hypothesis to recover some wave-vector information of the fluctuations from single-spacecraft measurements. I briefly explain the basis of this technique here.

Since incompressible MHD turbulence has a solenoidal magnetic field, $\nabla \cdot \mathbf{B} = 0$, the power spectral tensor of magnetic field fluctuations (see Section 3.7.2) can be described by four standard tensor forms multiplying four scalar functions [Oughton et al., 1997]. The power spectral tensor from single-

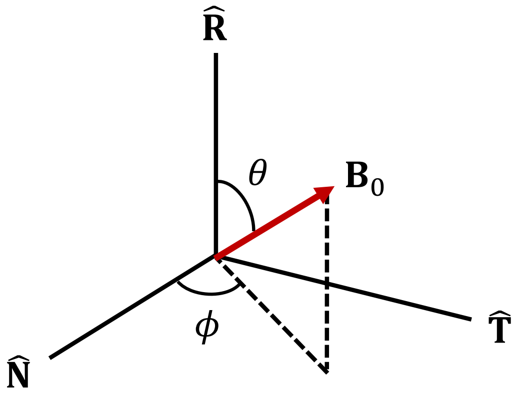

Figure 7.1: RTN co-ordinate system for $\mathbf{B}_0$, defining the angles θ and ϕ. Note, these two angles are different to θ_B and ϕ_B defined in Figure 2.6.

spacecraft measurements, $\mathsf{S}^{(r)}(f_{sc})$, is a reduced form of the full three dimensional tensor, $\mathsf{S}(\mathbf{k})$, as described in Section 3.7.3. This reduction results in an ambiguity in the observed power spectrum that can only be resolved if the full tensor is isotropic. In RTN coordinates, the magnetic field can be described in terms of two angles θ and ϕ (see Figure 7.1),

$$\mathbf{B}_0 = |\mathbf{B}_0|\cos\theta\hat{\mathbf{R}} + |\mathbf{B}_0|\sin\theta\cos\phi\hat{\mathbf{T}} + |\mathbf{B}_0|\sin\theta\sin\phi\hat{\mathbf{N}}, \tag{7.1}$$

where the angles are defined as:

$$\theta = \tan^{-1}\left(\frac{\sqrt{B_T^2+B_N^2}}{B_R}\right) \quad \text{and} \quad \phi = \tan^{-1}\left(\frac{B_N}{B_T}\right). \tag{7.2}$$

Note, these angles are different from θ_B and ϕ_B defined in Section 2.9. For anisotropic turbulence, $\mathsf{S}^{(r)}(f_{sc},\mathbf{v}_{sw})$ depends on the direction of $\mathbf{v}_{sw}$ relative to any symmetry in $\mathsf{S}(\mathbf{k})$. Previous work [Horbury et al., 2008; Podesta, 2009; Wicks et al., 2010; Forman et al., 2011] shows that this symmetry is organised by the direction of the local mean-field, $\hat{\mathbf{B}} = \mathbf{B}_0/|\mathbf{B}_0|$, so that $\mathsf{S}^{(r)}(f_{sc},\hat{\mathbf{B}})$. By defining a field-aligned co-ordinate system (Figure 7.2),

$$\hat{\mathbf{z}} = \hat{\mathbf{b}};\ \hat{\mathbf{y}} = \frac{\hat{\mathbf{z}}\times\mathbf{v}_{sw}}{|\hat{\mathbf{z}}\times\mathbf{v}_{sw}|};\ \hat{\mathbf{x}} = \hat{\mathbf{y}}\times\hat{\mathbf{z}}, \tag{7.3}$$

the transformation from RTN coordinates is $\mathbf{B}^{xyz} = \mathsf{M}\mathbf{B}^{RTN}$, where the trans-

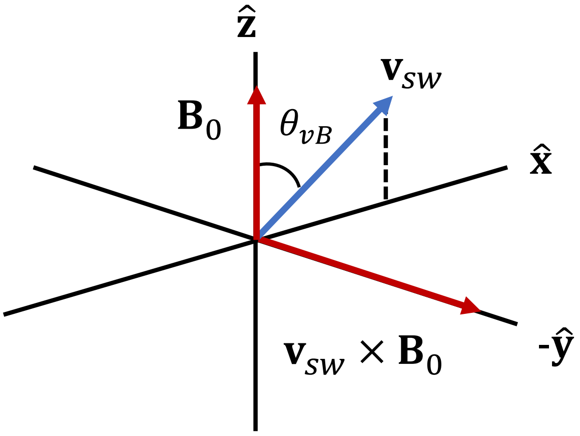

Figure 7.2: Co-ordinate system aligned along the local mean magnetic field.

formation matrix is:

$$\mathsf{M} = \begin{pmatrix} \sin\theta & -\cos\theta\cos\phi & -\cos\theta\sin\phi \\ 0 & \sin\phi & -\cos\phi \\ \cos\theta & \sin\theta\cos\phi & \sin\theta\sin\phi \end{pmatrix}, \tag{7.4}$$

so that $\mathbf{v}_{sw}$ lies in the x-z plane, Wicks et al. [2012] write the different components of the power spectral tensor in terms of the four scalar parameters (or Stokes parameters), $Tor(\mathbf{k})$, $Pol(\mathbf{k})$, $C(\mathbf{k})$, and $ikH(\mathbf{k})$:

$$P_{xx}(\mathbf{k}) = \frac{k_y^2}{k_\perp^2}Tor(\mathbf{k}) + \frac{k_x^2 k_z^2}{k_\perp^2 k^2}Pol(\mathbf{k}) + 2\frac{k_x k_y k_z}{k_\perp^2 k}C(\mathbf{k}), \tag{7.5}$$

$$P_{yy}(\mathbf{k}) = \frac{k_x^2}{k_\perp^2}Tor(\mathbf{k}) + \frac{k_y^2 k_z^2}{k_\perp^2 k^2}Pol(\mathbf{k}) - 2\frac{k_x k_y k_z}{k_\perp^2 k}C(\mathbf{k}), \tag{7.6}$$

$$P_{zz}(\mathbf{k}) = \frac{k_\perp^2}{k^2}Pol(\mathbf{k}), \tag{7.7}$$

$$P_{xy}(\mathbf{k}) = \frac{k_x k_y}{k_\perp^2}Tor(\mathbf{k}) + \frac{k_x k_y k_z^2}{k_\perp^2 k^2}Pol(\mathbf{k}) + \frac{(k_y^2 - k_x^2)k_z}{k_\perp^2 k}C(\mathbf{k}) + ik_z H(\mathbf{k}), \tag{7.8}$$

$$P_{xz}(\mathbf{k}) = -\frac{k_x k_z}{k^2}Pol(\mathbf{k}) - \frac{k_y}{k}C(\mathbf{k}) - ik_y H(\mathbf{k}), \tag{7.9}$$

$$P_{yz}(\mathbf{k}) = -\frac{k_y k_z}{k^2}Pol(\mathbf{k}) + \frac{k_x}{k}C(\mathbf{k}) + ik_x H(\mathbf{k}). \tag{7.10}$$

Here, the imaginary part of the off-diagonal components of the power spectral tensor are only functions of $H(\mathbf{k})$, which corresponds to the magnetic helicity defined by Equation 3.32. The reduction of $H(\mathbf{k})$ due to single-spacecraft measurements is:

$$\mathrm{Im}\left\{\mathsf{S}_{ij}^{(r)}(f_{sc},\hat{\mathbf{B}})\right\} = \varepsilon_{ij\ell}\iiint \mathbf{k}_m H(\mathbf{k})\delta(2\pi f_{sc} - \mathbf{k}\cdot\mathbf{v}_{sw})\,d^3\mathbf{k}, \tag{7.11}$$

where the indices: $i,j = x,y,z$. The component $\mathsf{S}_{xy}^{(r)}$ gives the helicity of fluctuations with a significant $k_\parallel$ and $\mathsf{S}_{yz}^{(r)}$ the helicity of fluctuations with a significant $k_\perp$. The component $\mathsf{S}_{xz}^{(r)}$ integrates to zero if the fluctuations are axis-symmetric along $\hat{y}$. In analogy with σ_m, the normalised helicity is:

$$\sigma_{ij}(f_{sc}) = \frac{2\,\mathrm{Im}\left\{\mathsf{S}_{ij}^{(r)}(f_{sc})\right\}}{\mathrm{Tr}\left\{\mathsf{S}^{(r)}(f_{sc})\right\}}. \tag{7.12}$$

Therefore, using Equation 7.12, I can separate the different contributions to magnetic helicity from fluctuations propagating quasi-parallel and oblique to $\mathbf{B}_0$, recovering information about the wave-vector of the fluctuations from single-spacecraft measurements.

7.2 Application to Solar Wind Measurements

For this study, I analyse *Wind* magnetic field measurements and ion moments from Jun 2004 to Oct 2018, as described in Chapter 6. I also include α-particle measurements from the SWE Faraday cups here. In addition to the filtering of unreliable SWE data described in Section 6.3.1, I neglect collisionally old wind with $N_c \geq 1$ [Maruca et al., 2013], where:

$$N_c \equiv \frac{R}{u_r \tau_c} = 1.31\times 10^7 \lambda_c R \left(\frac{n_p}{u_{p,r} T_p^{3/2}}\right), \tag{7.13}$$

which estimates the number of collisional timescales for protons that have elapsed during their travel to distance $R = 1$ AU (see also Section 4.1.2). Here,

Table 7.1: The four cases for $\mathbf{k}\cdot\mathbf{B}_{92}$ in the solar wind due to sector structure. Here, σ_L and σ_R give the sign of the magnetic helicity due to left-handed and right-handed fluctuations, respectively. The sign +(-) designates a positive (negative) helicity.

	I	**II**	**III**	**IV**
$\mathbf{B}_{92}$	Out	Out	In	In
$\mathbf{k}$	Out	In	Out	In
σ_L	$-$	$+$	$+$	$-$
σ_R	$+$	$-$	$-$	$+$

τ_c is the proton collisional timescale, $\lambda_c = 9.42 + 0.5\ln(T_p^3/n_p)$ is the Coulomb logarithm for protons, $u_{p,r}$ is the radial bulk velocity for protons in km/s, and n_p is given in cm^{-3}. I note that several assumptions are used to calculate N_c (see Section 4.1.2). Here, only proton-proton collisions are considered, not collisions between protons and other species. The choice of τ_c here is the most appropriate collisional scale for proton temperature anisotropy. I use N_c to filter out solar wind where $T_{p,\perp}/T_{p,\|}$ is close to isotropy due to significant collisional relaxation. This can be seen in Figure 7.3, where I plot the median N_c in the $\beta_{p,\|}$-$T_{p,\perp}/T_{p,\|}$ plane for my entire dataset. I do not expect these data to show the presence of fluctuations from kinetic instabilities and their inclusion in my analysis may act to obscure helicity arising from these fluctuations. Collisionally old wind ($N_c \geq 1$) accounts for 24.75% of my total dataset.

The heliospheric sector structure of the solar wind magnetic field leads to an ambiguity in the sign of the magnetic helicity due to the direction of propagation of the fluctuations with respect $\mathbf{B}_0$. I show in Table 7.1 the four cases for the sign of helicity of left and right-handed fluctuations in the solar wind, where ‘out’ and ‘in’ refer to the anti-sunward and sunward directions, respectively. I calculate the Parker-spiral angle, $\phi_{rB} = \arctan(B_{92,T}/B_{92,R})$, where $B_{92,R}$ and $B_{92,T}$ are the radial and tangential components of $\mathbf{B}_{92}$ in RTN coordinates (see Sections 2.9 and 6.2.1) and show its probability density function (PDF) for almost 15 years of data in Figure 7.4. The distribution

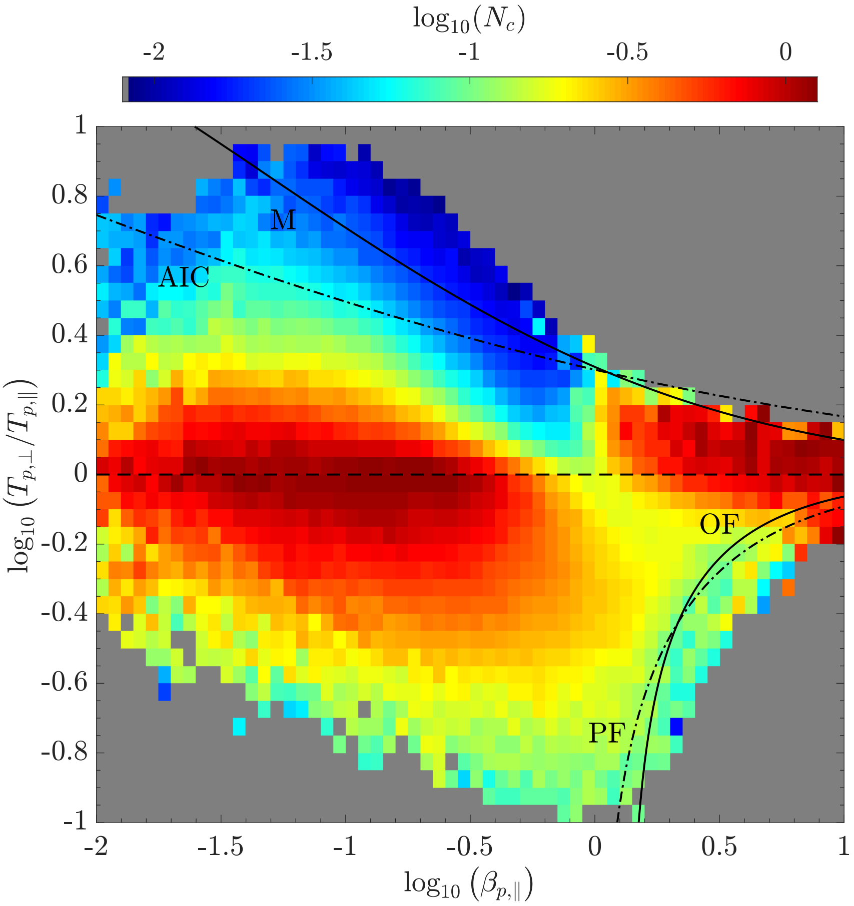

Figure 7.3: Median Coulomb number, N_c, as a function of $\beta_{p,\|}$ and $T_{p,\perp}/T_{p,\|}$. Here, N_c is calculated using Equation 7.13 for proton-proton collisions and a distance of 1 AU from the Sun. Collisionally old wind ($N_c \geq 1$) is primarily associated with plasma periods where $T_{p,\perp} \sim T_{p,\|}$. Also plotted are contours of constant maximum growth rate, $\gamma/\Omega_p = 10^{-2}$, for the proton temperature anisotropy instabilities: AIC, mirror-mode (M), parallel (PF) and oblique firehose (OF).

peaks at about -45° and 135°, showing that sector structure exists even in 92 s averages of the magnetic field. This structure will, therefore, lead to a change in the sign of the helicity when I transform into field-aligned coordinates. To remove this ambiguity, I calculate a running average of ϕ_{rB} over a two day period, which smooths out the large variability in the components of $\mathbf{B}_{92}$ over hourly and shorter timescales. If $\langle\phi_{rB}\rangle > 45°$ or $\langle\phi_{rB}\rangle < -135°$ from the radial direction then I reverse the signs of the $B_{92,R}$ and $B_{92,T}$ components so that inwards fields are rotated outwards, removing the ambiguity in the sign of magnetic helicity due to the direction $\mathbf{B}_{92}$.

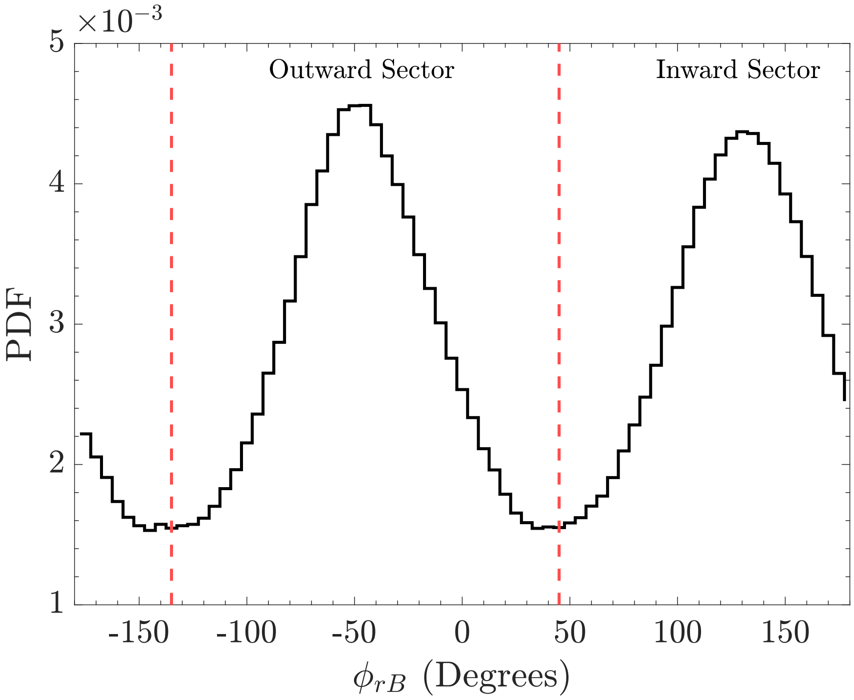

Figure 7.4: Probability density function of ϕ_{rB}, highlighting sector structure of the solar wind magnetic field, $\mathbf{B}_{92}$. There are two peaks at about -45° and 135°, and the red dashed lines separate inward and outward sectors.

I show in Figure 7.5, this procedure for a month of data from July 2012. I plot in panel (*a*) a spectrogram of σ_m from Figure 6.9, (*b*) the B_R and B_T components, (*c*) two day running average $\langle\phi_{rB}\rangle$, and (*d*) a spectrogram of σ_m with sector structure removed. The average ϕ_{rB} in panel (*c*) shows several intervals lasting about five days where it is almost constant, as well as times when it is more variable. When $\langle\phi_{rB}\rangle > 45^\circ$ or $\langle\phi_{rB}\rangle < -135^\circ$, the *Wind* spacecraft measures plasma from an inward sector and when $-135^\circ < \langle\phi_{rB}\rangle < 45^\circ$ plasma from an outward sector. At times where I identify a transition between different sectors, I plot a vertical black line. In panel (*d*) I show the magnetic helicity where the components $B_{92,R}$ and $B_{92,T}$ are inverted for inwards sectors to remove sector structure in the magnetic field measurements. This process works well when $\langle\phi_{rB}\rangle$ is smoothly varying but does sometimes leave remnants of inwards directed fields when $\langle\phi_{rB}\rangle$ is more variable. This failure of my sector structure identification is mainly due to the averaging over a two-day interval, which leads to blurring of a sector change if $\mathbf{B}_{92}$ is highly

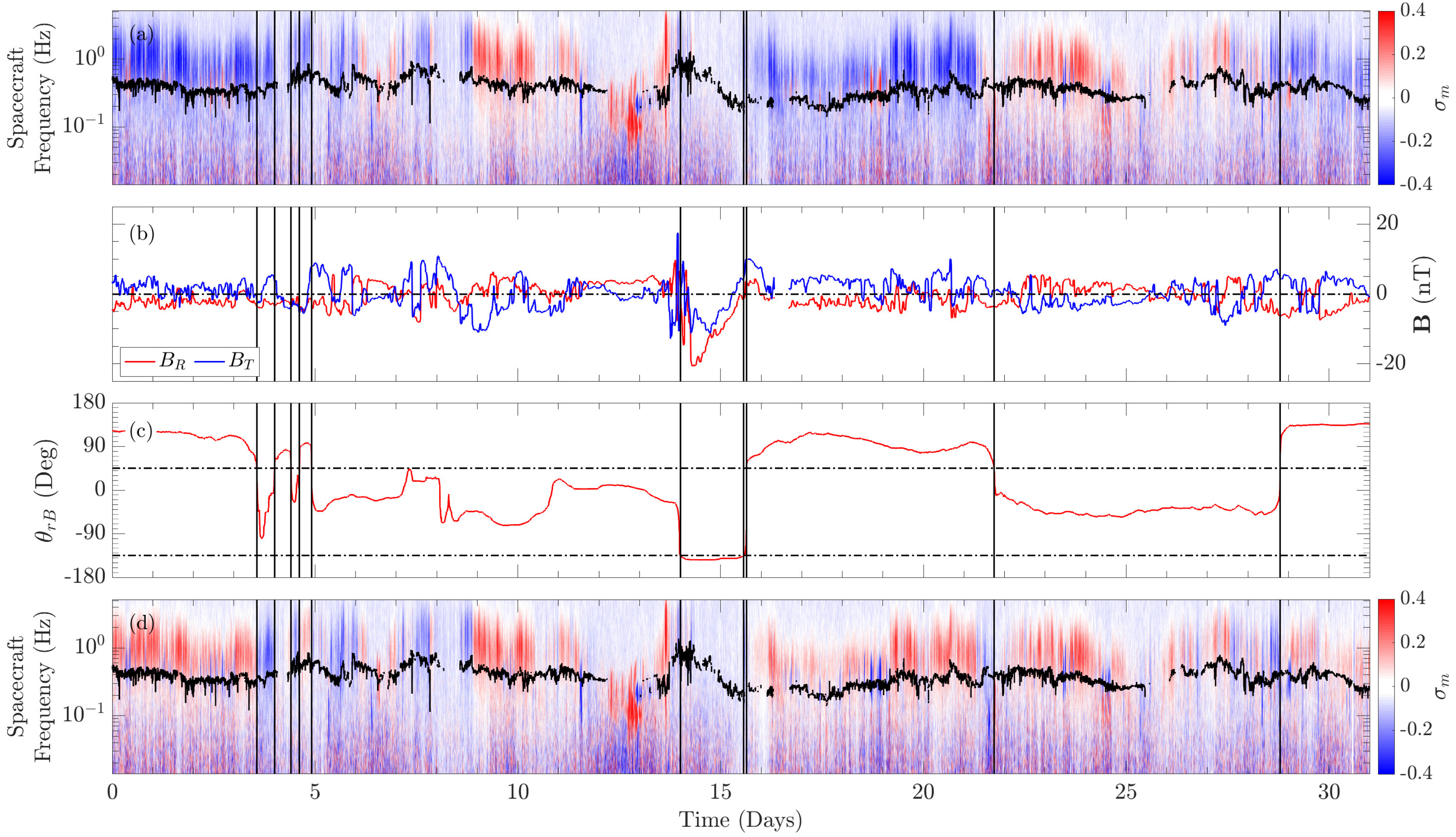

Figure 7.5: (*a*) Spectrogram of 92 s solar wind magnetic helicity spectra, σ_m from Figure 6.9 with f_{kc} in black, (*b*) the components of the magnetic field in RTN coordinates, B_R and B_T, smoothed using a 51-point median filter to highlight the sectoral structure of the solar wind, (*c*) two-day running average $\langle\phi_{rB}\rangle$ where the dashed lines indicate the thresholds $\langle\phi_{rB}\rangle = 45°$ and $\langle\phi_{rB}\rangle = -135°$, and (*d*) spectrogram of σ_m where sector structure has been removed. The vertical black lines indicate a transition between different sectors.

variable, e.g., 4-9th July in Figure 7.5. Despite this, the majority of the time (about 80% in Figure 7.5) my procedure is successful.

Once I have l accounted for sector structure, I transform the 11 Hz magnetic field from MFI into field-aligned coordinates (Equation 7.3) using a mean-field $\mathbf{B}_{92}$. I then compute the CWT to obtain $\mathsf{S}(f_{sc})$ as described in Section 6.2.2 and calculate the magnetic helicity spectra, σ_{ij} using Equation 7.12. In Figure 7.6, I show spectrograms of σ_m, σ_{xy}, σ_{yz}, and σ_{xz} from July 2012, with sector structure removed. Panels (a)-(c) show that σ_m is the integration of σ_{xy}, and σ_{yz} due to Taylor's hypothesis [Forman et al., 2011]: $\sigma_m \sim \sigma_{xy}\cos\theta + \sigma_{yz}\sin\theta$. Most of the signal contributing to σ_m arises from the σ_{yz} component. The third component $\sigma_{xz} \simeq 0$, indicating that the fluctuations are mostly axis-symmetric. There is a small enhancement in σ_{xz} at $f \simeq 0.33$ Hz, the spin frequency of the *Wind* spacecraft, indicating that most of this signal is likely artificial. Following Section 6.2.4, I estimate the amplitude of the σ_{xy} and σ_{yz} spectra at ion-kinetic scales by fitting a Gaussian to the coherent peak in each spectrum at frequencies $f \sim 0.8$ Hz, neglecting measurements where $f \geq f_{noise}$ (see Section 6.2.3). I designate the amplitude of the peak in each σ_{xy} and σ_{yz} spectrum as $\sigma_{\|}$ and $\sigma_{\perp}$, respectively.

To explore the source of solar wind fluctuations at ion-kinetic scales, I bin both $\sigma_{\|}$ and $\sigma_{\perp}$ in $\beta_{p,\|}$-$T_{p,\perp}/T_{p,\|}$ space using logarithmic bins of equal width $\Delta\log_{10}(\beta_{p,\|}) = \Delta\log_{10}(T_{p,\perp}/T_{p,\|}) = 0.05$. I restrict my analysis to $0.01 \leq \beta_{p,\|} \leq 10$ and $0.1 \leq T_{p,\perp}/T_{p,\|} \leq 10$. In my plots, I neglect any bins with fewer than 10 data points to improve statistical convergence. In Figure 7.7, I plot the PDF of the data:

$$\tilde{p} = \frac{n}{N\Delta\log_{10}(\beta_{p,\|})\Delta\log_{10}(T_{p,\perp}/T_{p,\|})}, \tag{7.14}$$

where n is the number of data points in each bin and N is the total number of data points. The PDF accounts for the changing bin size due to logarithmic axes, ensuring that the bins in the distribution are all statistically similar.

In this parameter space I can overplot contours of constant maximum

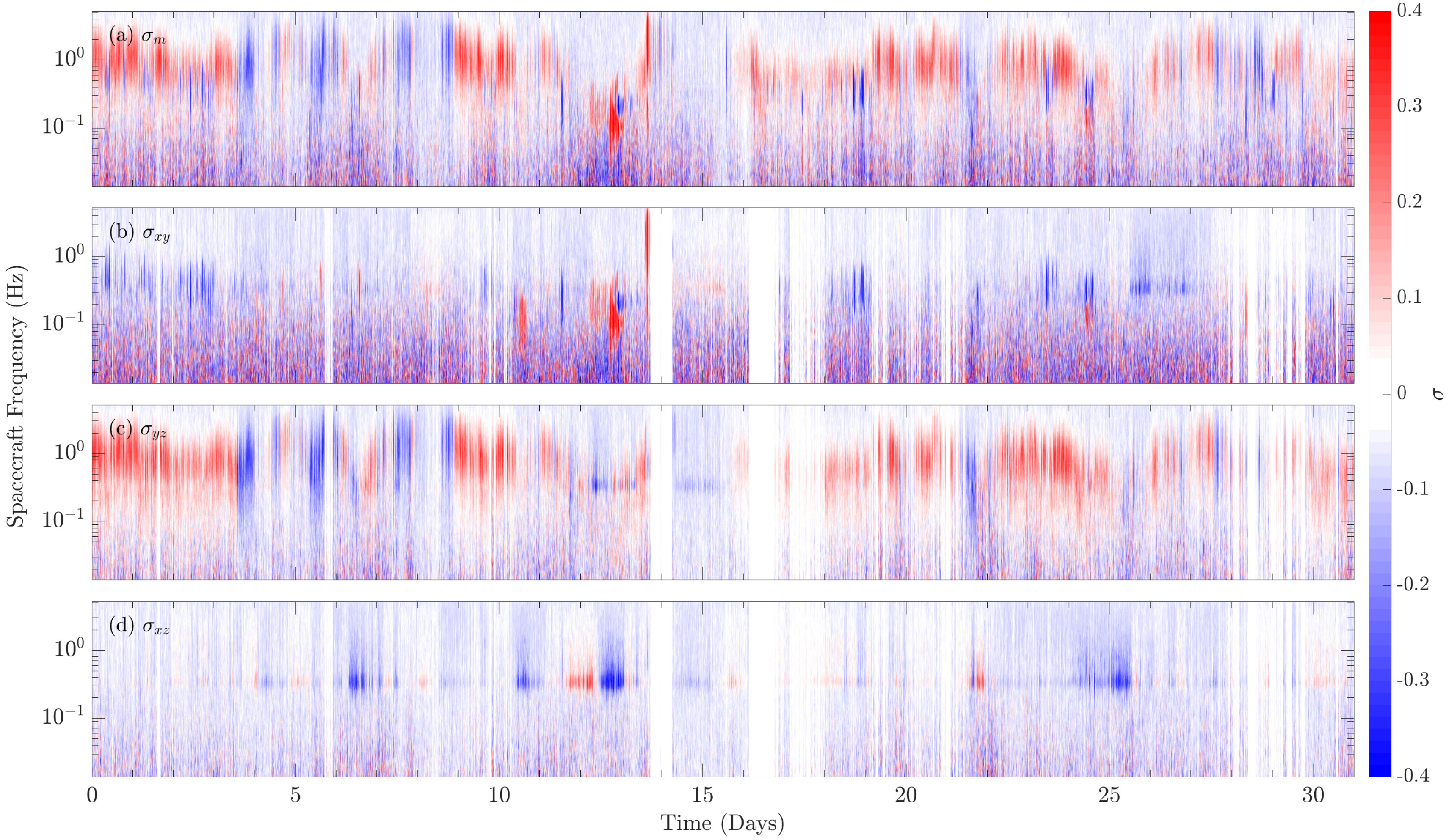

Figure 7.6: July 2012 spectrograms of (*a*) σ_m from Figure 6.9, and in field-aligned coordinates: (*b*) σ_{xy}, (*c*) σ_{yz}, and (*d*) σ_{xz}. Sector structure has been removed using the procedure described in the main text. White areas of the plots for all frequencies indicate where there are data gaps in the SWE measurements.

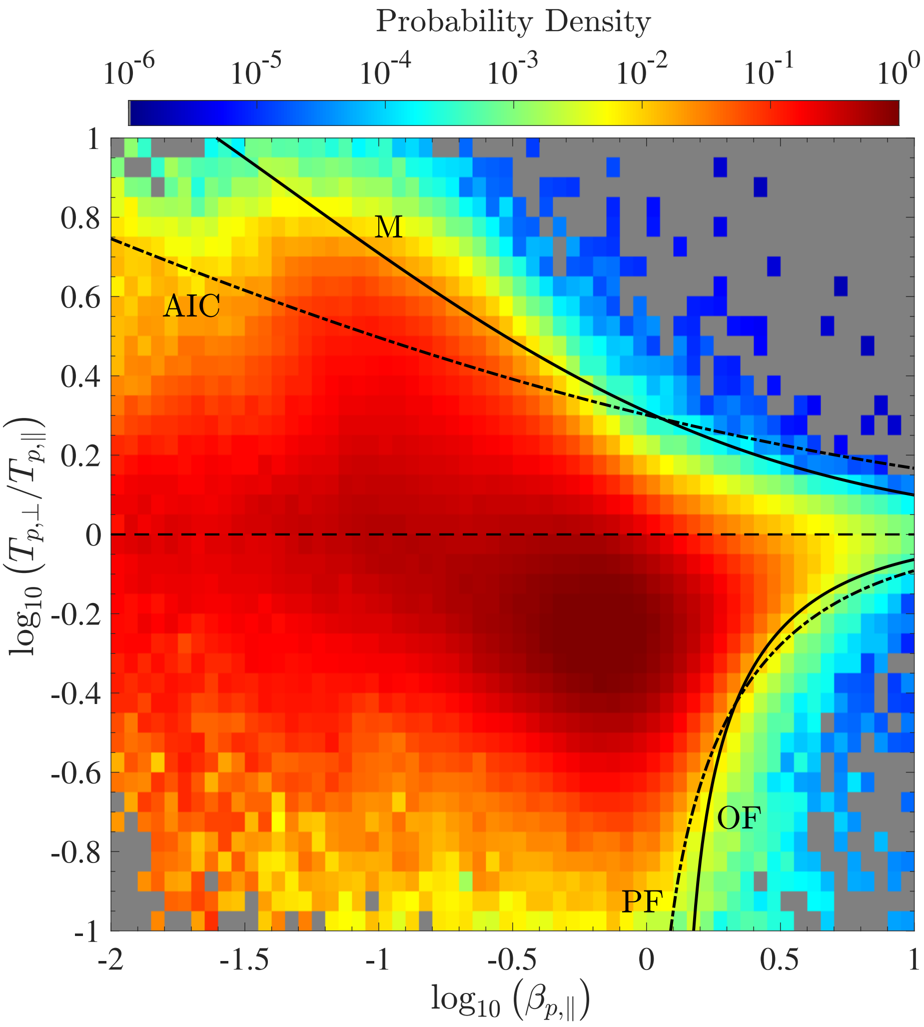

Figure 7.7: Probability density distribution of data across $\beta_{p,\parallel}$-$T_{p,\perp}/T_{p,\parallel}$ space with plotted contours of constant maximum growth rate, $\gamma/\Omega_p = 10^{-2}$, for the proton temperature anisotropy instabilities: AIC, mirror-mode (M), parallel (PF) and oblique firehose (OF).

growth rate, γ_m/Ω_p, for the four kinetic instabilities driven by proton temperature anisotropy: AIC, mirror-mode, parallel firehose and oblique firehose. To calculate these contours I use the results of a code (see Maruca et al. [2012a] and references therein) that uses linear Vlasov-Maxwell analysis (see Chapter 2 and Gary [1993]) to solve the kinetic dispersion relation for growing modes at different values of $\beta_{p,\parallel}$ and $T_{p,\perp}/T_{p,\parallel}$. The code assumes a homogeneous, magnetised, collisionless plasma with bi-Maxwellian species in the absence of any relative flow between them. While the solar wind is often inhomogeneous and there is significant evidence of drifts between different particle species (see Sec-

Table 7.2: Results from fitting Equation 7.15 to contours of different maximum growth rates γ_m/Ω_p for the Alfvén ion-cyclotron (AIC), mirror-mode (M), parallel firehose (PF), and oblique firehose (OF) instabilities.

Instability	Growth Rate γ_m/Ω_p	Fit Parameters a	b	c
AIC	10^{-3}	0.8939	-0.0123	0.3612
	10^{-2}	1.0009	-0.0000	0.3298
	10^{-1}	1.7496	0.0072	0.3767
M	10^{-3}	0.7833	-0.0057	0.6405
	10^{-2}	1.0410	-0.0039	0.6078
	10^{-1}	2.4523	0.0362	0.4435
PF	10^{-3}	-1.4456	-0.7047	0.8994
	10^{-2}	-1.5039	-0.5644	0.8783
	10^{-1}	-0.8088	1.4817	0.4188
OF*	10^{-3}	-	-	-
	10^{-2}	-1.3057	0.0362	0.9596
	10^{-1}	-1.0866	0.5069	0.5357

*There is no discernable difference between the contours $\gamma_m/\Omega_p = 10^{-3}$ and $\gamma_m/\Omega_p = 10^{-2}$ for the oblique firehose instability.

tion 4.2), these assumptions serve to provide estimates for the growth rates of the instabilities to provide context when interpreting my results. The plasma consists of protons, α-particles and electrons, with parameters for typical solar wind conditions: $v_A/c = 2\times10^{-4}$, $T_{e,\perp}/T_{e,\parallel} = 1$, $T_{\alpha,\parallel}/T_{p,\parallel} = 4$, $T_{e,\parallel}/T_{p,\parallel} = 1$, and $n_\alpha/n_p = 0.05$. From the code output, contours can be fit for different values of γ_m/Ω_p in the $\beta_{p,\parallel}$-$T_{p,\perp}/T_{p,\parallel}$ plane using the analytical model proposed by Hellinger et al. [2006]:

$$\frac{T_{p,\perp}}{T_{p,\parallel}} = 1 + \frac{a}{\left(\beta_{p,\parallel} - b\right)^c}, \tag{7.15}$$

where a, b, and c are the fit parameters (see also Section 2.7). I present in Table 7.2 the values for these 3 fit parameters for each of the four proton temperature anisotropy instabilities and different values of γ_m/Ω_p. In Figure 7.7, I plot the contours $\gamma_m/\Omega_p = 10^{-2}$ for the four proton temperature anisotropy instabilities. The distribution is in agreement with many other studies [e.g., Hellinger et al., 2006; Bale et al., 2009; Matteini et al., 2007], showing that at 1 AU, the solar wind proton temperature anisotropy is well-constrained by these instabilities.

7.3 Results

The presence of an α-particle drift with respect to the proton core can break the symmetry of the proton VDFs. Linear Vlasov-Maxwell theory shows that for a drift $v_d < v_A$ along $\mathbf{B}_0$, the growth rates of the AIC and parallel firehose temperature anisotropy instabilities are suppressed in the $-v_\parallel$ and $v_\parallel$ directions, respectively [Podesta & Gary, 2011a,b]. Therefore, $\mathbf{v}_d$ directed anti-sunward leads to a preferential driving of AIC and FMW waves in the anti-sunward and sunward directions, respectively. The propagation of AIC and FMW modes in different directions leads to sign changes in the helicity of these waves when $\sigma_\parallel$ is transformed from the plasma-frame to the spacecraft-frame. The possible cases for the sign of $\sigma_\parallel$ due to these fluctuations are summarised in Table 7.1. Since I have accounted for sector structure, only cases I and II are relevant here, and therefore, I hypothesise that $\sigma_\parallel < 0$ for both AIC and FMW modes present at ion-kinetic scales in the solar wind.

To test this hypothesis, I plot in Figure 7.8, the median $\sigma_\parallel$-value across the $\beta_{p,\parallel}$-$T_{p,\perp}/T_{p,\parallel}$ plane. The black dashed-lines show contours of constant γ_m/Ω_p for the AIC and parallel firehose instabilities, which have greater growth rates along $\mathbf{B}_0$. The solar wind plasma occupies a significant extent of parameter space in the regions unstable to both instabilities, as widely reported in the literature [Hellinger et al., 2006; Bale et al., 2009; Maruca et al., 2012a]. In these regions of parameter space, there are two distinct signatures at $T_{p,\perp} > T_{p,\parallel}$ and $T_{p,\perp} < T_{p,\parallel}$ where the median $\sigma_\parallel$ assumes more negative values. These signatures indicate the presence of coherent fluctuations that I attribute to growing modes from these instabilities. The minimum helicity is about $\sigma_\parallel \simeq -0.6$ for the AIC modes and $\sigma_\parallel \simeq -0.4$ for the FMW modes. Since $\sigma_\parallel < 0$ corresponds to left-handed helicity in the spacecraft frame, Figure 7.8 indicates

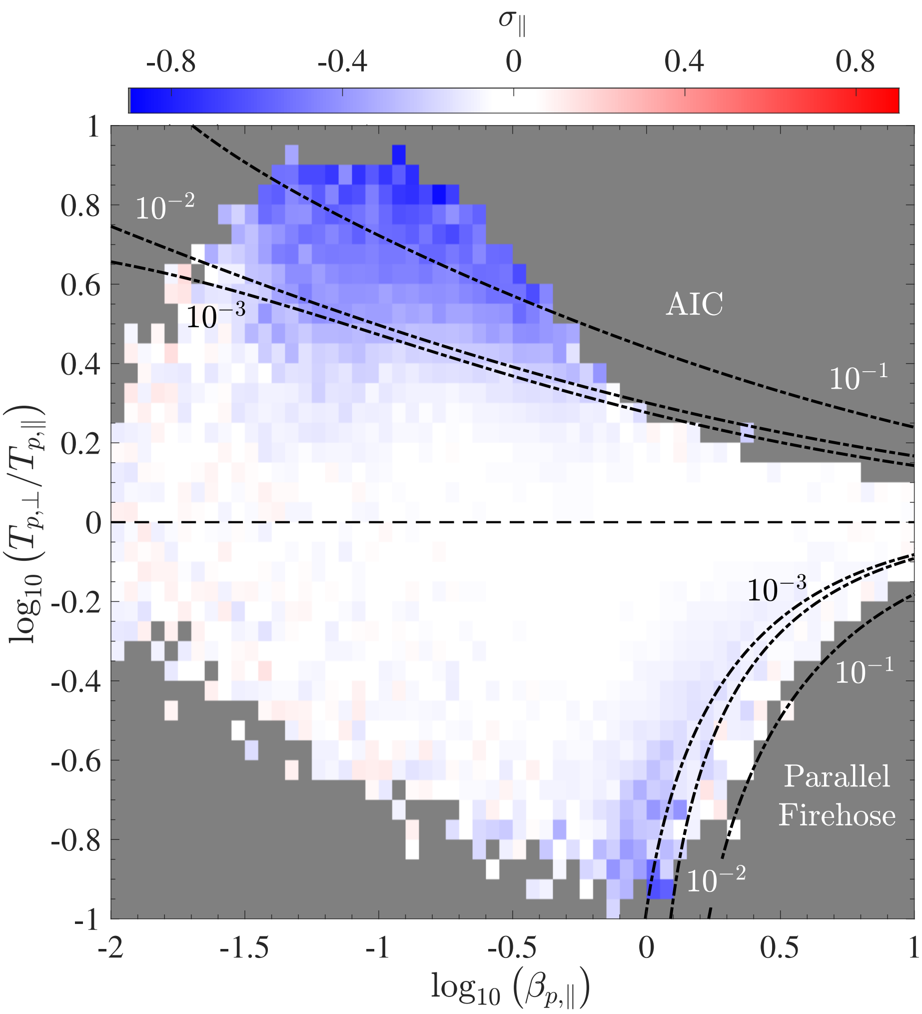

Figure 7.8: Median $\sigma_\|$ across the $\beta_{p,\|}$-$T_{p,\perp}/T_{p,\|}$ plane with contours of maximum growth rate, γ_m/Ω_p, for the AIC and parallel firehose instabilities.

that AIC modes are preferentially driven anti-sunward and that FMW modes are preferentially driven sunward. This result is consistent with my predictions as well as observations of quasi-parallel propagating waves in the solar wind [Tsurutani et al., 1994; Jian et al., 2009, 2010; He et al., 2011, 2012a,b; Podesta & Gary, 2011b; Klein et al., 2014; Jian et al., 2014; Bruno & Telloni, 2015; He et al., 2015a; Telloni et al., 2015; Telloni & Bruno, 2016; Wicks et al., 2016; Zhao et al., 2018, 2019]. In regions of parameter space that are stable to the parallel instabilities, $\sigma_\| \simeq 0$, which indicates a lack of coherence in the magnetic field fluctuations at ion-kinetic scales.

In Figure 7.9, I plot the median value of $\left|v_{d,\|}\right|/v_A$, the α-particle parallel

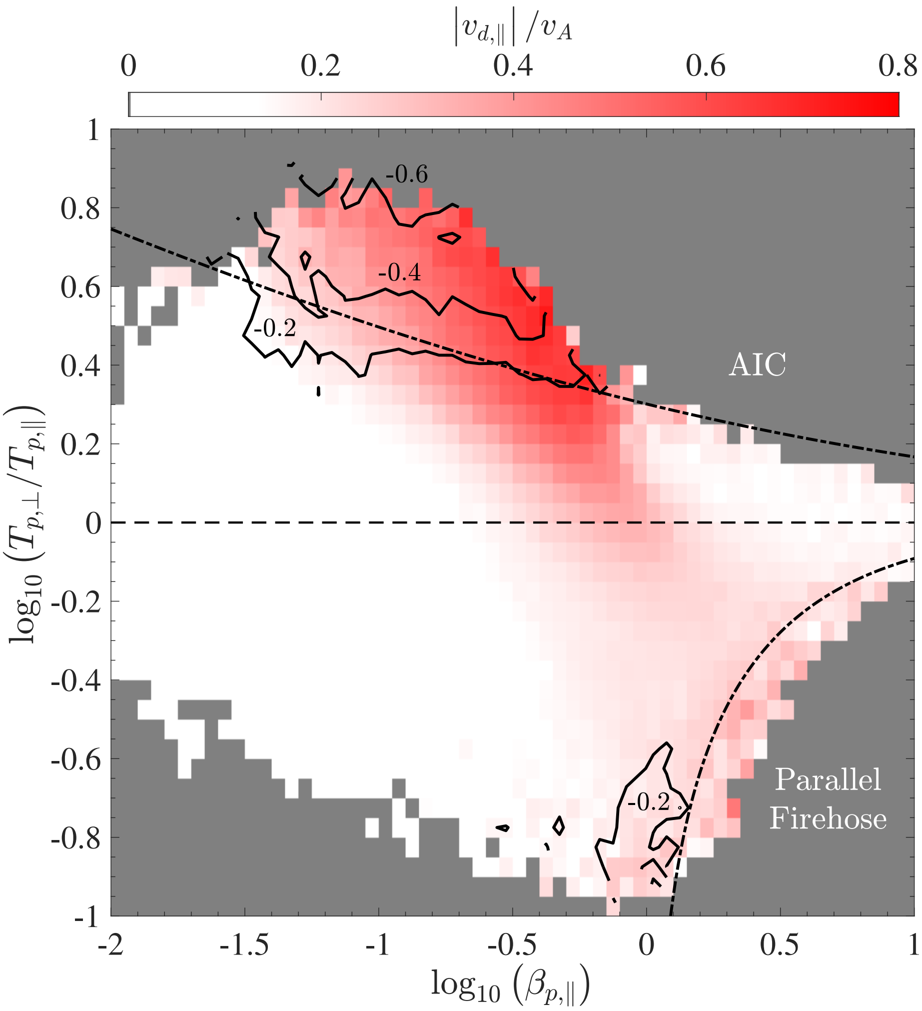

Figure 7.9: Median field-aligned α-particle proton drift, $\left|v_{d,\parallel}\right|/v_A$, across the $\beta_{p,\parallel}$-$T_{p,\perp}/T_{p,\parallel}$ plane with contours of constant maximum growth rate, $\gamma_m/\Omega_p = 10^{-2}$, for the AIC and parallel firehose instabilities. I also plot contours of constant $\sigma_\parallel$ from Figure 7.8 for reference.

drift speed normalised by the Alfvén speed, across the $\beta_{p,\parallel}$-$T_{p,\perp}/T_{p,\parallel}$ plane. I define the drift speed along the magnetic field as $v_{d,\parallel} = \mathbf{v}_d \cdot \mathbf{B}_0 / \left|\mathbf{B}_0\right|$. In the figure, I include contours of constant $\sigma_\parallel$ from Figure 7.8 to show the correlation between $\left|v_{d,\parallel}\right|/v_A$ and $\sigma_\parallel$ in this space. When a significant drift exists close to the unstable regions of the AIC and parallel firehose instabilities, a coherent signature in $\sigma_\parallel$ also exists. The drift is stronger for $T_{p,\perp}/T_{p,\parallel} > 1$, reaching a maximum of $\left|v_{d,\parallel}\right| \simeq 0.6\,v_A$ at $\beta_{p,\parallel} > 0.1$. This peak in $\left|v_{d,\parallel}\right|$ occurs in the region of parameter space dominated by fast wind streams, as seen in Figure 7.10, a plot of median v_{sw} across $\beta_{p,\parallel}$-$T_{p,\perp}/T_{p,\parallel}$ space. For parallel firehose unstable

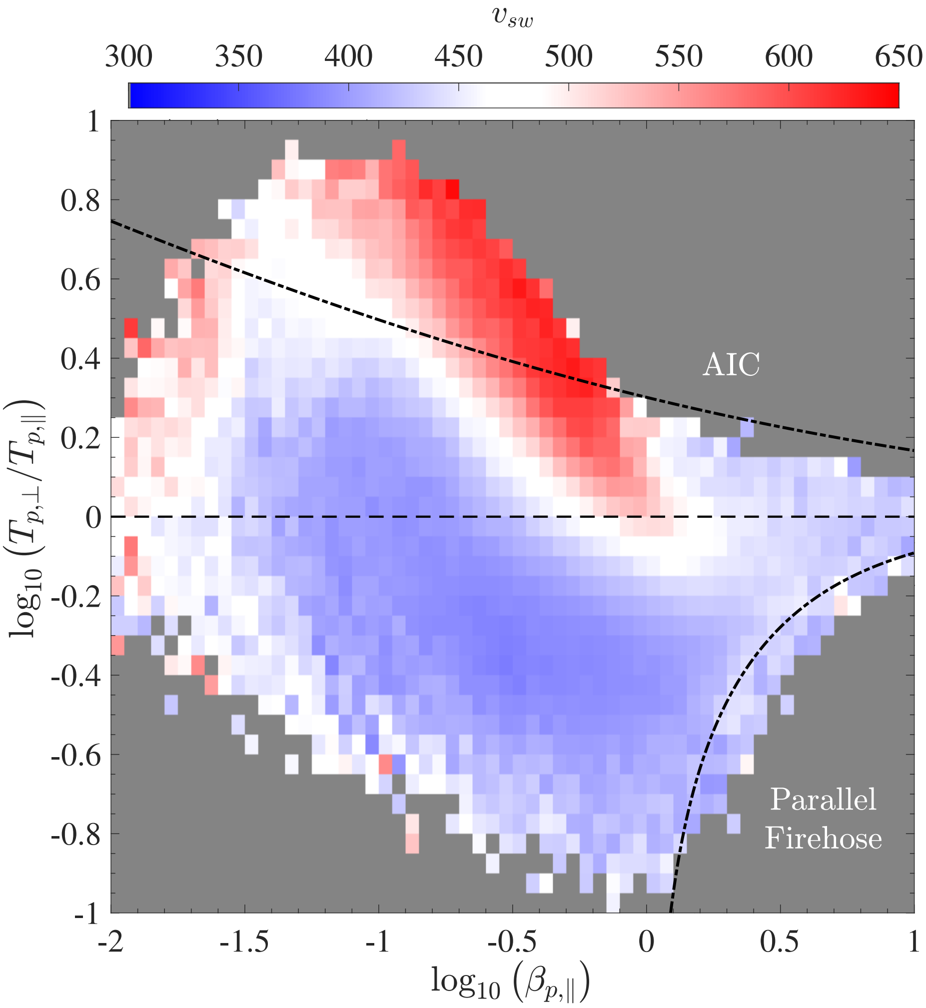

Figure 7.10: Median solar wind speed v_{sw} across the $\beta_{p,\parallel}$-$T_{p,\perp}/T_{p,\parallel}$ plane with contours of constant maximum growth rate, $\gamma_m/\Omega_p = 10^{-2}$, for the AIC and parallel firehose instabilities.

regions in the parameter space, the drift is significantly weaker, reaching a maximum of $\left|v_{d,\parallel}\right| \simeq 0.2\,v_A$. Therefore, the presence of a drift between ion species in the solar wind can explain the preferential driving associated with the AIC and FMW modes, which is consistent with previous studies [Podesta & Gary, 2011a; Verscharen et al., 2013a; Wicks et al., 2016; Klein et al., 2018].

I plot the median $\sigma_\perp$ in the same parameter space in Figure 7.11. I include contours of constant γ_m/Ω_p for the mirror-mode and oblique firehose instabilities since these have higher growth rates at angles oblique to $\mathbf{B}_0$. Throughout Figure 7.11, $\sigma_\perp > 0$ and peaks at $\sigma_\perp \simeq 0.3$ close to $\beta_{p,\parallel} \simeq 0.8$ and $T_{p,\perp} \sim T_{p,\parallel}$.

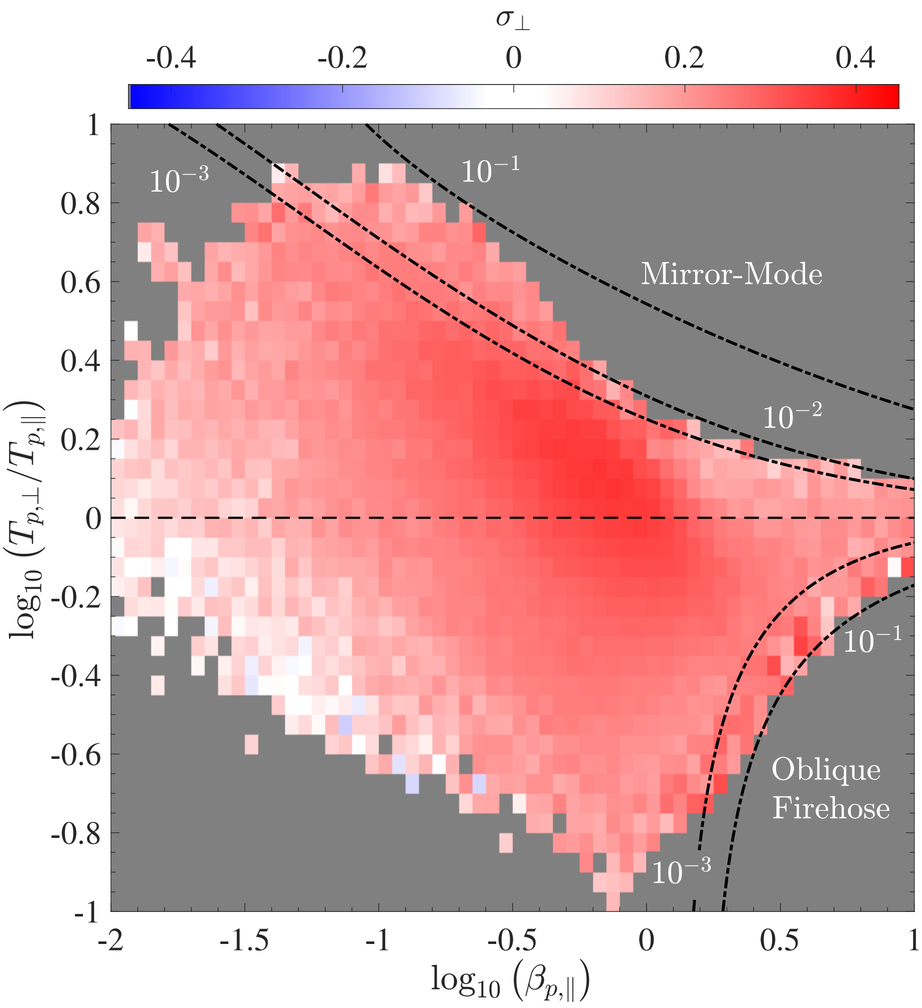

Figure 7.11: Median $\sigma_\perp$ across the $\beta_{p,\parallel}$-$T_{p,\perp}/T_{p,\parallel}$ plane with contours of constant maximum growth rate, γ_m/Ω_p, for the mirror-mode and oblique firehose instabilities.

This peak lies in a region of parameter space dominated by fast wind, which is typically more Alfvénic [Stansby et al., 2019b]. There is also a small enhancement in the helicity in the unstable region of the oblique firehose instability, suggesting the presence of driven modes with a right-handed helicity in the spacecraft-frame. I do not expect to observe a signature from mirror-modes because they represent structures with $\delta\mathbf{B}$ directed along $\mathbf{B}_0$, which will not be measurable using magnetic helicity.

The lack of a strong dependence of the distribution of $\sigma_\perp$ on $\beta_{p,\parallel}$ and $T_{p,\perp}/T_{p,\parallel}$ implies that the dominant source of these fluctuations is unlikely to be related to kinetic instabilities. Instead, due to the anisotropic nature of the turbulent cascade at ion-kinetic scales, I expect KAW-like fluctuations to contribute to $\sigma_\perp$. From linear Vlasov-Maxwell theory, right-handed KAWs with $k_\perp \gg k_\parallel$ at kinetic scales ($k_\perp \rho_p \gtrsim 1$) have $\sigma_\perp \simeq 1$ for $\mathbf{k} \cdot \mathbf{B}_0 > 0$ and $\sigma_\perp \simeq -1$ for $\mathbf{k} \cdot \mathbf{B}_0 < 0$ [Gary, 1986]. Therefore, Figure 7.11 is consistent with the presence of outward propagating right-handed fluctuations (Case I from Table 7.1) that I interpret as KAW-like fluctuations from the turbulent cascade. The peak $|\sigma_\perp| < 1$ is consistent with the non-linear nature of these fluctuations.

To investigate if the fluctuations that contribute to the coherent magnetic helicity actually exist at ion-kinetic scales, I plot in Figure 7.12, the median $k_\parallel d_p$ and $k_\perp d_p$ of the helicity peak in the $\beta_{p,\parallel}$-$T_{p,\perp}/T_{p,\parallel}$ plane. Here, I estimate $k_\parallel$ and $k_\perp$ using $k = 2\pi f_p / v_{sw}$, where f_p is the peak frequency of $\sigma_\parallel$ and $\sigma_\perp$, respectively. In Figure 7.12(a), $k_\parallel d_p \simeq 1$ in the region of parameter space unstable to the AIC instability, and $k_\parallel d_p \simeq 0.3$ for the parallel firehose instability. This range of $k_\parallel d_p$ is consistent with the expected region of wave-vector space where the growth-rates of these two instabilities are largest [Klein & Howes, 2015]. Across the parameter space, $k_\parallel d_p > 0.1$, indicating that all fluctuations measured using magnetic helicity are close to ion-kinetic scales, although there is no clear correlation in this space. However, in Figure 7.12(b), there is a clear correlation of $k_\perp d_p$ in this space. In stable regions, $k_\perp d_p \gtrsim 1$, which is consistent with KAW fluctuations [Howes & Quataert, 2010]. In regions unstable to the mirror instability, $k_\perp d_p \lesssim 1$ and the oblique firehose instability, $k_\perp d_p \simeq 1$, consistent with Klein & Howes [2015]. While there is no helicity signature due to mirror-mode fluctuations in Figure 7.11, it is interesting that Figure 7.12(b) shows such a clear correlation of $k_\perp d_p$ with the contours of the mirror-mode instability. I leave further investigation of this signature to a future study.

Finally, I investigate differences in the distributions of $\sigma_\parallel$ and $\sigma_\perp$ with different solar wind conditions. I check for differences due to wind speed, Alfvénicity, sector structure and drift speed, $v_{d,\parallel}$. There are no significant

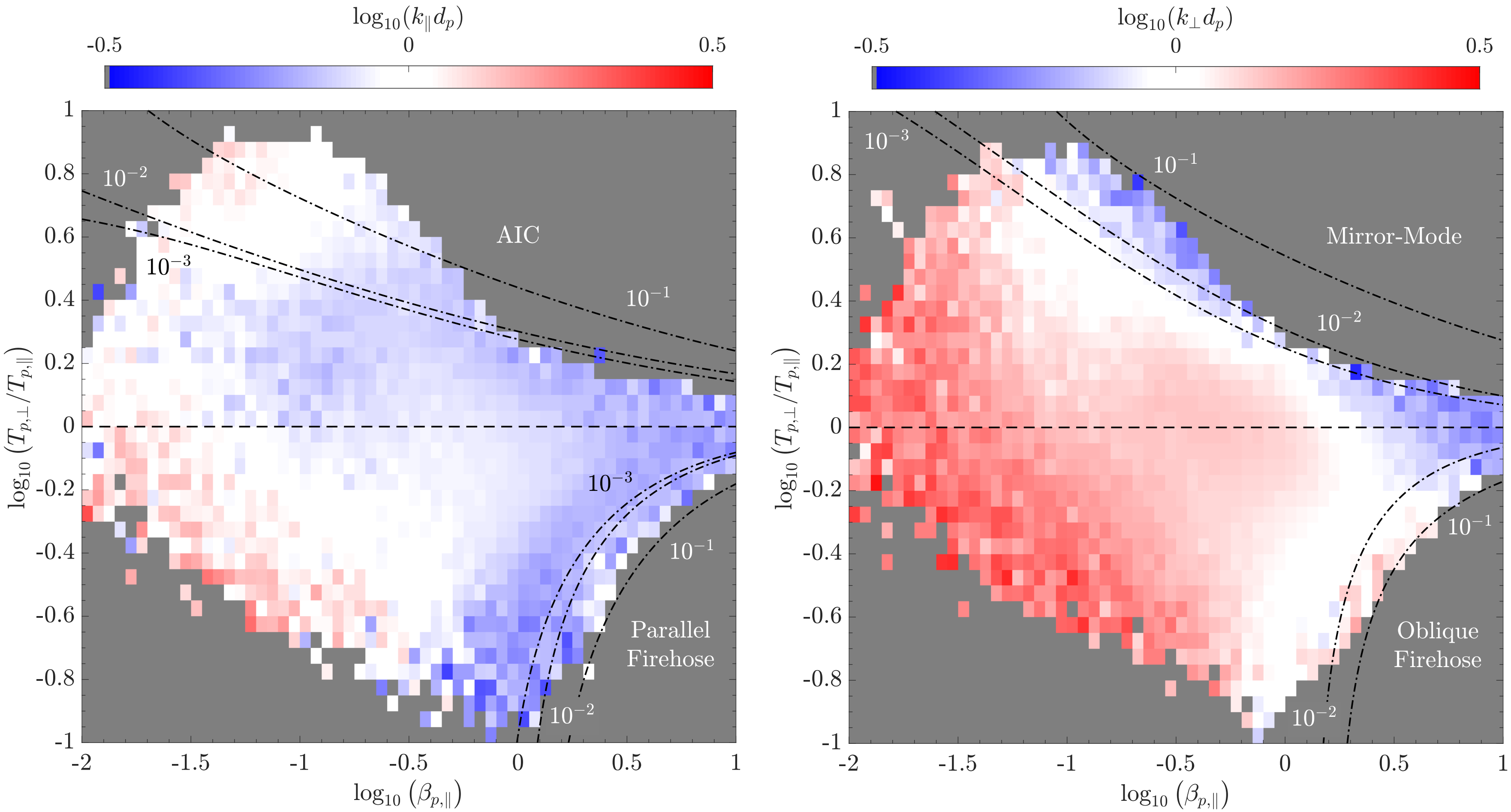

(a) $k_\parallel d_p$

(b) $k_\perp d_p$

Figure 7.12: Median (*a*) $k_\parallel d_p$ and (*b*) $k_\perp d_p$ of the helicity peak in the $\beta_{p,\parallel}$-$T_{p,\perp}/T_{p,\parallel}$ plane. I estimate $k_\parallel$ and $k_\perp$ using $k = 2\pi f_p/v_{sw}$, where f_p is the peak frequency of $\sigma_\parallel$ and $\sigma_\perp$, respectively. Also plotted are contours of constant maximum growth rate, γ_m/Ω_p, for the relevant proton temperature anisotropy instabilities.

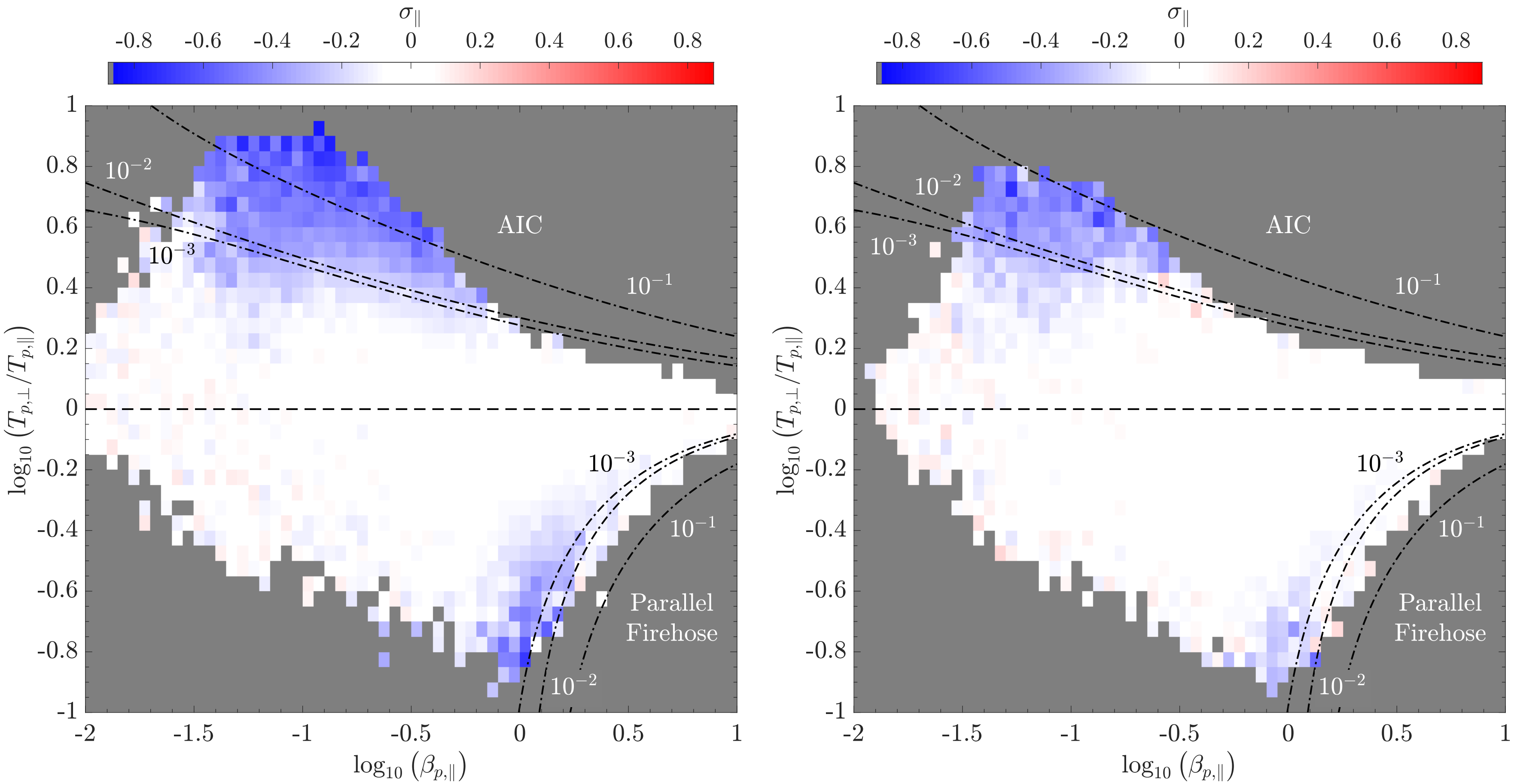

(a) Fast wind (≥ 450 km s^{-1})

(b) Slow wind (< 450 km s^{-1})

Figure 7.13: Median $\sigma_\parallel$ for (a) fast wind (≥ 450 km s^{-1}) and (b) slow wind (< 450 km s^{-1}) in the $\beta_{p,\parallel}$-$T_{p,\perp}/T_{p,\parallel}$ plane. Also plotted are contours of constant maximum growth rate, γ_m/Ω_p, for the AIC and parallel firehose instabilities.

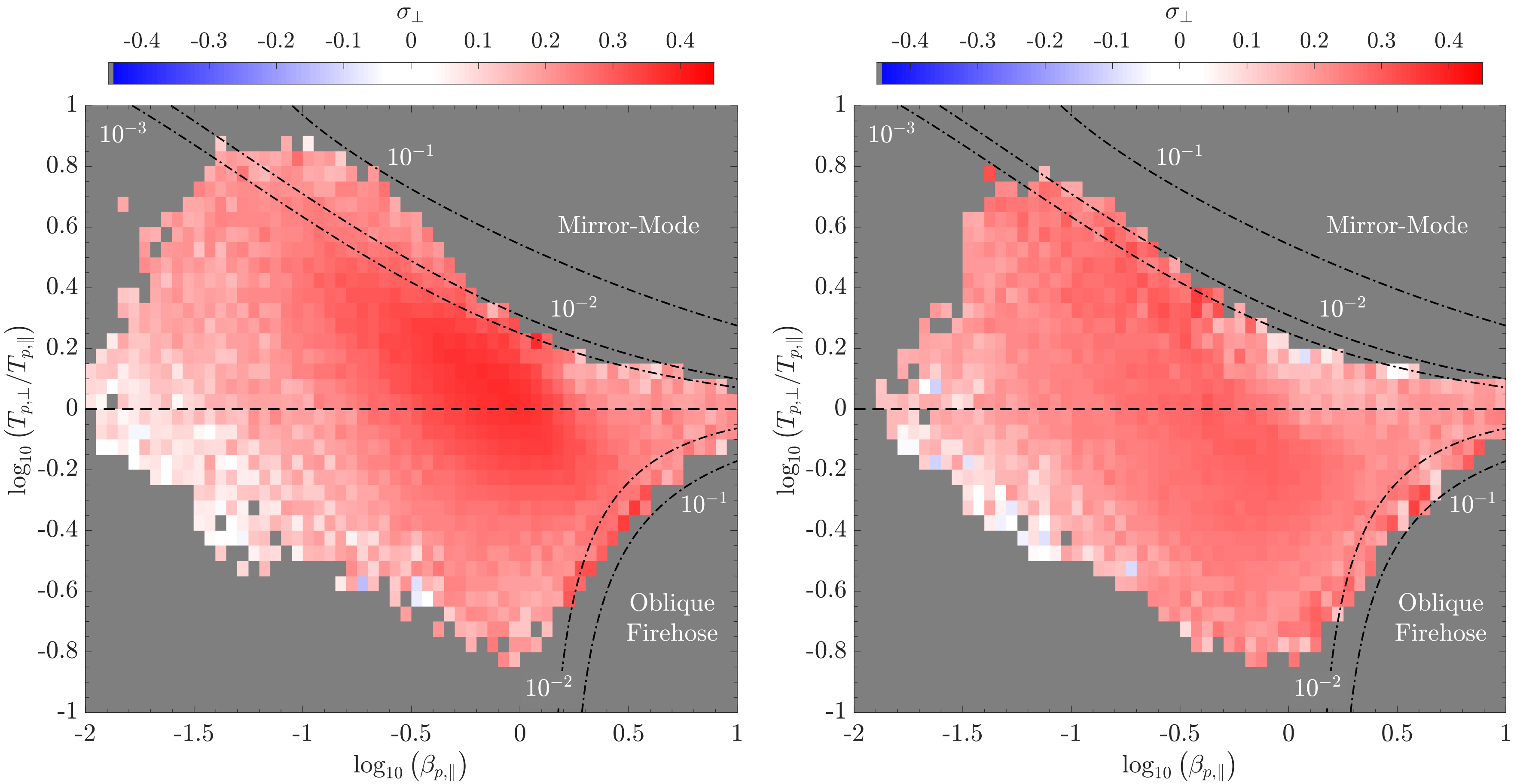

(a) Fast wind (≥ 450 km s^{-1})

(b) Slow wind (< 450 km s^{-1})

Figure 7.14: Median $\sigma_\perp$ for (*a*) fast wind (≥ 450 km s^{-1}) and (*b*) slow wind (< 450 km s^{-1}) in the $\beta_{p,\|}$-$T_{p,\perp}/T_{p,\|}$ plane. Also plotted are contours of constant maximum growth rate, γ_m/Ω_p, for the mirror-mode and oblique firehose instabilities.

changes for Alfvénicity or sector structure, and I do not show them here. In Figures 7.13 and 7.14, I show the distributions of $\sigma_{\|}$ and $\sigma_{\perp}$ in the $\beta_{p,\|}$-$T_{p,\perp}/T_{p,\|}$ plane for fast ($v_{sw} \geq 450$ km s^{-1}) and slow ($v_{sw} < 450$ km s^{-1}) wind. In Figure 7.13, it is clear that the helicity signature associated with both AIC and FMW waves is weaker in slow wind streams. While $\sigma_{\perp}$ is approximately constant in Figure 7.14, the peak in $\sigma_{\perp}$ is not present in slow wind. The same results hold true for solar wind with no α-particle drift ($|v_{d,\|}| < 0.1v_A$) compared to wind with significant drift speeds ($|v_{d,\|}| \geq 0.3v_A$), shown in Figures 7.15 and 7.16. In particular, FMW modes show a strong dependence on the presence of an α-particle drift. In contrast, AIC modes show a weaker dependence on this drift. I do not consider proton beams here, but their presence can also enhance the growth rates of AIC waves. By comparing Figures 7.9 and 7.10, it can be seen that fast solar wind is associated with larger drifts, whereas Alfvénicity does not show the same correlation with wind speed and drift speed, explaining the lack of dependence with Alfvénicity.

7.4 Discussion and Conclusions

In this chapter, I use a novel analysis technique to recover information about the wave-vector anisotropy of solar wind fluctuations using single-point spacecraft measurements. I separate the contributions to magnetic helicity into two components with respect to $\mathbf{B}_0$: one for fluctuations propagating at quasi-parallel angles and the other for those propagating at oblique angles. I analyse over 1.6 million magnetic field spectra and ion measurements from the *Wind* MFI and SWE instruments, quantifying the amplitude of the helicity contributions $\sigma_{\|}$ and $\sigma_{\perp}$ to explore the sources of fluctuations at ion-kinetic scales.

By plotting $\sigma_{\|}$ across $\beta_{p,\|}$-$T_{p,\perp}/T_{p,\|}$ space, I show that there is a significant negative enhancement in $\sigma_{\|}$ in unstable regions of both the AIC and parallel firehose instabilities. The median $\sigma_{\|}$ reaches a minimum of $\sigma_{\|} \simeq -0.6$ at $T_{p,\perp}/T_{p,\|} > 1$. In the spacecraft-frame, these quasi-parallel propagating fluctuations are left-handed, consistent with left-handed AIC waves propagat-

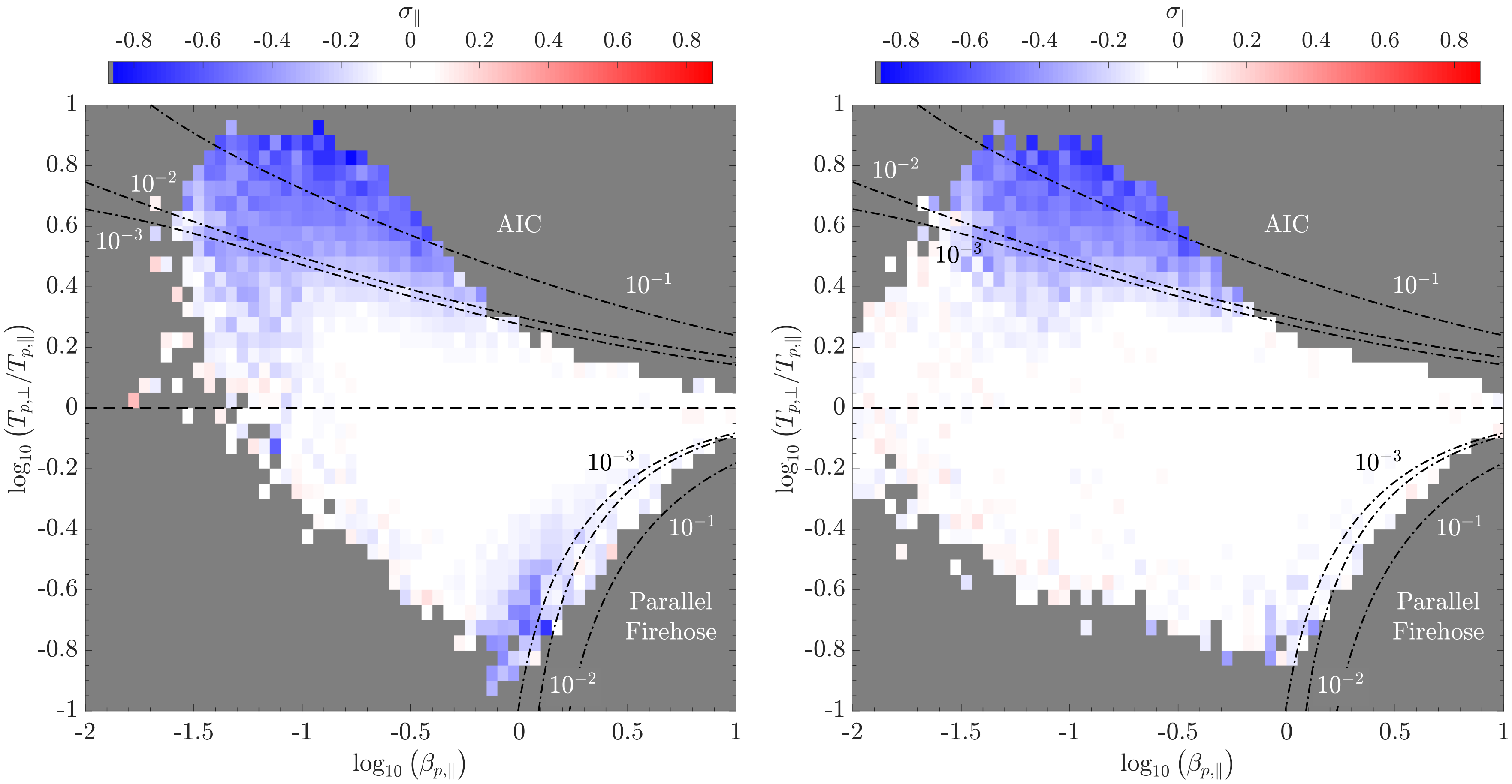

(a) Drift $v_{d,\parallel} \geq 0.3v_A$

(b) No drift $v_{d,\parallel} < 0.1v_A$

Figure 7.15: Median $\sigma_\parallel$ for plasma with (*a*) a strong α-particle drift $v_{d,\parallel} \geq 0.3v_A$ and (*b*) no drift $v_{d,\parallel} < 0.1v_A$ in the $\beta_{p,\parallel}$-$T_{p,\perp}/T_{p,\parallel}$ plane. Over-plotted are contours of constant maximum growth rate, γ/Ω_p, for the AIC and parallel firehose instabilities.

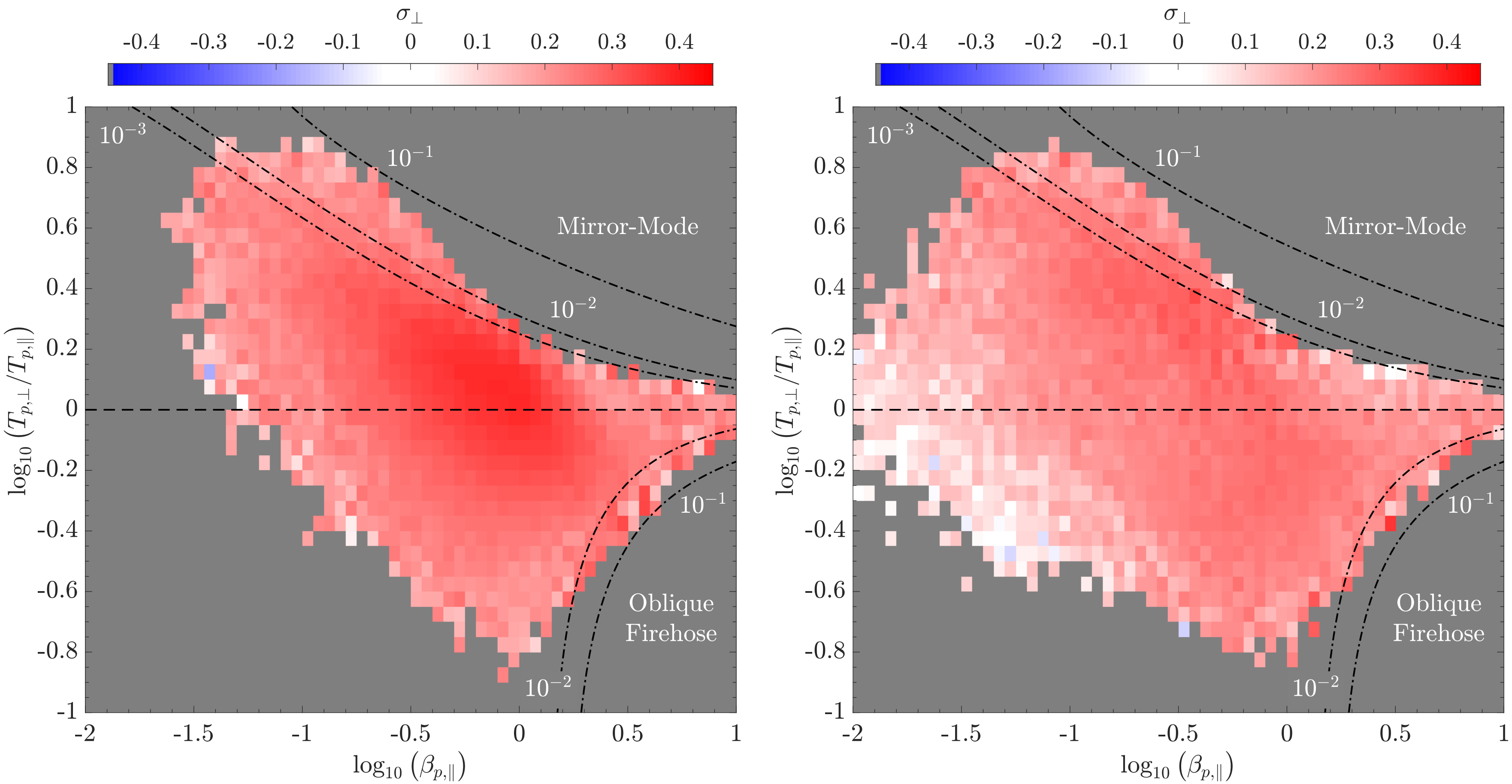

(a) Drift $v_{d,\parallel} \geq 0.3 v_A$

(b) No drift $v_{d,\parallel} < 0.1 v_A$

Figure 7.16: Median $\sigma_\perp$ for plasma with (a) a strong α-particle drift $v_{d,\parallel} \geq 0.3 v_A$ and (b) no drift $v_{d,\parallel} < 0.1 v_A$ in the $\beta_{p,\parallel}$-$T_{p,\perp}/T_{p,\parallel}$ plane. Over-plotted are contours of constant maximum growth rate, γ/Ω_p, for the mirror-mode and oblique firehose instabilities.

ing anti-sunward for $T_{p,\perp}/T_{p,\|} > 1$ and right-handed FMW waves propagating sunward in the plasma-frame for $T_{p,\perp}/T_{p,\|} < 1$. Using Taylor's hypothesis I show that the peak of the helicity spectra are associated with scales $k_{\|} d_p \gtrsim 0.3$, consistent with predictions of these waves from linear theory [Klein & Howes, 2015]. In regions of a negative enhancement in $\sigma_{\|}$, particularly for $T_{p,\perp}/T_{p,\|} > 1$, I also observe a substantial α-particle drift with respect to the proton flow, consistent with predictions [Podesta & Gary, 2011a,b]. By filtering for plasma with $|v_{d,\|}| < 0.1 v_A$ and plasma with $v_{d,\|} \geq 0.3 v_A$, I show that the helicity signatures are stronger in the latter case, especially for FMW waves. Elsewhere in $\beta_{p,\|} - T_{p,\perp}/T_{p,\|}$ space, $\sigma_{\|} \simeq 0$, which indicates no coherence in $\mathbf{B}$. This result suggests that fluctuations propagating quasi-parallel to $\mathbf{B}_0$ predominantly arise from ion instabilities, consistent with the background solar wind turbulence producing Alfvénic fluctuations with $k_{\perp} \gg k_{\|}$ [Horbury et al., 2008; Chen et al., 2010a,b; Wicks et al., 2010]. These results show that instabilities are active and modes generated by them are common in the solar wind, in agreement with Klein et al. [2018].

I also show that $\sigma_{\perp}$ is distributed throughout the entire parameter space occupied by the solar wind and peaks at $\sigma_{\perp} \simeq 0.3$, associated with scales $k_{\perp} d_p \gtrsim 1$. This peak occurs at $T_{p,\perp} \simeq T_{p,\|}$ and $\beta_{p,\|} \simeq 0.8$, which is strongest in a region of $\beta_{p,\|}$-$T_{p,\perp}/T_{p,\|}$ space dominated by fast wind, suggesting that these fluctuations are more Alfvénic. This peak is no longer present when I consider plasma with no significant α-particle drift, suggesting that the presence of this drift may also be linked to these fluctuations. Since $\sigma_{\perp} > 0$ and shows little dependence on $\beta_{p,\|}$ and $T_{p,\perp}/T_{p,\|}$, this signature is consistent with anisotropic fluctuations from the turbulent cascade with significant $k_{\perp}$ at ion-kinetic scales [Horbury et al., 2008; Chen et al., 2010a,b; Wicks et al., 2010]. While I interpret these fluctuations as KAW-like modes, I do not rule out that other non-linear turbulent fluctuations or structures contribute to this helicity signal. I conjecture that these fluctuations are insensitive to proton temperature anisotropy and instability growth, in agreement with Klein & Howes [2015].

Furthermore, since AIC and FMW modes do not appear to interact with the turbulent cascade, and there is no evidence of coherent helicity from turbulent fluctuations with significant $k_{\|}$, I provide evidence for a minimal role of quasi-parallel propagating fluctuations in the turbulence at ion-kinetic scales.

My results provide evidence that the behaviour of fluctuations at ion-kinetic scales is independent of the origin and macroscopic properties of the solar wind. For example, left-handed AIC modes are generated in both fast and slow wind streams, depending only on the local properties of the plasma such as proton temperature anisotropy and the presence of α-particle differential flow. I also find no evidence of a parallel-propagating contribution to the helicity from the turbulent cascade at these scales in the stable parameter regime. Any Alfvénic fluctuations from the cascade with a significant $k_{\|}$ would produce a signature in Figure 7.8 with a similar distribution to the right-handed signal in Figure 7.11. While I cannot rule out that at these scales all turbulent quasi-parallel propagating fluctuations have already dissipated, their existence is inconsistent with the anisotropy of the turbulence throughout the inertial range. Therefore, I can rule out the existence of imbalanced fluctuations with $k_{\|} \gtrsim k_{\perp}$ at ion-kinetic scales that are not created by instabilities. This novel result constrains theories of turbulence in the solar wind and their implications for energy transport and dissipation, in a similar way to Lacombe et al. [2014] for electron-kinetic scales.

To ensure that the correlations of different parameters in $\beta_{p,\|}$-$T_{p,\perp}/T_{p,\|}$ space are physical, I have tried to only plot parameters that do not show any systematic correlations with either $\beta_{p,\|}$ or $T_{p,\perp}/T_{p,\|}$. The magnetic helicity, which is the main result in this chapter, does not correlate with these parameters. I also examined a random sample of bins in this space to check the distribution of data, finding it to be approximately Gaussian. I confirmed this by comparing the median and mean values in each bin across this space, finding no discernible difference. A source of error in the helicity may arise from my Gaussian fitting algorithm (Section 6.2.4). The fit of a Gaussian function to the helicity spectrum for a peak with an amplitude $|\sigma| < 0.2$ is more uncertain, leading to more noise in the results. Despite this, the peaks in each distribution in the $\beta_{p,\parallel}$-$T_{p,\perp}/T_{p,\parallel}$ plane are larger at $\sigma_\parallel \simeq -0.8$ and $\sigma_\perp \simeq 0.4$, so they must be physical. I also do not expect the distribution of $\sigma_\parallel$ in this plane to be produced by just noise from the fitting algorithm. Another source of error could be my sector structure determination. From Figure 7.5, there are periods where my algorithm does not correctly identify the correct sector. Despite this, the majority of spectra have the correct sector assigned to them. Due to the large dataset that I use in this study, I expect the proportion of spectra with the incorrect sector assignment to be minimal.

In this study, I have averaged the helicity spectra over 92 s, the highest resolution of the SWE data. However, 92 s corresponds to $f \simeq 0.01$ Hz, which is located at the high-frequency end of the inertial range, not at ion-kinetic scales. Despite this, I show in Figure 7.12 that the fluctuations contributing to the magnetic helicity signature exist at ion-kinetic scales, $kd_p \simeq 1$. Using 92 s averaged spectra means that the measurement of a significant non-zero at these scales must correspond to fluctuations that exist for several proton gyro-periods, $\tau = 2\pi/\Omega_p$. By rejecting a spectrum if the angular deviation in $\mathbf{B}$ (see Section 5.3.5) exceeds 15° during the measurement period, I ensure that the fluctuations retain their anisotropy with respect to $\mathbf{B}_0$ over 92 s. In other words, the helicity is not spread across both σ_{xy} and σ_{yz} because the local mean-field direction is approximately constant.

My results in this chapter show that the fluctuations contributing to a coherent magnetic helicity signature at ion-kinetic scales are primarily Alfvénic, consistent with AIC waves and KAWs. Gary [1986] showed that the dispersion relation for Alfvén waves splits into KAWs or AIC waves at a critical angle, θ_{kB}, to the magnetic field that is dependent on β_p. At this angle, the polarisation and therefore, helicity changes sign. Since AIC waves are driven by instabilities and the turbulent cascade is made up of only quasi-perpendicular propagating fluctuations at ion-kinetic scales, only dissipation mechanisms consistent with these fluctuations can occur. Therefore, a natural parameter space to probe these processes is θ_{kB}-β_p. In the next chapter, I use this parameter space in order to explore what solar wind conditions show signatures of dissipation from the power spectra and attempt to identify possible evidence of heating.

Chapter 8

Probing Dissipation Mechanisms in the Solar Wind

In Chapter 6, I showed that magnetic helicity and power spectrum of magnetic field fluctuations are linked by $1/k_c$ at ion-kinetic scales, suggesting that they are associated with the same physical process. Then, in Chapter 7 I used magnetic helicity to characterise the fluctuations at these scales and their sources in the solar wind. I found evidence of Quasi-parallel propagating AIC and FMW waves driven by proton temperature anisotropy instabilities and quasi-perpendicular propagating KAW-like fluctuations from the turbulent cascade. In this final research chapter, I use the polarisation properties of the Alfvénic fluctuations to probe dissipation mechanisms of the turbulence at these scales, finding that they correlate with proton temperature, suggesting that the ergodicity hypothesis of solar wind fluctuations does not hold. I discuss the possible implications of this result and attempt to rule out instrumental or expansion effects. A manuscript on this work is currently in preparation.

8.1 Polarisation Properties of Alfvén Waves

In collisionless space plasmas such as the solar wind, the linearised Vlasov equation (A.1) describes waves and instabilities. Non-trivial solutions exist only when the complex frequency, $\omega = \omega_r + i\gamma$, solves the hot-plasma dispersion relation (see Section 2.6). The Alfvén wave ($\omega_r = kv_A \cos\theta_{kB}$) is ubiquitous in space plasmas and at low frequencies is an incompressible wave that propagates along a magnetic field with speed v_A, resulting in transverse perturbations to the field (Section 2.6.3). At frequencies close to the proton gyro-frequency, $\omega_r \lesssim \Omega_p$, the polarisation properties of Alfvén waves change depending on their direction of propagation with respect to $\mathbf{B}_0$ [Gary, 1986], the dispersion relation splitting into the AIC wave and KAW branches. These polarisation properties can be explored by solving the full electromagnetic dispersion relation [Stix, 1992].

The polarisation, P, of a wave gives the left- or right-handed sense of rotation in time of a fluctuating field vector at a fixed point in space, viewed in the direction parallel to $\mathbf{B}_0 = B_0 \hat{\mathbf{z}}$. It is defined as:

$$P = -\frac{i\delta E_y}{\delta E_x} \frac{\omega_r}{|\omega_r|}, \tag{8.1}$$

where δE_x and δE_y are components of the fluctuating electric field transverse to $\mathbf{B}_0$ [Stix, 1992; Gary, 1993]. A circularly polarised wave has $P = \pm 1$, where +1 (-1) designates right-handed (left-handed) polarisation. In this definition, a right-hand polarised wave has fluctuating field vectors that rotate in the same sense as the gyration of an electron, and left-hand polarised waves, the same sense as ions. For more general elliptical polarisation, the real part is taken, $\mathrm{Re}(P)$. The magnetic helicity, in contrast, is a measure of the spatial phase coherence between magnetic field components along $\mathbf{k}$ in a plasma [Woltjer, 1958a,b]. It is defined as an integral over the volume of the plasma and is an invariant of ideal MHD in the absence of $\mathbf{B}_0$ (see Section 3.2.2). The normalised magnetic helicity, $\sigma_m(\mathbf{k})$, is another diagnostic of the polarisation properties of fluctuations (see Section 3.7.4).

Gary [1986] explore the changing polarisation properties of Alfvén waves by numerically solving the full electromagnetic dispersion relation. They find that $\mathrm{Re}(P)$ changes sign depending on θ_{kB} and β_p. As the frequency of an Alfvén wave approaches Ω_p but remains $\omega_r \lesssim \Omega_p$, the wave has $\mathrm{Re}(P) < 0$ for all propagation angles in the cold-plasma limit ($\beta_p \ll 1$). However, from

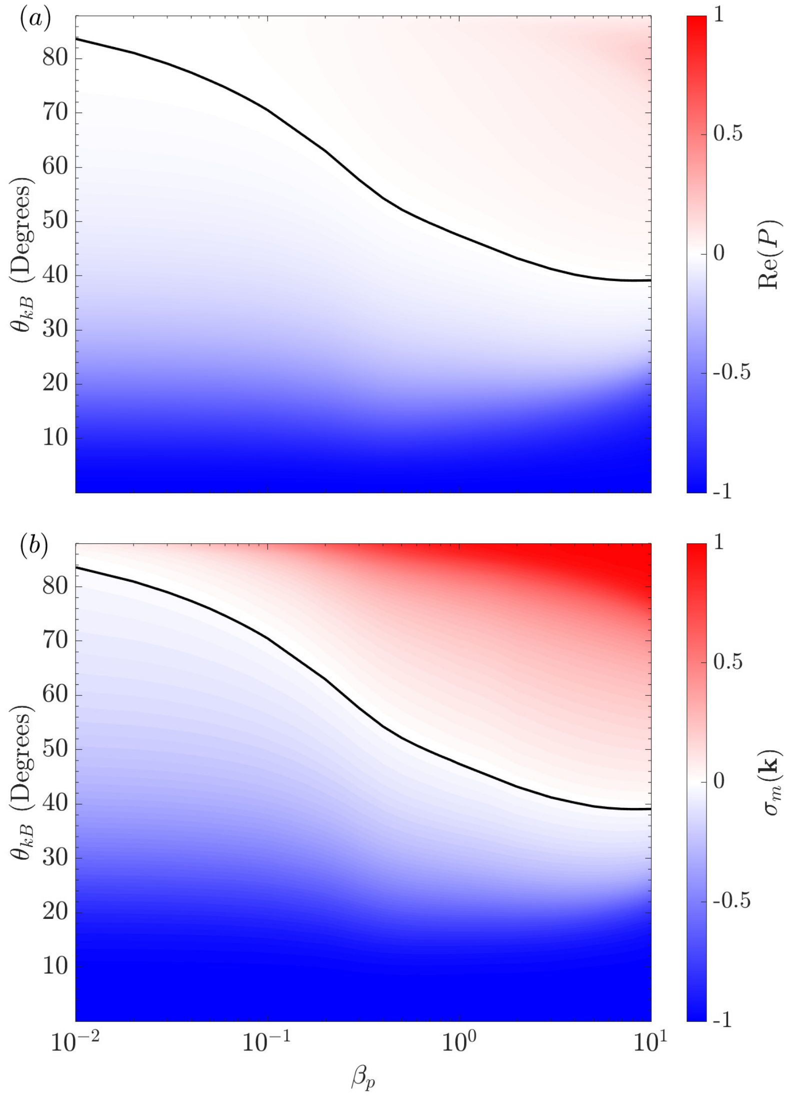

Figure 8.1: (a) The real part of the polarisation, Re(P), and (b) normalised magnetic helicity, $\sigma_m(\mathbf{k})$, of Alfvén waves with $k_\parallel = 0.1 d_p$ as a function of β_p and θ_{kB}, calculated using the NHDS code. The black lines indicate the angle θ_{kB} at which $\mathrm{Re}(P) = 0$ and $\sigma_m(\mathbf{k}) = 0$ for a value of β_p. Below the line, Alfvén waves are left-handed, and above, right-handed. Figure reproduced from Gary [1986].

Vlasov theory, at $\beta_p \sim 10^{-2}$, the wave has $\mathrm{Re}(P) < 0$ for a broad range of angles starting from the parallel direction ($\theta_{kB} = 0°$), but at highly oblique angles ($\theta_{kB} \gtrsim 80°$), has $\mathrm{Re}(P) > 0$. As β_p increases, the wave has $\mathrm{Re}(P) > 0$ for an increasing range of oblique angles that at $\beta_p \sim 10$, the transition occurs at about 40°.

I show the transition in both Re(P) and $\sigma_m(\mathbf{k})$ in Figure 8.1, where the black lines are isocontours of $\mathrm{Re}(P) = 0$ and $\sigma_m(\mathbf{k}) = 0$, respectively. To calculate these lines, I solve the linear Vlasov equation using the New Hampshire Dispersion relation Solver (NHDS) [Verscharen et al., 2013b; Verscharen & Chandran, 2018]. Here, $\mathbf{k} = k_\perp \hat{\mathbf{x}} + k_\parallel \hat{\mathbf{z}}$, and I assume a plasma consisting of protons and electrons with isotropic Maxwellian distributions, equal density, and no drifting components. I set $k_\parallel = 0.1\, d_p$ to probe the properties of Alfvén waves close to ion-kinetic scales and the angle θ_{kB} defines $k_\perp = k_\parallel \tan\theta_{kB}$. I also set $v_A/c = 10^{-4}$, which is typical for the solar wind.

8.2 The Properties of Alfvénic Fluctuations in the Solar Wind

The β_p-θ_{kB} plane in Figure 8.1 can be used to investigate the polarisation properties of Alfvénic fluctuations at ion-kinetic sales in the solar wind, in a similar way to the $\beta_{p,\parallel}$-$T_{p,\perp}/T_{p,\parallel}$ plane in the previous chapter. While the latter parameter space was chosen to investigate the fluctuations arising from instabilities at ion-kinetic scales, I chose this new space to probe possible signatures of turbulent dissipation. In this chapter, I use the same data and analysis methods described in Section 7.2.

I bin the data in $\log_{10}(\beta_p)$ and θ_{vB} using bins of width $\Delta\log_{10}(\beta_p) = 0.05$ and $\Delta\theta_{vB} = 5°$. I restrict my analysis to $10^{-2} \leq \beta_p \leq 10^1$ and include the full range of $\theta_{vB} = [0°, 180°]$ to account for any differences due to heliospheric sector structure. I use θ_{vB} here since I cannot determine $\mathbf{k}$ from single-spacecraft measurements (see Section 3.7.3). Previous studies [e.g., Horbury et al., 2008; Wicks et al., 2010; He et al., 2011] have shown that θ_{vB} can be used to measure a specific θ_{kB} in the solar wind, however, my results should be interpreted with this restriction in mind. In Figure 8.2, I plot the PDF,

$$\tilde{p} = \frac{n}{N \Delta\log_{10}(\beta_p) \Delta\theta_{vB}}, \tag{8.2}$$

of the data in the β_p-θ_{vB} plane, where n is the number of data points in a bin and N is the total number of data points. Here, I use only measurements of Alfvénic solar wind ($|\sigma_c| \geq 0.75$) and low collisionality ($N_c < 1$), which contain the strongest Alfvénic fluctuations. I also plot the isocontour of $\text{Re}(P) = 0$ in the β_p-θ_{kB} plane from Figure 8.1. I mirror this curve around the $\theta = 90°$ axis to account for heliospheric sector structure. The polarisation properties will not change since I remove the ambiguity in the sign of the magnetic helicity due to the direction of $\mathbf{B}_0$ (see Section 7.2). The distribution of data in Figure 8.2 shows two peaks at 65° and 115° around $\beta_p \sim 0.8$, highlighting the sector structure of the solar wind, although these peaks do not correspond to the two peaks (45° and 135°) for ϕ_{rB} seen in Figure 7.4. There are fewer data points at quasi-parallel angles, showing that the majority of data are associated with oblique angles between $\mathbf{v}_{sw}$ and $\mathbf{B}$. There is also a clear β_p dependence, with the majority of the data lying in the range $0.1 \lesssim \beta_p \lesssim 1$.

In Figure 8.3, I plot the median values of $\sigma_{||}$ and $\sigma_{\perp}$ for each bin in the β_p-θ_{vB} plane, as similarly plotted in Figures 7.8 and 7.11 in the previous chapter. Again, a negative value indicates left-handed fluctuations and a positive value, right-handed fluctuations. I neglect any bins with fewer than 20 data points to improve statistical convergence. From linear Vlasov-Maxwell theory and Figure 8.1, I expect KAW-like fluctuations with $\sigma_{\perp} < 0$ to exist within the area of the β_p-θ_{vB} plane enclosed by the two dashed lines at quasi-perpendicular angles, and AIC waves-like fluctuations with $\sigma_{||} > 0$ to exist elsewhere at quasi-parallel angles. Figure 8.3 is consistent with this hypothesis; I see a strong negative helicity peaking at $\sigma_{||} \simeq -0.8$ for quasi-parallel propagating waves at $0° \leq \theta_{vB} \leq 30°$ and $150° \leq \theta_{vB} \leq 180°$, and a weaker positive signal of $\sigma_{||} \simeq 0.4$ at angles $60° \leq \theta_{vB} \leq 120°$.

The distribution of $\sigma_{||}$ is consistent with the presence of quasi-parallel propagating AIC waves from kinetic instabilities in the solar wind identified in Chapter 7. I note that the helicity of predominantly right-handed fast magnetosonic-whistler waves can also contribute to the median $\sigma_{||}$ in this parameter space. However, since they are not Alfvénic, they are not bound by

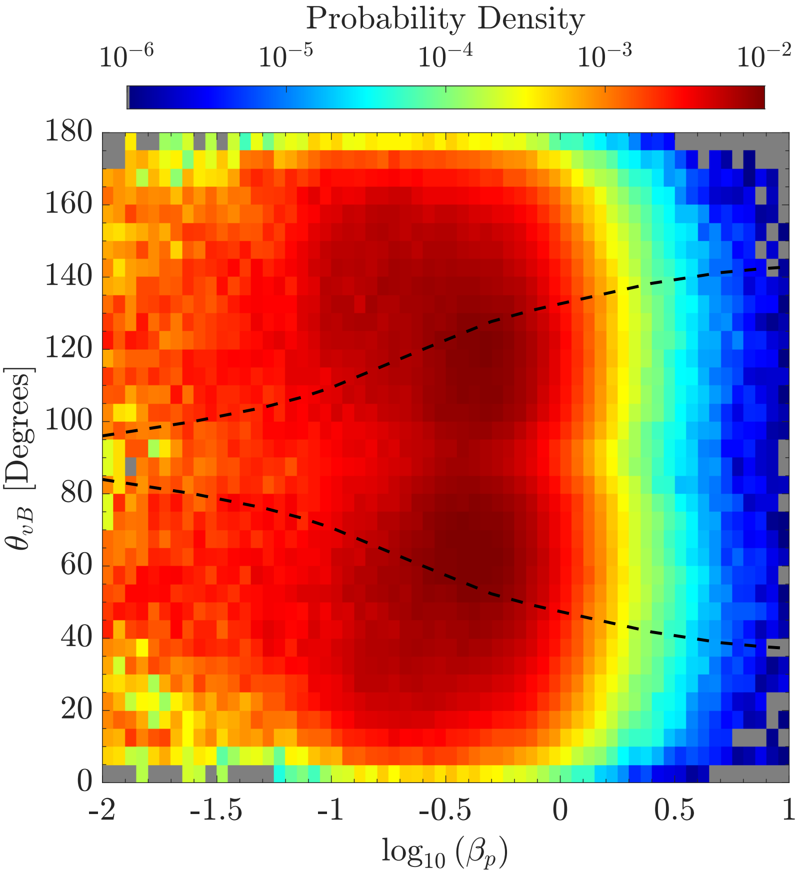

Figure 8.2: Probability density function (PDF) of solar wind data in the $\log_{10}(\beta_p)$-θ_{vB} plane, calculated using Equation 8.2. The black lines indicate the isocontours of $\mathrm{Re}(P) = 0$ in the β_p-θ_{kB} plane from Figure 8.1.

the polarisation properties given in Figure 8.1. The helicity of AIC waves also dominates the helicity of FMW waves in Figure 7.8, suggesting that this is not an issue in Figure 8.3. Elsewhere in Figure 8.3(a), the median value of $\sigma_{\parallel}$ is zero, showing that a coherent signal of parallel-propagating fluctuations at ion-kinetic scales in the solar wind is not measured at oblique angles.

In this chapter, I am primarily interested in the oblique KAW-like fluctuations from the turbulent cascade. In Figure 8.3(b), there are two peaks in the median $\sigma_{\perp}$ within the parameter space with $\mathrm{Re}(P) > 0$. Despite these peaks, the signal is spread across the parameter space, albeit weaker at quasi-parallel angles. While the linear theory of Alfvén waves is defined by θ_{kB}, single-spacecraft observations are only possible using θ_{vB}. I interpret this spread using Taylor's hypothesis due to the $\mathbf{k} \cdot \mathbf{v}_{sw}$ term in the δ-function in

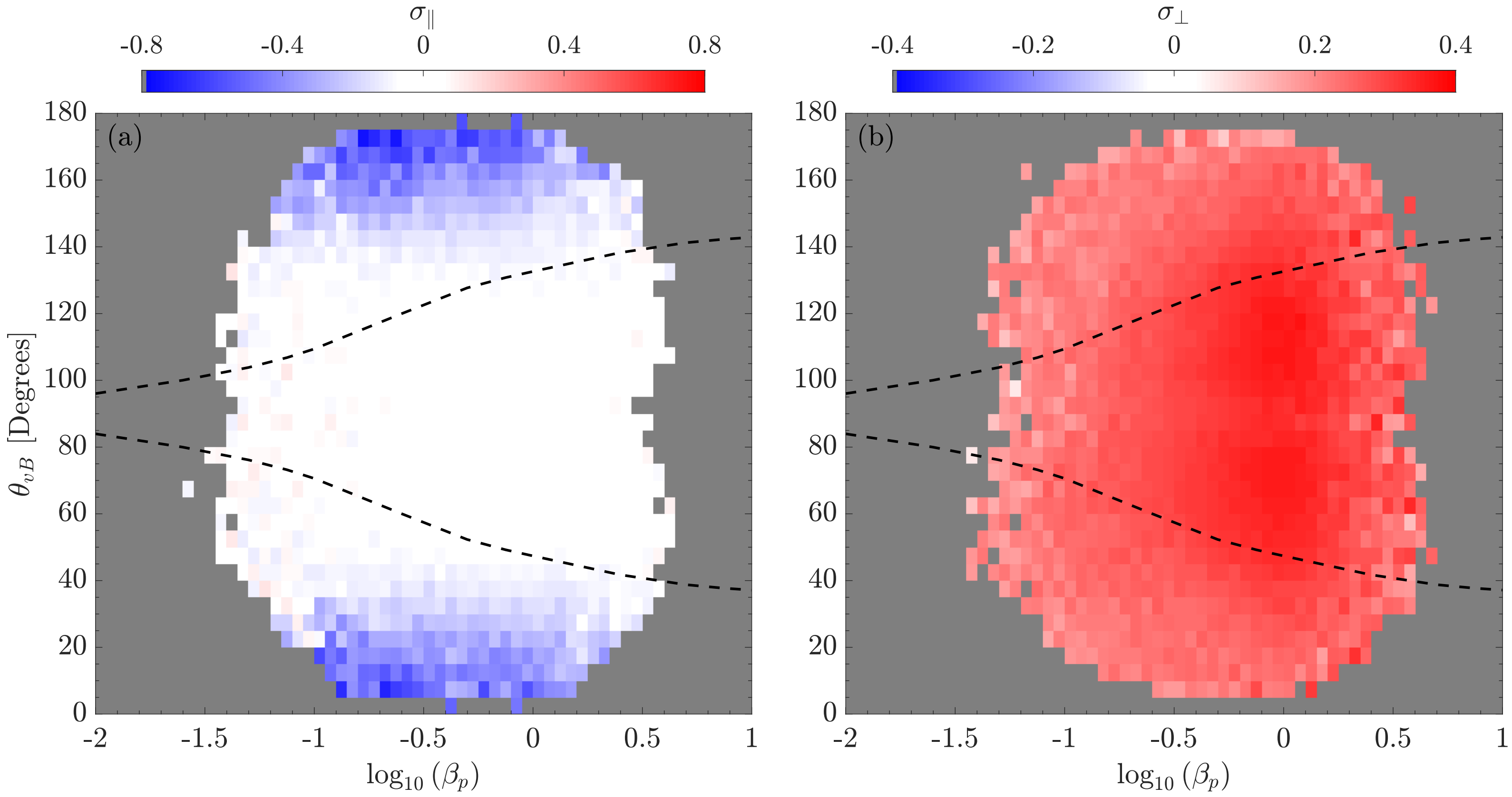

Figure 8.3: (*a*) Median $\sigma_\parallel$ and (*b*) median $\sigma_\perp$ across the β_p-θ_{vB} plane. The black dashed lines the isocontours of $\mathrm{Re}(P) = 0$ in the β_p-θ_{kB} plane from Figure 8.1. Note that the scales of the colour bars in panels (*a*) and (*b*) are different.

Equation 3.30. Therefore, a $\cos\theta_{kv}$ factor modifies the contribution of any mode to the reduced spectrum measured in the direction of $\mathbf{v}_{sw}$. If $\theta_{kv} = 0°$, then $\cos\theta_{kv} = 1$, and the waves are measured at their actual k. However, for oblique angles, $\theta_{kv} \gtrsim 60°$, waves are measured at a higher k. Since a turbulent spectrum decreases in amplitude with increasing k, the reduced spectrum is, therefore, most sensitive to the smallest $\mathbf{k}$ in the sampling direction. For parallel propagating fluctuations such as AIC waves, $\theta_{vB} \sim \theta_{kv}$, but for obliquely propagating fluctuations, fluctuations with different $\mathbf{k}$ and therefore, θ_{kB}, can contribute to a single value of θ_{vB}. I also know that the signal at $\theta_{vB} \lesssim 30°$ must be due to fluctuations with $\theta_{kB} \gtrsim 60°$ since they contribute to $\sigma_{\perp}$, i.e., have a significant $k_{\perp}$ component. The peaks in $\sigma_{\perp}$ within the dashed lines also suggest that there are turbulent fluctuations present at ion-kinetic scales in the solar wind that have at least some linear component consistent with the polarisation properties of Aflvén waves.

In Figure 8.4, I plot the distribution of $|v_{d,\|}|/v_A$ in the β_p-θ_{vB} plane. From comparison with Figure 8.3(b), where $\sigma_{\perp}$ is strongest in this plane there is also a large drift between α-particles and protons of $v_{d,\|} \simeq 0.4 v_A$. This result is similar to Figure 7.16 in Chapter 7 where I find that the peak in $\sigma_{\perp}$ disappears when comparing plasma with no drift versus a significant drift. Unexpectedly, the drift speed is not largest where $\sigma_{\|}$ is strongest at quasi-parallel angles in Figure 8.3(a). This result shows that the presence of α-particle beams are important to consider when considering both AIC/FMW waves from instabilities and KAW fluctuations from the turbulent cascade.

To explore the dissipation of energy from the turbulent cascade and its link with linear Alfvén wave physics, I use two spectral quantities. The first is the spectral exponent, α, in the ion-kinetic range (see Section 6.3.1) and the second is the ratio of energy between points of the power spectrum in the ion-kinetic range as shown in Figure 8.5:

$$\text{Ratio} = \frac{\delta B_1^2}{\delta B_2^2}\frac{f_2}{f_1}, \tag{8.3}$$

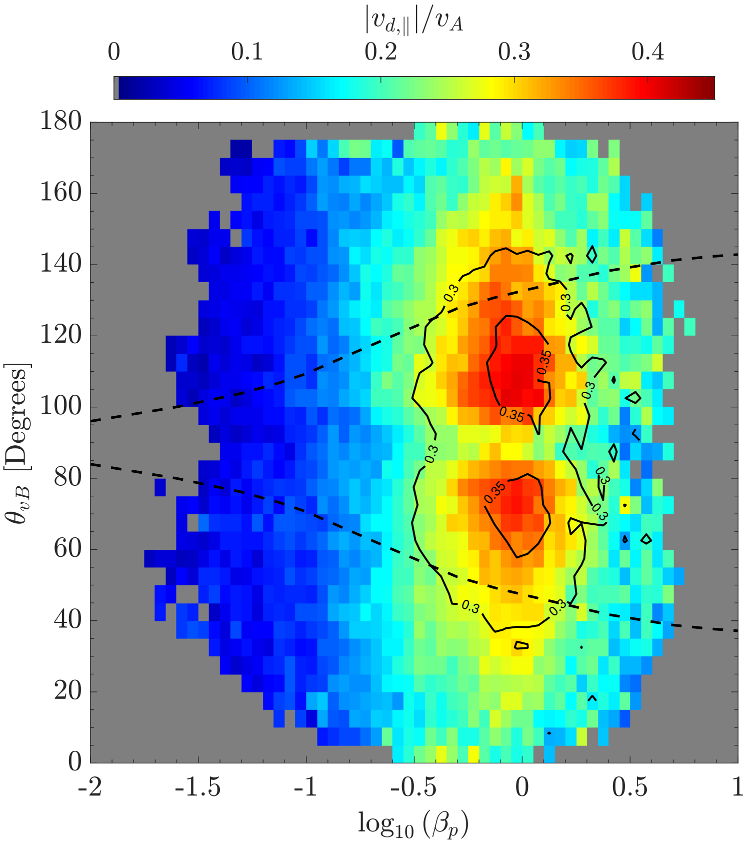

Figure 8.4: Median $|v_{d,\|}|/v_A$ across the β_p-θ_{vB} plane. The black dashed lines the isocontours of $\mathrm{Re}(P) = 0$ in the β_p-θ_{kB} plane from Figure 8.1. I also include contours of constant $\sigma_\perp$ from Figure 8.3(b).

where $f_1 = f_b$ and $f_2 = 3f_b$ so that the frequency range is constant. This range of frequencies is the same as used to calculate α in Chapter 6 so that both quantities are qualitatively similar measures of dissipation. I drop the factor of 3 hereafter since it is only a multiplicative constant. In Figure 8.6(a), I plot the median α as a function of $\log_{10}(\beta_p)$ and θ_{vB}. In Panel (a), the exponent is $\alpha \simeq -4$ at quasi-parallel angles where $\mathrm{Re}(P) < 0$, where I also see the strong $\sigma_\|$ signal in Figure 8.3(a), that I associated with AIC waves generated by kinetic instabilities. This signature also extends to more oblique angles at $\beta_p \simeq 1$. At oblique angles where there are peaks in $\sigma_\perp$ in Figure 8.3(b), $\alpha \simeq -3.4$. In other regions of the parameter space where $\mathrm{Re}(P) > 0$, the exponent is shallower. Except at $\beta_p < 0.1$ and $\beta_p > 1$, the exponent is steeper than the -2.8 value predicted for a cascade of KAW-like fluctuations [e.g., Boldyrev & Perez, 2012]. This result suggests that there may be damping of fluctuations

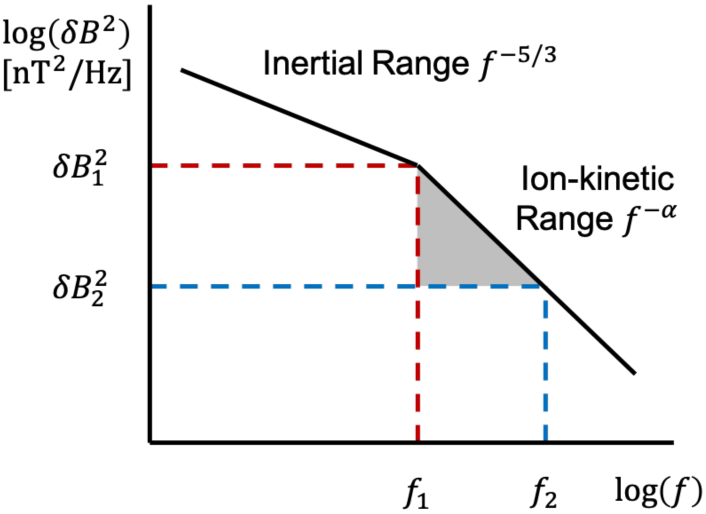

Figure 8.5: Schematic showing how the ratio of energy between two points in the ion-kinetic range of the magnetic field power spectrum is calculated.

that are associated with a coherent $\sigma_\perp$ signal.

If dissipation of turbulent fluctuations is ongoing as suggested by an exponent steeper than -2.8, then I also expect a larger decrease in energy of the power spectrum between f_b and $3f_b$. In Figure 8.6(b), I plot the median ratio $\log_{10}(\delta B_1^2/\delta B_2^2)$ across the β_p-θ_{vB} plane. This ratio eliminates any systematic effects that may cause a dependence on β_p. I see a drop in energy of a factor ~ 30 in regions of parameter space where there is also a strong $\sigma_\perp$ signal in Figure 8.3(b). This result suggests that right-handed KAW-like fluctuations are associated with a larger amount of energy removed from the cascade. This signature is consistent with steeper exponents in the ion-kinetic range in the same region of the parameter space. At quasi-parallel angles, the ratio is much closer to unity, suggesting little dissipation. This result is consistent with the injection of energy at these scales by kinetic instabilities, leading to a small peak in the power spectrum close to f_b. The presence of this peak may result in an incorrect determination of the energy ratio and therefore, may also explain the very steep slopes ($\alpha \simeq -4$) in the regions of parameter space associated with the strongest $\sigma_\parallel$ signal.

To investigate this result further and examine if it translates into particle heating, I plot the median $T_p/\langle T_p\rangle$ and $T_{p,\perp}/T_{p,\parallel}$ in the β_p-θ_{vB} plane in Fig-

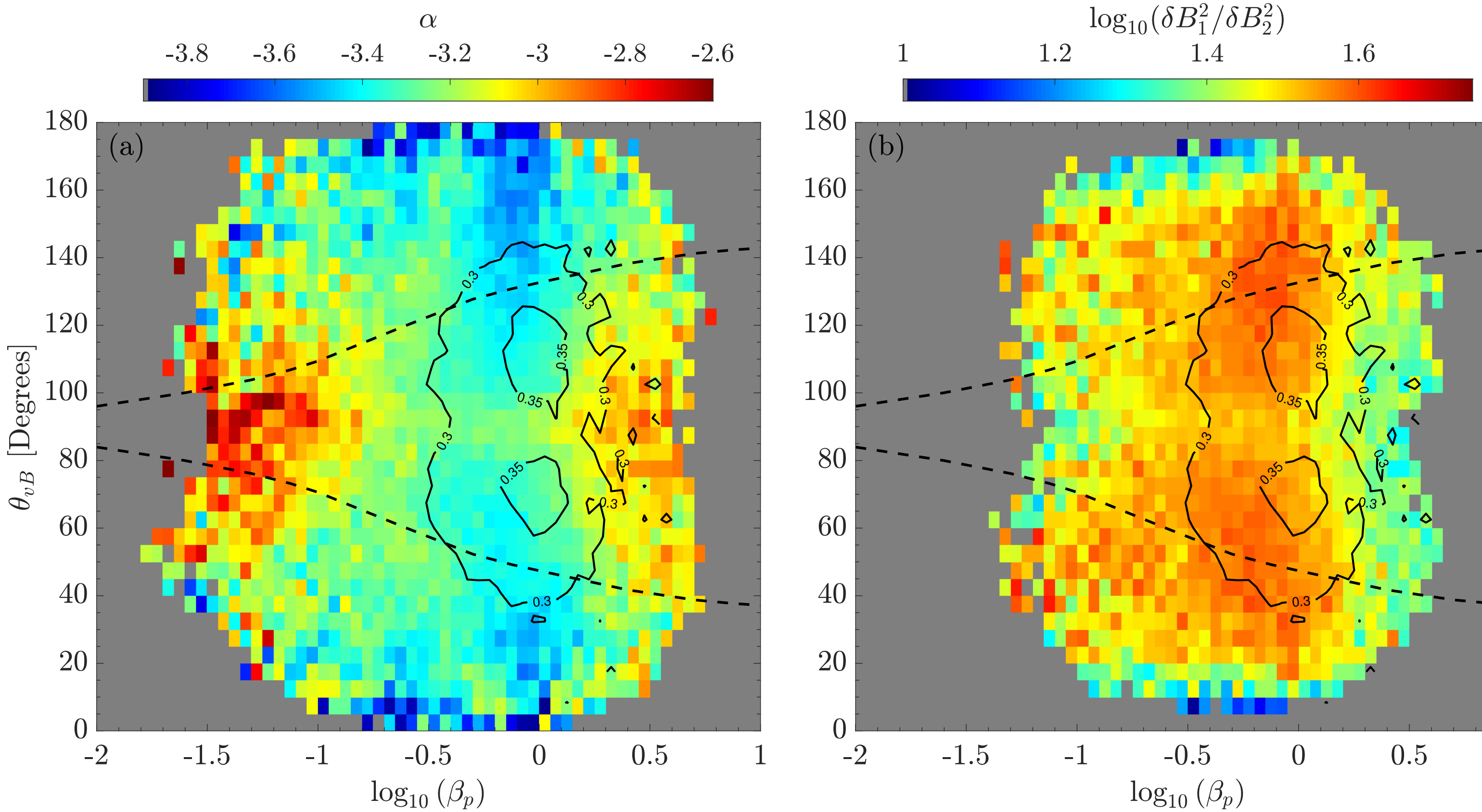

Figure 8.6: (*a*) Median spectral exponent, α, in the ion-kinetic range and (*b*) median $\log_{10}(\delta B_1^2/\delta B_2^2)$ [see main text] across the β_p-θ_{vB} plane. The black dashed lines the isocontours of $\mathrm{Re}(P) = 0$ in the β_p-θ_{kB} plane from Figure 8.1. I also include contours of constant $\sigma_\perp$ from Figure 8.3(*b*).

ure 8.7. Here, $\langle T_p \rangle$ is the average value of T_p over all angles for each bin in $\log_{10}(\beta_p)$. This column normalisation removes the systematic effect of increasing T_p along the x-axis of Figure 8.7 due to $\beta_p \propto T_p$, revealing the dependence of T_p on θ_{vB} for constant β_p. I see that both the median column-normalised T_p and median $T_{p,\perp}/T_{p,\|}$ show a clear dependence on θ_{vB} and β_p. In Panel (a), the median $T_p/\langle T_p \rangle$ shows little coherent variation across the β_p-θ_{vB} plane, whereas in Panel (b), the temperature anisotropy clearly shows higher perpendicular temperatures at quasi-parallel angles where $\mathrm{Re}(P) < 0$, and higher parallel temperatures at oblique angles where $\mathrm{Re}(P) > 0$. While at $\beta_p \lesssim 0.3$ there is a clear transition between the two cases that appears the follow the isocontours of $\mathrm{Re}(P) = 0$, this is not the case at higher β_p.

To explore this result in more detail, I plot the median value of $T_{p,\perp}/\left\langle T_{p,\perp} \right\rangle$ and $T_{p,\|}/\left\langle T_{p,\|} \right\rangle$ separately in the β_p-θ_{vB} plane in Figure 8.8. Similarly to Figure 8.7(b), I see a higher $T_{p,\perp}/\left\langle T_{p,\perp} \right\rangle$ at quasi-parallel angles and higher $T_{p,\|}/\left\langle T_{p,\|} \right\rangle$ at oblique angles. However, Figure 8.8 also shows enhancements in $T_{p,\perp}/\left\langle T_{p,\perp} \right\rangle$ where the $\sigma_\perp$ signal is strongest, as indicated by the contours of constant $\sigma_\perp$ from Figure 8.3. The higher $T_{p,\perp}$ at low β_p and quasi-parallel angles correlates with the helicity associated with AIC waves driven by kinetic instabilities [Kasper et al., 2002b; Matteini et al., 2007; Bale et al., 2009; Maruca et al., 2012b; Woodham et al., 2019]. In contrast, the enhancements in both temperatures at higher β_p and oblique angles correlates with the helicity of KAW-like fluctuations.

Different sectors in the solar wind are difficult to completely separate since there is no sharp boundary in ϕ_{rB} and hence, θ_{vB}, between inwards and outwards sectors (see Figure 7.4). Therefore, regions of the β_p-θ_{vB} plane in the figures presented here may include data from both inwards and outwards sectors. Any variations in temperature between different sectors will lead to a blurring of correlations in this parameter space. To account for this effect, I plot in Figure 8.9, column-normalised $T_{p,\perp}$ and $T_{p,\|}$ for inwards and outwards sectors separately. These plots show the considerable overlap of data in β_p-θ_{vB}

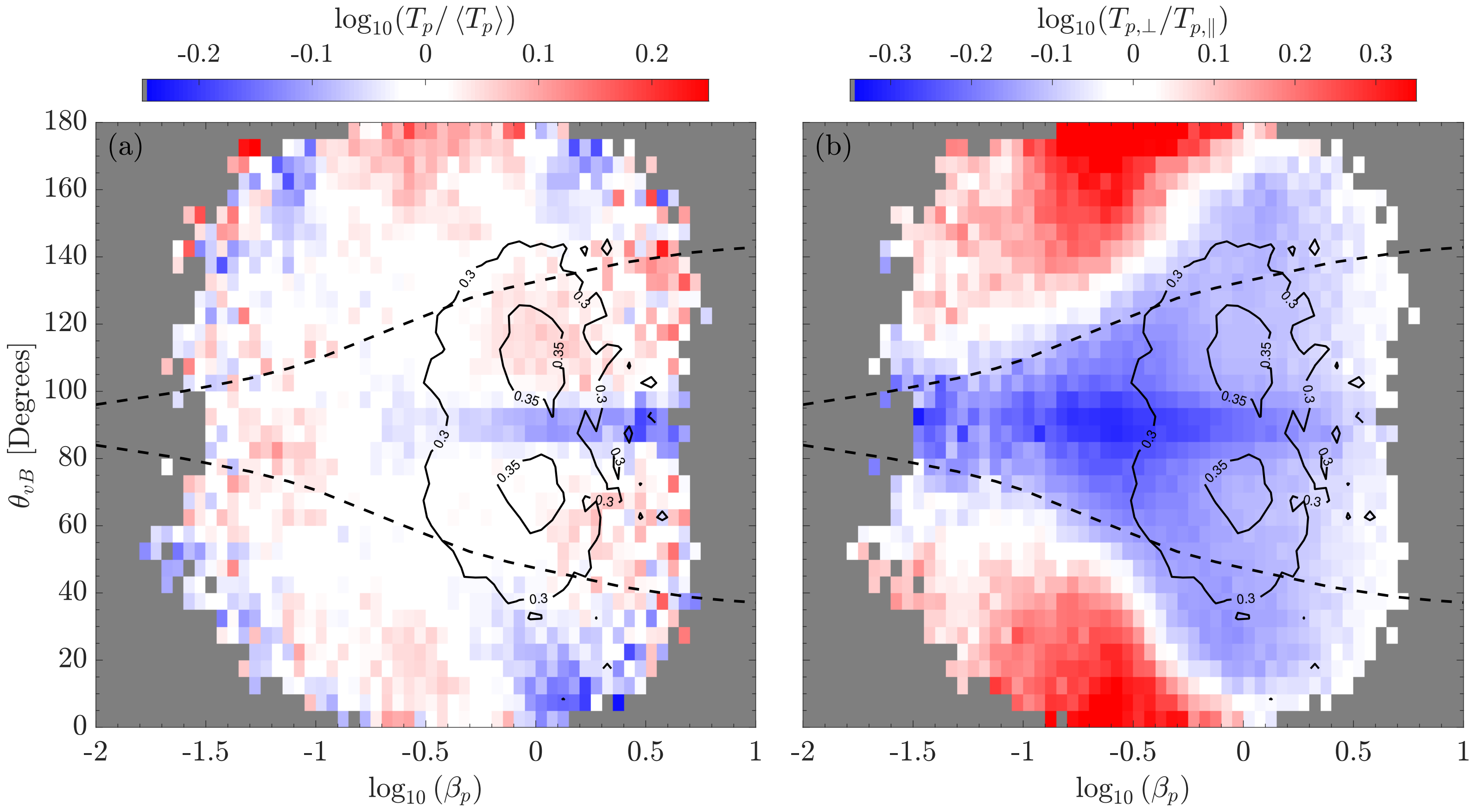

Figure 8.7: (*a*) Median proton temperature, $T_p/\langle T_p\rangle$, and (*b*) median proton temperature anisotropy, $T_{p,\perp}/T_{p,\parallel}$, across the β_p-θ_{vB} plane. Here, $\langle T_p\rangle$ is the average value of T_p over all angles for each bin in $\log_{10}(\beta_p)$. This column normalisation removes the systematic effect of $\beta_p \propto T_p$, revealing the dependence of T_p on θ_{vB} for constant β_p. The black dashed lines the isocontours of $\mathrm{Re}(P) = 0$ in the β_p-θ_{kB} plane from Figure 8.1. I also include contours of constant $\sigma_\perp$ from Figure 8.3(*b*).

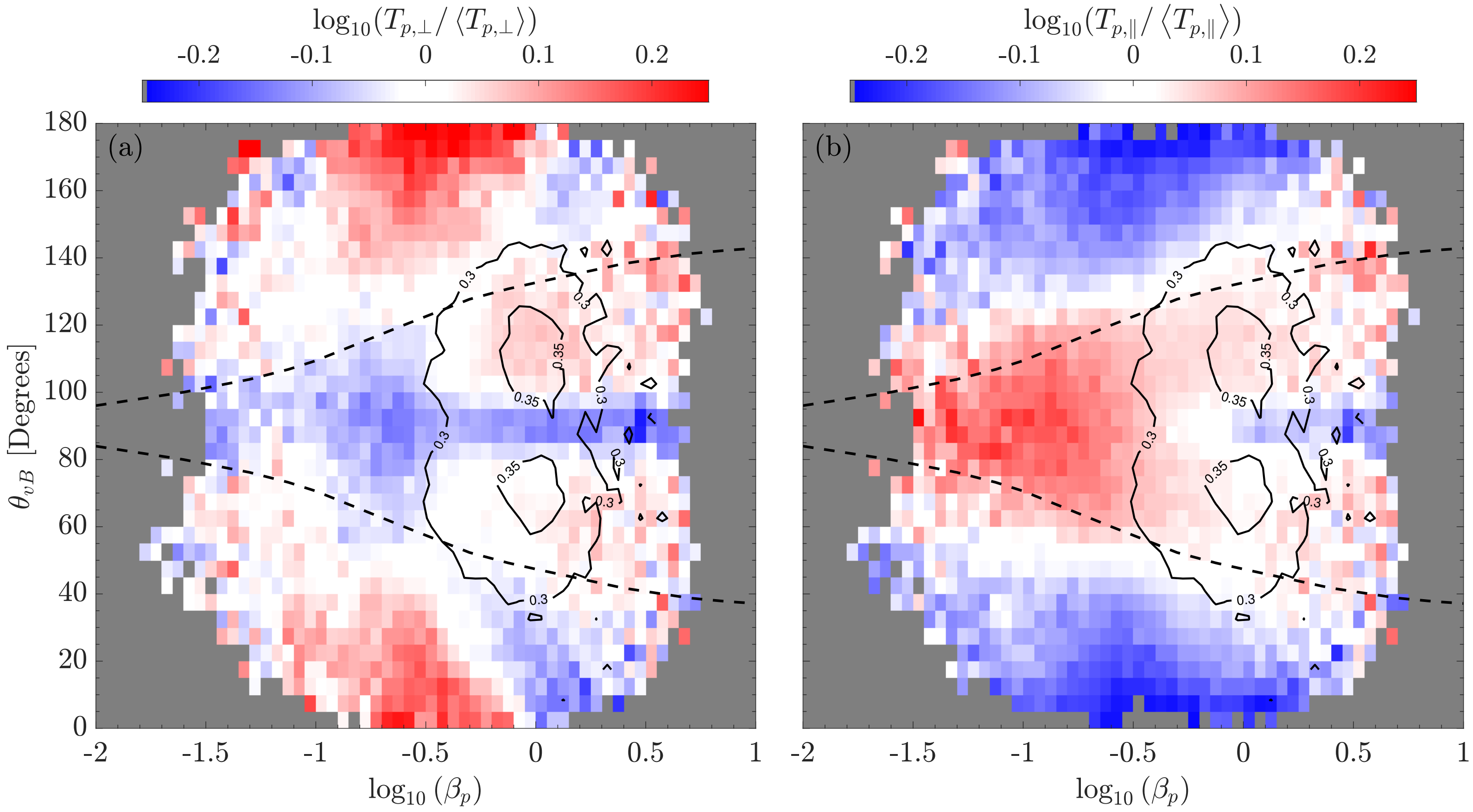

Figure 8.8: (*a*) Median proton perpendicular temperature, $T_{p,\perp}/\langle T_{p,\perp}\rangle$, and (*b*) median proton parallel temperature, $T_{p,\parallel}/\left\langle T_{p,\parallel}\right\rangle$, across the β_p-θ_{vB} plane. Here, $\left\langle T_{p,\perp/\parallel}\right\rangle$ is the average value of $T_{p,\perp/\parallel}$ over all angles for each bin in $\log_{10}(\beta_p)$. This column normalisation removes the systematic effect of $\beta_p \propto T_{p,\perp/\parallel}$, revealing the dependence of $T_{p,\perp/\parallel}$ on θ_{vB} for constant β_p. The black dashed lines the isocontours of $\mathrm{Re}(P) = 0$ in the β_p-θ_{kB} plane from Figure 8.1. I also include contours of constant $\sigma_\perp$ from Figure 8.3(*b*).

space for both sectors. By splitting the data according to sector structure, the enhancements in both $T_{p,\perp}$ and $T_{p,\|}$ are stronger. In particular, $T_{p,\|}$ shows a clear correlation with the isocontour of $\mathrm{Re}(P) = 0$ over the entire β_p range. The peak in $T_{p,\perp}$ at oblique angles and $\beta_p \simeq 1$ is also stronger.

To confirm the correlation between the peak in $T_{p,\|}/\left\langle T_{p,\|}\right\rangle$ and the angle at which the polarisation of Alfvén waves changes sign, I take cuts of $T_{p,\|}/\left\langle T_{p,\|}\right\rangle$ along θ_{vB} for constant β_p. In Figure 8.10, I show these cuts for inward and outward sectors (i.e., panel (*b*) in Figures 8.9(I) and 8.9(II), respectively). Here, I shift θ_{vB} so that $\theta^*_{vB} = 0$ corresponds to the angle at which the polarisation of Alfvén waves changes sign at that value of β_p, i.e., $\mathrm{Re}(P) > 0$. For both inward and outward sectors, the peaks in $T_{p,\|}/\left\langle T_{p,\|}\right\rangle$ are aligned for all values of β_p shown and straddle the line $\theta^*_{vB} = 0$, peaking on the perpendicular side ($\theta_{vB} \sim 90^\circ$) around $|\theta^*_{vB}| \simeq 20^\circ$. At either side of the peaks, $T_{p,\|}/\left\langle T_{p,\|}\right\rangle$ becomes negative and there is a systematic trend as β_p increases. This result confirms that the correlation between the peak in $T_{p,\|}/\left\langle T_{p,\|}\right\rangle$ with the dashed lines in Figure 8.9 exists and is not due to my plotting method.

8.3 Discussion: The Ergodicity Hypothesis

The angular dependence of proton temperature that correlates with the polarisation properties of Alfvénic fluctuations at ion-kinetic scales in the solar wind is a completely unexpected result. It is generally assumed that the nature and properties of the fluctuations are independent of $\theta_{vB} \sim \phi_{rB}$; in other words, the fluctuations are ergodic (see Section 3.7.1). Therefore, sampling different θ_{vB} measures different components of statistically the same set of turbulent fluctuations. If the background turbulence distribution does not depend on θ_{vB}, i.e., the fluctuations exist everywhere in space, then I expect no correlation between $T_p/\langle T_p\rangle$ and polarisation properties of Alfvénic fluctuations at ion-kinetic scales. In contrast, I find a clear correlation in the θ_{vB}-β_p plane. While I expect polarisation properties to affect proton temperature, I do not measure the polarisation of all fluctuations at once due to Taylor's hypothesis, just the

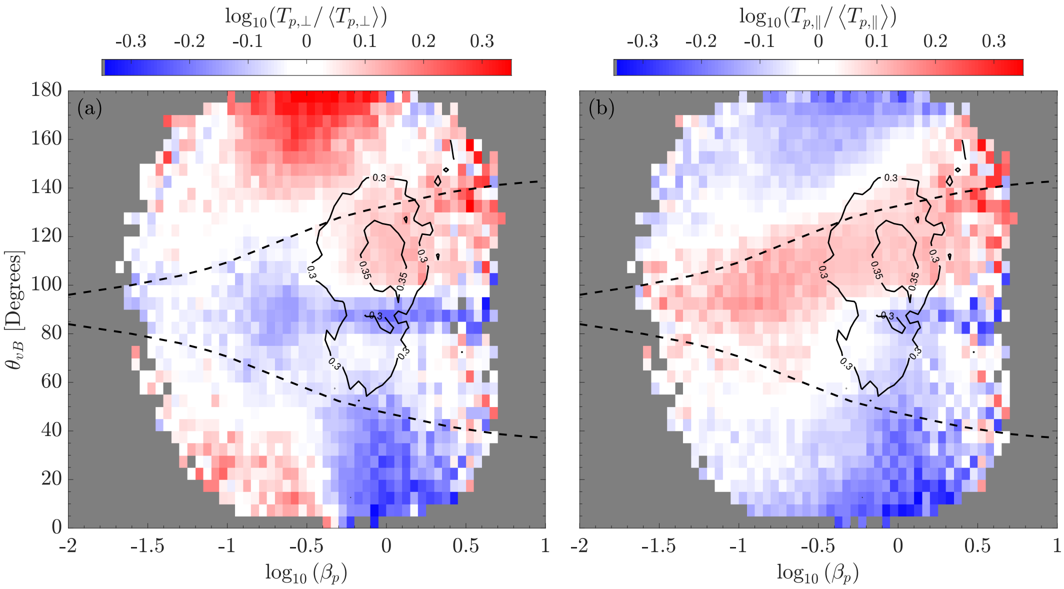

(I) Inwards Sectors

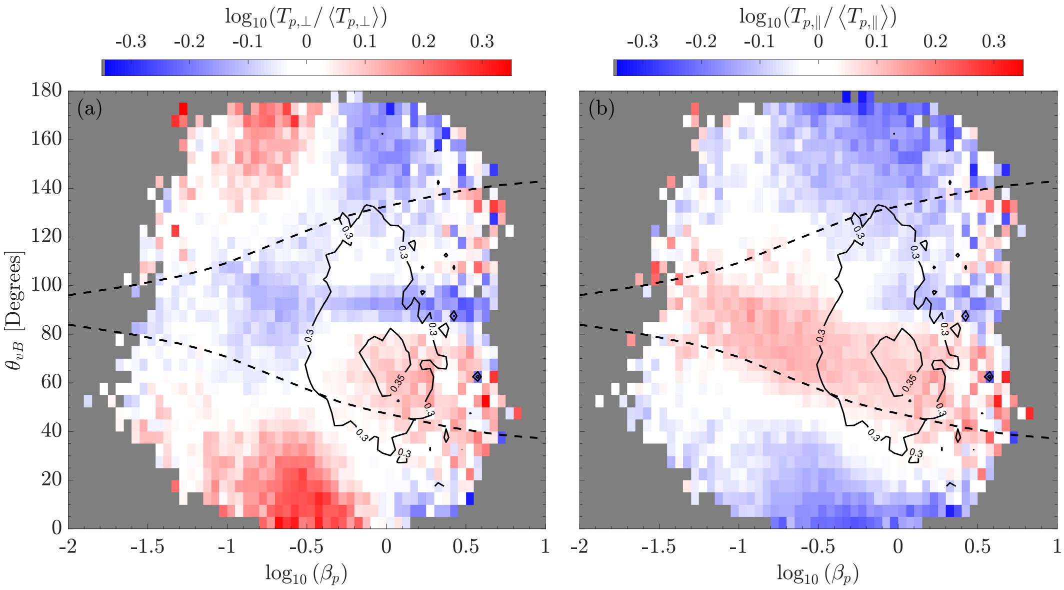

(II) Outwards Sectors

Figure 8.9: Distributions of $T_{p,\parallel}$ and $T_{p,\perp}$ in the $\log_{10}(\beta_p)$-θ_{vB} plane for inwards (I) and outwards (II) sectors. The black dashed lines the isocontours of $\mathrm{Re}(P) > 0$ in the β_p-θ_{kB} plane from Figure 8.1. I also include contours of constant $\sigma_\perp$ from Figure 8.3(b).

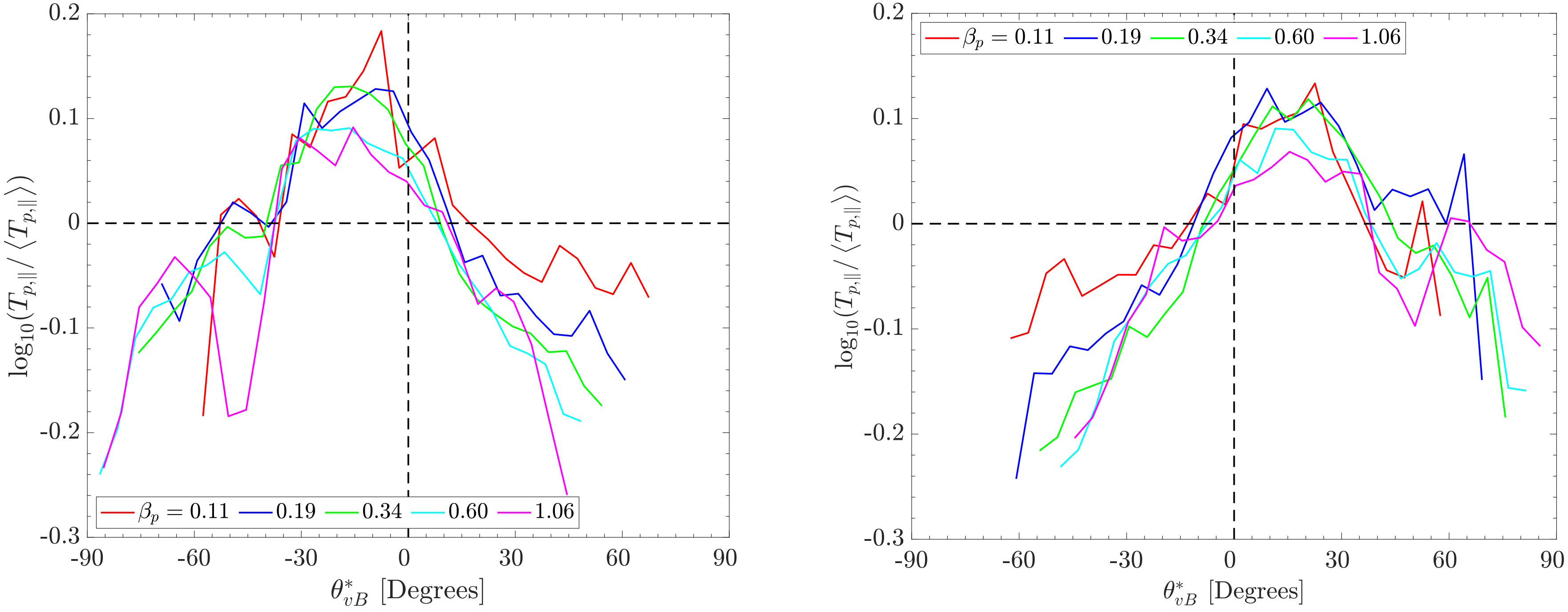

(a) Inwards Sectors

(b) Outwards Sectors

Figure 8.10: Cuts of $T_{p,\|}/\left\langle T_{p,\|}\right\rangle$ as a function of θ^*_{vB} for different values of β_p for inwards (I) and outwards (II) sectors. Here, θ^*_{vB} is a shifted angle so that the critical angle θ_{vB} for the change sign in the polarisation at a particular value of β_p is zero.

dominantly radial fluctuations due to the $\mathbf{k} \cdot \mathbf{v}_{sw}$ term in Equation 3.30. It is these fluctuations that affect the distribution of $T_p / \langle T_p \rangle$ in θ_{vB}. This result suggests that the nature of the fluctuations and the heating processes are *not* independent of θ_{vB}, in violation of the ergodicity hypothesis.

If this interpretation is correct, studies that sample many angles θ_{vB} as the solar wind traverses a single spacecraft to build up a picture of the turbulence in the plasma [e.g., Horbury et al., 2008; Wicks et al., 2010; He et al., 2011] need to be interpreted very carefully. This is because the ergodicity hypothesis cannot be used to sample different fluctuations of the same background distribution using θ_{vB}. Instead, my results suggest the existence of different types of fluctuations at different θ_{vB}. Therefore, different physical processes associated with different fluctuations may lead to changes in $T_{p,\perp}$ and $T_{p,\|}$ with θ_{vB} and β_p. The enhancement in $T_{p,\perp} / \left\langle T_{p,\perp} \right\rangle$ at quasi-parallel angles in Figure 8.8(a) is likely related to the driving of AIC waves by proton temperature anisotropy instabilities [He et al., 2011, 2012a,b; Klein et al., 2014; Bruno & Telloni, 2015] that are associated with the peak in $\sigma_{\|}$ at these angles (Figure 8.3). This driving is enhanced by the presence of an α-particle proton differential flow (see Chapter 7 and Figure 8.4), consistent with Podesta & Gary [2011a,b].

The peaks in $T_{p,\perp} / \left\langle T_{p,\perp} \right\rangle$ at oblique angles, on the other hand, are unlikely due to instabilities. Since these enhancements correlate with $\sigma_{\perp}$ in Figure 8.3(b), they may be explained by the damping of KAW fluctuations. This interpretation is consistent with a larger decrease in δB^2 in Figure 8.6 that correlates with $T_{p,\perp} / \left\langle T_{p,\perp} \right\rangle$. I also find a correlation with steeper exponents than the predicted -2.8 at ion-kinetic scales, although the agreement is weaker. A common dissipation mechanism proposed for KAW-like fluctuations is Landau damping [e.g., Howes, 2008; Schekochihin et al., 2009; Chen et al., 2019]; however, this leads to parallel heating. Instead, perpendicular heating may arise from processes such as stochastic heating [Chandran et al., 2010, 2013], although more work is needed to confirm this. One unanswered question here is the role of the α-particle drift with respect to the protons, which peaks in the same part of the β_p-θ_{vB} plane as $\sigma_\perp$ and $T_{p,\perp}$. This result suggests that the presence of strong drifts provide another route for heating where beam driven waves interact with the core distribution, leading to perpendicular heating.

The variation of $T_{p,\|}/\left\langle T_{p,\|}\right\rangle$ in the β_p-θ_{vB} plane in Figure 8.8(b) is more difficult to interpret. The correlation of temperature with polarisation properties is clearer when I separate solar wind data according to sector structure in Figure 8.9. By accounting for the temperature in one sector is larger than the other, I show that the peaks in $T_{p,\|}/\left\langle T_{p,\|}\right\rangle$ are bounded by the isocontours of $\mathrm{Re}(P) > 0$ in Figure 8.10, suggesting that right-handed KAWs are associated with larger $T_{p,\|}$. This result could also be a signature of proton Landau damping of KAWs, although, this is typically stronger at higher $\beta_p \gtrsim 1$ [Gary & Borovsky, 2004; Gary & Nishimura, 2004]. Direct evidence of energy transfer between the fluctuations and protons is needed to confirm this result, which is more convincing than just showing a correlation in this space. This evidence will require higher-resolution data than provided by Wind, and I discuss this further as future work in the next chapter.

I note that caution must be given when interpreting these results, since several other effects may also explain the temperature dependence seen in the β_p-θ_{vB} plane, for example, instrumental effects and the role of solar wind expansion [Matteini et al., 2007]. I will now discuss these effects in turn, showing that they cannot completely replicate my results.

8.4 Analysis Caveats

8.4.1 Instrumentation and Measurement Uncertainties

The SWE Faraday cups onboard the *Wind* spacecraft measure a reduced VDF (Equation 5.6) that depends on the average direction of $\mathbf{B}_0$ over the measurement interval of ~92 s [Kasper, 2002]. Due to the geometry of the instruments and their orientation with respect to the spacecraft body, the direction of $\mathbf{B}_0$ can cause inherent uncertainty in the measurements of $T_{p,\|}$ and $T_{p,\perp}$ (see Section 5.3.5). For example, if $\mathbf{B}_0$ is directed along the axis of the cups, then $T_{p,\|}$

is well-defined but $T_{p,\perp}$ is not. Likewise, uncertainty in $T_{p,\|}$ is largest when $\mathbf{B}_0$ is directed out of the ecliptic plane by a significant angle, $\phi_B \gtrsim 60^\circ$ [Kasper et al., 2006]. In Figure 8.11, I plot the percentage uncertainty in $w_{p,\|}$ and $w_{p,\perp}$ in the β_p-θ_{vB} plane, which are the fitted parameters from the SWE data (see Chapter 5). Figure 8.11 shows the location in parameter space where the uncertainty in the temperature measurements is largest.

In Panel (*a*) I see that $w_{p,\perp}$ has a larger uncertainty ($\sim$40%) at quasi-parallel angles, which is almost independent of β_p. While $T_{p,\perp}/\left\langle T_{p,\perp}\right\rangle$ in Figure 8.8(*a*) is larger at these angles, there is a clear dependence with β_p. Therefore, increased uncertainty in the temperature measurements alone cannot completely account for this feature in the β_p-θ_{vB} plane. At quasi-perpendicular angles, the uncertainty is less than 10%, suggesting that the enhancements in $T_{p,\perp}$ in Figure 8.8(*a*) at $\beta_p \simeq 1$ and $40 \lesssim \theta_{vB} \lesssim 140$ are unlikely to result from instrumental effects. From Figure 8.11(*b*), the uncertainty in $w_{p,\|}$ is largest at $\theta_{vB} \simeq 90^\circ$, although there is a larger spread to $60^\circ \lesssim \theta_{vB} \lesssim 120^\circ$ at $\beta_p \gtrsim 0.3$. By comparing with Figure 8.8(*b*), the enhancement in $T_{p,\|}$ that correlates with the isocontours of $\mathrm{Re}(P) > 0$ over the entire β_p range does not coincide exactly with the regions of β_p-θ_{vB} space where these measurements have increased uncertainty. I also expect that any increased uncertainty in the $T_{p,\|}$ measurements would lead to increased noise that would act to destroy any correlation in this space, weakening the enhancement seen in Figure 8.8(*b*). Therefore, I conclude that the increased uncertainty in $T_{p,\|}$ at oblique angles is unlikely to be the sole cause of this enhancement.

Another source of uncertainty from the SWE measurements arises from the changing magnetic field direction throughout the measurement interval [Maruca & Kasper, 2013]. A large angular fluctuation in $\mathbf{B}$ over the integration time, ψ_B, can lead to the blurring of anisotropies in the proton thermal speeds due to a broadening of the reduced VDFs, increasing uncertainty in these measurements. To reduce this blurring effect, I neglect SWE measurements with angular deviations $\psi_B > 15^\circ$ (see Chapter 6). Maruca [2012] provide

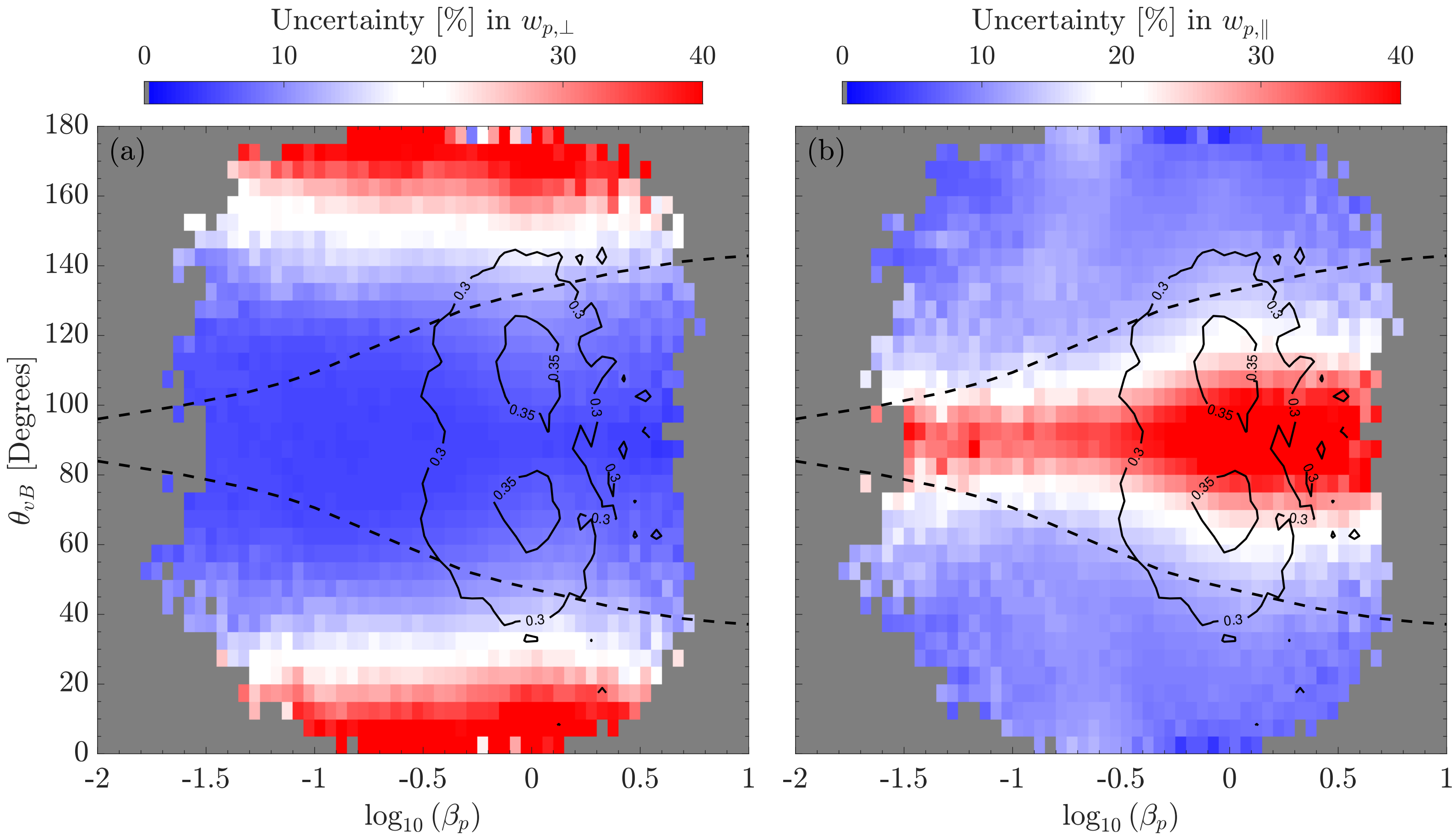

Figure 8.11: Median percentage uncertainty in (*a*) $w_{p,\perp}$ and (*b*) $w_{p,\parallel}$, across the β_p-θ_{vB} plane. The black dashed lines the isocontours of $\mathrm{Re}(P) > 0$ in the β_p-θ_{kB} plane from Figure 8.1. I also include contours of constant $\sigma_\perp$ from Figure 8.3(*b*).

an alternative dataset to account for large deviations in the magnetic field direction, using the average $\mathbf{B}_0$ for each rotation of the spacecraft (∼3 s) to calculate $T_{p,\perp}$ and $T_{p,\|}$ rather than the ∼92 s integration time used by Kasper [2002]. This dataset exists from 1994 to 2010 and so, to compare with my results in Figure 8.8, I plot in Figure 8.12, the median column-normalised $T_{p,\perp}$ and $T_{p,\|}$ in the β_p-θ_{vB} plane using the Maruca dataset. I use data from 2005-2010 to ensure that the *Wind* is only located at L1 for comparison with my dataset. While the data periods of both datasets are not the same, both $T_{p,\perp}/\left\langle T_{p,\perp}\right\rangle$ and $T_{p,\|}/\left\langle T_{p,\|}\right\rangle$ show a similar, albeit slightly reduced, correlation with both β_p and θ_{vB}. This result shows that the temperature dependence in the β_p-θ_{vB} plane is unlikely to be solely due to measurement effects.

8.4.2 CGL Spherical Expansion

Another possible source of variation in proton temperature with θ_{vB} is due to the expansion of the solar wind as it flows out into the heliosphere. The CGL equations (see Section 2.5.4) can be written as:

$$\frac{d}{dt}\left(\frac{T_{p,\perp}}{B_0}\right) = 0 \quad \text{and} \quad \frac{d}{dt}\left(\frac{T_{p,\|}B_0^2}{n_p^2}\right) = 0. \tag{8.4}$$

Assuming spherical expansion with a constant radial velocity, $\mathbf{v}_{sw} = v_{sw}\hat{\mathbf{r}}$, the continuity equation gives $n_p \propto 1/r^2$. The radial evolution of the magnetic field in the equatorial plane follows the Parker spiral [Parker, 1958],

$$B_0 \propto \frac{\sqrt{\cos^2\phi_0 + r^2\sin^2\phi_0}}{r^2}, \tag{8.5}$$

which gives a radial dependence of $B_0 \propto 1/r^2$ when $\phi_0 = 0°$ and $B_0 \propto 1/r$ when $\phi_0 = 90°$ (see also Equation 2.70). Here, $\tan\phi_0 = r_0\tan\phi_{rB}/r \equiv r_0\Omega_0/v_{sw}$, where the subscript 0 indicates initial value. Therefore, a value of v_{sw} sets the value of ϕ_0 at a given radius. From Equations 8.4 and 8.5,

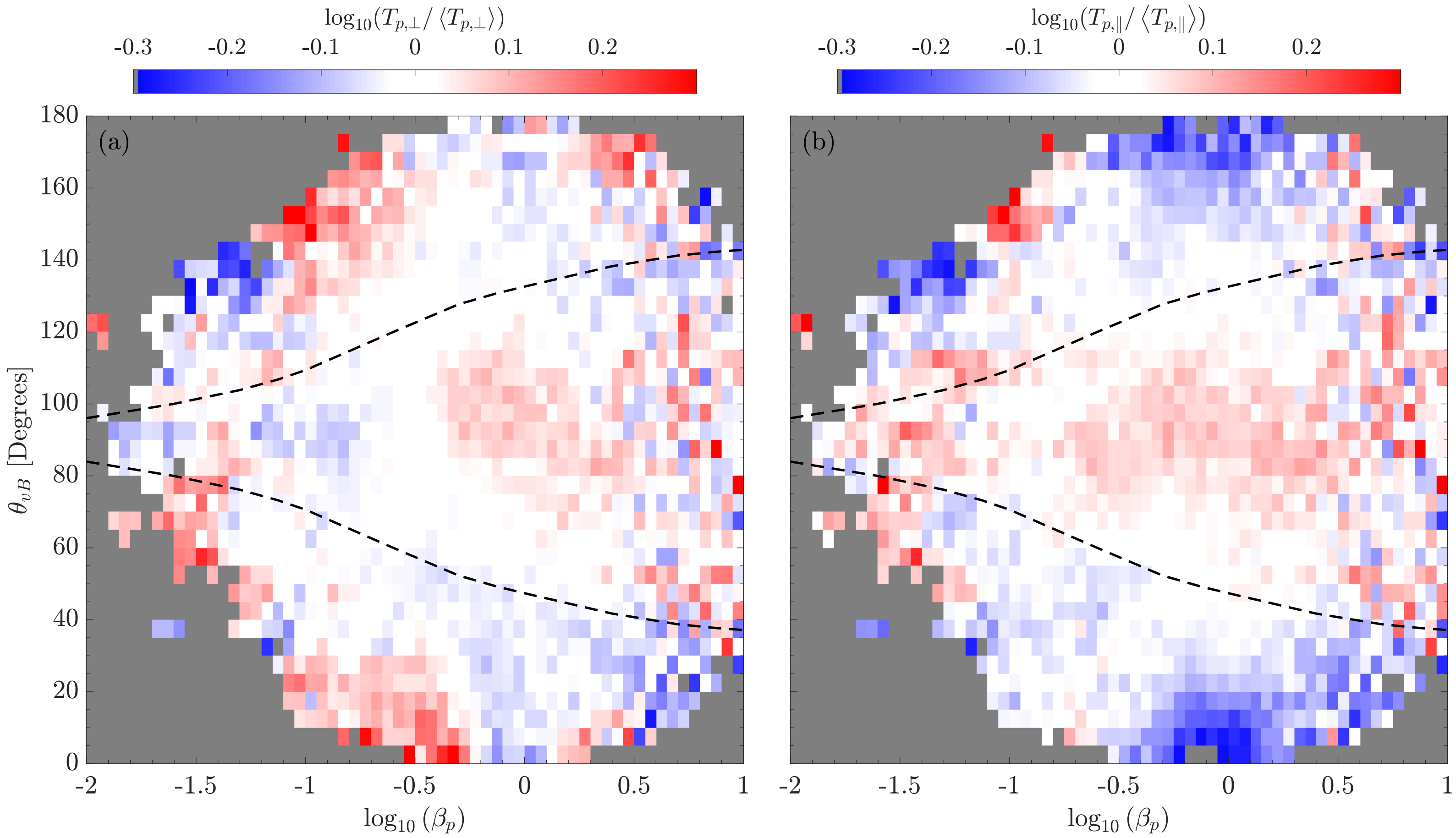

Figure 8.12: Maruca SWE dataset: (*a*) Median proton perpendicular temperature, $T_{p,\perp}/\langle T_{p,\perp}\rangle$, and (*b*) median proton parallel temperature, $T_{p,\parallel}/\left\langle T_{p,\parallel}\right\rangle$, across the β_p-θ_{vB} plane. Here, $\left\langle T_{p,\perp/\parallel}\right\rangle$ is the average value of $T_{p,\perp/\parallel}$ over all angles for each bin in $\log_{10}(\beta_p)$. This column normalisation removes the systematic effect of $\beta_p \propto T_{p,\perp/\parallel}$, revealing the dependence of $T_{p,\perp/\parallel}$ on θ_{vB} for constant β_p. The black dashed lines the isocontours of $\mathrm{Re}(P) > 0$ in the β_p-θ_{kB} plane from Figure 8.1. I also include contours of constant $\sigma_\perp$ from Figure 8.3(*b*).

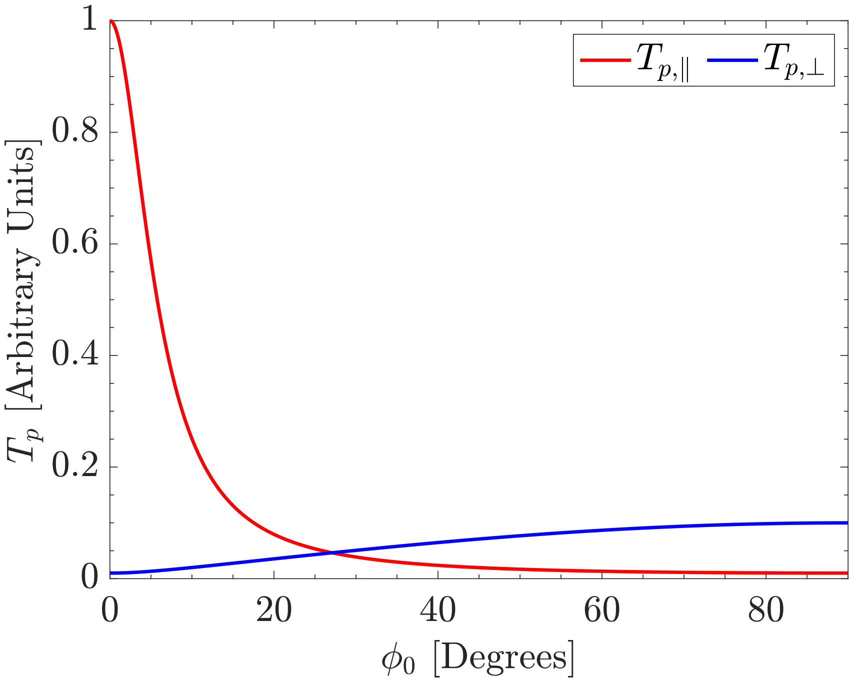

Figure 8.13: The temperature profiles $T_{p,\parallel}$ and $T_{p,\perp}$ as a function of ϕ_0 for CGL spherical expansion.

$$T_{p,\perp} = T_{\perp,0}\frac{\sqrt{\cos^2(\phi_0) + R^2\sin^2(\phi_0)}}{R^2}, \tag{8.6}$$

$$T_{p,\parallel} = \frac{T_{\parallel,0}}{\cos^2(\phi_0) + R^2\sin^2(\phi_0)}, \tag{8.7}$$

where $R = r/r_0$. Equations 8.6 and 8.7 can be used to investigate the dependence of temperature on ϕ_0. Since at 1 AU, the radial component of $\mathbf{v}_{sw}$ dominates, I can use ϕ_0 as a proxy for θ_{vB}. In Figure 8.13, I plot the variation of $T_{p,\perp}$ and $T_{p,\parallel}$ with ϕ_0 for a constant $R = 10$ and $T_{\perp,0} \equiv T_{\parallel,0} = 1$. I see that there is a lack of cooling for $T_{p,\parallel}$ at small ϕ_0, which decreases to zero with increasing ϕ_0. On the other hand, $T_{p,\perp}$ is largest at $\phi_0 \gtrsim 60°$ and approaches zero for $\phi_0 \simeq 0°$. This result is opposite to Figure 8.8, which in general shows larger $T_{p,\parallel}$ at $\theta_{vB} \simeq 90°$ and larger $T_{p,\perp}$ at $\theta_{vB} \simeq 0°$. Therefore, spherical expansion is insufficient to explain my results.

8.4.3 Radial Expansion and Compression

A variation in proton temperature can also arise from radial expansion or compression due to interactions between slow and fast wind streams: $v' = \partial v/\partial r$, where $v' < 0$ indicates compression and $v' > 0$, expansion. In the Lagrangian frame, which follows a solar wind stream, $v' = v_0'/(1+v_0't)$, where $v'(t=0) = v_0'$. The magnetic field in this frame is:

$$B = B_0 \frac{\sqrt{\sin^2(\phi_0) + \cos^2(\phi_0)\,(1+v_0't)^2}}{1+v_0't}, \tag{8.8}$$

and,

$$n_p = \frac{n_0}{1+v_0't}. \tag{8.9}$$

The variation of proton temperature with ϕ_0 becomes [Jason TenBarge, *private communication*]:

$$T_{p,\perp} = T_{\perp,0} \frac{\sqrt{\sin^2(\phi_0) + \cos^2(\phi_0)\,(1+v_0't)^2}}{1+v_0't}, \tag{8.10}$$

$$T_{p,\parallel} = T_{\parallel,0} \frac{1}{\sin^2(\phi_0) + \cos^2(\phi_0)\,(1+v_0't)^2}, \tag{8.11}$$

In Figure 8.14, I plot $T_{p,\parallel}$ and $T_{p,\perp}$ in the β_p-ϕ_0 plane using Equations 8.10 and 8.11 in the case of expansion ($v_0' = 0.25$) and compression ($v_0' = -0.25$). I extend the variation of T_p with ϕ_0 over all values of β_p to compare with the column-normalised temperatures in Figure 8.8. By comparing Figures 8.8 and 8.14, I find that neither radial expansion or compression due to stream interactions can explain the variation of $T_{p,\perp}$ in this plane. While expansion leads to larger values of $T_{p,\perp}$ at small angles in panel (*b*), the enhancement of $T_{p,\perp}$ in Figure 8.8(*a*) clearly varies β_p. The same argument holds for the enhancement in $T_{p,\perp}$ at oblique angles for radial compression in panel (*a*). For $T_{p,\parallel}$ in panels (*c*) and (*d*) of Figure 8.14, radial expansion better explains the

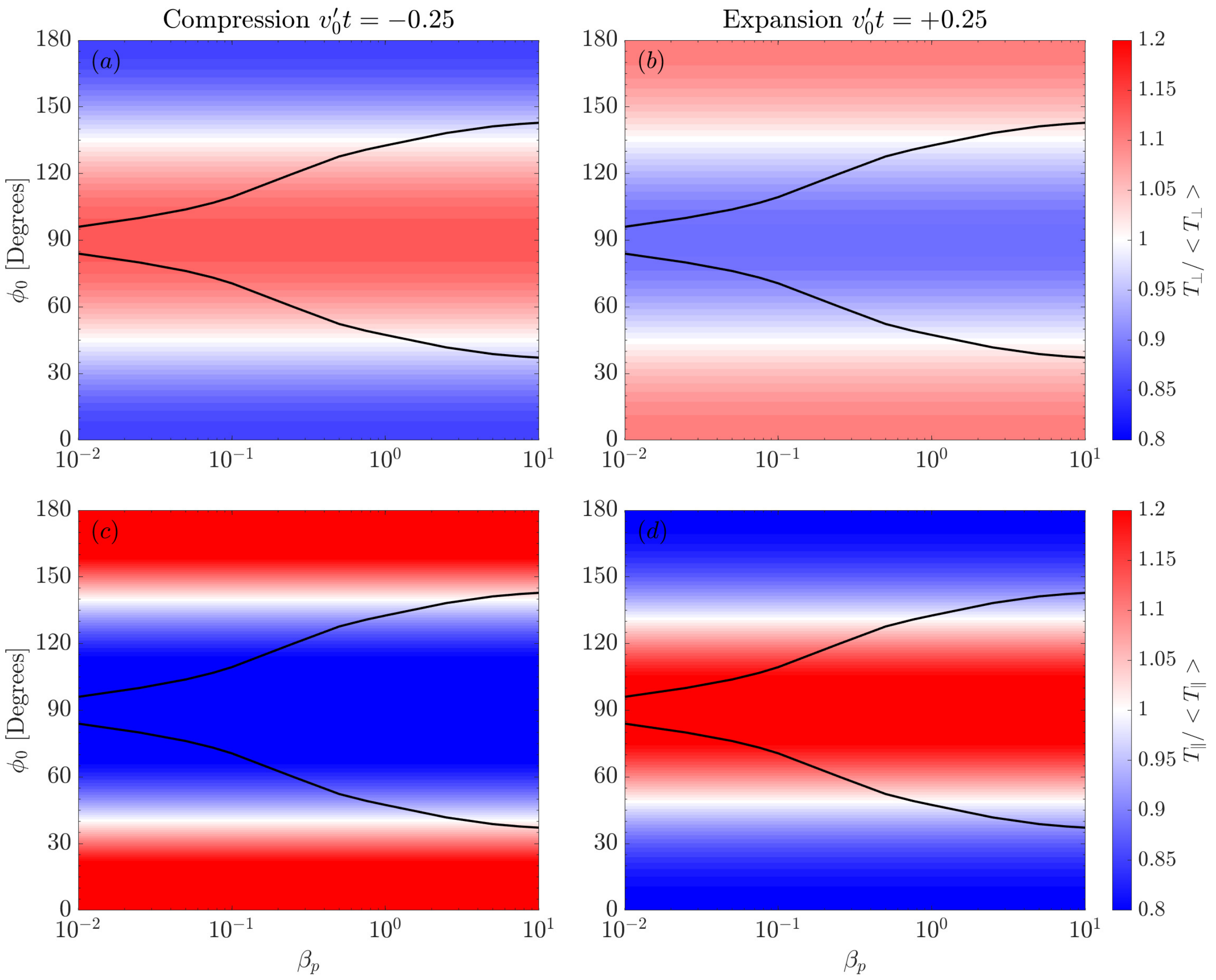

Figure 8.14: Column-normalised $T_{p,\perp}$ and $T_{p,\parallel}$ as a function of β_p and ϕ_0 for (a) radial expansion with $v_0' = 0.2$ and (b) for radial compression with $v_0' = -0.2$ (see main text). The black dashed lines the isocontours of $\text{Re}(P) > 0$ in the β_p-θ_{kB} plane from Figure 8.1.

variation of $T_{p,\|}$ for all β_p in the β_p-θ_{vB} plane in Figure 8.8(b). However, radial expansion does not account for the correlation of $T_{p,\|}$ with the polarisation properties of Alfvénic fluctuations.

8.5 Conclusions

In this chapter, I use the polarisation properties of radial Alfvénic fluctuations in the solar wind to probe turbulence dissipation mechanisms and find evidence of solar wind heating. I find that the polarisation properties of these fluctuations are consistent with linear Vlasov theory. The peak in magnetic helicity signature at ion-kinetic scales and how it varies with different solar wind properties (β_p and θ_{vB}) is in agreement with the dispersion relation of linear Alfvén waves [Gary, 1986]. Remarkably, this result shows that linear plasma physics has an important influence on the non-linear turbulent cascade at these scales. I also find that the spectral index of magnetic fluctuations at frequencies immediately above the break frequency, f_b, is correlated with the polarisation of Alfvén waves. It is steepest ($\alpha \lesssim -3.6$) at quasi-parallel angles in θ_{vB} where $\sigma_\|$ is largest, and steeper ($\alpha \simeq -3.3$) than the expected value of -2.8 at oblique angles where $\sigma_\perp$ and α-particle drifts are strongest. These regions of the β_p-θ_{vB} plane are associated with AIC waves from kinetic instabilities and KAW turbulence, respectively. The drop in energy in the power spectrum between f_b and $3f_b$ is also larger at oblique angles, consistent with steeper exponents. These results suggest that the KAW-like fluctuations in the solar wind are associated with dissipation of the turbulent cascade.

In order to investigate these possible signatures of energy dissipation, I look for corresponding signatures of proton heating. I find that the proton temperature, when normalised to remove its proportionality with β_p, shows a clear dependence on θ_{vB}, in violation of the ergodicity hypothesis. I find that $T_{p,\|}$ is generally higher in the parameter-space occupied by KAW-like fluctuations and $T_{p,\perp}$ higher in the parameter-space occupied by AIC waves, with small enhancements also associated with KAW-like fluctuations. This finding suggests that wave-particle interactions play an important role in the mediation of proton temperature anisotropy in the solar wind. In particular, heating mechanisms associated with KAWs may lead to both parallel [Gary & Borovsky, 2004] and perpendicular [Chandran et al., 2010, 2013] heating. Together, these results show that the polarisation properties of radial Alfvénic fluctuations depend on θ_{vB} (and β_p) and correlate with proton temperature. This may be direct evidence of local heating in the solar wind and suggests it is the properties of Alfvén waves at ion-kinetic that determine the level of heating of protons, and therefore, the large-scale evolution of the solar wind. Direct evidence of energy transfer between the fluctuations and protons is needed to confirm this result. This evidence will require higher-resolution data than provided by *Wind*.

There are several caveats that should be noted concerning the validity of my interpretations. The instrument geometry of the SWE Faraday cups onboard the *Wind* can lead to increased uncertainty in temperature measurements (see Chapter 5). While it is unlikely that my temperature results are entirely an instrumental effect, I cannot rule this out. Nevertheless, I conclude that noise in the measurements alone cannot completely replicate the correlation of proton temperature in the β_p-θ_{vB} plane. To determine if the blurring of the temperature anisotropy can explain the temperature results by the changing direction of $\mathbf{B}$ over 92 s, I have used a different dataset where there mean-field direction is averaged over 3 s [Maruca & Kasper, 2013]. However, I find the same results in the β_p-θ_{vB} plane. I also show that spherical expansion of the solar wind cannot explain the correlation of $T_p/\langle T_p\rangle$ in the β_p-θ_{vB} plane. However, radial expansion due to stream interactions can lead to enhancements in $T_{p,\|}/\left\langle T_{p,\|}\right\rangle$ at oblique angles and $T_{p,\perp}/\left\langle T_{p,\perp}\right\rangle$ at quasi-parallel angles. Despite this, radial expansion does not explain the correlation between $T_{p,\|}/\left\langle T_{p,\|}\right\rangle$ and the isocontours of $\mathrm{Re}(P) > 0$ as a function of β_p.

I emphasise that my conclusions do not invoke causality, just correlation. However, the way I measure the spectral exponent is independent of T_p, and yet, it correlates in the β_p-θ_{vB} plane with wave properties, as well as proton temperature itself. This implies that the θ_{vB} dependence of T_p is physical. I cannot rule out that the temperature correlations I observe may be a lack of cooling rather than heating, or that the magnetic fluctuations are generated by cooling of the proton distribution. However, while the adiabatic expansion (cooling) of the solar wind will cause the temperature to vary with θ_{vB}, this cannot fully explain the correlations of T_p in the β_p-θ_{vB} plane, especially when accounting for sector structure. Further work is needed to confirm these results and develop a theory for the processes that lead to this preferential direction, which I discuss in the next chapter.

Chapter 9

Conclusions and Future Work

In this thesis, I have characterised solar wind fluctuations at ion-kinetic scales to probe their associated physical processes. I have completed three different statistical studies using almost 15 years of data from the *Wind* spacecraft. I calculate the spectral properties of the magnetic field fluctuations and compare with moments of the proton VDFs in order to probe turbulent dissipation processes and kinetic instabilities at these scales. This work is the most detailed analysis of magnetic field fluctuations at ion-kinetic scales in the solar wind to date, accomplished using the first in-flight determination of the MFI noise-floor.

In my first study, I undertake a statistical analysis of the spectral steepening of the magnetic field power spectrum and onset of a coherent magnetic helicity signature at ion-kinetic scales, quantifying the frequencies associated with these spectral features and comparing them with characteristic protons scales. The different scales, d_p, ρ_p, and $1/k_c$, are associated with different plasma processes that can reveal which dissipation mechanisms may be active at these scales in order to damp the turbulent fluctuations and heat protons. Using a Morlet wavelet transform, I calculate the magnetic field power and helicity spectra averaged over 92 s to compare with the same cadence proton data from the SWE Faraday cups. I develop algorithms to determine the spectral break frequency, amplitude and low-frequency bound of the helicity peak at ion-kinetic scales. I find that the spectral steepening and helicity peak correlate best with the cyclotron resonance scale, $1/k_c$, suggesting they are linked and possibly due to the same physical process. While this result suggests cyclotron resonance is a dissipation mechanism at least 40% of the time in the solar wind, this interpretation is inconsistent with the anisotropic nature of the cascade, suggesting that other processes must be at work.

I use magnetic helicity in my second study to diagnose the fluctuations that exist at ion-kinetic scales using their polarisation properties. A better understanding of the processes at work, in particular, those associated with $1/k_c$, can be obtained by understanding the nature and origin of the fluctuations at these scales. I build on my analysis techniques from my first study, using a mean-field-aligned coordinate system in order to separate components of the magnetic helicity with wave-vectors parallel and perpendicular to $\mathbf{B}$. By accounting for the sector structure of the solar wind, I use the $\beta_{p,\|}$-$T_{p,\perp}/T_{p,\|}$ parameter space in order to identify the presence of any instability-driven fluctuations at these scales. I find that quasi-parallel fluctuations at ion-kinetic scales arise only from kinetic instabilities driven by proton temperature anisotropy and an α-particle-proton differential flow. This differential flow leads to preferential driving of AIC modes anti-sunward and FMW modes sunward. In contrast, quasi-perpendicular fluctuations from the turbulent cascade are consistent with KAW-like fluctuations and show little dependence on proton temperature anisotropy and β_p. The helicity from these three populations for fluctuations is stronger for plasma with a larger drift speed between α-particles and protons. The lack of quasi-parallel turbulent fluctuations at ion-kinetic scales suggests they are either not produced by the cascade or are completely damped before the cascade reaches these scales, although the former is more consistent with previous studies [Horbury et al., 2008; Chen et al., 2010a; Wicks et al., 2010].

Since Alfvénic fluctuations at ion-kinetic scales appear to be the dominant constituent of the turbulent cascade, I use the polarisation properties of these fluctuations from linear theory to probe the possible dissipation mechanisms consistent with right-handed KAW-like fluctuations in the solar wind. In my third study, I use the β_p-θ_{vB} parameter space where θ_{vB} is a proxy for θ_{kB}, which cannot be determined from single-spacecraft measurements. I find that quasi-perpendicular fluctuations are associated with steeper exponents in the transition range than the -2.8 value predicted for KAW turbulence and a larger drop in energy in the power spectrum at ion-kinetic scales, suggesting ongoing damping of the fluctuations at these scales. I also find that proton temperature shows a clear dependence on θ_{vB} in the solar wind. In particular, there are enhancements in the proton parallel and perpendicular temperatures that may be consistent with plasma heating by the dissipation of the KAW-like fluctuations, possibly through Landau/transit-time damping and stochastic heating. There are also signatures of radial expansion due to stream interactions, resulting in variations of T_p with θ_{vB}.

The results of my third study lead to the failure of the ergodicity hypothesis for solar wind turbulence. I place caution on my interpretations since the correlations of T_p in the β_p-θ_{vB} plane can be affected by measurement uncertainties of the SWE instrument, solar wind expansion and compression, and sector structure. I am unable to completely rule out that these correlations may arise from instrument effects. More work is needed to confirm these results. In particular, I propose using a different instrument on another spacecraft, for example, the electrostatic analyser on *Ulysses* spacecraft. Does a different instrument produce the same temperature dependence on θ_{vB}, or is it due to limitations of Faraday cups? How does the temperature dependence on θ_{vB} change with heliocentric distance?

Despite this, I have shown that the radial direction is special in the solar wind, not just for macroscopic effects, but also for dissipation. The proton temperature can change by a factor of up to ~ 2 depending on the polarisation properties of the radial fluctuations. The peaks in $T_{p,\|}$ and $T_{p,\perp}$ are located about $\theta_{vB} \simeq 15 - 20^{\circ}$ more oblique than the line where the polarisation of Alfvén waves is zero. Also, $T_{p,\perp}$ is only enhanced when a significant α-particle drift is present. These results all derive from using a 92 s local mean-field. Therefore, all of these effects must occur in a small number ($\sim$ 10-100) of gyroperiods, i.e., they are unlikely due to large-scale dynamical processes such as expansion. Only turbulence can drive fluctuations on these 92 s time-scales, but the plasma kinetics respond at these scales too. This implies rapid heating that does not have to be dissipation, but rather wave-particle interactions from instabilities and other processes. However, this heating is continuous and omnipresent, having an impact on the macroscopic temperature of the plasma. These results change the interpretation of turbulent heating throughout the Universe and conclusions drawn from non-expanding boxes may be of limited value for expanding plasmas.

I have presented three novel studies that probe a very important part of fundamental plasma physics. My first study sets the groundwork, the second places existing work into a global context and breaks new ground in the understanding of wave-particle interactions and anisotropy of solar wind turbulence. The third study is not only novel but also, if confirmed, potentially paradigm-shifting for the understanding of wave-particle interactions, heating and dissipation in the solar wind. This work shows that assumptions used previously were wrong. It identifies specific mechanisms that are important, namely: KAWs, Landau damping, beam-core wave interactions, and the importance of the radial direction in microscopic processes.

There are several avenues for future work to continue probing the physical processes at kinetic scales in the solar wind. In this thesis, I used data from the *Wind* spacecraft due to the availability of a large dataset suitable for statistical studies. However, there are several other spacecraft that are well-placed to continue my research. For example, *Cluster* and MMS provide magnetic field data to electron-kinetic frequencies from their search coil magnetometers and ion and electron moments at higher than a 92 s cadence. It would be interesting to apply my analysis techniques presented here to study magnetic helicity at sub-ion and electron-kinetic scales in the solar wind and magnetosheath. Do similar processes occur at electron-kinetic scales as ion-kinetic scales? What is the role of electron-scale instabilities? Are there any differences between ion and electron-kinetic scales and between the solar wind and magnetosheath? The higher resolution data also enables the use of different analysis methods that require electric field measurement or full particle VDFs, for example, the field-particle correlation technique devised by Klein & Howes [2016] in order to directly observe energy transfer between electromagnetic fluctuations and particles [Chen et al., 2019]. These two missions are also multi-spacecraft, consisting of four spacecraft in a tetrahedron formation. This formation enables the determination of the full wave-vector of the fluctuations without the drawbacks of Taylor's hypothesis.

Another avenue for future work includes the use of high-resolution 3D hybrid or PIC simulations. Simulations can shed light on physical processes in the solar wind and be used in tandem with *in-situ* observations to understand the physics of the transition range. What does the $k_{\|}$-$k_{\perp}$ distribution of magnetic helicity look like in a freely decaying or driven turbulence simulation? Does a 1D cut through the simulation box to simulate single-spacecraft measurements reproduce the magnetic helicity observed the solar wind? Simulations can also be set up with a fixed simulation box or an expanding box to simulate expansion effects in the solar wind. One way to test the effect of solar wind expansion on turbulence at ion-kinetic scales in the solar wind would be to investigate the variation of T_p with θ_{vB} in an expanding box and fixed simulation.

Finally, the recently launched *Parker Solar Probe* and soon to be launched *Solar Orbiter* missions will provide unparalleled measurements of the outer corona and inner heliosphere, respectively. These missions will provide the opportunity to understand better the formation and acceleration of the solar wind as well as heating of the corona and the links with turbulent dissipation and kinetic processes discussed in this thesis. The radial evolution of these processes in the heliosphere can also be explored. The analysis methods employed in this these can be applied to *Parker Solar Probe* and *Solar Orbiter* data to explore the role of fluctuations at kinetic scales in the corona and their evolution with increasing heliocentric distance. This will enable the diagnosis of the source and nature of the fluctuations that are crucial for the acceleration and heating of the solar wind.

Appendix A

The Dielectric Tensor from Kinetic Theory

To calculate the dispersion relation and growth/damping rate for electromagnetic fluctuations in a homogeneous plasma with a uniform background magnetic field, the linearised Vlasov equation is used [e.g., Stix, 1992; Gary, 1993]:

$$\left[\frac{\partial}{\partial t} + \mathbf{v}\cdot\frac{\partial}{\partial \mathbf{x}} + \frac{q_j}{m_j}\left(\mathbf{v}\times\mathbf{B}_0\right)\cdot\frac{\partial}{\partial \mathbf{v}}\right]\delta f_j = -\frac{q_j}{m_j}\left(\delta\mathbf{E} + \mathbf{v}\times\delta\mathbf{B}\right)\cdot\frac{\partial f_{0,j}(\mathbf{v})}{\partial \mathbf{v}}, \quad \text{(A.1)}$$

where $f_j(\mathbf{x},\mathbf{v},t) = f_{0,j}(\mathbf{v}) + \delta f_j(\mathbf{x},\mathbf{v},t)$ and $f_{0,j}(\mathbf{v})$ evolves slowly compared to the timescale of the fluctuations. For a gyrotropic equilibrium distribution function with $\mathbf{k} = k_\perp\hat{\mathbf{e}}_\perp + k_\parallel\hat{\mathbf{e}}_\parallel$, Equation A.1 can be solved for δf_j by taking into Fourier space. Then by substituting δf_j and using Equation 2.16b to solve for $\tilde{\mathbf{j}}(\mathbf{k},\omega)$, the dielectric tensor becomes:

$$\boldsymbol{\epsilon}(\mathbf{k},\omega) = \left(1 - \sum_s \frac{\omega_{p,j}^2}{\omega^2}\right)\mathbf{1} - \sum_j \sum_{\ell=-\infty}^{\ell=\infty} \frac{2\pi\omega_{p,j}^2}{n_{0,j}\omega^2}$$
$$\int_0^\infty \int_{-\infty}^\infty v_\perp dv_\perp dv_\parallel \left(k_\parallel \frac{\partial f_{0,j}}{\partial v_\parallel} + \frac{\ell\Omega_j}{v_\perp}\frac{\partial f_{0,j}}{\partial v_\perp}\right)\frac{\mathsf{S}_{j,\ell}\left(v_\parallel, v_\perp\right)}{k_\parallel v_\parallel + \ell\Omega_j - \omega}, \quad \text{(A.2)}$$

where the tensor $\mathsf{S}_{j,\ell}$ is given by:

$$\mathsf{S}_{j,\ell}\left(v_{\|},v_{\perp}\right)=\begin{bmatrix}\frac{\ell^2\Omega_j^2}{k_\perp^2}J_\ell^2 & \frac{i\ell v_\perp\Omega_j}{k_\perp}J_\ell J_\ell' & \frac{\ell v_\|\Omega_j}{k_\perp}J_\ell^2\\ -\frac{i\ell v_\perp\Omega_j}{k_\perp}J_\ell J_\ell' & v_\perp^2 J_\ell'^2 & -iv_\|v_\perp J_\ell J_\ell'\\ \frac{\ell v_\|\Omega_j}{k_\perp}J_\ell^2 & iv_\|v_\perp J_\ell J_\ell' & v_\|^2 J_\ell^2\end{bmatrix}, \tag{A.3}$$

and $J_\ell, J_\ell' = dJ_\ell/d\xi_j$ are Bessel functions with the argument $\xi_j = k_\perp v_\perp/\Omega_j$:

$$J_\ell(\xi)=\sum_{m=0}^{\infty}\frac{(-1)^m}{m!\Gamma(m+\ell+1)}\left(\frac{\xi}{2}\right)^{2m+\ell}, \tag{A.4}$$

where $\Gamma(n)=(n-1)!$ is the gamma function. Equation A.2 can be solved using assumptions for a chosen distribution function to derive analytical dispersion relations, or it can be solved numerically for the exact dispersion relations. For a plasma with a streaming bi-Maxwellian distribution function (Equation 2.22) with temperature anisotropy $A_j = T_{j,\perp}/T_{j,\|}-1$, the dielectric tensor becomes:

$$\boldsymbol{\epsilon}(\mathbf{k},\omega)=\mathbf{1}+\sum_j\begin{pmatrix}\epsilon_{j,1} & \epsilon_{j,2} & \epsilon_{j,4}\\ -\epsilon_{j,2} & \epsilon_{j,1}-\epsilon_{j,0} & -\epsilon_{j,5}\\ \epsilon_{j,4} & \epsilon_{j,5} & \epsilon_{j,3}\end{pmatrix}, \tag{A.5}$$

where

$$\epsilon_{j,0}=\frac{2\omega_{p,j}^2}{\omega k_\| w_{j,\|}}\sum_\ell \eta_j\Lambda_\ell'(\eta_j)\left[Z\left(\zeta_{j,\ell}\right)-\frac{k_\| w_{j,\|}}{2\omega}A_j Z'\left(\zeta_{j,\ell}\right)\right], \tag{A.6}$$

$$\epsilon_{j,1}=\frac{\omega_{p,j}^2}{\omega k_\| w_{j,\|}}\sum_\ell \frac{\ell^2\Lambda_\ell(\eta_j)}{\eta_j}\left[Z\left(\zeta_{j,\ell}\right)-\frac{k_\| w_{j,\|}}{2\omega}A_j Z'\left(\zeta_{j,\ell}\right)\right], \tag{A.7}$$

$$\epsilon_{j,2}=\frac{i\,\mathrm{sgn}\left(q_j\right)\omega_{p,j}^2}{\omega k_\| w_{j,\|}}\sum_\ell \ell\Lambda_\ell'(\eta_j)\left[Z\left(\zeta_{j,\ell}\right)-\frac{k_\| w_{j,\|}}{2\omega}A_j Z'\left(\zeta_{j,\ell}\right)\right], \tag{A.8}$$

$$\epsilon_{j,3} = -\frac{\omega_{p,j}^2}{k_\parallel^2 w_{j,\parallel}^2} \sum_\ell \left(1 - \frac{A_j}{A_j+1}\frac{\ell\Omega_j}{\omega}\right)\left(1+\frac{\ell\Omega_j}{\omega}\right)\Lambda_\ell\left(\eta_j\right) Z'\left(\zeta_{j,\ell}\right), \tag{A.9}$$

$$\epsilon_{j,4} = \frac{k_\perp}{2k_\parallel}\frac{\omega_{p,j}^2}{\omega\Omega_j} \sum_\ell \left(A_j + 1 - \frac{\ell\Omega_j}{\omega}A_j\right)\frac{\ell\Lambda_\ell\left(\eta_j\right)}{\eta_j} Z'\left(\zeta_{j,\ell}\right), \tag{A.10}$$

$$\epsilon_{j,5} = -\frac{i\,\mathrm{sgn}\left(q_j\right)}{k_\perp k_\parallel}\frac{\omega_{p,j}^2}{2\omega\Omega_j} \sum_\ell \left(A_j + 1 - \frac{\ell\Omega_j}{\omega}A_j\right)\Lambda_\ell'\left(\eta_j\right) Z'\left(\zeta_{j,\ell}\right). \tag{A.11}$$

Here, sgn is the sign function, $Z(\zeta)$ is the plasma dispersion relation with argument $\zeta_{j,\ell} = \left(\omega - \ell\Omega_j\right)/k_\parallel w_{j,\parallel}$:

$$Z(\zeta) = \frac{1}{\pi^{1/2}}\int_{-\infty}^{\infty}\frac{\exp\left(-z^2\right)dz}{z-\zeta}, \tag{A.12}$$

and $Z(\zeta)' = dZ(\zeta)/d\zeta = -2[1+\zeta Z(\zeta)]$. Finally, $\Lambda_\ell\left(\eta_j\right) = I_\ell\left(\eta_j\right)\exp\left(-\eta_j\right)$ and $\Lambda_\ell'\left(\eta_j\right) = d\Lambda_\ell\left(\eta_j\right)/d\eta_j$, where $\eta_j = k_\perp^2 w_{j,\perp}^2/2\Omega_j^2$ and $I_\ell(\eta_j)$ is the modified Bessel function:

$$I_\ell(\eta) = i^{-\ell}J_\ell(i\eta) = \sum_{m=0}^{\infty}\frac{1}{m!\Gamma(m+\ell+1)}\left(\frac{\eta}{2}\right)^{2m+\ell}. \tag{A.13}$$

The dielectric tensor for an isotropic plasma can be recovered by setting $A_j = 0$ [Baumjohann & Treumann, 1997b].

Appendix B

The Cyclotron Resonance Wave-number

The cyclotron resonance condition for protons is given by equating the Doppler-shifted wave frequency in the plasma rest-frame to the proton gyro-frequency (Section 2.6.2, see also Stix [1992]):

$$\omega\left(k_{\|}\right) - k_{\|}v_{\|} = \pm\Omega_p. \tag{B.1}$$

The ± sign takes into account the sense of the polarisation of the wave. Since the fluctuating electric field of AIC waves rotates in the same direction as the ion gyration and the resonant interaction is most effective if $k_{\|}v_{\|} < 0$, the resonance condition reduces to:

$$\omega\left(k_{\|}\right) + k_{\|}\left|v_{\|}\right| = \Omega_p. \tag{B.2}$$

To obtain the minimum wave-number, $k_{\|} = k_c$ [Leamon et al., 1998b], for dissipation by cyclotron resonance with the background solar wind proton distribution, I substitute for $\left|v_{\|}\right| = w_{p,\|}$ and the dispersion relation of Alfvén waves, $\omega = k_{\|}v_A$ [e.g., Gary, 1993],

$$k_c = \frac{\Omega_p}{v_A + w_{p,\|}} \equiv \frac{1}{d_p + \sigma_p}, \tag{B.3}$$

where σ_p is the characteristic scale associated with protons drifting along $\mathbf{B}_0$, which for a plasma with isotropic temperature is equivalent to the proton gyro-radius, ρ_p.

Bibliography

Acuña, M. H., Ogilvie, K. W., Baker, D. N., et al. 1995, Space Science Reviews, 71, 5

Alessio, A. M. 2016, Digital Signal Processing and Spectral Analysis for Scientists: Concepts and Applications (Springer Signals and Communication Technology)

Alexandrova, O., Carbone, V., Veltri, P., & Sorriso-Valvo, L. 2007, Planetary and Space Science, 55, 2224

—. 2008, The Astrophysical Journal, 674, 1153

Alexandrova, O., Chen, C. H. K., Sorriso-Valvo, L., Horbury, T. S., & Bale, S. D. 2013, Space Science Reviews, 178, 101

Alexandrova, O., Lacombe, C., Mangeney, A., & Grappin, R. 2011, arXiv:1111.5649v1

Alexandrova, O., Lacombe, C., Mangeney, A., Grappin, R., & Maksimovic, M. 2012, The Astrophysical Journal, 760, 121

Alexandrova, O., Mangeney, A., Maksimovic, M., et al. 2006, Journal of Geophysical Research: Space Physics, 111, A12208

Alexandrova, O., & Saur, J. 2008, Geophysical Research Letters, 35, L15102

Alexandrova, O., Saur, J., Lacombe, C., et al. 2009, Physical Review Letters, 103, 165003

Alterman, B. L., Kasper, J. C., Stevens, M. L., & Koval, A. 2018, The Astrophysical Journal, 864, 112

Asbridge, J. R., Bame, S. J., & Feldman, W. C. 1974, Solar Physics, 37, 451

Asbridge, J. R., Bame, S. J., Feldman, W. C., & Montgomery, M. D. 1976, Journal of Geophysical Research, 81, 2719

Bale, S. D., Kasper, J. C., Howes, G. G., et al. 2009, Physical Review Letters, 103, 211101

Bale, S. D., Kellogg, P. J., Mozer, F. S., Horbury, T. S., & Reme, H. 2005, Physical Review Letters, 94, 215002

Barnes, A. 1966, Physics of Fluids, 9, 1483

Batchelor, G. K. 1970, The Theory of Homogenous Turbulence (Cambridge University Press)

Baumjohann, W., & Treumann, R. A. 1997a, Advanced Space Plasma Physics (Imperial College Press)

—. 1997b, Basic Space Plasma Physics (Imperial College Press)

Behannon, K. W. 1978, Reviews of Geophysics, 16, 125

Belcher, J. W., & Davis Jr., L. 1971, Journal of Geophysical Research, 76, 3534

Bellan, P. M. 2008, Fundamentals of Plasma Physics (Cambridge University Press)

Bennett, W. R. 1948, Bell System Technical Journal, 27, 446

Beresnyak, A., & Lazarian, A. 2008, The Astrophysical Journal, 682, 1070

Berger, L., Wimmer-Schweingruber, R. F., & Gloeckler, G. 2011, Physical Review Letters, 106, 151103

Bieber, J. W., Wanner, W., & Matthaeus, W. H. 1996, Journal of Geophysical Research, 101, 2511

Biskamp, D. 2003, Magnetohydrodynamic Turbulence (Cambridge University Press)

Biskamp, D., Schwarz, E., & Drake, J. F. 1996, Physical Review Letters, 76, 1264

Biskamp, D., Schwarz, E., Zeiler, A., Celani, A., & Drake, J. F. 1999, Physics of Plasmas, 6, 751

Boldyrev, S. 2006, Physical Review Letters, 96, 1

Boldyrev, S., Chen, C. H. K., Xia, Q., & Zhdankin, V. 2015, The Astrophysical Journal, 806, 238

Boldyrev, S., Horaites, K., Xia, Q., & Perez, J. C. 2013, The Astrophysical Journal, 777, 41

Boldyrev, S., & Perez, J. C. 2012, The Astrophysical Journal, 758, L44

Bourouaine, S., Alexandrova, O., Marsch, E., & Maksimovic, M. 2012, The Astrophysical Journal, 749, 102

Bourouaine, S., Marsch, E., & Neubauer, F. M. 2010, Geophysical Research Letters, 37, 1

—. 2011, Astronomy & Astrophysics, 536, A39

Bourouaine, S., Verscharen, D., Chandran, B. D., Maruca, B. A., & Kasper, J. C. 2013, Astrophysical Journal Letters, 777, L3

Boyd, T. J. M., & Sanderson, J. J. 2003, The Physics of Plasmas (Cambridge University Press)

Bracewell, R. N. 1999, The Fourier Transform & Its Applications (McGraw-Hill)

Brandenburg, A., Subramanian, K., Balogh, A., & Goldstein, M. L. 2011, The Astrophysical Journal, 734, 9

Brown, R. G., & Hwang, P. Y. C. 2012, Introduction to Random Signals and Applied Kalman Filtering with Matlab Exercises, 4th edn. (Wiley)

Bruno, R., & Bavassano, B. 1997, Geophysical Research Letters, 24, 2267

Bruno, R., & Carbone, V. 2013, Living Reviews in Solar Physics, 10, 2

Bruno, R., & Telloni, D. 2015, The Astrophysical Journal Letters, 811, L17

Bruno, R., Telloni, D., Sorriso-Valvo, L., et al. 2019, Astronomy & Astrophysics, 96, 1

Bruno, R., & Trenchi, L. 2014, The Astrophysical Journal Letters, 787, L24

Bruno, R., Trenchi, L., & Telloni, D. 2014, The Astrophysical Journal Letters, 793, L15

Camporeale, E., Carè, A., & Borovsky, J. E. 2017, Journal of Geophysical Research: Space Physics, 122, 10,910

Celnikier, L., Harvey, C., Jegou, R., Kemp, M., & Moricet, P. 1983, Astronomy and Astrophysics, 126, 293

Chandran, B. D. 2018, Journal of Plasma Physics, 84

Chandran, B. D., Quataert, E., Howes, G. G., Xia, Q., & Pongkitiwanichakul, P. 2009, Astrophysical Journal, 707, 1668

Chandran, B. D., Schekochihin, A. A., & Mallet, A. 2015, Astrophysical Journal, 807, 39

Chandran, B. D. G. 2008, The Astrophysical Journal, 685, 30

Chandran, B. D. G., Li, B., Rogers, B. N., Quataert, E., & Germaschewski, K. 2010, The Astrophysical Journal, 720, 503

Chandran, B. D. G., Verscharen, D., Quataert, E., et al. 2013, The Astrophysical Journal, 776, 45

Chen, C. H., Bale, S. D., Salem, C., & Mozer, F. S. 2011a, Astrophysical Journal Letters, 737, 2

Chen, C. H., Howes, G. G., Bonnell, J. W., et al. 2013a, in AIP Conference Proceedings, Vol. 1539, 143

Chen, C. H. K. 2016, Journal of Plasma Physics, 82

Chen, C. H. K., Boldyrev, S., Xia, Q., & Perez, J. C. 2013b, Physical Review Letters, 110, 1

Chen, C. H. K., Horbury, T. S., Schekochihin, A. A., et al. 2010a, Physical Review Letters, 104, 255002

Chen, C. H. K., Howes, G. G., Bonnell, J. W., et al. 2013cin , 143

Chen, C. H. K., Klein, K. G., & Howes, G. G. 2019, Nature Communications, 10, 740

Chen, C. H. K., Leung, L., Boldyrev, S., Maruca, B. A., & Bale, S. D. 2014, Geophysical Research Letters, 41, 8081

Chen, C. H. K., Mallet, A., Schekochihin, A. A., et al. 2012a, The Astrophysical Journal, 758, 120

Chen, C. H. K., Mallet, A., Yousef, T. A., Schekochihin, A. A., & Horbury, T. S. 2011b, Monthly Notices of the Royal Astronomical Society, 415, 3219

Chen, C. H. K., Matteini, L., Schekochihin, A. A., et al. 2016, The Astrophysical Journal Letters, 825, L26

Chen, C. H. K., Salem, C. S., Bonnell, J. W., Mozer, F. S., & Bale, S. D. 2012b, Physical Review Letters, 109, 035001

Chen, C. H. K., Wicks, R. T., Horbury, T. S., & Schekochihin, A. A. 2010b, The Astrophysical Journal, 711, L79

Chew, G. F., Goldberger, M. L., & Low, F. E. 1956, Proceedings of the Royal Society A: Mathematical and Physical Sciences, 236

Chiuderi, C., & Velli, M. 2015, Basics of Plasma Astrophysics (Springer UNITEXT for Physics)

Cho, J., & Lazarian, A. 2004, The Astrophysical Journal, 615, L41

Cho, J., & Vishniac, E. T. 2000, The Astrophysical Journal, 539, 273

Coleman, P. J. 1966, Physical Review Letters, 17, 207

—. 1968, The Astrophysical Journal, 153, 371

Cooley, J. W., & Tukey, J. W. 1965, Mathematics of Computation, 19, 297

Cranmer, S. R., & van Ballegooijen, A. A. 2005, The Astrophysical Journal Supplement Series, 156, 265

Dasso, S., Milano, L. J., Matthaeus, W. H., & Smith, C. W. 2005, The Astrophysical Journal Letters, 635, L181

Davidson, P. A. 2017, Introduction to Magnetohydrodynamics (Cambridge University Press)

Denskat, K. U., Beinroth, H. J., & Neubauer, F. M. 1983, Journal of Geophysics, 54, 60

Dmitruk, P., Matthaeus, W. H., & Seenu, N. 2004, The Astrophysical Journal, 617, 667

Dorland, W., & Hammett, G. W. 1993, Physics of Fluids B, 5, 812

Drake, J. F., & Swisdak, M. 2014, Physics of Plasmas, 21, 072903

Durovcová, T., Šafránková, J., Němeček, Z., & Richardson, J. D. 2017, The Astrophysical Journal, 850, 164

Ebert, R. W., McComas, D. J., Elliott, H. A., Forsyth, R. J., & Gosling, J. T. 2009, Journal of Geophysical Research: Space Physics, 114

Egedal, J., Daughton, W., & Le, A. 2012, Nature Physics, 8, 321

Elsässer, W. M. 1950, Physical Review, 79, 183

Feldman, W. C., Asbridge, J. R., Bame, S. J., & Montgomery, M. D. 1974, Reviews of Geophysics, 12, 715

Forman, M. A., Wicks, R. T., & Horbury, T. S. 2011, The Astrophysical Journal, 733, 76

Forsyth, R. J., Balogh, A., & Smith, E. J. 2002, Journal of Geophysical Research: Space Physics, 107, 1405

Franci, L., Landi, S., Matteini, L., Verdini, A., & Hellinger, P. 2015, Astrophysical Journal, 812, 21

Frisch, U. 1995, Turbulence: The Legacy of A.N. Kolmogorov (Cambridge University Press)

Gabor, D. 1946, Journal of the Institution of Electrical Engineers, 93, 429

Galtier, S. 2006, Journal of Plasma Physics, 72, 721

—. 2016, Introduction to Modern Magnetohydrodynamics (Cambridge University Press)

Galtier, S., & Buchlin, E. 2007, The Astrophysical Journal, 656, 560

Galtier, S., Pouquet, A., & Mangeney, A. 2005, Physics of Plasmas, 12, 1

Gary, S. P. 1986, Journal of Plasma Physics, 35, 431

—. 1993, Theory of Space Plasma Microinstabilities (Cambridge University Press)

—. 1999, Journal of Geophysical Research, 104, 6759

—. 2015, Philosophical Transactions of the Royal Society A: Mathematical, Physical and Engineering Sciences, 373, 20140149

Gary, S. P., Anderson, B. J., Denton, R. E., Fuselier, S. A., & McKean, M. E. 1994a, Physics of Plasmas, 1, 1676

Gary, S. P., & Borovsky, J. E. 2004, Journal of Geophysical Research: Space Physics, 109, A06105

Gary, S. P., Jian, L. K., Broiles, T. W., et al. 2015, Journal of Geophysical Research: Space Physics, 121, 30

Gary, S. P., & Lee, M. A. 1994, Journal of Geophysical Research, 99, 11297

Gary, S. P., McKean, M. E., Winske, D., et al. 1994b, Journal of Geophysical Research, 99, 5903

Gary, S. P., & Nishimura, K. 2004, Journal of Geophysical Research: Space Physics, 109, A02109

Gary, S. P., Skoug, R. M., Steinberg, J. T., & Smith, C. W. 2001, Geophysical Research Letters, 28, 2759

Gary, S. P., & Smith, C. W. 2009, Journal of Geophysical Research: Space Physics, 114, 1

Gershman, D. J., Zurbuchen, T. H., Fisk, L. A., et al. 2012, Journal of Geophysical Research: Space Physics, 117

Ghosh, S., Siregar, E., Roberts, D. A., & Goldstein, M. L. 1996, Journal of Geophysical Research, 101, 2493

Goldreich, P., & Sridhar, S. 1995, The Astrophysical Journal, 438, 763

Goldstein, B. E., Neugebauer, M., Zhang, L. D., & Gary, S. P. 2000, Geophysical Research Letters, 27, 53

Goldstein, M. L., Roberts, D. A., & Fitch, C. A. 1994, Journal of Geophysical Research, 99, 11,519

Goldstein, M. L., Roberts, D. A., & Matthaeus, W. H. 1995, Annual Review of Astronomy and Astrophysics, 33, 283

Greco, A., Servidio, S., Matthaeus, W. H., & Dmitruk, P. 2010, Planetary and Space Science, 58, 1895

Gurnett, D. A., & Bhattacharjee, A. 2017, Introduction to Plasma Physics with Space, Laboratory and Astrophysical Applications (Cambridge University Press)

Hamilton, K., Smith, C. W., Vasquez, B. J., & Leamon, R. J. 2008, Journal of Geophysical Research: Space Physics, 113, A01106

Hansteen, V. H., Leer, E., & Lie-Svendsen, Ø. 1999, in Proceedings of the 9th European Meeting on Solar Physics: Magnetic Fields and Solar Processes, Vol. 448, 1091

Harmon, J. K., & Coles, W. A. 2005, Journal of Geophysical Research: Space Physics, 110, 1

Harris, F. J. 1978, Proceedings of the IEEE, 66, 51

Harten, R., & Clark, K. 1995, Space Science Reviews, 71, 23

He, J., Marsch, E., Tu, C., Yao, S., & Tian, H. 2011, Astrophysical Journal, 731, 85

He, J., Tu, C., Marsch, E., & Yao, S. 2012a, Astrophysical Journal Letters, 745, L8

—. 2012b, Astrophysical Journal, 749, 86

He, J., Wang, L., Tu, C. Y., Marsch, E., & Zong, Q. 2015a, The Astrophysical Journal Letters, 800, L31

He, J., Tu, C. Y., Marsch, E., et al. 2015b, The Astrophysical Journal Letters, 813, L30

Hellinger, P., & Trávníček, P. M. 2014, Astrophysical Journal Letters, 784, L15

Hellinger, P., Trávníček, P. M., Kasper, J. C., & Lazarus, A. J. 2006, Geophysical Research Letters, 33, L09101

Heuer, M., & Marsch, E. 2007, Journal of Geophysical Research, 112, 1

Hnat, B., Chapman, S. C., & Rowlands, G. 2005, Physical Review Letters, 94

Hollweg, J. V., & Lee, M. A. 1989, Geophysical Research Letters, 16, 919

Horbury, T. S., Forman, M. A., & Oughton, S. 2008, Physical Review Letters, 101, 175005

Horbury, T. S., Wicks, R. T., & Chen, C. H. K. 2012, Space Science Reviews, 172, 325

Howes, G. G. 2008, Physics of Plasmas, 15

Howes, G. G., Bale, S. D., Klein, K. G., et al. 2012, Astrophysical Journal Letters, 753, 2

Howes, G. G., Cowley, S. C., Dorland, W., et al. 2006, The Astrophysical Journal, 651, 590

—. 2008, Journal of Geophysical Research: Space Physics, 113

Howes, G. G., & Quataert, E. 2010, The Astrophysical Journal Letters, 709, L49

Howes, G. G., Tenbarge, J. M., Dorland, W., et al. 2011, Physical Review Letters, 107, 1

Hundhausen, A. J. 1970, in Solar-Terrestrial Physics: Part II, ed. C. de Jager & E. R. Dyer, Vol. 29 (Springer Netherlands)

—. 1972, Coronal expansion and Solar Wind (Springer Physics and Chemistry in Space)

Hundhausen, A. J., Asbridge, J. R., Bame, S. J., Gilbert, H. E., & Strong, I. B. 1967a, Journal of Geophysical Research, 72, 87

Hundhausen, A. J., Bame, S. J., & Ness, N. F. 1967b, Journal of Geophysical Research, 72, 5265

Ibscher, D., & Schlickeiser, R. 2014, Physics of Plasmas, 21

Iroshnikov, P. S. 1964, Soviet Astronomy, 7, 566

Isenberg, P. A., Maruca, B. A., & Kasper, J. C. 2013, The Astrophysical Journal, 773, 164

Issautier, K., Mangeney, A., & Alexandrova, O. 2010, in AIP Conference Proceedings, Vol. 1216, 148

Jian, L. K., Russell, C. T., Luhmann, J. G., et al. 2010, Journal of Geophysical Research: Space Physics, 115, A12115

—. 2009, The Astrophysical Journal, 701, L105

Jian, L. K., Wei, H. Y., Russell, C. T., et al. 2014, The Astrophysical Journal, 786, 123

Kasper, J. C. 2002, PhD thesis, Massachusetts Institute of Technology

Kasper, J. C., Lazarus, A. J., & Gary, S. P. 2002a, Geophysical Research Letters, 29, 1839

—. 2002b, Geophysical Research Letters, 29, 20

—. 2008, Physical Review Letters, 101, 261103

Kasper, J. C., Lazarus, A. J., Steinberg, J. T., Ogilvie, K. W., & Szabo, A. 2006, Journal of Geophysical Research: Space Physics, 111, A03105

Kasper, J. C., Stevens, M. L., Korreck, K. E., et al. 2012, Astrophysical Journal, 745, 162

Kasper, J. C., Stevens, M. L., Lazarus, A. J., Steinberg, J. T., & Ogilvie, K. W. 2007, The Astrophysical Journal, 660, 901

Kasper, J. C., Klein, K. G., Weber, T., et al. 2017, The Astrophysical Journal, 849, 126

Kellogg, P. J., & Horbury, T. S. 2005, Annales Geophysicae, 23, 3765

Kepko, L., Viall, N. M., Antiochos, S. K., et al. 2016, Geophysical Research Letters, 43, 4089

Khintchine, A. 1934, Mathematische Annalen, 109, 604

Kiyani, K. H., Chapman, S. C., Khotyaintsev, Y. V., Dunlop, M. W., & Sahraoui, F. 2009, Physical Review Letters, 103, 075006

Kiyani, K. H., Chapman, S. C., Sahraoui, F., et al. 2013, The Astrophysical Journal, 763, 10

Kiyani, K. H., Osman, K. T., & Chapman, S. C. 2015, Philosophical Transactions of the Royal Society A: Mathematical, Physical and Engineering Sciences, 373, 20140155

Klein, K. G., Alterman, B. L., Stevens, M. L., Vech, D., & Kasper, J. C. 2018, Physical Review Letters, 120, 205102

Klein, K. G., & Howes, G. G. 2015, Physics of Plasmas, 22, 032903

—. 2016, The Astrophysical Journal Letters, 826, L30

Klein, K. G., Howes, G. G., Tenbarge, J. M., et al. 2012, Astrophysical Journal, 755

Klein, K. G., Howes, G. G., TenBarge, J. M., & Podesta, J. J. 2014, The Astrophysical Journal, 785, 138

Klein, K. G., Kasper, J. C., Korreck, K. E., & Stevens, M. L. 2017, Journal of Geophysical Research: Space Physics, 122, 9815

Kobayashi, S., Sahraoui, F., Passot, T., et al. 2017, The Astrophysical Journal, 839, 122

Kolmogorov, A. N. 1941, Doklady Akademiia Nauk SSSR, 32, 16

Koval, A., & Szabo, A. 2013, in AIP Conference Proceedings, Vol. 1539, 211

Kraichnan, R. H. 1965, Physics of Fluids, 8, 1385

Lacombe, C., Alexandrova, O., Matteini, L., et al. 2014, The Astrophysical Journal, 796, 5

Leamon, R. J., Matthaeus, W. H., Smith, C. W., & Wong, H. K. 1998a, The Astrophysical Journal Letters, 181

Leamon, R. J., Matthaeus, W. H., Smith, C. W., et al. 2000, The Astrophysical Journal, 537, 1054

Leamon, R. J., Smith, C. W., Ness, N. F., Matthaeus, W. H., & Wong, H. K. 1998b, Journal of Geophysical Research, 103, 4775

Leamon, R. J., Smith, C. W., Ness, N. F., & Wong, H. K. 1999, Journal of Geophysical Research: Space Physics, 104, 22331

Lepping, R. P., Acuña, M. H., Burlaga, L. F., et al. 1995, Space Science Reviews, 71, 207

Levy, E. H. 1976, Nature, 261, 394

Lion, S., Alexandrova, O., & Zaslavsky, A. 2016, The Astrophysical Journal, 824, 47

Lithwick, Y., & Goldreich, P. 2001, The Astrophysical Journal, 562, 279

Lithwick, Y., Goldreich, P., & Sridhar, S. 2007, The Astrophysical Journal, 655, 269

Livi, S., Marsch, E., & Rosenbauer, H. 1986, Journal of Geophysical Research, 91, 8045

Loureiro, N. F., & Boldyrev, S. 2017a, The Astrophysical Journal, 850, 182

—. 2017b, Physical Review Letters, 118, 245101

Luo, Q. Y., & Wu, D. J. 2010, The Astrophysical Journal, 714, L138

Mallet, A., & Schekochihin, A. A. 2017, Monthly Notices of the Royal Astronomical Society, 466, 3918

Maneva, Y. G., & Poedts, S. 2018, Astronomy & Astrophysics, 613, 10

Mangeney, A. 1991, in Advances in solar System Magnetohydrodynamics (Cambridge University Press)

Manoharan, P. K., Kojima, M., & Misawa, H. 1994, Journal of Geophysical Research: Space Physics, 99, 23411

Mariani, F., Ness, N. F., Burlaga, L. F., Bavassano, B., & Villante, U. 1978, Journal of Geophysical Research, 83, 5161

Mariani, F., Villante, U., Bruno, R., Bavassano, B., & Ness, N. F. 1979, Solar Physics, 63, 411

Marino, R., Sorriso-Valvo, L., D'Amicis, R., et al. 2012, Astrophysical Journal, 750, 41

Markovskii, S. A., & Vasquez, B. J. 2013a, The Astrophysical Journal, 768, 62

Markovskii, S. A., & Vasquez, B. J. 2013b, in Solar Wind 13, Vol. 1539, 239

—. 2016, The Astrophysical Journal, 820, 15

Markovskii, S. A., Vasquez, B. J., & Smith, C. W. 2008, The Astrophysical Journal, 675, 1576

—. 2015, The Astrophysical Journal, 806, 78

—. 2016, The Astrophysical Journal, 833, 212

Maron, J., & Goldreich, P. 2001, Astrophysical Journal, 554, 1175

Marsch, E. 2006, Living Reviews in Solar Physics, 3, 1

Marsch, E., Ao, X. Z., & Tu, C. Y. 2004, Journal of Geophysical Research, 109, A04102

Marsch, E., & Goldstein, H. 1983, Journal of Geophysical Research, 88, 9933

Marsch, E., Mühlhäuser, K. H., Rosenbauer, H., Schwenn, R., & Denskat, K. U. 1981, Journal of Geophysical Research, 86, 9199

Marsch, E., Mühlhäuser, K. H., Rosenbauer, H., Schwenn, R., & Neubauer, F. M. 1982a, Journal of Geophysical Research, 87, 35

Marsch, E., Mühlhäuser, K. H., Schwenn, R., et al. 1982b, Journal of Geophysical Research, 87, 52

Marsch, E., & Tu, C.-Y. 1990, Journal of Geophysical Research, 95, 11945

Marsch, E., & Tu, C. Y. 2001, Journal of Geophysical Research: Space Physics, 106, 227

Marsch, E., Vocks, C., & Tu, C. Y. 2003, Nonlinear Processes in Geophysics, 10, 101

Maruca, B. 2012, PhD thesis, Harvard University

Maruca, B. A., Bale, S. D., Sorriso-Valvo, L., Kasper, J. C., & Stevens, M. L. 2013, Physical Review Letters, 111, 241101

Maruca, B. A., & Kasper, J. C. 2013, Advances in Space Research, 52, 723

Maruca, B. A., Kasper, J. C., & Bale, S. D. 2011, Physical Review Letters, 107, 1

Maruca, B. A., Kasper, J. C., & Gary, S. P. 2012a, The Astrophysical Journal, 748, 137

—. 2012b, Astrophysical Journal, 748

Matteini, L., Hellinger, P., Landi, S., Trávníček, P. M., & Velli, M. 2012, Space Science Reviews, 172, 373

Matteini, L., Hellinger, P., Schwartz, S. J., & Landi, S. 2015, Astrophysical Journal, 812, 13

Matteini, L., Landi, S., Hellinger, P., et al. 2007, Geophysical Research Letters, 34, L20105

Matteini, L., Stansby, D., Horbury, T. S., & Chen, C. H. K. 2018, The Astrophysical Journal, 869, L32

Matthaeus, W. H., Breech, B., Dmitruk, P., et al. 2007, The Astrophysical Journal, 657, L121

Matthaeus, W. H., & Goldstein, M. L. 1982a, Journal of Geophysical Research, 87, 6011

—. 1982b, Journal of Geophysical Research, 87, 10,347

—. 1986, Physical Review Letters, 57, 495

Matthaeus, W. H., Goldstein, M. L., & Smith, C. W. 1982, Physical Review Letters, 48, 1256

Matthaeus, W. H., Servidio, S., & Dmitruk, P. 2008, Physical Review Letters, 101, 149501

Matthaeus, W. H., Servidio, S., & Dmitruk, P. 2010, in AIP Conference Proceedings, Vol. 1216, 184

Matthaeus, W. H., & Smith, C. 1981, Physical Review A, 24, 2135

Matthaeus, W. H., & Velli, M. 2011, Space Science Reviews, 160, 145

McComas, D. J., Ebert, R. W., Elliott, H. A., et al. 2008, Geophysical Research Letters, 35, L18103

McComas, D. J., Elliott, H. A., Schwadron, N. A., et al. 2003, Geophysical Research Letters, 30

McComas, D. J., Bame, S. J., Barraclough, B. L., et al. 1998, Geophysical Research Letters, 25, 1

McComas, D. J., Barraclough, B. L., Funsten, H. O., et al. 2000, Journal of Geophysical Research: Space Physics, 105, 10419

Meyrand, R., & Galtier, S. 2013, Physical Review Letters, 111, 1

Milano, L. J., Matthaeus, W. H., Dmitruk, P., & Montgomery, D. C. 2001, Physics of Plasmas, 8, 2673

Montgomery, D. C., & Tidman, D. A. 1964, Plasma Kinetic Theory (McGraw-Hill)

Narita, Y. 2012, Plasma Turbulence in the Solar System (Springer Briefs in Physics)

—. 2017, Nonlinear Processes in Geophysics, 24, 203

Narita, Y., Gary, S. P., Saito, S., Glassmeier, K. H., & Motschmann, U. 2011, Geophysical Research Letters, 38

Narita, Y., & Marsch, E. 2015, The Astrophysical Journal, 805, 24

Ness, N. F. 1970, Space Science Reviews, 11, 459

Neugebauer, M. 1976, Journal of Geophysical Research, 81, 78

Neugebauer, M., Goldstein, B. E., Bame, S. J., & Feldman, W. C. 1994, Journal of Geophysical Research: Space Physics, 99, 2505

Neugebauer, M., Goldstein, B. E., Smith, E. J., & Feldman, W. C. 1996, Journal of Geophysical Research, 101, 17047

Nyquist, H. 1928, Transactions of the American Institute of Electrical Engineers, 47, 617

Ogilvie, K. W. 1975, Journal of Geophysical Research, 80, 1335

Ogilvie, K. W., Chornay, D. J., Fritzenreiter, R. J., et al. 1995, Space Science Reviews, 71, 55

Oughton, S., Matthaeus, W. H., Wan, M., & Osman, K. T. 2015, Philosophical Transactions of the Royal Society A: Mathematical, Physical and Engineering Sciences, 373, 20140152

Oughton, S., Rädler, K.-H., & Matthaeus, W. H. 1997, Physical Review E, 56, 2875

Owens, M. J., & Forsyth, R. J. 2013, Living Reviews in Solar Physics, 10

Parker, E. N. 1958, The Astrophysical Journal, 128, 664

—. 1963, Interplanetary Dynamical Processes, Interscience Monographs and Texts in Physics and Astronomy, Vol. 8 (Interscience Publishers)

Passot, T., & Sulem, P. L. 2015, Astrophysical Journal Letters, 812, L37

Perez, J. C., & Boldyrev, S. 2009, Physical Review Letters, 102, 1

Perez, J. C., & Chandran, B. D. 2013, Astrophysical Journal, 776

Perri, S., & Balogh, A. 2010, The Astrophysical Journal, 714, 937

Perri, S., Carbone, V., & Veltri, P. 2010, The Astrophysical Journal Letters, 725, L52

Perri, S., Goldstein, M. L., Dorelli, J. C., & Sahraoui, F. 2012, Physical Review Letters, 109, 1

Phillips, J. L., Bame, S. J., Barnes, A., et al. 1995, Geophysical Research Letters, 22, 3301

Podesta, J. J. 2009, The Astrophysical Journal, 698, 986

Podesta, J. J., & Bhattacharjee, A. 2010, Astrophysical Journal, 718, 1151

Podesta, J. J., & Gary, S. P. 2011a, The Astrophysical Journal, 742, 41

—. 2011b, The Astrophysical Journal, 734, 15

Price, C. P., Swift, D. W., & Lee, L.-C. 1986, Journal of Geophysical Research, 91, 101

Reisenfeld, D. B., Gary, S. P., Gosling, J. T., et al. 2001, Journal of Geophysical Research: Space Physics, 106, 5693

Rezeau, L., Roux, A., & Russell, C. T. 1993, Journal of Geophysical Research: Space Physics, 98, 179

Roberts, O. W., & Li, X. 2015, The Astrophysical Journal, 802, 1

Roberts, O. W., Li, X., & Jeska, L. 2015, The Astrophysical Journal, 802, 2

Roberts, O. W., Li, X., & Li, B. 2013, The Astrophysical Journal, 769, 58

Roberts, O. W., Narita, Y., Li, X., Escoubet, C. P., & Laakso, H. 2017, Journal of Geophysical Research: Space Physics, 122, 6940

Rudakov, L., Mithaiwala, M., Ganguli, G., & Crabtree, C. 2011, Physics of Plasmas, 18, 12307

Russell, C. T. 1972, in NASA Special Pub. 308, Solar Wind, 365

Russell, C. T., Luhmann, J. G., & Strangeway, R. J. 2016, Space Physics: An Introduction (Cambridge University Press)

Šafránková, J., Němeček, Z., Němec, F., et al. 2015, Astrophysical Journal, 803, 1

Šafránková, J., Němeček, Z., Přech, L., & Zastenker, G. N. 2013, Physical Review Letters, 110, 025004

Sahraoui, F., Belmont, G., & Goldstein, M. L. 2012, Astrophysical Journal, 748, 100

Sahraoui, F., Goldstein, M. L., Belmont, G., Canu, P., & Rezeau, L. 2010, Physical Review Letters, 105, 131101

Sahraoui, F., Goldstein, M. L., Robert, P., & Khotyaintsev, Y. V. 2009, Physical Review Letters, 102, 231102

Salem, C. S., Howes, G. G., Sundkvist, D., et al. 2012, The Astrophysical Journal, 745, L9

Schekochihin, A. A. 2018, Journal of Plasma Physics (to be published)

Schekochihin, A. A., & Cowley, S. C. 2007, in Magnetohydrodynamics - Historical Evolutions and Trends, ed. S. S. Molokov, R. Moreau, & H. K. Moffatt (Springer: Fluid Mechanics and Its Applications), 85

Schekochihin, A. A., Cowley, S. C., Dorland, W., et al. 2008, Plasma Physics and Controlled Fusion, 50

—. 2009, The Astrophysical Journal Supplement Series, 182, 310

Servidio, S., Carbone, V., Primavera, L., Veltri, P., & Stasiewicz, K. 2007, Planetary and Space Science, 55, 2239

Shoji, M., Omura, Y., Tsurutani, B. T., Verkhoglyadova, O. P., & Lembege, B. 2009, Journal of Geophysical Research: Space Physics, 114

Smith, C. W., Hamilton, K., Vasquez, B. J., & Leamon, R. J. 2006, The Astrophysical Journal Letters, 645, L85

Smith, C. W., Matthaeus, W. H., Zank, G. P., et al. 2001a, Journal of Geophysical Research, 106, 8253

Smith, C. W., Mullan, D. J., Ness, N. F., Skoug, R. M., & Steinberg, J. T. 2001b, Journal of Geophysical Research, 106, 18625

Smith, C. W., Vasquez, B. J., & Hollweg, J. V. 2012, The Astrophysical Journal, 745, 8

Sorriso-Valvo, L., Marino, R., Carbone, V., et al. 2007, Physical Review Letters, 99

Stansby, D., Horbury, T. S., & Matteini, L. 2019a, Monthly Notices of the Royal Astronomical Society, 482, 1706

—. 2019b, Monthly Notices of the Royal Astronomical Society, 482, 1706

Steinberg, J. T., Lazarus, A. J., Ogilvie, K. W., Lepping, R. P., & Byrnes, J. B. 1996, Geophysical Research Letters, 23, 1183

Stix, T. H. 1992, Waves in Plasmas (American Institute of Physics)

Swanson, D. G. 2008, Plasma Kinetic Theory (CRC Press)

Tatsuno, T., Dorland, W., Schekochihin, A. A., et al. 2009, Physical Review Letters, 103, 015003

Taylor, G. I. 1938, Proceedings of the Royal Society A: Mathematical and Physical Sciences, 164, 476

Telloni, D., & Bruno, R. 2016, Monthly Notices of the Royal Astronomical Society: Letters, 463, L79

Telloni, D., Bruno, R., D'Amicis, R., Pietropaolo, E., & Carbone, V. 2012, The Astrophysical Journal, 751, 19

Telloni, D., Bruno, R., & Trenchi, L. 2015, The Astrophysical Journal, 805, 46

TenBarge, J. M., & Howes, G. G. 2012, Physics of Plasmas, 19, 55901

Tenbarge, J. M., & Howes, G. G. 2013, Astrophysical Journal Letters, 771, 2

TenBarge, J. M., Podesta, J. J., Klein, K. G., & Howes, G. G. 2012, The Astrophysical Journal, 753, 107

Tenerani, A., & Velli, M. 2017, The Astrophysical Journal, 843, 26

Thomas, B. T., & Smith, E. J. 1980, Journal of Geophysical Research, 85, 6861

Torrence, C., & Compo, G. P. 1998, Bulletin of the American Meteorological Society, 79, 61

Tsurutani, B. T., Arballo, J. K., Mok, J., et al. 1994, Geophysical Research Letters, 21, 633

Tu, C. Y., & Marsch, E. 1995, Space Science Reviews, 73, 1

—. 2001, Journal of Geophysical Research, 106, 8233

—. 2002, Journal of Geophysical Research: Space Physics, 107, 1

Tu, C. Y., Marsch, E., & Qin, Z. R. 2004, Journal of Geophysical Research: Space Physics, 109, 1

Turner, A. J., Gogoberidze, G., Chapman, S. C., Hnat, B., & Müller, W. C. 2011, Physical Review Letters, 107, 1

Vafin, S., Lazar, M., Fichtner, H., Schlickeiser, R., & Drillisch, M. 2018, Astronomy & Astrophysics, 613, 23

Vafin, S., Riazantseva, M., & Pohl, M. 2019, The Astrophysical Journal, 871, L11

van Dyke, M. 1982, An Album of Fluid Motion (The Parabolic Press)

Vasquez, B. J., & Markovskii, S. A. 2012, The Astrophysical Journal, 747, 19

Velli, M., Grappin, R., & Mangeney, A. 1989, Physical Review Letters, 63, 1807

Veltri, P., Nigro, G., Malara, F., Carbone, V., & Mangeney, A. 2005, Nonlinear Processes in Geophysics, 12, 245

Verdini, A., Grappin, R., Pinto, R., & Velli, M. 2012, The Astrophysical Journal Letters, 750, L33

Verscharen, D. 2012, PhD thesis

Verscharen, D., Bourouaine, S., & Chandran, B. D. 2013a, Astrophysical Journal, 773, 163

Verscharen, D., Bourouaine, S., Chandran, B. D., & Maruca, B. A. 2013b, Astrophysical Journal, 773

Verscharen, D., Chandran, B. D., Bourouaine, S., & Hollweg, J. V. 2015, Astrophysical Journal, 806

Verscharen, D., & Chandran, B. D. G. 2018, Research Notes of the AAS, 2, 13

Verscharen, D., Klein, K. G., & Maruca, B. A. 2019, Living Reviews in Solar Physics (to be published), arXiv:1902.03448

Verscharen, D., & Marsch, E. 2011, Annales Geophysicae, 29, 909

Vlasov, A. A. 1945, Journal of Physics USSR, 9, 25

Weber, E. J., & Davis, L. J. 1967, The Astrophysical Journal, 148, 217

Welch, P. D. 1967, IEEE Transactions on Audio and Electroacoustics, AU-15, 70

Wicks, R. T., Forman, M. A., Horbury, T. S., & Oughton, S. 2012, The Astrophysical Journal, 746, 103

Wicks, R. T., Horbury, T. S., Chen, C. H. K., & Schekochihin, A. A. 2010, Monthly Notices of the Royal Astronomical Society, 407, L31

Wicks, R. T., Mallet, A., Horbury, T. S., et al. 2013, Physical Review Letters, 110, 1

Wicks, R. T., Alexander, R. L., Stevens, M. L., et al. 2016, The Astrophysical Journal, 819, 6

Wiener, N. 1930, Acta Mathematica, 55, 117

Wilson III, L. B., Stevens, M. L., Kasper, J. C., et al. 2018, The Astrophysical Journal Supplement Series, 236, 41

Woltjer, L. 1958a, Proceedings of the National Academy of Sciences, 44, 489

—. 1958b, Proceedings of the National Academy of Sciences, 44, 833

Woodham, L. D., Wicks, R. T., Verscharen, D., & Owen, C. J. 2018, The Astrophysical Journal, 856, 49

Woodham, L. D., Wicks, R. T., Verscharen, D., et al. 2019, The Astrophysical Journal Letters, 884, L53

Xu, F., & Borovsky, J. E. 2015, Journal of Geophysical Research: Space Physics, 120, 70

Yao, S., He, J. S., Marsch, E., et al. 2011, Astrophysical Journal, 728, 146

Yoon, P. H. 2017, Reviews of Modern Plasma Physics, 1, 4

Zhao, G. Q., Feng, H. Q., Wu, D. J., et al. 2018, Journal of Geophysical Research: Space Physics, 123, 1715

Zhao, G. Q., Feng, H. Q., Wu, D. J., Pi, G., & Huang, J. 2019, The Astrophysical Journal, 871, 175